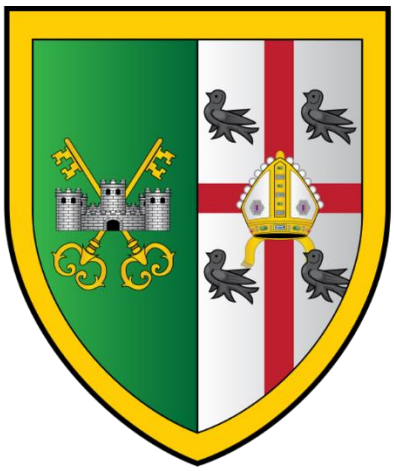
Measuring Fracture Resistance Behaviour of Tungsten Using Chevron-Notched Micro-Cantilevers

Bo-Shiuan Li

Supervisors: Prof. D.E.J. Armstrong, Prof. T.J. Marrow,

Prof. S.G. Roberts





St. Peter's College

University of Oxford

Michaelmas Term 2017

Preface

This thesis describes the work carried out by the author in the Department of Materials, University of Oxford, from October 2013 to December 2017, under the supervision of Prof. D.E.J. Armstrong, Prof. T.J. Marrow, and Prof. S.G. Roberts.

No part of this thesis has been previously submitted for a degree at this or any other university. The work of other authors has been drawn upon and has been referenced and acknowledged in the text. A list of references is given at the end of the thesis.

Some of the work in the thesis has been reported at the following conferences and in the following publications:

Conferences

- **Micro Materials User Meeting 2017 -** Stable High-Temperature Micro-Fracture Tests of Tungsten Cantilevers up to 700 °C *(invited)*
- **MRS Spring 2017** - Microscale Fracture Experiments of Chevron-Notched Tungsten Cantilevers up to 700 °C
- **Gordon Research Seminar on Thin Film and Small Scale Mechanics 2016 -** Extreme Fracture Resistance Behaviour of Tungsten at the Nanoscale *(invited)*
- **European Student Divertor Research Workshop 2016 -** Microscale Fracture Testing of Tungsten Alloy for Nuclear Fusion
- **ECI Nanomechanical Testing in Materials Research and Development V 2015 -** High-Temperature Fracture Test Using Chevron-Notched Tungsten Microcantilevers
- **12th International Conference on Mechanical Behaviour 2015 -** Multi-scale Fracture Behaviour of Tungsten Alloys for Nuclear Fusion

Abstract

The fracture properties of tungsten-tantalum alloy (W-1%Ta), one of the candidate material for the plasma facing components in proposed fusion reactor design, were investigated using microscale chevron-notched cantilever bending tests at both ambient and high temperature (700 °C) conditions.

Finite element analysis (FEA) were used to optimise the crack stability of the chevron notch design and obtain the geometry-dependent stress-intensity factors (SIFs) and stiffness vs. crack length relationships. Room temperature chevron-notched micro-cantilevers of single-crystal silicon were used to validate the FE-calculated SIFs. The average fracture toughness (K_{Ic}) measured from Si cantilevers was 0.85±0.04 MPa·$m^{0.5}$, which was in good agreement with previously reported macroscopic values (0.7~1 MPa·$m^{0.5}$). This result showed no size-effect in fracture toughness of the intrinsically brittle silicon, and chevron-notched micro-cantilever was an effective micro-specimen geometry for measuring fracture toughness.

Stable crack growth (SCG) accompanied with plastic deformation were observed in most room temperature tested chevron-notched W-1%Ta micro-cantilevers. Linear-elastic fracture mechanical analysis (LEFM) previously used for the brittle Si cantilevers will underestimate the true fracture toughness of the semi-brittle W-1%Ta, hence an elastic-plastic fracture mechanical analysis (EPFM) was employed to measure the fracture toughness using the fracture resistance curve (J-R curve) approach. The average EPFM-calculated fracture toughness at crack instability (K_{Qc}) was 25.8±2.3 MPa·$m^{0.5}$, whereas the average LEFM-calculated fracture toughness was 4.3±0.2 MPa·$m^{0.5}$. The EPFM-calculated microscopic K_{Qc} were significantly higher than previously reported macroscopic value, possibly due to the larger crack tip plastic zone to specimen size ratio. Using Irwin's estimation, the crack tip plastic zone radius of W-1%Ta micro-cantilevers ranged from 200~1500 nm, which were significantly larger than the crack tip plastic zone radius of the intrinsically brittle silicon (~5 nm), suggesting the size effect seen in fracture toughness might arise from the larger plastic zone to specimen size ratio.

Chevron-notched W-1%Ta micro-cantilevers up to 700 °C were tested using a high-temperature nanoindenter (Micro Materials® NanoTest Xtreme). Prior testing, the temperature of the indenter and sample were carefully matched to minimise the thermal drift effects. The

EPFM-calculated K_{Qc} increased gradually with temperature, until a sharp increase (40.5±3.2 $MPa \cdot m^{0.5}$) was observed at 700 °C. This microscopic brittle-to-ductile transition temperature (BDTT) was significantly higher than the macroscopic BDTT (700 vs. 200 °C), possibly due to the higher strain rate used and the tantalum addition. The amount of SCG also increased with temperature, ranging from 500 nm at RT to 800 nm at 700 °C. The larger microscopic K_{Qc} (compared to macroscopic K_{Ic} in the same temperature regime) and SCG were probably caused by the combination of the extended crack tip plastic zone and extensive dislocation shielding effects, due to the thermally-activated dislocation activities.

This thesis has demonstrated micro-fracture tests using chevron-notched cantilevers are capable of measuring the fracture resistance curves from the semi-brittle W-1%Ta. Due to larger crack tip plastic zone to specimen size ratio, the EPFM-calculated K_{Qc} were significantly higher than macroscopic values. A specimen size effect to fracture toughness is suggested, which should be carefully considered when performing micro-fracture testing of ductile materials.

Acknowledgements

I would like to thank my supervisors, Dave Armstrong, James Marrow, and Steve Roberts for all their supports, guidance, and mentoring over the last four years. From frequent discussions I not only learnt material science, but also the way to think scientifically. I am truly grateful for the opportunity to study under their supervision.

I would like to thank Angus Wilkinson for allowing me to attend the Micromechanics meetings. I will try my very best to continue annoying everyone with questions.

Thanks to members in the Department of Materials for providing all the trainings and supports: Gareth Hughes, Gabriella Chapman, Greg Cook, and Graham Wyatt for EM-related, Laurie Walton and Pete Flaxman for workshop, Karen Disney and Rebecca Bradford for administrative, Mimi Nguyen and Paula Toppings for practical demonstrations.

I also want to thank Andy Bird and Adrian Harris from Micro Materials® for all their help on the "Hot Nanoindenter"

Thanks to members of the MFFP/Micromechanics group for making 21 Banbury such a nice place to work: Ed Tarleton, Slava Kuksenko, Anna Kareer, Phani Karamched, Maria Auger, Jicheng Gong, James Gibson, Katie Plummer, and Helen Pratt. The Watanabe Office: Junnan Jiang, Luke Hewitt, General Tanaka, Chris Jones, Kris Bhojwani, and Yehven Zayachuk.

Also, I would like to thanks my Taiwanese friends. I am fortunate to have your supports during many events I hosted and to keep me company.

Finally, thanks to Mum, Dad, and Niki, for supporting me all the way through my DPhil. I will not be able to finish this journey without your kind encouragements and loves.

List of Abbreviations

3PBT	Three-point bending test
4PBT	Four-point bending test
AFM	Atomic force microscopy
ASTM	American Society for Testing and Materials
BCC	Body centre cubic
BDTT	Brittle-to-ductile transition temperature
CBN	Cubic boron nitride
CRSS	Critical resolved shear stress
CSM	Continuous stiffness measurement
CVD	Chemical vapour deposition
DCB	Double-cantilever beam
DDD	Discrete dislocation dynamic
DENT	Double edge notched tensile
DEMO	DEMOnstration reactor
DIC	Digital image correlation
DT	Deuterium tritium
EBSD	Electron backscatter diffraction
ECCI	Electron channelling contract imaging
EDM	Electric discharge machining
EPFM	Elastic-plastic fracture mechanics
FCC	Face centred cubic
FIB	Focused ion beam
FEA	Finite element analysis
IPF	Inverse pole figure
ITER	International Thermonuclear Experimental Reactor
JET	Joint European Torus
LEFM	Linear-elastic fracture mechanics
ODS	Oxide dispersion strengthened

PFCs	Plasma facing components
PID	Proportional integral derivative
PKA	Primary knock on atom
PVD	Physical vapour deposition
RAFS	Reduced activation ferritic steel
SCG	Stable crack growth
SEM	Scanning electron microscopy
SIA	Self-interstitial atom
SIF	Stress-intensity factor
SRIM	Stopping Range of Ions in Matter
TEM	Transmission electron microscopy
UFG	Ultra-fine grained
WOF	Work-of-fracture

Contents

I INTRODUCTION 1

1.1 Nuclear Fusion.....1

1.2 Materials for Nuclear Fusion……..4

1.2.1 Tungsten for Fusion……5

1.2.2 Fracture Properties of Tungsten……..6

1.2.3 Radiation Damage Effects to Mechanical Properties……8

1.2.4 Micromechanical Tests in Characterising Radiation Damage……..11

II LITERATURE REVIEW **13**

2.1 Overview of Fracture Mechanics…….13

2.1.1 Linear-Elastic Fracture Mechanics……...13

2.1.2 Elastic-Plastic Fracture Mechanics……...19

2.1.3 Fracture Resistance Curves……...23

2.1.4 Summary……...24

2.2 Micro-Fracture Tests…….25

2.2.1 Nanoindentation……25

2.2.2 Micro-Cantilever……..26

2.2.3 Micro-Pillar……...31

2.2.4 Other Geometries……..32

2.2.5 Micro-Fracture Tests Summary……37

2.3 High-Temperature Micro-Fracture Tests……..…….39

2.4 Chevron-Notched Specimen……..45

2.4.1 Early Developments of Chevron-Notched Specimens…….45

2.4.2 Theoretical Basis for Chevron-Notched Specimens…….48

2.4.3 Materials with Rising R-Curve Behaviour……..……50

2.5 Literature Review Summary……52

2.6 Research Aims……52

III EXPERIMENTAL METHODS 47

3.1 Sample Preparation……...47

3.2 Scanning Electron Microscopy……50

3.3 Electron Backscatter Diffraction……..50

3.4 Focused Ion Beam……..52

3.5 Nanoindentation……55

3.5.1 Basic Operation…….56

3.5.2 Continuous Stiffness Measurement……..58

3.5.3 NanoVision® Scanning Stage……...59

3.6 High-Temperature Nanoindentation……...61

3.6.1 Micro Materials® NanoTest Xtreme…….62

3.6.2 Testing in Vacuum……63

3.6.3 Thermal Drift Control……...64

3.6.4 Degradation of Indenter at High Temperature……..67

3.6.5 Load Partial-Unload Method……68

IV FINITE ELEMENT MODELLING AND VALIDATION OF CHEVRON-NOTCHED MICRO-CANTILEVERS 70

4.1 Introduction to Finite Element Analysis……..70

4.2 Modelling Methodologies……..71

4.2.1 3-D Modelling of Chevron-Notched Micro-Cantilever……71

4.2.2 Mesh Convergence Study……73

4.2.3 Calculation of the J-integral using the Contour Integral Method……75

4.3 Optimisation of the Chevron Notch Geometry……...79

4.4 Validation using Single-Crystal Silicon Micro-Cantilever…….84

4.5 Summary……87

V ROOM TEMPERATURE MICRO-FRACTURE TESTS OF W-1%TA MICRO-CANTILEVERS 88

5.1 Introduction……88

5.2 Elastic-Plastic Triangular Cantilevers……90

5.3 Continuous Stiffness Measurement Tested Cantilever……..96

5.3.1 Effect of the Indenter Spring Stiffness……..97

5.3.2 Scattering of the CSM-Measured Stiffness……...99

5.3.3 Post-Test Fractography and Crack Length Measurements…….101

5.4 The Load Partial-Unload Stiffness Measurement Method……..103

5.4.1 Effects of Tip Embedding to Loading/Unloading Stiffness……...105

5.4.2 Effects of Loading/Unloading Rate and Thermal Drift to Displacement...108

5.4.3 Effects of Tip Embedding to Stiffness Values at Initial Cycles…….111

5.4.4 Effects of Hold Time to Unloading Stiffness…….114

5.4.5 Summary of Load Partial-Unload Method Optimisation……....118

5.5 Room Temperature Load Partial-Unload Tested Cantilevers……119

5.5.1 Cantilever B3 (stable crack growth with clear distinction between stable/unstable crack growth regime)……..120

5.5.2 Cantilever B2 (stable crack growth with ductile fracture surface)…….122

5.5.3 Cantilever B1 (no stable crack growth, fracture along grain boundary)….125

5.5.4 Test Summary…….127

5.6 Fracture Mechanical Analysis……128

5.6.1 Linear-Elastic Fracture Mechanics – Methodology & Analysis…….128

5.6.2 Elastic-Plastic Fracture Mechanics – Methodology……...130

5.6.3 Elastic-Plastic Fracture Mechanics – Analysis……...133

5.6.4 Fracture Mechanical Analysis Summary……136

5.6.5 Specimen Size for Elastic-Plastic Fracture Mechanical Analysis……..137

5.7 Summary of the Room Temperature Cantilevers……138

VI HIGH TEMPERATURE MICRO-FRACTURE TESTS OF W-1%TA MICRO-CANTILEVERS 139

6.1 Thermal Drift Effects in High-Temperature Micro-Fracture Tests……...139

6.1.1 Thermal Drift Effects to Displacement Measurements……..140
6.1.2 Thermal Drift Effects to Surface Scanning…….145
6.1.3 Thermal Drift Effects Summary…….147
6.2 High-Temperature Micro-Fracture Tests…….149
6.2.1 Temperature Effect to Modulus, Yield Stress, and Hardness of Tungsten.150
6.2.2 Micro-Cantilever Tested at 400 °C (L2)…….153
6.2.3 Micro-Cantilever Tested at 500 °C (E4)…….156
6.2.4 Micro-Cantilever Tested at 600 °C (E3)…….159
6.2.5 Micro-Cantilever Tested at 700 °C (E2)…….163
6.2.6 Test Summary…….166
6.3 Elastic Plastic Fracture Mechanical Analysis……...168
6.4 Discussions……174
6.4.1 Temperature Effects to Crack Blunting……..174
6.4.2 Temperature Effects to Creep Relaxation……...177
6.4.3 Brittle-to-Ductile Transition Temperature……..178
6.4.4 Strain Rate and Impurity Effects to the BDTT……...181
6.5 Summary……...184
VII CONCLUSIONS AND FUTURE WORK 185
7.1 Summary of Results……185
7.2 Future Works……...188
7.2.1 Micro-Fracture Tests on Ion-Irradiated Tungsten……...188
7.2.2 Measuring the Macroscopic Fracture Resistance Behaviour of Tungsten..189
7.2.3 Modelling of Dislocation-Crack Tip Interaction……191
VIII REFERENCES 192

I INTRODUCTION

Nuclear energy has renewed its interest to the scientific communities over the last decades because of the increasing worldwide energy demand whilst addressing climate change [1]. Current nuclear fission reactors seek for extension beyond its original 40 years lifetime, which requires management of material aging. Next generation fission reactors (Gen IV) are designed to satisfy the requirements for both safer operation and higher efficiency [2]. Nuclear fusion, on the other hand, is extremely attractive, with almost no generation of greenhouse gases, long-life radioactive isotopes, and potentially unlimited energy production. The utmost issue for commercializing Gen IV fission and future fusion reactors is developing suitable structural materials to withstand the extreme operating environment for a profitable amount of time [3].

1.1 Nuclear Fusion

Most fusion experiments use the deuterium-tritium (D-T) reaction to generate fusion power. The D-T reaction, shown in **Eq. 1.1**, yields a helium nucleus (α particle) and a neutron. The neutron carries 14.1 MeV, which is approximately 80 % of the generated energy, is used for electricity production. The helium nucleus uses its energy (4 MeV) to heat the plasma for sustaining the fusion reaction. Over the past decades, fusion researchers have focused on the development of magnetic confinement reactors to generate laboratory-scale fusion reaction. One successful example is the Joint European Torus (JET) at the Culham Centre for Fusion Energy in Oxfordshire, UK. However, successful generation of fusion power will depend on a triple product, consisting of temperature, reactant density, and confinement time [4]. Currently, the confinement time can only be extended by enlarging the plasma volume. Hence, larger reactors are essential to commercialise fusion reactors.

$$^{2}_{1}D + ^{3}_{1}T \rightarrow ^{4}_{2}He + n^{0} \ (\boldsymbol{Eq.\ 1.1})$$

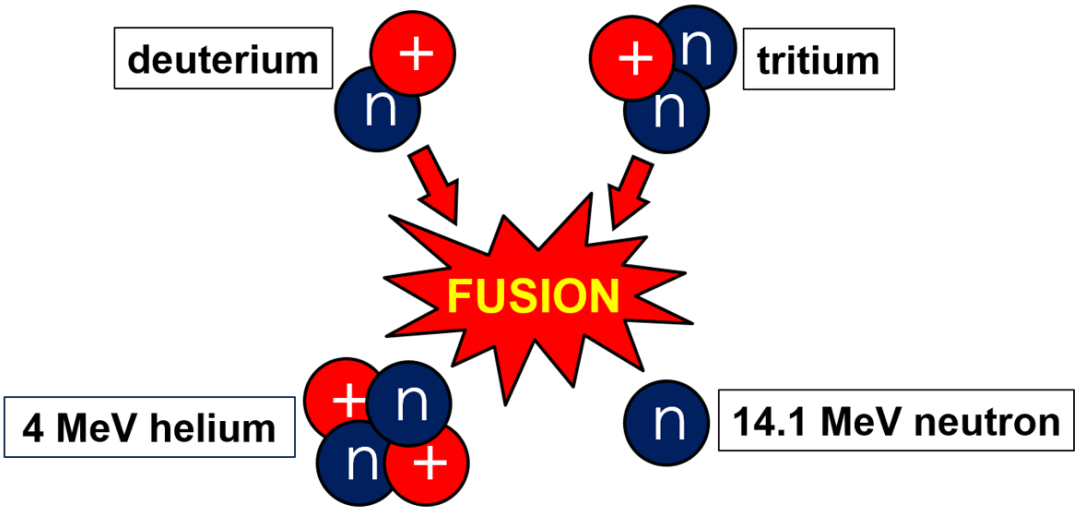


Fig. 1.1 The deuterium-tritium (D-T) fusion reaction

The International Thermonuclear Experimental Reactor (ITER) at Cadarache, France is the next step towards commercialising fusion power. It is funded and managed by seven members, including the EU, India, China, Russia, Japan, South Korea, and the US. It will be a scaled-up version of JET, with dimensions twice the size and plasma volume ten times of JET [5]. For a size comparison, schematic drawing of JET and ITER is given in **Fig. 1.2**, and dimensions are provided in **Table. 1.1**. ITER aims to achieve the long-awaited goal; from lab-scale plasma physic experiment to a self-sustainable power-generating facility. The successor of ITER, the Demonstration Power Plant, DEMO, will be the first commercial fusion power plant in the world, aiming to produce at least four times that of ITER's fusion power on a continual basis [8].

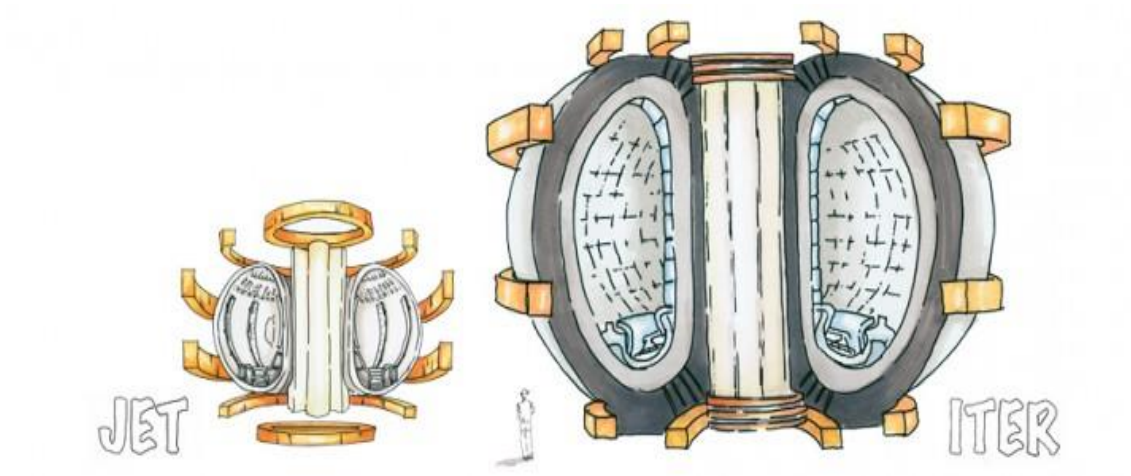


Fig. 1.2 Schematic drawings of JET and ITER for size comparison

	JET	**ITER**
Radius (m)	3	6.2
Volume (m^3)	90	840
Power Factor Q	0.65	10
Fusion Power (MW)	16.1	500
Partner	EU (managed by EUROfusion)	China, EU, India, Korea, Russia, US

Table 1.1 Dimension details for JET and ITER [6]

1.2 Materials for Nuclear Fusion

High-performance structural materials are critical for the successful design of proposed fusion reactors. For example, the plasma facing components (PFCs) are required to operate in an environment which comprises of highly energetic neutrons, transmutation gases (He and H), and intensive plasma-generated heat fluxes. It is predicted that the first wall of ITER will reach 120 dpa (displacement per atom, a common unit for quantifying radiation damage) of neutron damage, with 1200 appm of helium concentration generated over an estimated five years operation time [7]. On the other hand, the divertor will require materials to withstand an additional heat flux of 15 MW/m^2, which introduces massive cyclic thermal-mechanical stresses [3]. For optimum thermal efficiency, it also needs to operate above 700 °C. **Fig. 1.3** illustrates the general temperature and radiation damage (in dpa) requirements for both advanced fission and fusion reactors.

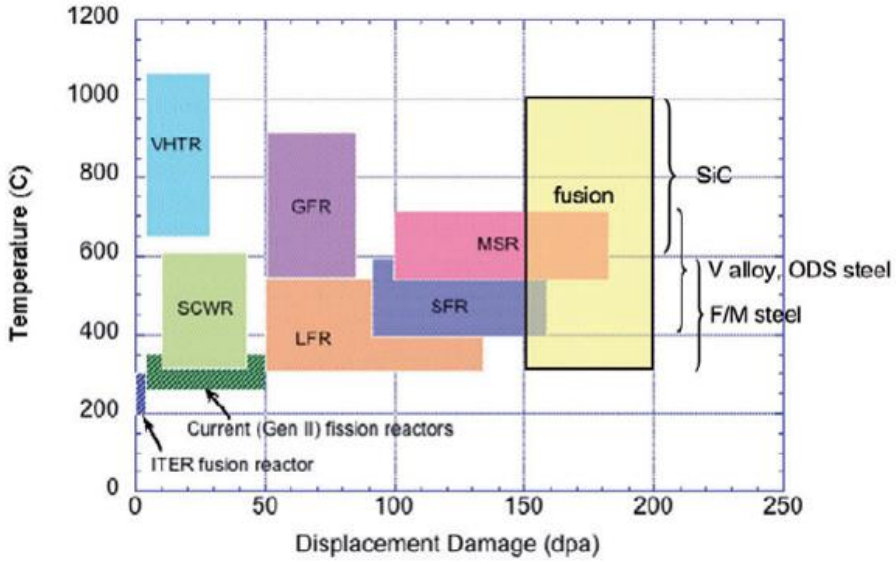


Fig. 1.3 Overview of operating temperature and radiation damage requirements for structural materials in current (Gen II, Gen III), proposed (Gen IV), and fusion reactors [3]

Only few materials can provide the necessarily mechanical properties to withstand the extreme fusion environment. In addition, to address the long-term environmental impact, strong emphasis has been placed on low-activation fusion structural materials [8]. Conventional high-activation strengthening solutes such as Mo and Nb are replaced by low-activation elements, such as W and V. This will further limit suitable materials to only eight elements: C, Ti, Si, Fe, V, Cr, W, and Ta. Examples of developed structural material systems for fusion reactor are: (1) reduced-activation oxide dispersion strengthened (ODS) ferretic/martensitic (RAFM-ODS) steels, (2) refractory metals (W, Cr), and (3) silicon carbide composites (SiC/SiC) [9]. The focus of this thesis is tungsten-based alloys for fusion structural applications, hence the mechanical properties of tungsten, before and after irradiation, will be briefly discussed in the following section.

1.2.1 Tungsten for Fusion

Tungsten possesses the highest melting point of all metals (~3500 K), high thermal conductivity (~1.75 W/cm·K at RT), excellent high temperature strength (~500 MPa at 1273 K), and high recrystallization temperature (~1500 K) which are all desired for fusion environment. The creep strength can also be enhanced by introducing dispersed oxides such as lanthana or yttria to stabilise the grains [10]. However, major issue for tungsten as a structural material is its intrinsic brittleness (~5 $MPa \cdot m^{0.5}$ at RT), and high brittle-to-ductile transition temperature (BDTT around 500 K for pure tungsten). Moreover, neutron irradiation will shift tungsten's BDTT even higher, further narrowing the operation temperature window for tungsten as a structural material [11].

1.2.2 Fracture Properties of Tungsten

Tungsten is a body-centre cubic (BCC) metal that generally exhibits low fracture toughness at room temperature (~5 MPa·$m^{0.5}$) [12] which undergoes a brittle-to-ductile transition (BDT) at temperatures above ~200 °C [13]. Fracture toughness vs. temperature for polycrystalline tungsten is shown in **Fig. 1.4**, where the BDTT also increases with strain rate [14]. The intrinsic brittleness of a material is defined by its Peierls stress, which is the stress required to move a dislocation through a perfect crystal at 0 K. The strong-bonding and non-close packed BCC structure of tungsten gives rise to a high Peierls stress, hence resulting the low dislocation mobility and intrinsic brittleness at room temperature [15]. The BDTT follows an Arrhenius relationship between the thermally-activated activation energy for dislocation glide and the applied strain rate, given in **Eq. 1.2**.

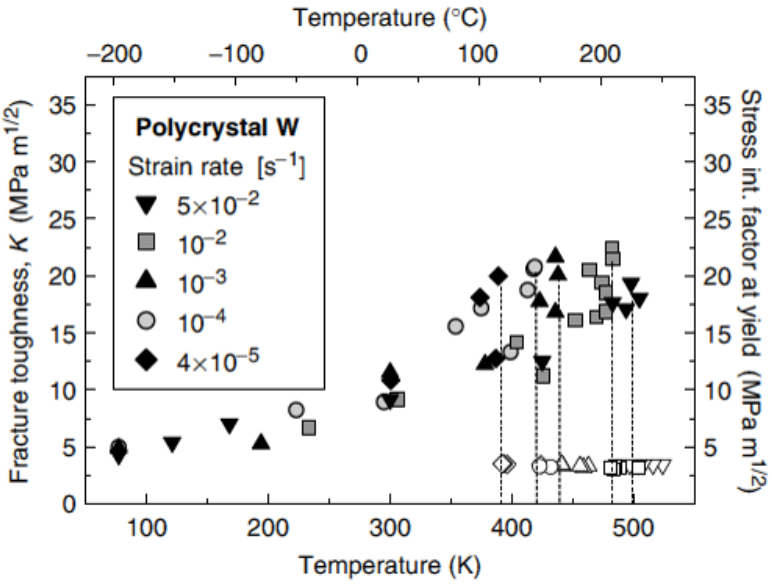


Fig. 1.4 Fracture toughness (solid symbols) measured in polycrystalline tungsten. Open symbols represent ductile specimens. T_{BDT} increases with increasing strain rate. For ductile specimens (no fracture), the stress intensity factor at yield is shown on the right axis [14]

$$T_{BDT} = \frac{-E_{BDT}}{k}\left[\ln\left(\frac{\dot{\varepsilon}}{A}\right)\right] \quad (\boldsymbol{Eq.\,1.2})$$

where E_{BDT} is the activation energy for dislocation glide, $\dot{\varepsilon}$ is the strain rate, k is the Boltzmann constant, and A is another constant

In addition. the value of E_{BDT} strongly depends on the impurity content - pure tungsten has value of 1.05 eV, whereas sintered tungsten has a higher value of 1.45 eV, due to the dislocation-solute interaction [14]. Therefore, the BDTT can be modified extrinsically through applied strain rate, and also intrinsically through impurity content.

To improve the intrinsic brittleness of tungsten as a structural material, developments have mainly focus on ductilisation and decreasing the BDTT. Currently, three ductilisation strategies are employed: (1) alloying, (2) refining grain size, and (3) synthesising tungsten composites. Rhenium (Re) is the only known alloying element to improve the ductility of tungsten [16]. Re modifies the core structure of the 1/2<111> type screw dislocation, improving its mobility by decreasing the Peierls stress [17]. It also increases the number of available slip systems by changing the slip plane from {110} to {112} type [18]. However, the usage of W-Re alloy in a fusion environment is not favourable due to the high cost and formation of brittle second phases after irradiation [19]. Charpy tests ranging from 400~1100 °C had been conducted on W-Ta, W-V, and W-Mo alloys. However, all results showed lower toughness and an increase in the BDTT [20]. Therefore, tungsten cannot be easily ductilised by alloying elements, except with rhenium.

Another strategy to ductilise tungsten is to employ grain refinement. Ultrafine grain (UFG) materials exhibit an attractive combination of improved strength and pseudo-plasticity from grain delamination [21]. This can be done either by severe plastic deformation (SPD) [22]

or mechanical alloying [23]. However, due to high costs, both techniques are not suitable for producing industrial scale structural components. Currently, only small quantity of UFG-tungsten can be produced on a laboratory-based scale.

Tungsten can also be ductilised through fibre reinforcements. He et al. had successfully fabricated tungsten fibre reinforced tungsten copper composite [24]. By infiltrating the copper at high temperature, a stronger yet more ductile tungsten-based composite could be formed. This created an extrinsic toughening mechanism, as the cracks were capable of deflecting at the fibre/matrix interface, allowing energy dissipation via interfacial debonding and friction. Fracture tests of this composite showed significant amount stable crack propagation before final catastrophically failure [25]. However, manufacturing of tungsten composites still suffers from industrial scale production; it is currently impossible to produce reactor-scale structural components.

1.2.3 Radiation Damage Effects to Mechanical Properties

Radiation damage from energetic particles (neutrons, ions, and protons) creates defects that accumulate within the crystalline material matrix. **Fig. 1.5** illustrates the process of an energetic particle interacting with the crystal lattice and forming displacement cascade. However, at reactor operating temperature (~$0.3T_m$ for commercial light water reactors), the thermal energy is sufficient for the irradiation-induced defects, such as vacancies and self-interstitial atoms (SIAs) to diffuse and recombine with each other. Therefore, the actual displacement damage is usually a fraction of its calculated value. As dose increases, the retained point defects evolve into more complicated microstructures, such as defect clusters, dislocation loops/lines, voids, bubbles, and precipitates. The accumulation effects of these irradiation-induced defects will modify material properties, usually undesirable, such as dimensional

instability, hardening, embrittlement, increasing the BDTT, and creep [26]. Since the primary goal of this thesis is to measure the fracture properties of tungsten, the next following context will focus on the irradiation-induced embrittlement and shift in BDTT.

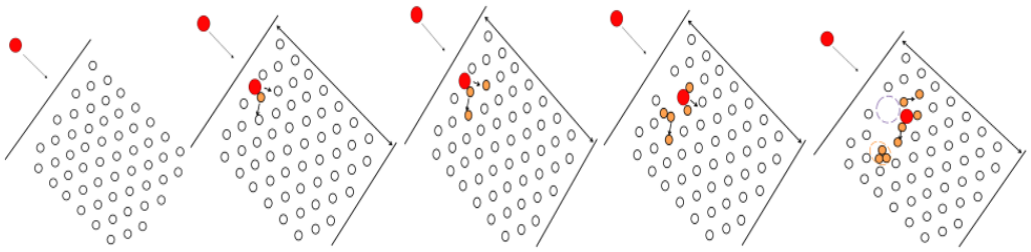


Fig. 1.5 A charged particle interacts with crystal lattice and forms displacement cascade. Red atom is the primary knock on atom (PKA), dotted atom indicates a vacancy, and orange atoms are the SIAs

The primary mechanism for irradiation-induced embrittlement is the hardening produced by the irradiation-induced defects. **Fig. 1.6** illustrates the embrittlement processes sequentially: (1) generation of defects by displacement damage coming from the neutron/ion bombardments, usually in form of single and small clusters of vacancies and SIAs, (2) diffusion of defects enhance solute diffusion and formation of nanoscale defect clusters, (3) dislocation pinning and hardening by defect clusters, and (4) less ductility and hardening-induced shift in the BDTT [27]. An empirical equation is used to describe the irradiation-induced embrittlement, shown in **Eq. 1.3**. Increase in the yield stress, $\Delta\sigma_y$, due to the irradiation-induced hardening, will raise the temperature at which the critical stress σ_c is reached.

$$M\left[\sigma_{yu}(T) + \Delta\sigma_y\right] = \sigma_c \quad (\boldsymbol{Eq.\,1.3})$$

where M is a non-dimensional stress concentration coefficient, and $\sigma_{yu}(T)$ is the unirradiated yield stress

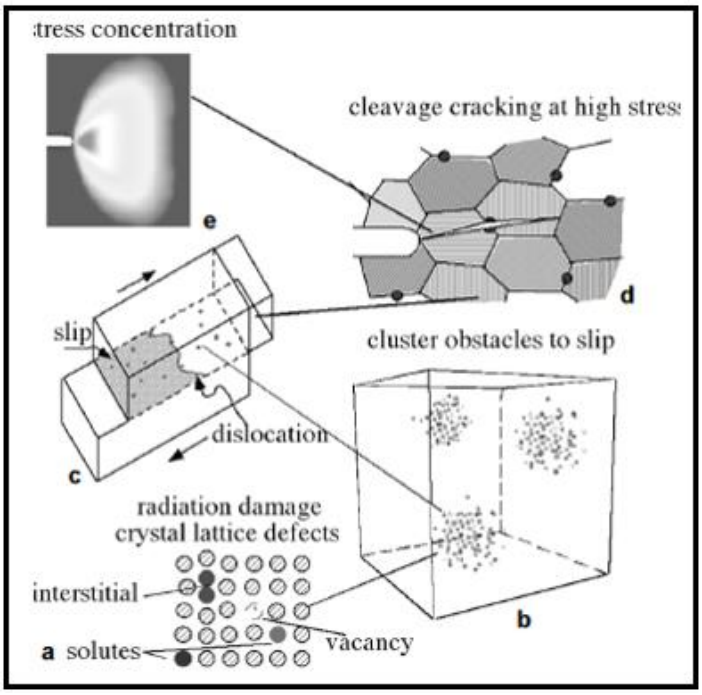


Fig. 1.6 Illustration of the basic embrittlement processes: **(a)** creation of irradiation-induced defects, **(b)** formation of nanoscale defect clusters, **(c)** pinning of dislocations and hardening by defect clusters, **(d)** hardening enhanced cleavage fracture, and **(e)** stress concentration [28]

Irradiation-induced nanoscale defect clusters will act as obstacles for dislocation motion, hence increasing the Peierls stress. However, $\Delta\sigma_y$ is not just a simple summation of the contributions from individual features - it is a combined effect of the nanoscale clusters superimposing on each other and also with pre-existing microstructures, i.e. dislocation lines, solute atoms, and precipitates. Mechanical tests and modelling at the dislocation level, will have to be carried out in parallel to fully understand the irradiation-induced embrittlement.

1.2.4 Micromechanical Tests in Characterising Radiation Damage

Micro-scale mechanical testing is preferable regardless of the type of irradiation. For neutron irradiation, there is a strong desire to limit the volume of radioactive material being tested. For ion irradiation, due to the energy loss from charged particle and electron interaction, the damaged layer is only micro-metre thick. Therefore, it is necessarily to employ micro-scale mechanical testing techniques to extract the mechanical properties from very thin damaged layer. **Table 1.2** summarises the benefits of micro-scale mechanical testing for both neutron and ion beam irradiated specimen [29].

Neutron Irradiation	Ion Irradiation
Reduce the amount of radioactive materials	Obtaining mechanical properties from accelerated irradiation
Large number of tests improve statistics	Large number of tests improve statistics
Re-testing old archived sample	Measures the entire dose profile
Testing localised areas	Control measurement possible at each specimen
Fundamental quantitative defect-dislocation interaction studies are possible	Fundamental quantitative defect-dislocation interaction studies are possible

Table 1.2 Benefits of micro-scale mechanical testing on neutron and ion beam irradiated materials for nuclear applications, redrawn from [29]

While nanoindentation is now a rather developed technique to measure the change in hardness (plastic properties) of materials after irradiation [30], micro-scale fracture test remains less developed. Fracture toughness calculation via fracture mechanical analysis is based on stringent specimen size requirements (based on the crack tip plastic zone to specimen size ratio), it is certain that the size requirements for linear-elastic fracture mechanics (LEFM) will fail to

comply in micro-fracture tests. Elastic-plastic fracture mechanics (EPFM), on the other hand, has a less stringent specimen size requirement. It is therefore a more suitable fracture mechanical analysis when the crack tip plastic zone is comparable to the micrometre specimen, which is often the case in structural materials. It is also desired to perform micro-fracture tests at elevated temperature. However, stable high-temperature micro-fracture tests are more difficult, as it requires special instrumentation (high-temperature nanoindenter) and special expertise. Therefore, the aim of this thesis is to improve current micro-fracture testing technique to the extent that it can measure the high-temperature fracture properties tungsten.

II LITERATURE REVIEW

As the main contribution of this thesis is to improve current micro-fracture testing technique for measuring the high-temperature fracture properties of tungsten, it is necessarily to know the applicability and limitations of linear-elastic and elastic-plastic fracture mechanical analysis (LEFM and EPFM) and the advantages/drawbacks of each micro-specimen design. Therefore, this chapter will first give a very brief overview of fracture mechanics, then critically review various micro-fracture test specimen design. In addition, developments and applications of chevron-notched specimens are also discussed. Lastly, very recent works on high-temperature micro-fracture tests are presented.

2.1 Overview of Fracture Mechanics

Fracture mechanical analysis provides a quantitative treatment of fracture. It allows measurements of material toughness and provides a basis for predicting the loads that structures can withstand without crack propagation. Fracture mechanical analysis are generally categorised into two groups: linear-elastic fracture mechanics (LEFM) and elastic-plastic fracture mechanics (EPFM), depending on the amount of non-linearity deformation the material exhibit. Both linear-elastic and elastic-plastic fracture mechanics will be briefly described in the following section.

2.1.1 Linear-Elastic Fracture Mechanics

Early practice of fracture mechanics analysis were mainly conducted on linear elastic materials. The equivalent energy and stress intensity approaches that are used to quantify the linear elastic fracture behaviour will be described, followed by Irwin's estimation of the crack tip plastic zone based on elastic stress analysis.

The energy approach

The first quantitative fracture analysis of cracked solids was conducted by Griffith [31]. He noted that when a crack is introduced to a stressed elastic plate, a balance between the decreases in potential energy and the increase in surface energy resulting from the crack must be maintained; an existing crack would only extend if sufficient surface energy responsible for opening the two crack surfaces were supplied externally. For a through-thickness crack in a plate configuration, shown in **Fig. 2.1**, the decrease in potential energy and the surface energy associated with crack formation can be mathematically expressed using **Eq. 2.1**

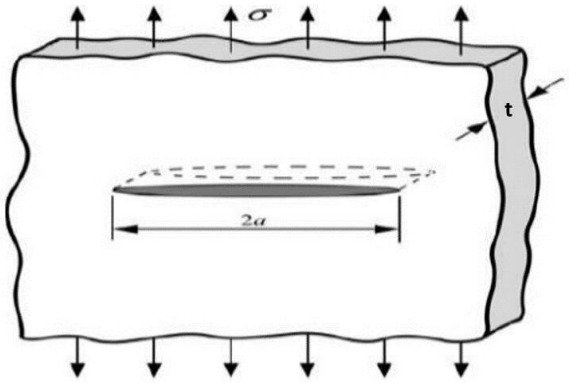


Fig. 2.1 A through-thickness crack in an infinite wide plate subjected to a remote tensile stress σ

$$U = -\frac{\pi\sigma^2 a^2 t}{E} + 4at\gamma_s + U_0 \ (\boldsymbol{Eq.\ 2.1})$$

where U is the potential energy of the body with crack, the first term on the right is the energy release rate G, U_0 is the potential energy of the body without crack, σ is the applied stress, a is the half crack length, t is the plate thickness, E is the elastic modulus, and γ_s is the surface energy.

Determine the condition for equilibrium by differentiating the potential energy U with respect to crack length and set to zero

$$\frac{\partial U}{\partial a} = 4t\gamma_s - \frac{2\pi\sigma^2 at}{E} = 0 \ (\boldsymbol{Eq.2.2})$$

then the surface energy can be expressed as

$$2\gamma_s = \frac{\pi\sigma^2 a}{E} \ (\boldsymbol{Eq.2.3})$$

finally the fracture stress can be expressed as

$$\sigma = \sqrt{\frac{2E\gamma_s}{\pi a}} \ (\boldsymbol{Eq.2.4})$$

It should be noted that the Griffith relation did not consider the crack tip radius, it was derived for an elastic material containing a very sharp crack. The crack tip radius has to be atomically sharp to amplify the local stress above the atomic cohesive strength. However, by considering the crack size and the fracture stress, Griffith was able to obtain a surface energy of 0.25 MPa·m$^{0.5}$ for soda lime silica glass, which was in excellent agreement with its theoretical value of 0.15 MPa·m$^{0.5}$ [31]. This fortuitous result neglecting the finite crack tip radius is probably due to the energy loss during the transfer of stored strain energy to surface energy. Nevertheless, the Griffith relation laid a cornerstone in the modern development of fracture mechanics.

The stress intensity factor (SIF) approach

Fracture of cracked solids may also be analysed using stress analysis based on elastic theory. Using modifications of analytical methods described by Westergaard [32], Irwin [33]

published solutions for the crack tip stress distributions associated with three major loading modes, opening, sliding, and tearing. Illustration of three loading modes is illustrated in **Fig. 2.2**.

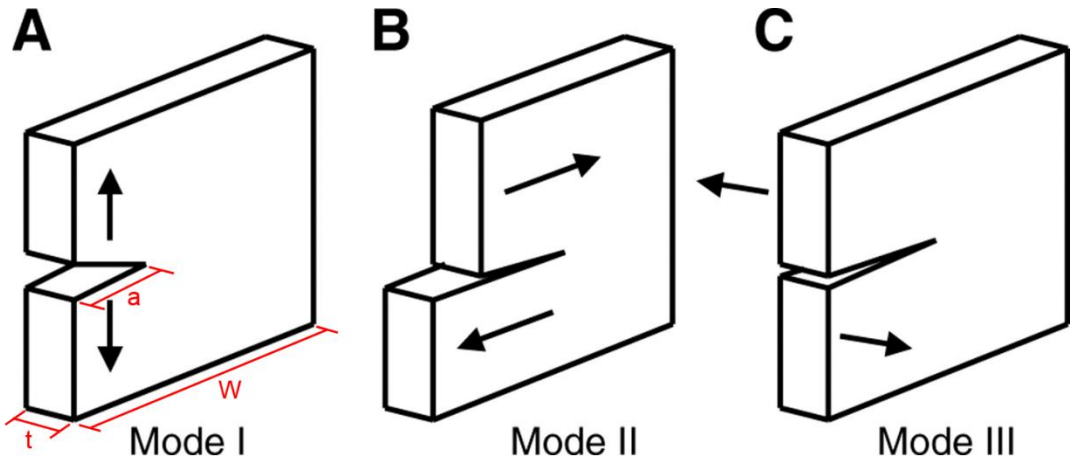


Fig. 2.2 Three modes of loading that can be applied to a crack

During Mode I loading (majority of actual engineering situations), the stress state around an atomically sharp crack in a semi-infinite solid is described by:

$$\sigma_x = \frac{K_I}{\sqrt{2\pi r}}\cos\frac{\theta}{2}\left(1 - \sin\frac{\theta}{2}\sin\frac{3\theta}{2}\right) \ (\boldsymbol{Eq.2.5})$$

$$\sigma_y = \frac{K_I}{\sqrt{2\pi r}}\cos\frac{\theta}{2}\left(1 + \sin\frac{\theta}{2}\sin\frac{3\theta}{2}\right) \ (\boldsymbol{Eq.2.6})$$

$$\tau_{xy} = \frac{K_I}{\sqrt{2\pi r}}\left(\sin\frac{\theta}{2}\cos\frac{\theta}{2}\cos\frac{3\theta}{2}\right) \ (\boldsymbol{Eq.2.7})$$

$$\sigma_z = \nu(\sigma_x + \sigma_y) \ (\boldsymbol{Eq.2.8})$$

where θ and r are the coordinates relative to the crack tip, shown in **Fig. 2.3**, and K_I is the stress intensity factor in a Mode I crack. For finite specimens, K_I is given by

$$K_I = \sigma f\sqrt{\pi a} \ (\boldsymbol{Eq.2.9})$$

where σ is the applied stress, and f is a geometry factor. These equations predict that the local stresses are infinite at the crack tip, which is of course unrealistic. The material will yield wherever the local stress is greater than the yield strength, so yielding limits the actual stress near the crack tip. In Irwin's analysis, unstable fracture occurred when K_I reached a critical value, K_{Ic}, given by

$$K_{Ic} = \sigma_f f\sqrt{\pi a} \ (\boldsymbol{Eq.2.10})$$

where σ_f is the fracture stress

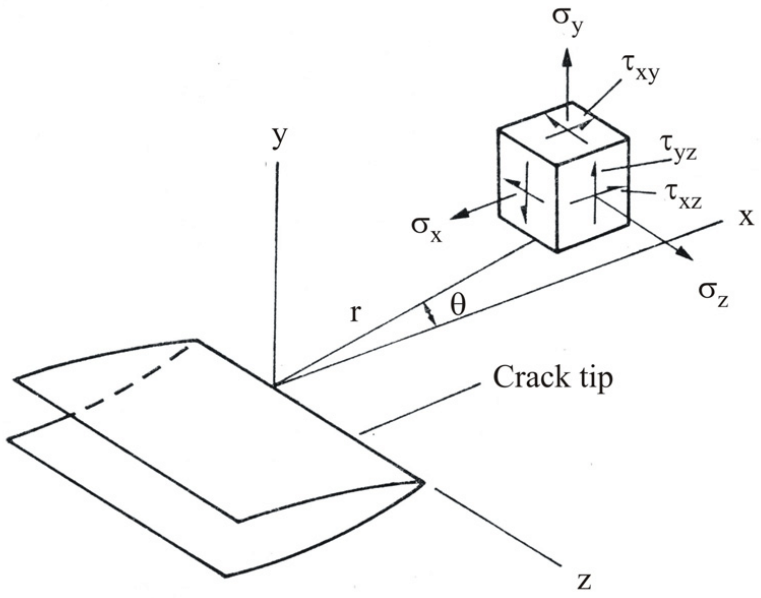


Fig. 2.3 Coordinate axis and distribution of stresses in the vicinity of crack tip

Crack tip plasticity

Linear elastic stress analysis of sharp cracks predicts infinite stresses at the crack tip. However, in real materials, stresses at the crack tip are finite because the crack tip radius must be finite. Inelastic material deformation, such as plastic deformation of metal, leads to relaxation of the crack tip stresses. Elastic stress analysis becomes increasingly inaccurate as the inelastic

region (plastic zone) at the crack tip grows. LEFM provides simple corrections (i.e. the effective compliance adjustment) when moderate crack tip yielding occurs. The size of the crack tip plastic zone can be estimated using Irwin's approach [34], where the elastic stress analysis was used to estimate the plane-strain elastic-plastic boundary, described in **Eq. 2.11**.

$$r_y = \frac{1}{2\pi}\left[\frac{K}{\sigma_{YS}}\right]^2 \quad (\boldsymbol{Eq.\,2.11})$$

where σ_{ys} is the yield stress, K is the fracture toughness. In plane strain, yielding is supressed by the triaxial stress state, and the Irwin plastic zone is smaller by a factor of 3, using **Eq. 2.12**.

$$r_y = \frac{1}{6\pi}\left[\frac{K}{\sigma_{YS}}\right]^2 \quad (\boldsymbol{Eq.\,2.12})$$

If strain hardening is neglected, the stress distribution for $r = r_y$ can be represented by a horizontal line at $\sigma_{yy} = \sigma_{ys}$, illustrated in **Fig. 2.4**.

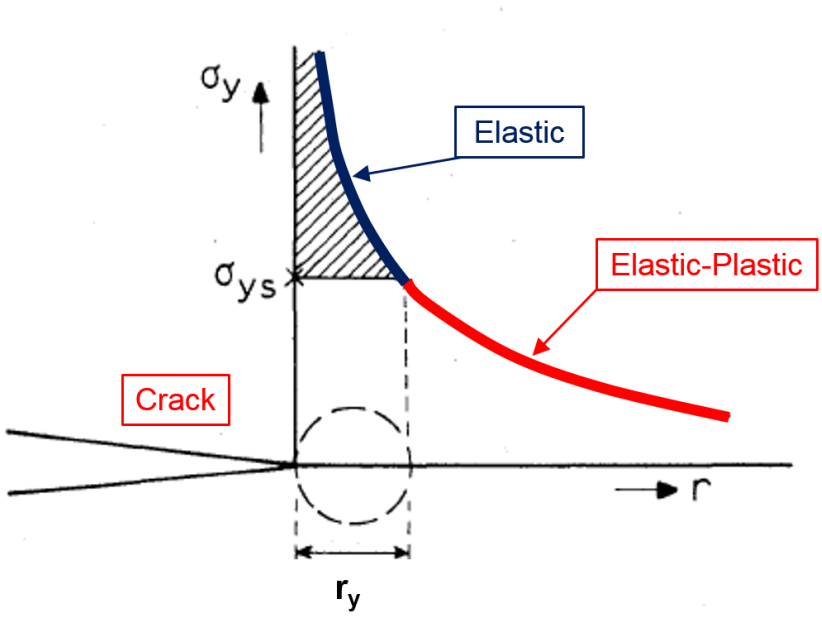


Fig. 2.4 First-order estimation of the crack tip plastic zone. The shaded area represents load that must be redistributed after yielding occurs [35]

2.1.2 Elastic-Plastic Fracture Mechanics

LEFM is only valid when non-linear deformation is confined to a small region surrounding the crack tip. According to ASTM E 399 [36], the size requirements for a valid K_{Ic} are given in **Eq. 2.13** and **2.14**. In most metals, it is virtually impossible to characterise the fracture behaviour with LEFM, unless a very large test specimen is made (probably economically unfavourable). Therefore, elastic-plastic fracture mechanical (EPFM) analysis is a more suitable method to characterise the fracture behaviour of metallic materials in the presence of crack tip plasticity. EPFM applies to materials that exhibit time-independent, non-linear deformation behaviour (i.e. plastic deformation). The elastic-plastic fracture parameter, the J contour integral, is used to describe the crack tip conditions in elastic-plastic materials. Critical values of J is able to provide nearly size-independent measures of fracture toughness, even for significant amount of crack tip plasticity. Although there are still specimen size criterions for the applicability of J, but are much less restrictive than LEFM.

$$t, a \geq 2.5 \left[\frac{K_{Ic}}{\sigma_{ys}}\right]^2 \quad (\boldsymbol{Eq.\,2.13})$$

$$0.45 \leq \frac{a}{W} \leq 0.55 \; (\boldsymbol{Eq.\,2.14})$$

where a is the crack length, t is the specimen thickness, K_{Ic} is the rough estimate of the plane-strain fracture toughness (can come from data of similar material), and σ_{ys} is the yield stress

The J contour integral

The J integral was developed to quantify the fracture behaviour in a material experiencing both elastic and plastic deformations. Using a line integral related to energy in the vicinity of a crack, Rice [37] was able to solve two-dimensional crack problems in the presence of plastic deformation. The form of this line integral, defined as J, is given in **Eq. 2.15**.

$$J = \int \left(W dy - \boldsymbol{T} \frac{\partial \boldsymbol{u}}{\partial \boldsymbol{x}} ds \right) \quad (\boldsymbol{Eq.\,2.15})$$

where W is the strain energy density, $\boldsymbol{T}$ is the traction vector acting on the contour, $\boldsymbol{u}$ is the displacement vector, and W is the strain energy density, given in **Eq. 2.16**

$$W = \int_0^{\varepsilon_{ij}} \sigma_{ij} \varepsilon_{ij} \quad (\boldsymbol{Eq.\,2.16})$$

In the case of a closed contour, Rice showed that the line integral was equal to zero. In **Fig. 2.5** (contour C+C'+Q+R), both dy and T_i along the contour segment Q and R are found to be zero. Therefore, $J_Q = J_R = 0$, which leads to the fact that $J_C = J_{C'}$. Since the paths along contours C and C' are opposite in sign, it shows that the J integral is path independent and that J can be determined from a stress analysis where σ and ε are defined on some arbitrary contour away from and surrounding a crack tip.

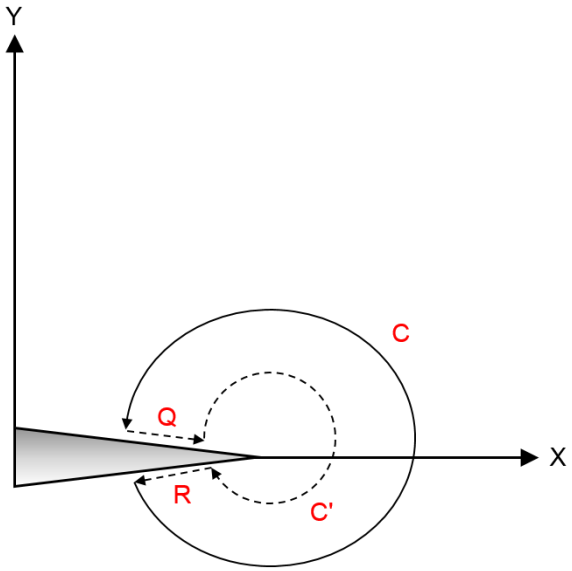


Fig. 2.5 Arbitrary line contour surrounding the crack tip

Rice presented an alternative and equivalent definition for J [38], which was defined as the pseudo-potential energy difference between two identically loaded bodies possessing slightly different crack lengths. The change in strain energy ΔU associated with an incremental crack extension Δa is portrayed in **Fig. 2.6** and equal to $J\Delta a$ or $J = (du/da)$, where

$$J = \int_0^P \left(\frac{\partial u}{\partial a}\right)_P dP \ (for\ fixed\ load) \quad (\boldsymbol{Eq.\ 2.17})$$

$$J = -\int_0^\delta \left(\frac{\partial P}{\partial a}\right)_u du \ (for\ fixed\ displacement) \quad (\boldsymbol{Eq.\ 2.18})$$

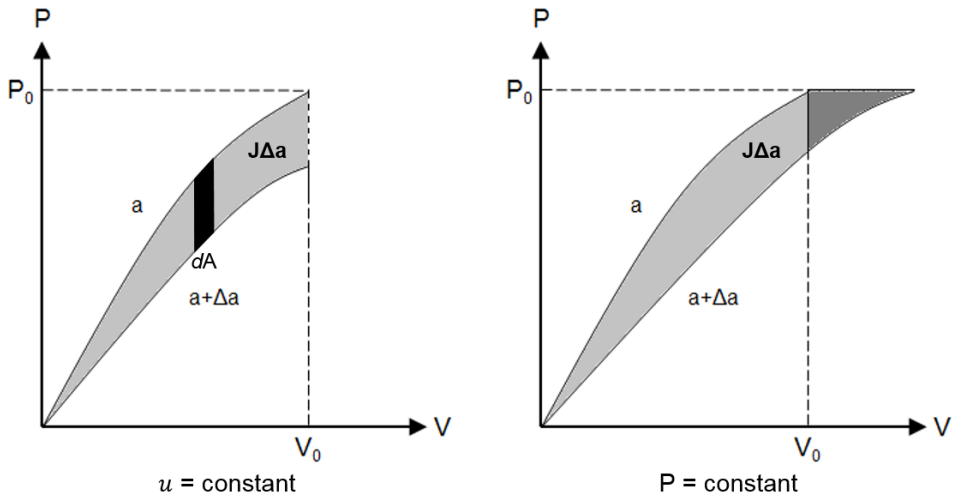


Fig. 2.6 Determination of J integral based on fixed displacement and fixed load

From **Eq. 2.17** and **2.18,** J can be determined from load-displacement curves recorded for specimens containing different crack lengths. For either linear or non-linear elastic conditions, J is the energy made available at the crack tip per unit crack extension, *da*. That is, J is equivalent to the crack driving force. Therefore,

$$J = \frac{K^2}{E'} \quad (\boldsymbol{Eq.2.19})$$

where E' = E, the elastic modulus for plane stress

E' = E/(1-ν²) for plane strain

J becomes a measure of the intensity of the entire elastic-plastic stress-strain field that surrounds the crack tip. J is analogous to K as long as the stress-strain curve for an elastic-plastic solid is the same as a nonlinear elastic solid. Therefore, J can be used as a failure criterion in the same manner as K when this criterion complies.

2.1.3 Fracture Resistance Curves

Most materials with high toughness do not fail catastrophically at the J value for crack initiation. Instead, these materials exhibit a fracture resistance behaviour (rising R-curve), where J increases with crack extension. In metal, a rising R-curve is normally associated with crack blunting and ductile crack growth via coalescence of micro-voids (additional energy required due to formation of new free surfaces). **Fig. 2.7** schematically illustrates a typical fracture resistance curve for ductile materials. In the initial stage, the curve is very steep, as only small amount of crack growth occurred due to blunting. As J increases, the material at the crack tip fails locally and then the crack extends. Due to the rising R-curve, the initial crack growth is usually stable (additional energy required to extend crack), but instability can still occur when the driving force curve is tangent to the resistance curve, as indicated in **Fig. 2.8**.

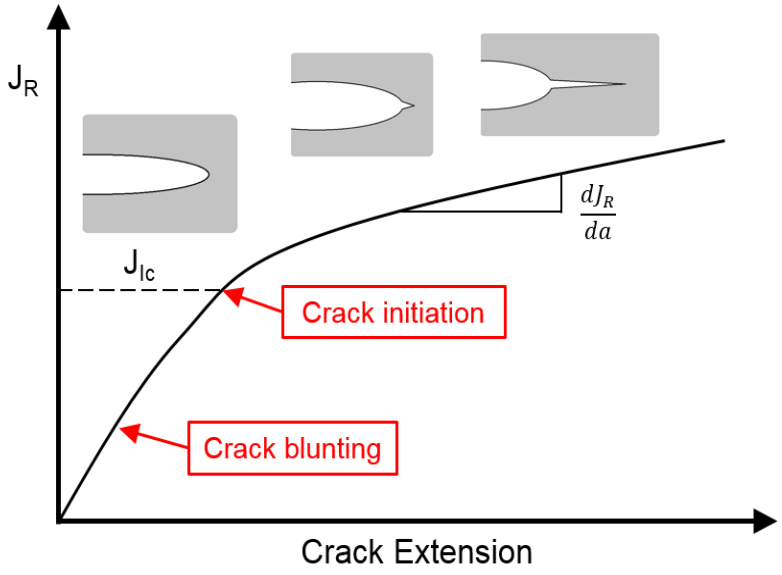


Fig. 2.7 Schematic fracture resistance curve for a ductile material

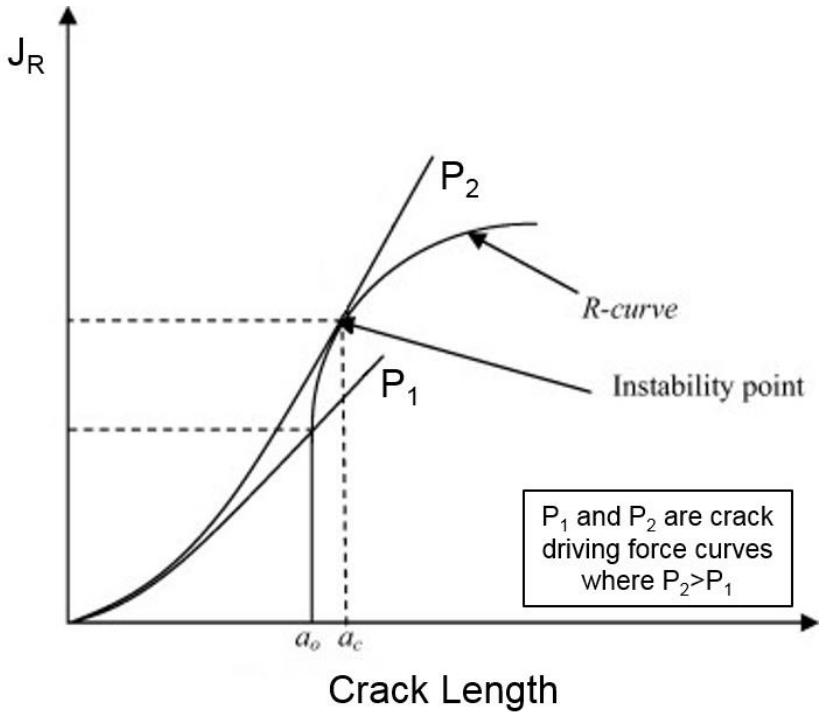


Fig. 2.8 Schematic crack driving force/resistance curve showing the tangent point for crack instability

2.1.4 Summary

This section provides background knowledge for quantifying the micro-cantilever results via fracture mechanical analysis. It also provides the theoretical basis for the J-integral, which will be calculated by the finite element based contour integral method to optimise and validate the chevron notch geometry (will be described in Chapter 4). A comprehensive review of fracture mechanics can be found in various classical textbooks [35, 39].

2.2 Micro-Fracture Tests

This section describes the various micro-scale fracture testing methods for measuring fracture toughness. Advantages and drawbacks for both indentation-based and FIB-based micro-fracture methods are critically reviewed.

2.2.1 Nanoindentation

Indentation-based methods using a sharp pyramidal indenter have gained huge popularity due to the relative ease of testing and sample preparation. In such methods, the fracture toughness is calculated using the measurements of the crack length emanating from the residual indentation impression, shown in **Fig. 2.9**, and the maximum load at which fracture occurs. A simplified formulation for calculating the fracture toughness in the case of long cracks (c/a>1) is given in **Eq. 2.20** (the Lawn-Evans-Marshall model) [40].

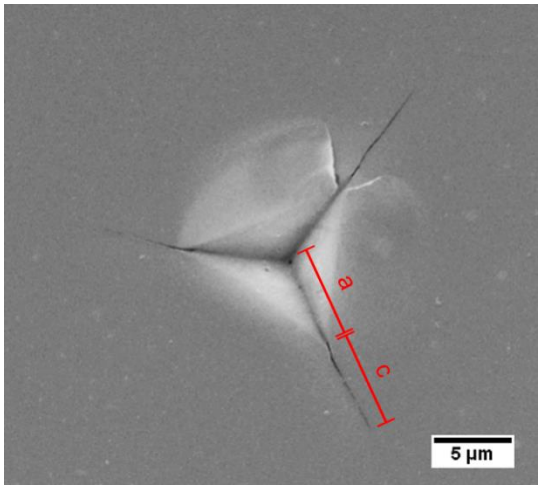


Fig. 2.9 Radial cracks emanating from the edges of a Berkovich indent on single crystal Si (**a** is the distance between indent centre to point, **c** is the crack length emanating from the residual indent)

$$K_c = \alpha \sqrt{\frac{E}{H}} \frac{P_{max}}{c^{\frac{3}{2}}} \quad (\boldsymbol{Eq.2.20})$$

where α is a coefficient of approximately 0.016, E is the elastic modulus, H is the hardness, P_{max} is the maximum fracture load, and c is the surface crack length (measurements from top view)

The main drawback of the indentation-based method is the influence from the underlying substrate when testing thin films or ion-irradiated materials (layer of interest usually range from 0.1 μm to 2 μm), which may either enhance or inhibit the development of indentation plastic zone. In addition, large residual stresses pre-existing in thin films can alter the fracture behaviour, which complicates the indentation-based fracture toughness measurements unless both substrate effect and residual stresses are precisely known.

2.2.2 Micro-Cantilever

FIB-based methods were recently developed to resolve the issues (substrate and residual stresses effects) associated with the indentation-based method for fracture testing. These methods generally used a nanoindenter to apply force and measure displacement on a focused-ion beam (FIB) milled micro-specimen. The most popular micro-fracture specimen design is the pre-notched single-cantilever beam, shown in **Fig. 2.10**. It was first developed by Di Maio et al. [41] to measure the fracture toughness of tungsten-carbide coating. It has now extended its applicability to a wide range of brittle/semi-brittle materials [42-45]. In the case of brittle materials, the plane-strain fracture toughness K_{Ic} can be easily calculated using **Eq. 2.21**.

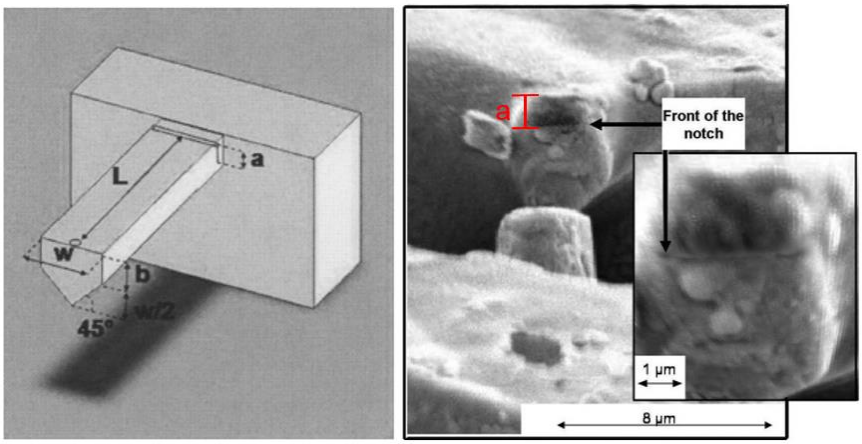


Fig. 2.10 Schematic drawing of the pentagonal cantilever design. Post-test SEM is used to measure the actual notch depth **a** [41]

$$K_{Ic} = \sigma_f \sqrt{\pi a} F\left(\frac{a}{b}\right) \quad (\boldsymbol{Eq.2.21})$$

where σ_f is the fracture stress calculated using simple beam theory, a is notch depth measured after test, b is the cantilever thickness, and $F(a/b)$ is a dimensionless shape factor calculated from finite element simulation

Wurster et al. [46] first extended the cantilever-based method to semi-brittle tungsten. The pre-notched single-crystal tungsten micro-cantilevers were tested *in-situ* in a SEM. Crack length were measured using the SEM images extracted from *in-situ* videos, shown in **Fig. 2.11**, and also by measurement of compliance. The fracture resistance curves were calculated using EPFM analysis. However, lack of machine stability (*in-situ* tests were carried out using a custom made micro-indenter rather than a real nanoindenter), compliance measurements were strongly affected by the frame stiffness, which resulted fewer data points in the crack length measurements, shown in **Fig. 2.12**. In addition, crack deviation from the notch plane to the

cleavage plane, observed in the *in-situ* images, also introduced additional uncertainties to the crack length measurements.

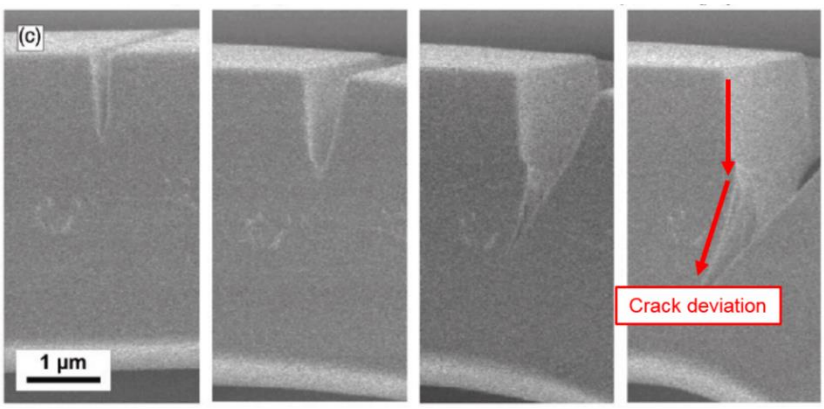


Fig. 2.11 Sequence of SEM images of a cantilever during the *in-situ* test. Crack deviation from the original notch plane to the cleavage plane is clearly observed [46]

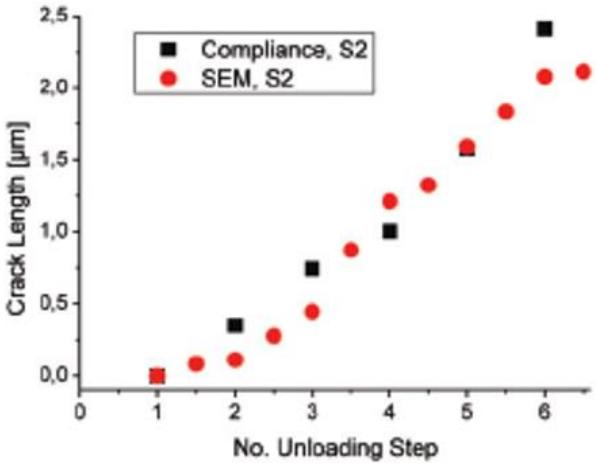


Fig. 2.12 Crack length measured using both SEM and compliance measurements [46]

Motz et al. [47] investigated the fatigue crack growth behaviour of a notched micro-cantilever, fabricated on a FCC nickel-based superalloy (CMSX-4). The cantilever is cyclic loaded *in-situ* a SEM using a tungsten grip (to maintain sufficient frame stiffness). The crack length, J-integrals, and Bauschinger displacements were measured to investigate the effect of

dislocation pile-up on fatigue crack growth behaviour. The main deduction of this work was that the back stresses generated due to dislocation pile-up at the neutral axis retarded the crack velocity, hence increasing the fatigue lifetime as compared to the same material under a tensile load geometry. Therefore, the effect of dislocation pile-up to fracture toughness calculation when using a cantilever bending geometry should be considered. However, the nature of the back stresses (tensile or compressive) was not investigated, as it will require *in-situ* EBSD or electron channelling contrast imaging (ECCI) setup which was not available in their SEM.

A major drawback of the cantilever-based method is that specimen preparation via FIB-milling can introduce structural damage, which may alter the mechanical responses measured from the micro-specimen [48]. Hoffmann el al. [49] also reported that gallium-induced displacement damage can penetrate as deep as 200 nm in gold, which introduced significant pre-strain at the root of the pre-notch. In addition, the FIB-milled pre-notch is not atomically sharp; it has a finite notch root radius of approximately 30~50 nm (when using milling current of 10 pA). Additional load were often required to nucleate a "real" crack at the bottom of the notch, which resulted in overestimating the real fracture toughness [41]. Lastly, the time associated with FIB-milling a micro-cantilever is long. It takes about 6~8 hours for an experienced user to fabricate a proper cantilever worth testing. Considering the time and cost one has to spend on the FIB, this technique provides significantly fewer statistic as compared to conventional macroscopic fracture tests.

To overcome some of the existing issues associated with micro-cantilever fracture tests, Mueller et al. [50] replaced the conventional straight notch with a chevron notch. Due to the increasing crack front as the crack propagates, chevron-notched cantilever provided some amount of crack stability even when the load was applied in bending. The large stress

concentration at the top chevron apex nucleated a "real" pre-crack automatically during loading, eliminating the cumbersome effort for fatigue pre-cracking and effectively avoided the notch root radius effect. In addition, the pre-crack was nucleated underneath the chevron apex, so the possible effect of FIB damage to the crack tip was also minimised. The chevron-notched cantilever geometry and representative load-displacement curves of quartz are shown in **Fig. 2.13**. Using the unstable fracture load (the load when catastrophically failure occurred), and the finite element calculated stress intensity factor, the plane-strain fracture toughness K_{Ic} can be calculated using **Eq. 2.22**.

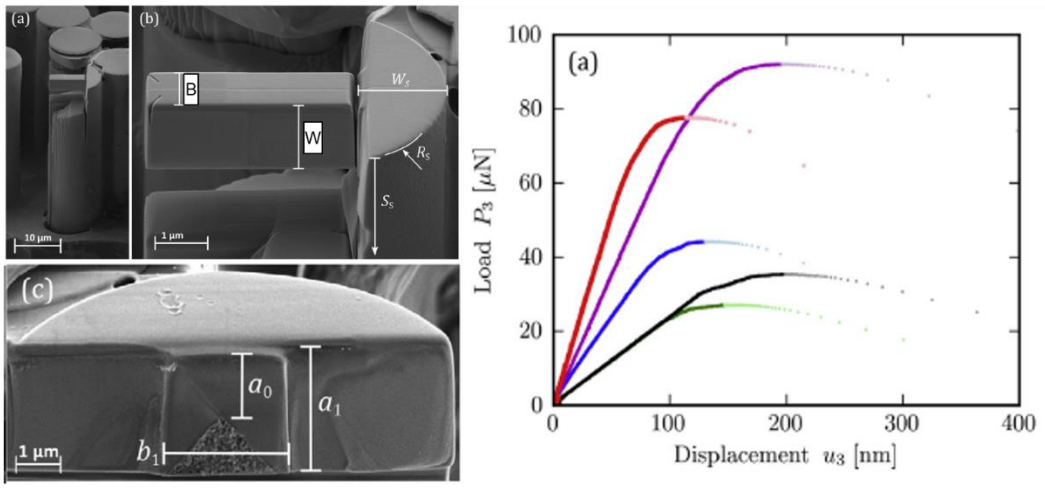


Fig. 2.13 Example of a chevron-notched cantilever fabricated on fused quartz. Gradual softening and displacement jumps from the load-displacement curves are indications of stable crack growth [50]

$$K_I = \frac{P}{B\sqrt{W}} F_v(a) \quad (\boldsymbol{Eq.\,2.22})$$

where P is the unstable fracture load, B, W are the cantilever geometry, and $F_v(a)$ is the geometry-dependent SIF calculated from finite element simulation (a is the crack length)

Although stable crack growth are observed in most chevron-notched cantilevers, the associated stable crack length were not measured. Therefore, only LEFM solution was applied and this method is still limited to brittle materials. Nevertheless, chevron-notched cantilever, due to its crack stability and using a real pre-crack, is an advantageous specimen design for micro-fracture tests. To measure the fracture resistance behaviour from semi-brittle tungsten, it is not only necessary to exhibit stable crack growth but also to measure the crack length. A new test method with capability to measure crack length has to be developed.

2.2.3 Micro-Pillar

A relative simple method for measuring fracture toughness at the microscale was recently developed based on nanoindentation of FIB-milled micro-pillars [51]. Example of a TiN micro-pillar is shown in **Fig. 2.14**. When indented with a sharp Berkovich indenter, the pillar fractured by splitting at reproducible loads that occurred as displacement jumps in the load-displacement curves. The effects of residual stresses (usually from lattice mismatch between deposited and substrate materials) can also be minimised by making the pillar diameter equal to its height [52]. Using this method, the fracture toughness of brittle materials can be calculated using **Eq. 2.23**.

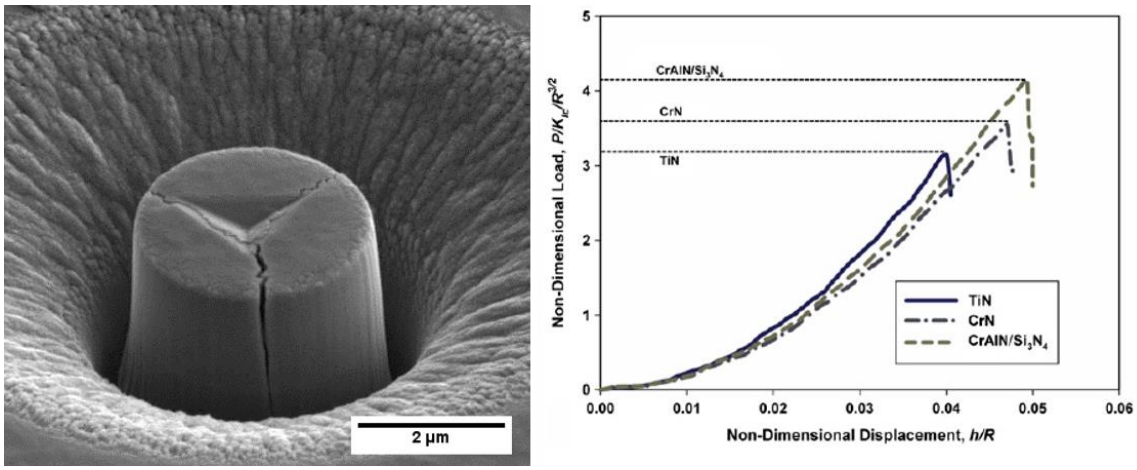


Fig. 2.14 Example of a TiN micro-pillar after splitting and the load-displacement curve [51]

$$K_c = \gamma \frac{P_c}{R^{\frac{3}{2}}} \ (\boldsymbol{Eq.\ 2.23})$$

where P_c is the fracture load, R is the pillar radius, and γ is the dimensionless coefficient calculated from elastic FE analysis (only modulus and Poisson's ratio are used in the FE model)

The micro-pillar splitting method was successfully demonstrated on physical vapour deposited (PVD) TiN coating, where the fracture toughness values were in good agreement with macroscopically measured values (~3 MPa·$m^{0.5}$). However, the dimensionless coefficient γ is a material-dependent parameter which required extensive cohesive zone modelling and assumed linear elasticity. The effect of friction between the indenter tip and the pillar may also have a significant effect on the fracture toughness measurements, which wasn't considered in their research. Nevertheless, the micro-pillar splitting method has the advantages of negligible residual stresses within the thin film, ease of specimen fabricating, and eliminates the needs for measuring the crack geometries after test.

2.2.4 Other Geometries

As fracture in bending is mostly catastrophic, it is difficult to study materials that exhibit fracture resistance behaviours. Liu et al. [53] developed a double cantilever beam (DCB) design to achieve stable crack growth, shown in **Fig. 2.15**. The DCB has a FIBed pre-notch in the centre, and both arms are compressed *in-situ* using a blunt diamond punch. The onset of crack initiation was associated with a sudden load drop, shown in the load-displacement in **Fig. 2.16**. As the DCB was further compressed, the crack was able to propagate stably after initiation. Hence, the fracture toughness for crack initiation could be calculated using **Eq. 2.24**.

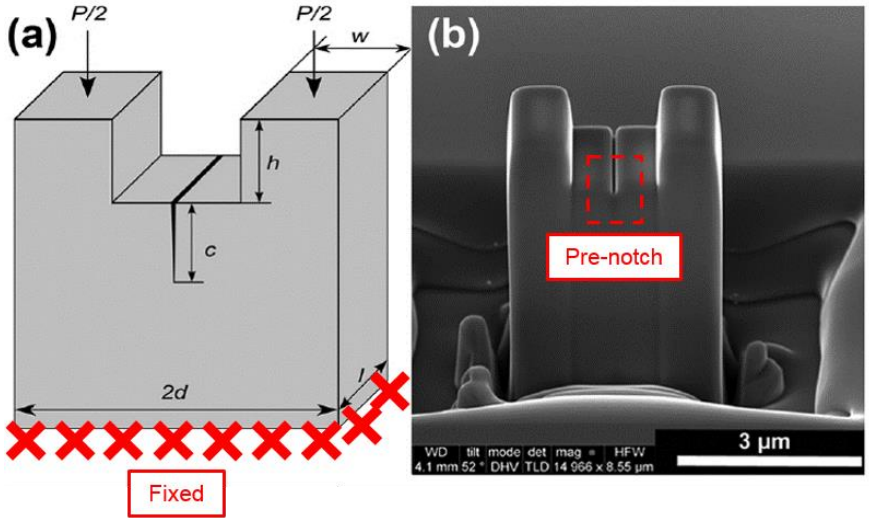


Fig. 2.15 Schematic drawing and SEM image of a SiC double cantilever beam [53]

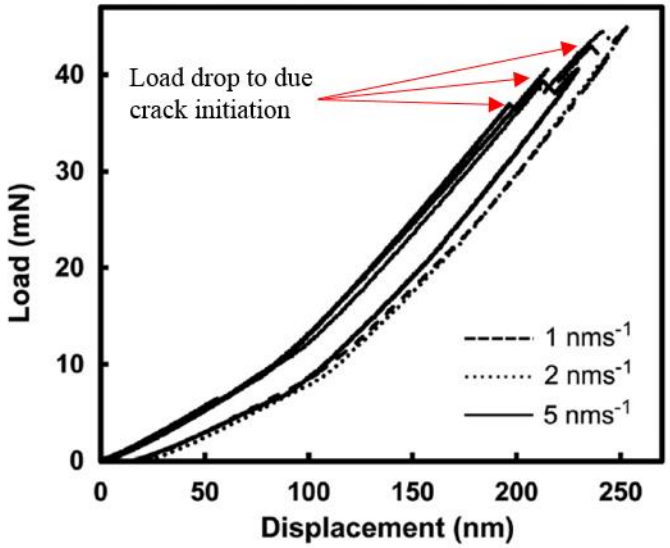


Fig. 2.16 Load-displacement curves of the SiC DCB, where the load drop indicates the crack initiation [53]

$$K_{Ic} = \sqrt{3}\frac{(c-uh)}{ld^{\frac{3}{2}}}P_C \ (\boldsymbol{Eq.2.24})$$

where c, l, d, h are the specimen geometry, P_c is the crack initiation load, and u is the friction coefficient between the indenter and specimen.

The major difficulty of the DCB method is to obtain the friction coefficient u, which can only be determined *in-situ*. Tampered cantilever surfaces (not completely flat and have rounded edges) also introduce additional error to the friction coefficient calculation, and therefore the real geometry should be taken into account using finite element modelling. Nevertheless, the DCB method provides a stable crack geometry for determining the fracture initiation toughness of brittle ceramic coatings.

Jaya et al. [54] developed a double-clamped beam geometry to achieve stable crack growth from functional graded coatings (PtNiAl-bonded). The rectangular beam had a FIBed pre-notch in the centre, and was compressed *in-situ* above the pre-notch using a blunt wedge indenter. Fracture toughness was calculated using the first pop-in load (crack nucleation) and the FE-calculated stress intensity factor (SIF). This micro-specimen geometry was similar to a three-point bending beam, however, with two ends fixed to the matrix instead of supported by the roller pins. The specimen geometry and load-displacement curve are given in **Fig. 2.17**.

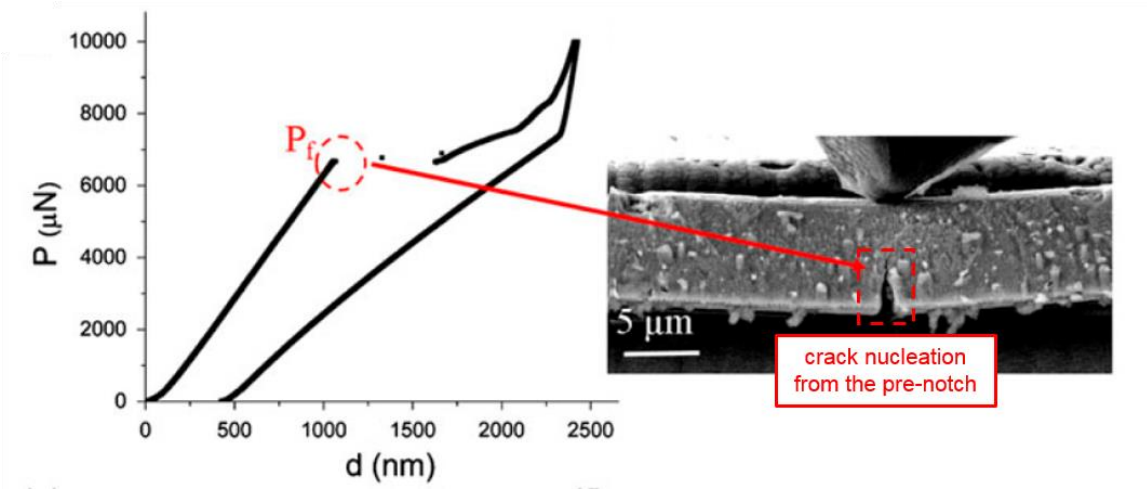


Fig. 2.17 The double clamped beam geometry and its corresponding load-displacement curve. The first pop-in load, P_f, indicates crack nucleation [54]

The main drawback for this geometry is that cracks can also nucleate at the clamped edges [55]. Shown in **Fig. 2.18**, if the pre-notch is too blunt, edge cracks can nucleate before the pre-notch crack, as sharp edges are also favourable sites for stress concentration. Alignment of the indenter loading position to the pre-notch is also very important [56]. Shown in **Fig. 2.19**, misalignment by 10 μm brought approximately 30% of Mode II crack component (K_{II}) to the Mode I SIFs. In addition, the crack tip plastic zone is relatively close to the loading position of the indenter, crack behaviour can be strongly affected by the stress field from the indenter. Nevertheless, the double clamped beam geometry provides sufficient crack stability so that a real crack can be generated and used for fracture toughness calculation.

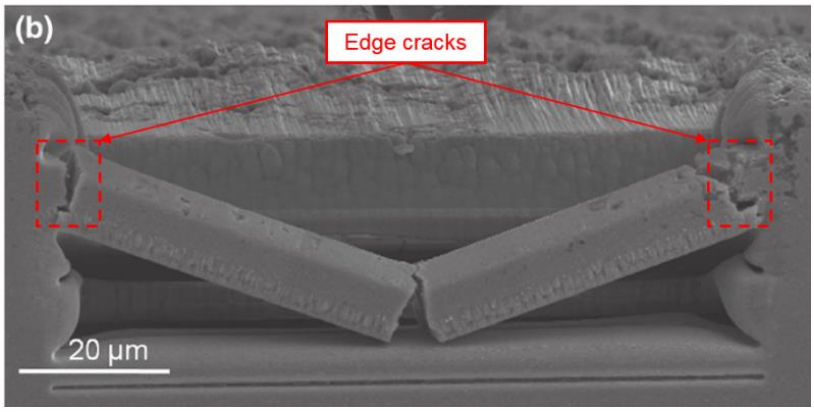


Fig. 2.18 Edge cracks in the double clamped beam due to the blunt pre-notch [55]

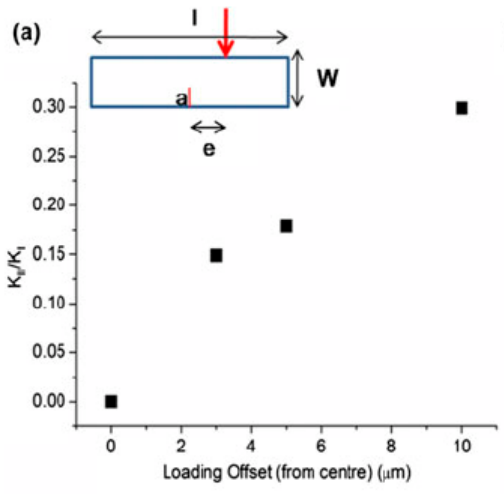


Fig. 2.19 Ratio of K_{II}/K_I (calculated via FEA) as a function of the loading misalignment. The ratio increases with loading misalignment [54]

McLean et al. [57] used a double edge notched tensile (DENT) micro-specimen to measure the fracture toughness of bismuth-doped copper grain boundaries. The DENT specimen was first prepared via FIB, then Pt-tacked to the tensile frame. Pre-notches were FIB-milled on both sides of the grain boundary. Finally, tests were conducted *in-situ* in a SEM. From the fracture load and the SIF, the fracture toughness were calculated using **Eq. 2.25**. The DENT micro-specimen geometry and corresponding stress-strain curves are shown in **Fig. 2.20**.

$$K_{Ic} = \sigma_f \sqrt{\pi a} F\left(\frac{a}{b}\right) \quad (\mathbf{Eq.\ 2.25})$$

where σ_f is the fracture load, a, b are the noth length and half-specimen width, and $F(a/b)$ is the FE-calculated SIF

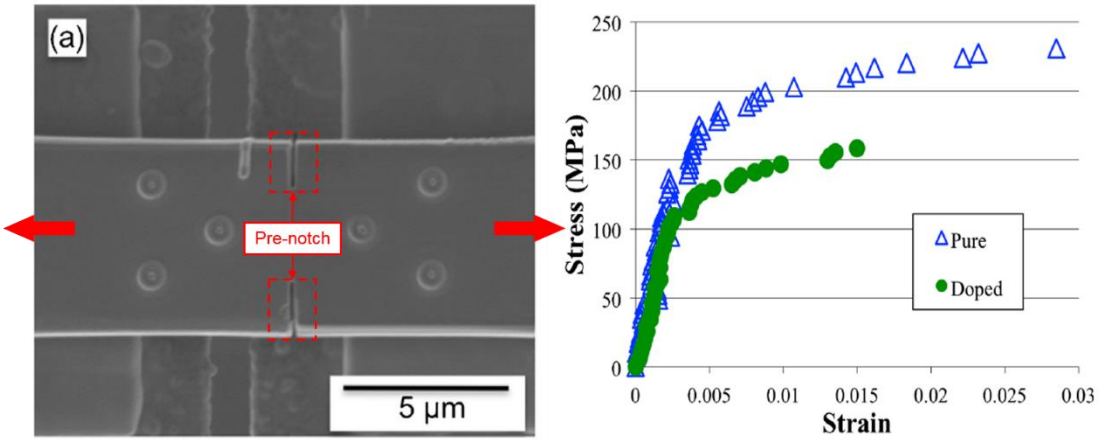


Fig. 2.20 DENT specimen geometry. Stress-strain curves for pure copper and bismuth-doped specimens. The doped specimen exhibits less ductility and fractured intergranularly [57]

Despite the significant ductility observed from the stress-strain curves, the fracture toughness for both pure and doped specimens were extremely low (0.3~0.5 MPa·$m^{0.5}$). This was probably due to the deformation of the Pt (used to tack the specimen with load frame) which resulted larger strain values. Digital image correlation (DIC) could have been used to accurately measure the true deformation from the specimen.

2.2.5 Micro-Fracture Tests Summary

A brief summary of current micro-fracture test methods is given in **Table 2.1**. As discussed, each method has its own advantages and drawbacks; one has to apply the most suitable method depending on the fracture behaviour of the materials (i.e. utilise crack stability design for measuring the fracture resistance curve). Jaya et al. [58] used different micro-specimen geometries (cantilever, pillar, double-cantilever, and double-clamped beam) to measure the fracture toughness of single crystal Si. The microscopically measured K_{Ic} had an average value of approximately 0.8 MPa·$m^{0.5}$, which was in good agreement with macroscopically measured value. Nevertheless, Si is an intrinsically brittle material with no

fracture resistance behaviour. Therefore, the only required input for K_{Ic} calculation is the fracture load (at crack initiation or instability) and the geometry-dependent SIFs. Using either crack initiation or instability load will yield the same K_{Ic} value.

Current micro-fracture test methods are only capable of measuring fracture toughness from intrinsically brittle materials. When measuring the fracture resistance behaviour from more ductile materials via EPFM analysis, both crack stability and also crack length measurements are required. Further improvements should be made to current micro-fracture test methods so that fracture resistance behaviour from more ductile materials can be effectively measured.

Test method	Underlying Substrate Effect	Residual Stress from Fabrication	Notch Type	Crack Stability	Crack Length Measurements	LEFM Applicability	EPFM Applicability
nanoindentation-based	Yes	Yes	No	No	Only surface crack	Yes	No
Micro-cantilever	No	Yes	FIB-notched (straight, chevron)	Yes (depending on notch type)	Yes	Yes	Yes
Micro-pillar	Yes	No	No	No	No	Yes	No
Double-cantilever beam	Yes	Yes	FIB-notched	Yes	Yes	Yes	Yes
Double-clamped beam	No	Yes	FIB-notched	Yes	Yes	Yes	Yes
Micro-tensile bar	No	No	FIB-notched	No	No	Yes	No

Table 2.1 Summary of current micro-fracture test methods

2.3 High-Temperature Micro-Fracture Tests

Only four high-temperature (tests above 300 °C) micro-fracture papers were published to date in the open literature. All consisted of testing FIB-fabricated micro-specimens using a high-temperature nanoindenter. Experimental methods, results, and drawbacks will be discussed briefly.

Hintsala et al. [59] performed high-temperature micro-fracture tests on single crystal Si, using pre-notched double-clamped rectangular beams (DCBs) shown in **Fig.2.21**. The DCB had dimensions of approximately 12 x 3 x 3 μm, which were tested *in-situ* in a SEM. The LEFM K_{Ic} remained constant at 0.75±0.1 MPa·$m^{0.5}$ until 300 °C, then gradually increased to 1.6±0.2 MPa·$m^{0.5}$ due to the thermally-activated dislocation activities. A BDTT of approximately 450 °C was reported. However, due to the lower strain rate (~10^{-5} s^{-1}) and probably different doping concentration (not reported), the microscopic value is in between 450~600 °C, which was a rather gradual transition compared to the macroscopic sharp transition reported by Roberts et al. [60]. Representative LD curves and K_{Ic} vs. temperatures are shown in **Fig. 2.22**.

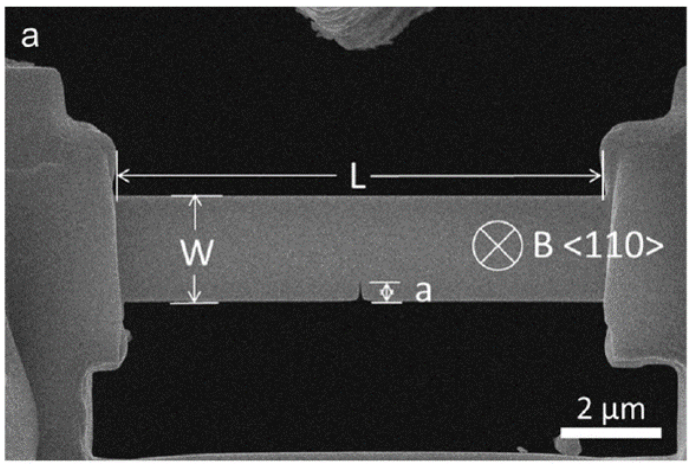


Fig. 2.21 SEM micrograph of the pre-notched double-clamped bending beam [59]

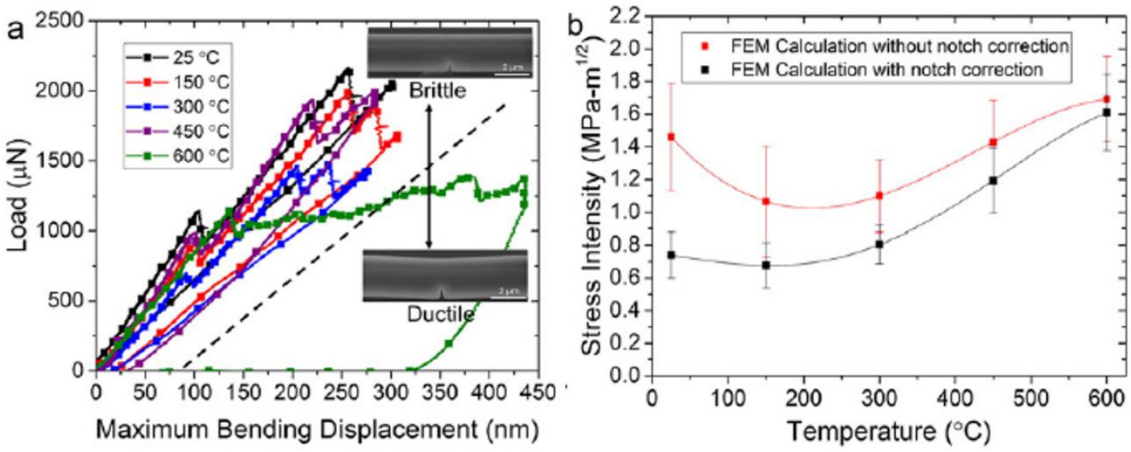


Fig. 2.22 (a) Load-displacement curves from Si DCBs up to 600 °C **(b)** K_{Ic} (with/without the notch root radius correction) gradually increases with temperature [59]

Armstrong et al. [61] performed high-temperature micro-cantilever bending tests on single crystal silicon up to 770 °C, using the Micro Materials® NanoTest Xtreme. The cantilevers had a triangular cross section, with dimensions of approximately 27 x 4 x 5 μm. However, the main aim of this work was to demonstrate the feasibility of high-temperature micro-cantilever bending experiments using the prototype vacuum system, so no attempts were made to calculate for K_{Ic} (only un-notched cantilevers were tested). A gradual brittle-to-ductile transition behaviour, defined as when stress-strain curve deviated from linearity, was captured at tests above 600 °C. It was also evident by the clear slip band formations on the cantilever surface, shown in **Fig.2.23**.

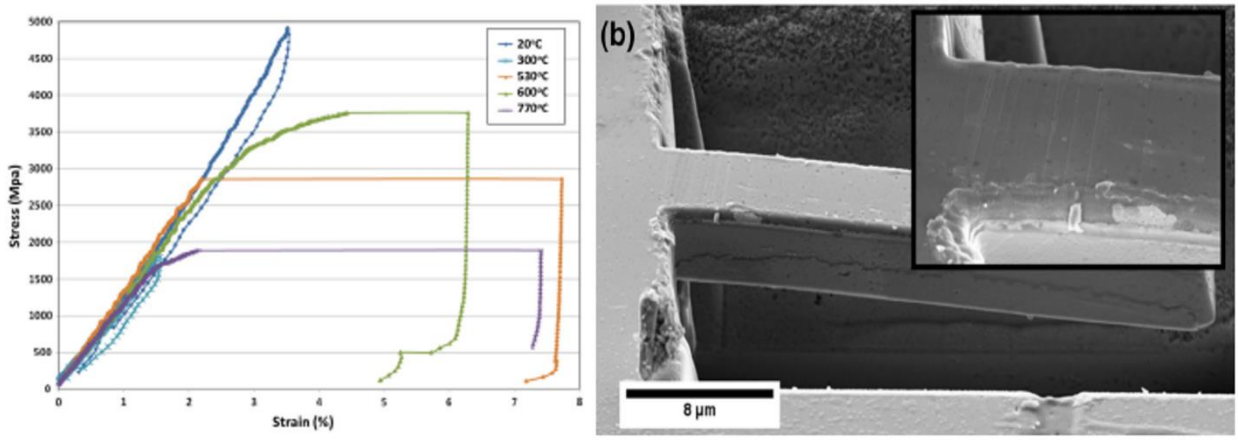


Fig. 2.23 (a) Stress-strain curves for single-crystal Si cantilevers tested from RT to 770 °C **(b)** Post-test SEM micrograph of the cantilever tested at 770 °C, showing clear traces of slip bands on the cantilever surface [61]

Best et al. [62] performed high-temperature micro-fracture tests on notched CrN cantilevers using an custom-made Alemnis® SEM indenter. The cantilevers had a rectangular cross section, with dimensions of 8 x 3 x 3 µm. The K_{Ic} remained constant at 3.3±0.3 MPa·$m^{0.5}$ throughout the entire temperature range (from RT to 500 °C). However, K_{Ic} was reduced to half of its original value after re-cooling back to RT. The author claimed that it was probably due to effect of residual gallium diffusion during elevated temperature, however, no microstructural analysis was conducted to further prove this.

Jaya et al. [63] performed extensive high-temperature micro-fracture tests on pre-notched single-crystal silicon cantilevers (rectangular cross section, dimensions of approximately 8.5 x 2 x 2 µm). Tests ranging from RT to 600 °C were carried out on the same Alemnis® SEM indenter used by Best et al. The measured K_{Ic} remained constant at approximately 1 MPa·$m^{0.5}$ until 300 °C, then it gradually increased to 1.8 MPa·$m^{0.5}$ at 600 °C. The higher BDTT (compared to 545 °C from Roberts et al. [94]) was also due to the larger strain rate used (~10^{-5} s^{-1}), as the BDTT

follows an Arrhenius activation energy relationship shown in **Eq. 2.26** [60]. The likely increase of BDTT using such strain rate is approximately 100 °C, therefore provides a possible explanation for the higher microscopic BDTT. In addition, the BDTT is extremely sensitive to impurity content, therefore the microscopic BDTT cannot be directly compared with the macroscopic value, unless the impurity level is known. However, effects of the temperature-dependent dislocation activities with both K_{Ic} and crack morphology were demonstrated - from singular sharp crack at RT to multiple crack deflections at 600 °C. Representative load-displacement curves, crack trajectories, and K_{Ic} vs. temperatures are shown in **Fig. 2.24** and **2.25**.

$$\dot{\varepsilon} \propto exp\left(\frac{-U}{kT_{BDT}}\right) \quad (\boldsymbol{Eq.2.26})$$

where $\dot{\varepsilon}$ is the strain rate, U is the activation energy for dislocation velocity (2.1 eV for intrinsic silicon), k is the Boltzmann constant, T_{BDT} is the BDTT

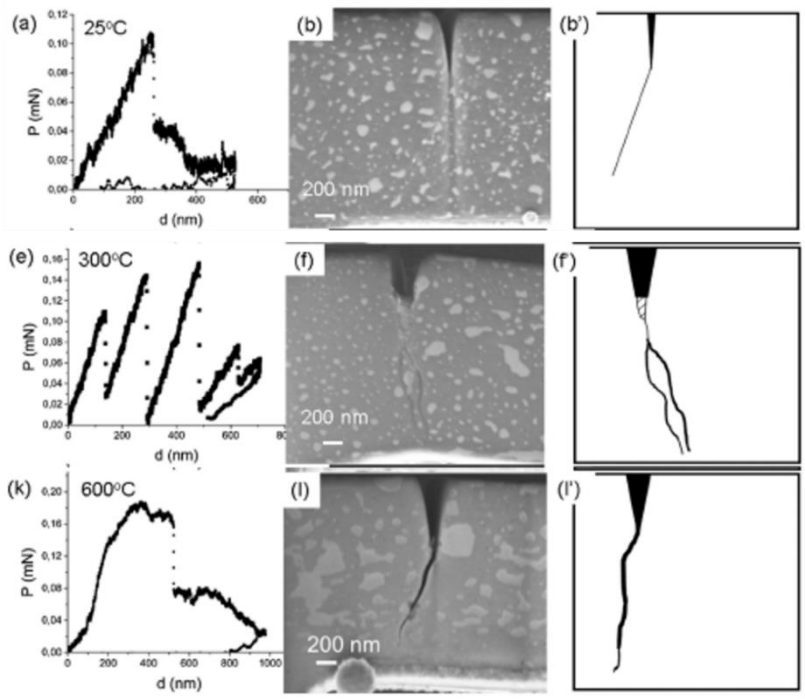


Fig. 2.24 Representative load-displacement curves and crack trajectories at various temperatures, showing transition from single sharp crack at RT to crack deflections at higher temperatures [63]

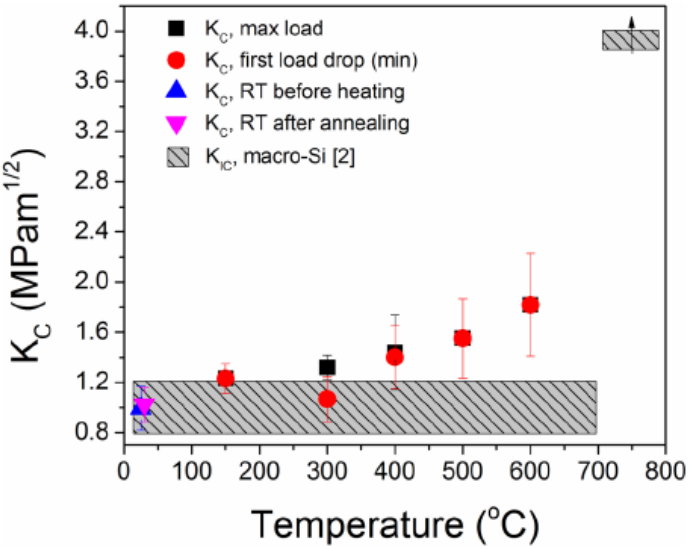


Fig. 2.25 Fracture toughness vs. temperature from Jaya's work, showing a gradual BDT behaviour at tests above 300 °C [63]

Results from recent high-temperature micro-fracture publications are summarised in **Table 2.2**. All tests were performed on intrinsically brittle materials (with macroscopic K_{Ic}<3 MPa·$m^{0.5}$). The crack tip plastic zone at the highest testing temperature were estimated using the corresponding yield stress and fracture toughness, using Irwin's crack tip plastic zone estimation, given in **Eq. 2.27** [34]. Even at the highest testing temperature, most crack tip plastic zone were still reasonably small compared to the specimen size (except for Si at 770 °C), hence allowing LEFM to calculate valid K_{Ic} values. In addition, most specimens in the high-temperature micro-fracture works were loaded monotonically to final failure, with no quantitative measurements of the crack length, even when stable crack growth were observed in some systems. A lack of excellent thermal stability prevented the accurate stiffness measurements required to obtain the

crack length. Therefore, a new temperature matching strategy and an accurate stiffness measurement method should be developed in order to measure fracture toughness in the presence of non-negligible crack tip plasticity.

$$r_y = \frac{1}{2\pi}\left[\frac{K}{\sigma_{ys}}\right]^2 \quad (\boldsymbol{Eq.2.27})$$

where K and σ_{ys} are fracture toughness and yield stress, both using values at the highest testing temperature

Authors	Material	Temperature Range (°C)	K_{Ic} (MPa·m$^{0.5}$)	σ_{ys} at Highest Testing Temp (GPa)	r_y at Highest Testing Temp (nm)	BDTT (°C)	Stable Crack Growth
Hintsala et al. [59]	SC-Si	25 ~ 600	0.7~1.6	~1 [64]	~400	300	Yes
Armstrong et al. [61]	SC-Si	25 ~ 770	None	~0.1 [65]	~40000	600	No
Best et al. [62]	CrN	25 ~ 500	3.3±0.3 (1.9±0.5 after cooling)	~3 [66]	~200	No	No
Jaya et al. [63]	SC-Si	25 ~ 600	1~1.8	~1 [64]	~400	300	Yes

Table 2.2 Summary of recent high-temperature micro-fracture works

2.4 Chevron-Notched Specimen

This section will first give a brief overview on the early developments of chevron-notched fracture specimen, as it brings several advantages over conventional fatigue pre-cracked specimen. The theoretical basis of the chevron notch geometry for crack stability are also described. The EPFM analysis used in this thesis is slightly different than the conventional plane-strain fracture toughness calculation (K_{Ic}), so materials with rising R-curve behaviour will also be discussed. Advantages and disadvantages for chevron-notched specimens are summarised in **Table 2.3**.

Advantages	Disadvantages
Fatigue pre-cracking not required	Notch machining difficulty
Crack stability	Test standard exists only for brittle materials
Crack path well-defined	Extensive FE modelling for obtaining SIFs (for non-standard specimens)
Only unstable fracture load required for K_{Ic} calculation (assuming LEFM)	
Less stringent specimen size limitation	

Table 2.3 Advantages and disadvantages of chevron-notched fracture specimens

2.4.1 Early Developments of Chevron-Notched Specimens

Nakayama et al. [67] first introduced the concept of an unsymmetrical notch, shown in **Fig. 2.26**, into bending specimens. This allowed some stable crack growth to occur before final failure. Utilising this design eliminated the need for fatigue pre-cracking, as it was extremely time consuming and difficult for brittle refractory metals. Tattersall et al. [68] later introduced a symmetrical notch into a three-point bending bar to measure the work-of-fracture (WOF) of brittle materials, shown in **Fig. 2.27**. Similarly, a pre-crack could be initiated at very low load,

and maintain its stability until a critical crack length is reached. The WOF was then calculated using the area under the load-displacement curve and the crack opening area. Pook [69] later suggested using the symmetrical-notched bending bar to determine the plane-strain fracture toughness (K_{Ic}) of metals. By introducing suitable side grooves to the straight-edged notch, one should be possible to omit the pre-cracking stage. Pook's side-grooved notch is the present day chevron notch. However, he only applied analytical solutions to calculate the SIFs as a function of crack length for various type of chevron notches, shown in **Fig. 2.23**. Experimental studies using chevron-notched specimen to obtain K_{Ic} were not performed.

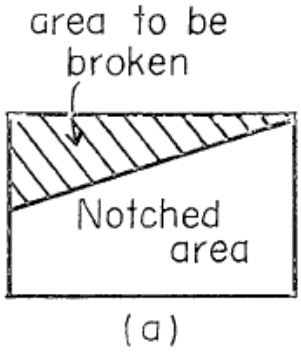


Fig. 2.26 Cross section of the unsymmetrically-notched bending beam by Nakayama et al. [67]

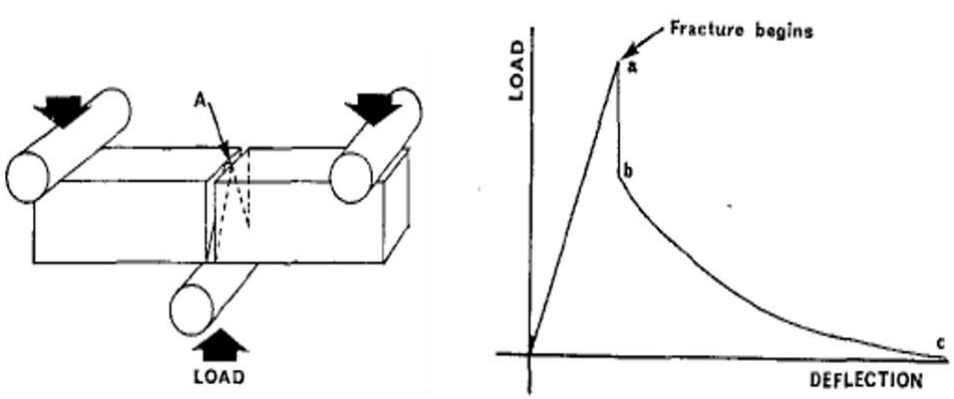


Fig. 2.27 Initial design of a chevron-notched 3-PB specimen by Tattersall et al. [68]. The LD curve showed stable crack growth from point a to c, and beyond point c is crack instability

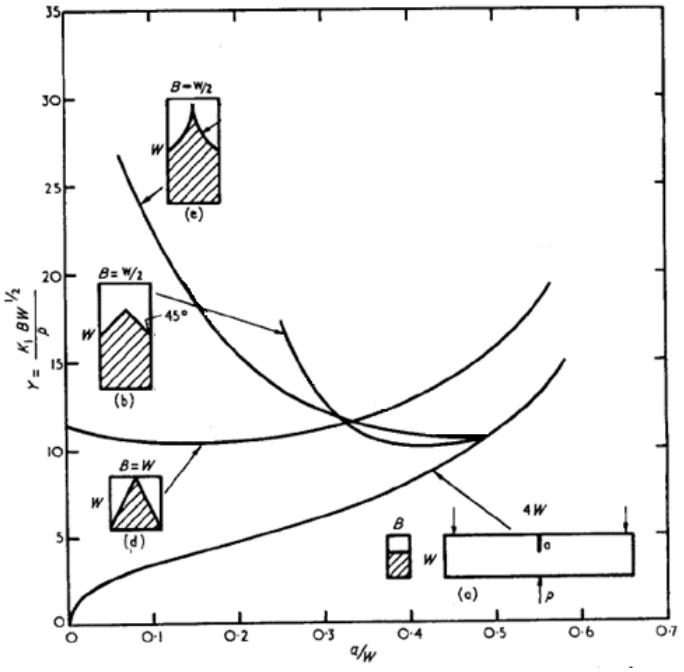


Fig. 2.28 Various types of side-grooved (chevron-notched) bending bars and their respective normalised SIF vs. crack length plots [69]

Barker et al. [70] proposed the short rod geometry to determine the plane-strain fracture toughness. The specimen was loaded by a knife-edge loading fixture. The K_{Ic} values obtained from short rod specimens agreed well with values obtained from ASTM E399 compact-tension specimens, hence validating this specimen design. Munz et al. [71] proposed a square cross-sectioned bar specimen and conducted extensive experimental compliance calibrations to determine the SIFs. Schematic drawings for both short rod and square bar specimen are given in **Fig. 2.29**. The main difficulty for proposing a new fracture specimen design is determination of the geometry-dependent SIFs. Therefore, extensive round robin studies were carried out by various research institutes to obtain accurate and reliable SIFs for both geometries [72-74].

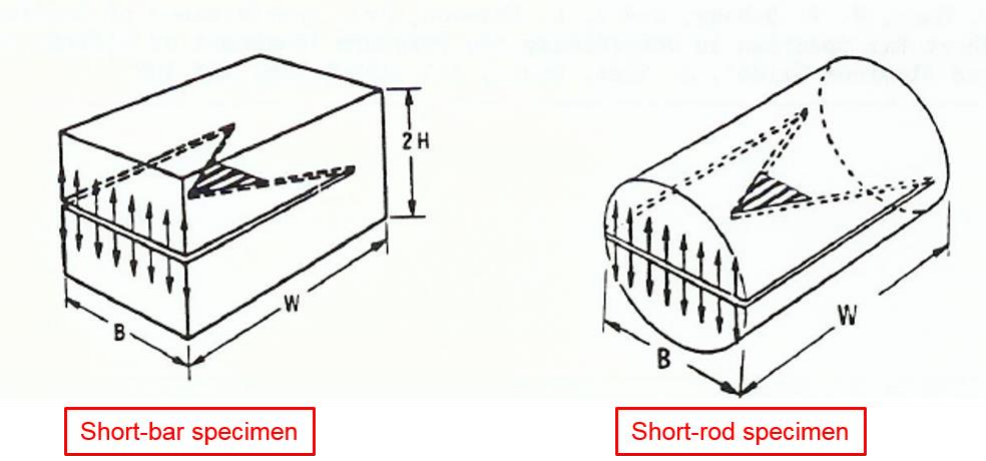


Fig. 2.29 Schematic drawings of both chevron-notched short bar and rod

2.4.2 Theoretical Basis for Chevron-Notched Specimens

The theoretical basis for these benefits are described using both geometrical-dependent stress intensity factors (SIFs) and crack driving force approaches. **Fig. 2.30** illustrates the unique SIF solution for a chevron-notched specimen compared to a straight-notched specimen. The dashed curve show the non-dimensional SIFs for a straight-notched (SN) specimen as a function of the normalised crack length α (α=a/B, with respect to thickness). This curve is a monotonically increasing function with crack length. The solid curve shows the solution for a chevron-notched specimen. For $\alpha=\alpha_0$, the initial SIF is very large due to the sharp chevron apex, but it rapidly decreases as the crack length increases, due to the increasing crack front. A minimum value Y_{min} is reached (labelled with a black open circle in **Fig. 2.30**) when the crack length is between α_0 ($\alpha_0=a_0/B$) and α_1 ($\alpha_1=a_1/B$). For $\alpha \geq \alpha_1$, the SIFs for both chevron-notched and straight-notched specimen are the same because now the crack configurations are identical.

Fig. 2.31 shows the fracture toughness K plotted against crack length. The solid line begins at α_0 and levelling off at K_{Ic} is the ideal fracture resistance curve for a brittle material (flat R-curve, no resistance behaviour). The dashed curves show the "crack driving force" for various

values of applied load on a chevron-notched specimen. Because of the extremely large K value at $\alpha=\alpha_0$, a very small load P_1, is enough to initiate a crack the chevron apex. At load P_1, the crack grows until the crack driving force equals K_{Ic}, which is the intersection point between the dashed curve and the horizontal line at point A. Further increases in load are required to extend the crack to point B and C. At the maximum load, P_{max}, the crack driving curve is then tangent to the K_{Ic} line at point D. Thus, the critical K value at unstable fracture equals to K_{Ic}. In addition, the tangent point D also corresponds to the minimum value of SIF on the crack driving force curve. Therefore, the plane-strain fracture toughness K_{Ic} can be calculated using **Eq. 2.28**.

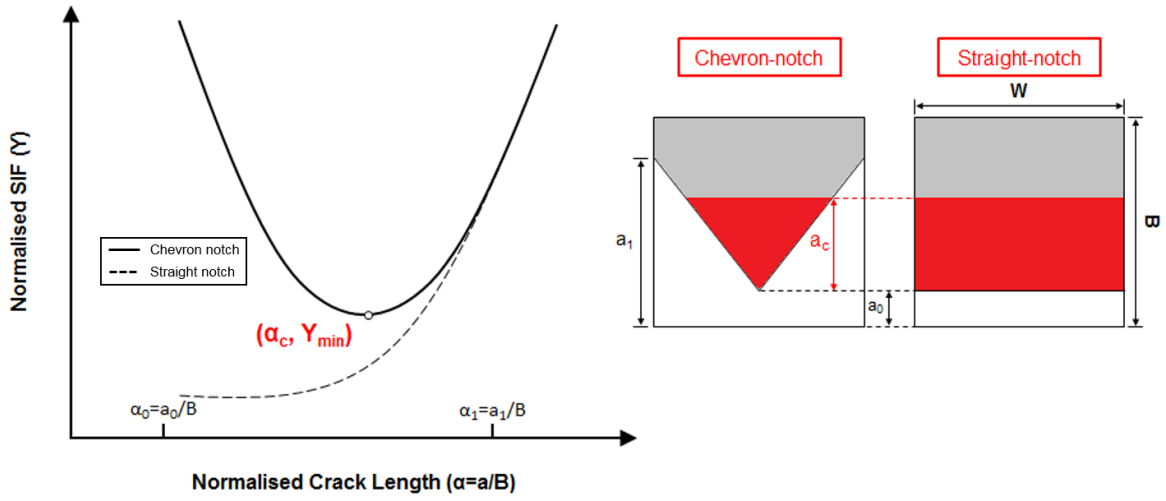


Fig. 2.30 Normalised SIF (Y) vs. crack length (α) plots for both chevron and straight-notched bending bar. The red-shaded area indicates crack opening area

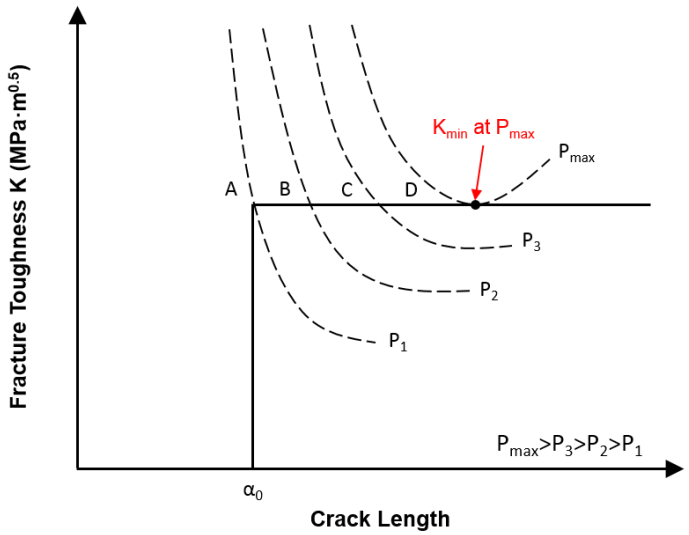


Fig. 2.31 Crack driving force curves of a brittle material with a flat fracture resistance behaviour

$$K_{Ic} = P_c \frac{Y_{min}}{B\sqrt{W}} \quad (\boldsymbol{Eq.2.28})$$

where P_c is the maximum fracture load (at crack instability), Y_{min} is the minimum normalised SIF at crack instability (calculated via linear elastic FE analysis), B, W are the beam thickness and width

2.4.3 Materials with Rising R-Curve Behaviour

The plane-strain fracture toughness calculation using maximum load at crack instability described previously can only be applied to brittle linear-elastic materials with no fracture resistance behaviour (flat R-curve). However, most metallic materials exhibit fracture resistance behaviour (rising R-curve). Using chevron-notched specimen on these materials will require SIFs as a function of crack length, so that the threshold K values at each crack increment can be calculated. This will require both experimental and modelling work to obtain the SIFs vs. crack length relationships. Shannon et al. [75] used experimental compliance measurements to develop

polynomial equations for SIFs as a function of crack length for chevron-notched square-bar specimens.

Fig. 2.32 illustrates the application of the fracture resistance curve concept to a material with a rising R-curve. The R-curve (solid curve) begins at the initial crack length α_0. The dashed curves are the crack driving force curves for various applied load values on a chevron-notched specimen. As the load is increased, the crack grows stably (from point A to B, C and D, consequently) until the load reaches P_{max}. At this load and crack length, crack growth become unstable (point D). However, the instability point (the tangent point between crack driving force curve and fracture resistance curve) does not correspond to K_{min} (solid symbol). Therefore, using P_{max} and Y_{min} will underestimates the true K_{Ic} value. Therefore, the fracture resistance curve approach is suggested as it calculates K progressively (with crack growth) until the point of crack instability.

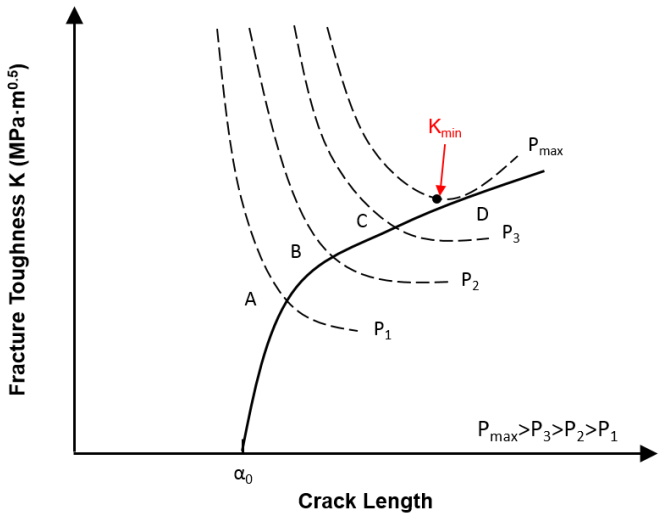


Fig. 2.32 Crack driving force curves (at various load, function of crack length) of a ductile material with a rising R-curve

2.5 Literature Review Summary

This literature review provides a brief background of both LEFM and EPFM analysis. In the case for brittle materials, fracture behaviour can be characterised via LEFM, using a single toughness value K_{Ic}. In the case for the semi-brittle tungsten, its fracture behaviour has to be characterised via EPFM, due to fracture resistance behaviour (R-curve) associated with the microscopic dislocation activities. Various micro-fracture test methods and specimen designs are discussed. Recent work on high-temperature micro-fracture tests are also discussed. For R-curve calculation via EPFM analysis, crack stability, usage of real pre-crack, and a well-defined crack path are preferred, which can all be provided by introducing a chevron notch. Developments and theoretical basis for chevron-notched fracture specimens are also described. The chevron notch approach, especially on materials exhibiting R-curve behaviour, will require extensive information of the SIFs as a function of crack length.

2.6 Research Aims

This thesis aims to improve current micro-cantilever bending tests to the extent so that the fracture properties of tungsten can be measured at high temperatures (~700 °C). This requires high-temperature loading by nanoindentation and a stable micro-fracture specimen design. The fracture toughness and resistance curves as a function of temperature can then be calculated to quantify the brittle-to-ductile transition of tungsten at the microscale. The results are compared with macroscopic values to investigate the effects of specimen size to fracture toughness. The following chapters will first use finite-element simulation to validate the chevron-notched micro-cantilever design. Then, micro-fracture test results ranging from room temperature up to 700 °C will be reported.

III EXPERIMENTAL METHODS

This section describes the experimental techniques used in this thesis, including sample preparation, scanning electron microscopy (SEM), electron backscattered diffraction (EBSD), focused-ion beam (FIB), and both room temperature and high temperature nanoindentation. Only brief discussions of sample preparation, SEM, and EBSD will be given, since only basic techniques were being used. Micro-cantilever fabrication via FIB and nanoindentation, especially at elevated temperature, will be discussed in more detail.

3.1 Sample Preparation

An ingot of industrial grade tungsten-1%tantalum (W-1%Ta) alloy was produced by Plansee® (Reutte, Austria) prior to this project via powder consolidation (>2000 °C), high pressure torsion (>2000 bar), and hot forging. Result of this process route gave the tungsten alloy a very fine, highly-textured, and pancake-like grain structure, shown in **Fig. 3.1**. The ingot was then sectioned into 11x1x1 mm rectangular matchsticks via electrical discharge machining (EDM) by the mechanical workshop at Oxford's Physics Department.

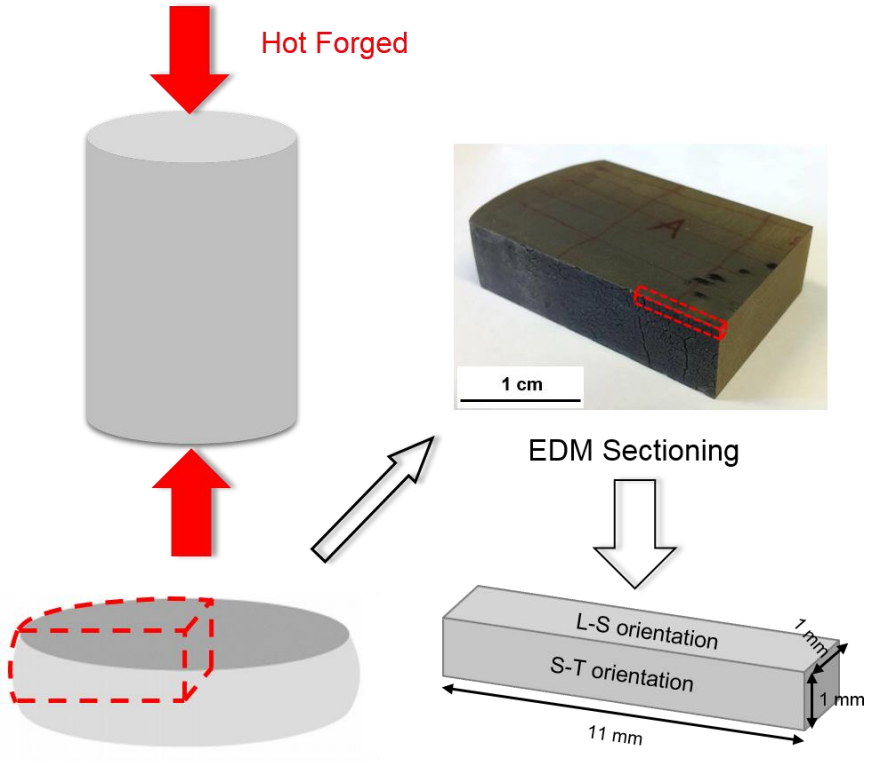


Fig. 3.1 Hot forged W-1%Ta ingot. Notations L-S (longitudinal-short transverse) & S-T (short transverse-transverse) were used to label the various orientations

Mechanical and chemo-mechanical grinding/polishing were carried out to reveal the grain structures and remove the residual stresses from processing and EDM sectioning. Matchsticks were mounted on a brass sample holder, mechanically grinded with silicon carbide grit paper to a 4000 grit finish, followed by successively finer diamond paste polishing (6, 3, 1 μm), shown in **Fig. 3.2**. For EBSD analysis, which requires a damage-free surface, additional chemo-mechanical polishing via 40 nm colloidal silica suspension was used. This final polishing procedure removed the residual stresses from previous polishing steps and also slightly etched the sample surface to reveal the grain structure.

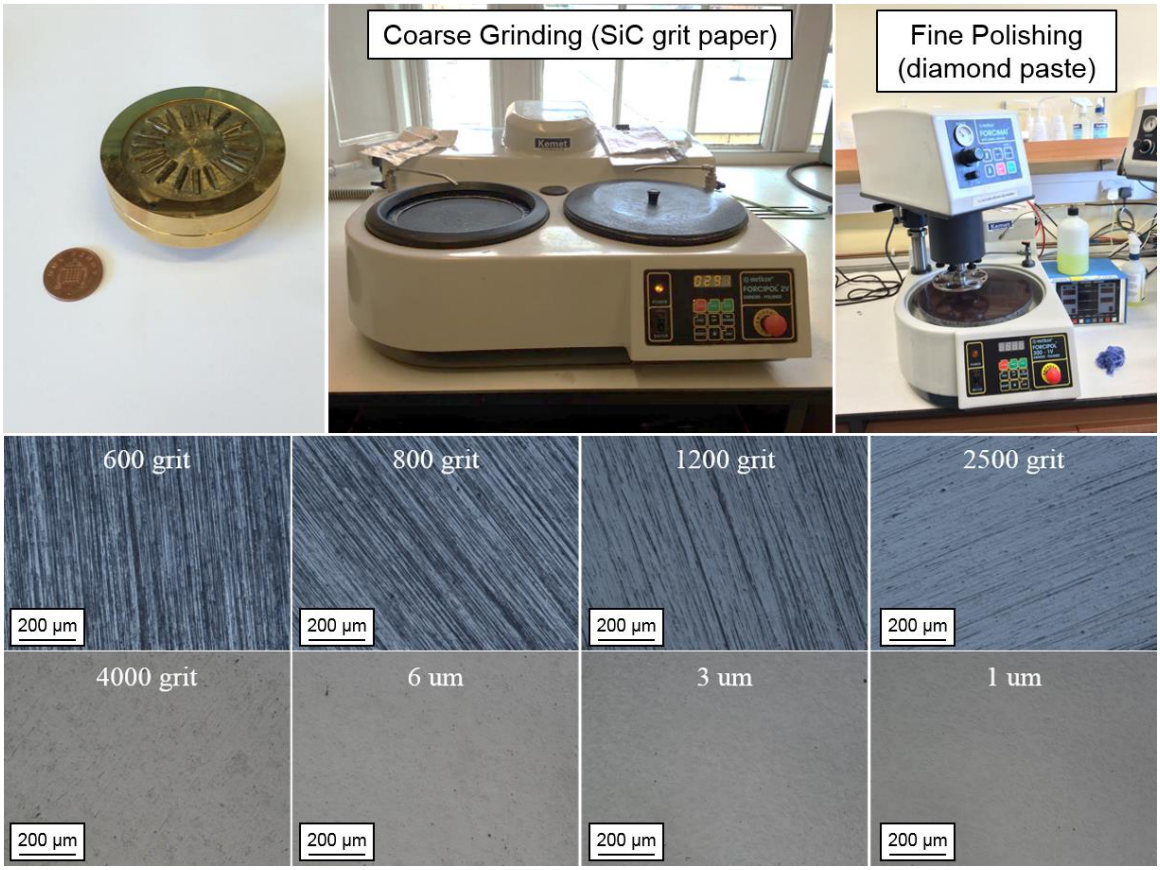


Fig. 3.2 Instruments used for sample preparation and optical micrographs of the sample surface after each polishing step

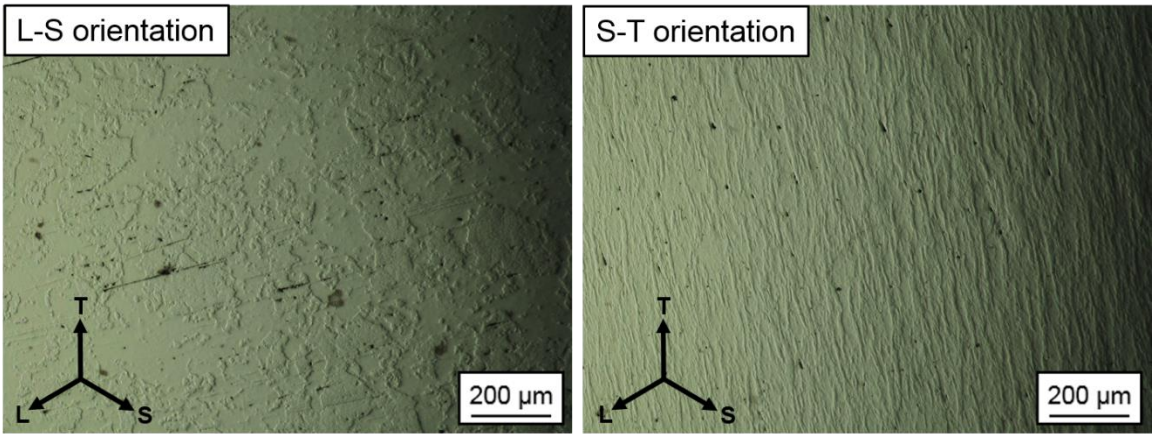


Fig. 3.3 Optical micrographs of the W-1%Ta after colloidal silica polishing. The highly-textured grain structures of each orientation is revealed

3.2 Scanning Electron Microscopy

Scanning electron microscopy (SEM) is a standard analytical technique for high-resolution topography and compositional analysis. Micrographs in this thesis were mostly taken using the secondary electron detector using a Zeiss® Auriga dual beam FIB/SEM microscope, to image the micro-cantilevers, and to examine the fracture surface. An inLens detector was also used to image the fracture surface as better contrast of topology can usually be achieved.

3.3 Electron Backscatter Diffraction

Electron backscatter diffraction (EBSD) is a powerful technique for analysing the crystal structures of materials. Schematic representation of an EBSD setup is shown in **Fig. 3.4**. Electrons emitted from the JEOL 6500F SEM interact with the sample, and the backscattered electrons are channelled along the low index crystal planes, producing Kikuchi patterns that can be used to index specific crystal orientations. The Kikuchi patterns, shown on the phosphor screen, was captured using a CCD camera. Commercial EBSD software (EDAX® TSL Orientation Imaging Microscopy 5.3) was used to index the crystal orientation automatically.

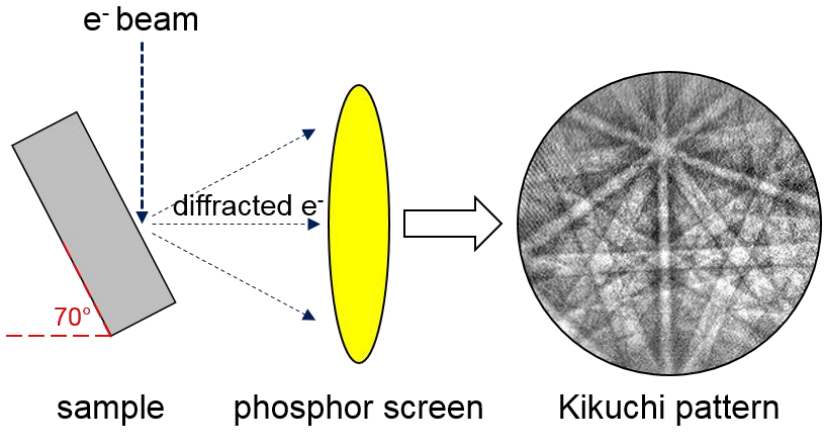


Fig. 3.4 Schematic representation of an EBSD setup

Area of 200 x 200 μm was scanned on both orientations (L-S & S-T) via EBSD for grain size analysis. Shown in **Fig. 3.5**, the grains in the S-T orientation were elongated along the short-transverse (S) direction due to the hot forging. Grain radius is approximately ~28 μm along the long axis, and approximately 2 μm along the short axis. The grains in the L-S orientation, however, is much more equiaxed and have an average radius of approximately 38 μm. Micro-cantilevers were fabricated on the S-T orientation so that multiple grains (usually 5~7) could be included in a single micro-cantilever. This is to make sure that the fracture properties measured are from the real microstructures of the W-1%Ta alloy, rather than from a single crystal W.

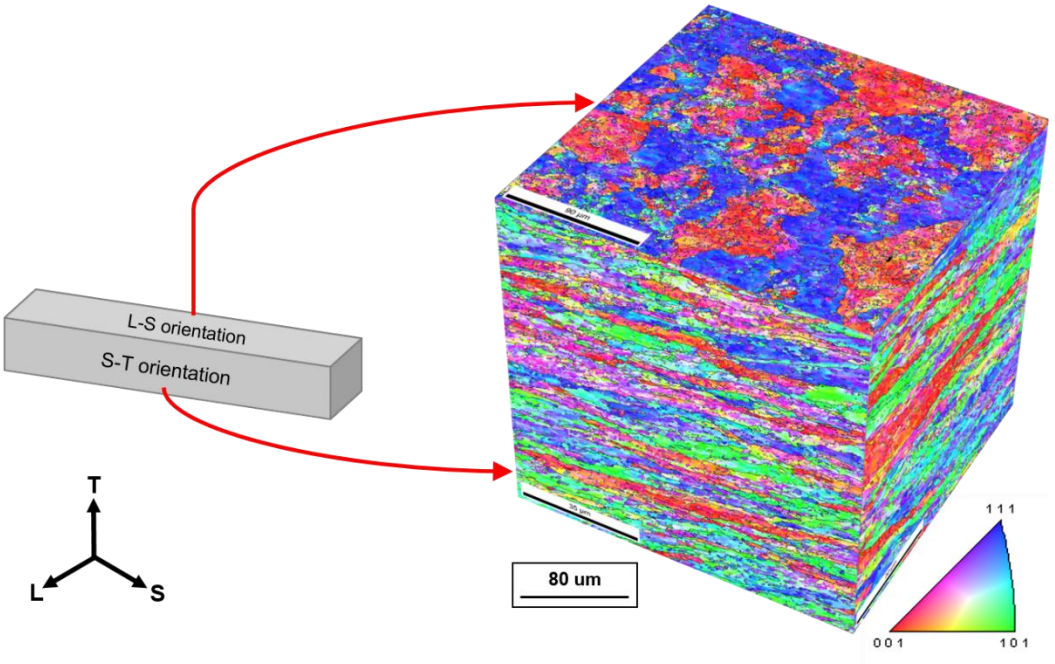


Fig. 3.5 Inverse pole figure (IPF) maps of both L-S & S-T orientations produced using EBSD. High-angle grain boundaries (with misorientation > 15°) were indicated as black borderlines, so that the grain size could be calculated

3.4 Focused Ion Beam

Focused ion beam (FIB) microscopes, unlike SEMs, emit gallium (Ga^+) ions instead electrons. Ga^+ ions are emitted from a gallium liquid metal source, with accelerating voltages from 5~30 keV. Emission current is usually around 2 μA, then refined using various apertures which gives control over the beam spot size (5~500 nm, depending on the aperture used). The Ga^+ beam is scanned over the sample and secondary electrons are collected to form images, which is similar to a SEM. A photo of the FIB used in this thesis (dual beam Zeiss® Auriga) and its schematic representation are shown in **Fig. 3.6(a)** and **(b).** Ga^+ ions can also experience elastic scattering with target atoms, shown in **Fig. 3.6(c)**. By focusing the beam and continuously scanning across the selected area, atoms will be displaced from their original lattice site and eventually removed, hence achieving precise micro-machining. This micro-machining method is currently the main method for fabricating micro-specimens used in micro-mechanical tests.

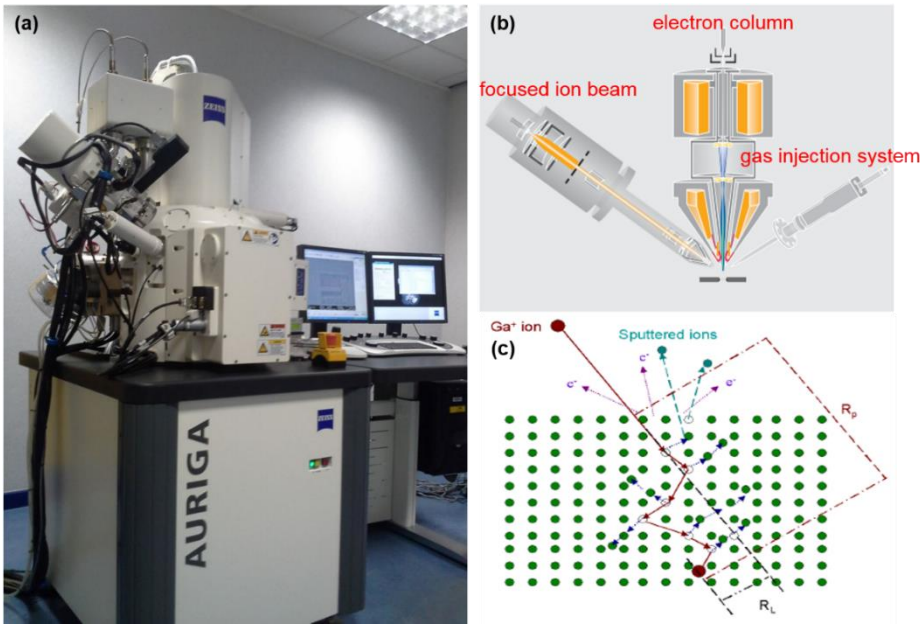


Fig. 3.6(a), (b) Zeiss® Auriga dual-beam FIB used for this work and **(c)** schematic image of the displacement damage caused by the Ga^+ ions interacting with a solid body [76]

The dual-beam Zeiss® Auriga FIB/SEM, equipped with both electron and ion beam column, was used to fabricate the micro-cantilevers. This allows high-resolution imaging and precise FIB machining at the same time, hence significantly reducing the irradiation damage associated with Ga^+ ion beam. The procedures for micro-cantilever fabrication were as follows:

(1) Use 4 nA beam current to roughly mill the U-shaped trenches to create the initial shape of the cantilever **Fig. 3.7(a)**

(2) Use 1 nA beam current to polish away the re-deposited materials from the previous stage to create a smoother surface **Fig. 3.7(b)**

(3) Use 600 pA beam current to undercut the cantilever to make it freestanding. This can be done via tilting the stage 45° and perform box cuts from both sides, shown in **Fig. 3.7(c)**. A pentagonal cross-section is obtained, shown in **Fig. 3.7(d)**

(4) Use 100 pA to further polish down the cantilever to its final geometry, shown in **Fig. 3.8(a)**

(5) Use 10 pA beam current to mill the chevron notch with a tilted angle from both sides, shown in **Fig. 3.8(b)**

(6) SEM and EBSD images of a typical chevron-notched micro-cantilever fabricated on the S-T orientation are shown in **Fig. 3.9(a**) and **(b)**

Typical cantilevers used in this thesis have length of approximately 10 μm, width and thickness of approximately 3 μm**.** This is to ensure the entire cantilever can be positioned within the thin ion-irradiated zone (typically 1~3 μm for tungsten, depending on the implantation energy used). The chevron angle is approximately 90°, which is of crucial importance to crack stability and will be discussed in the chevron notch optimisation section in Chapter 4.

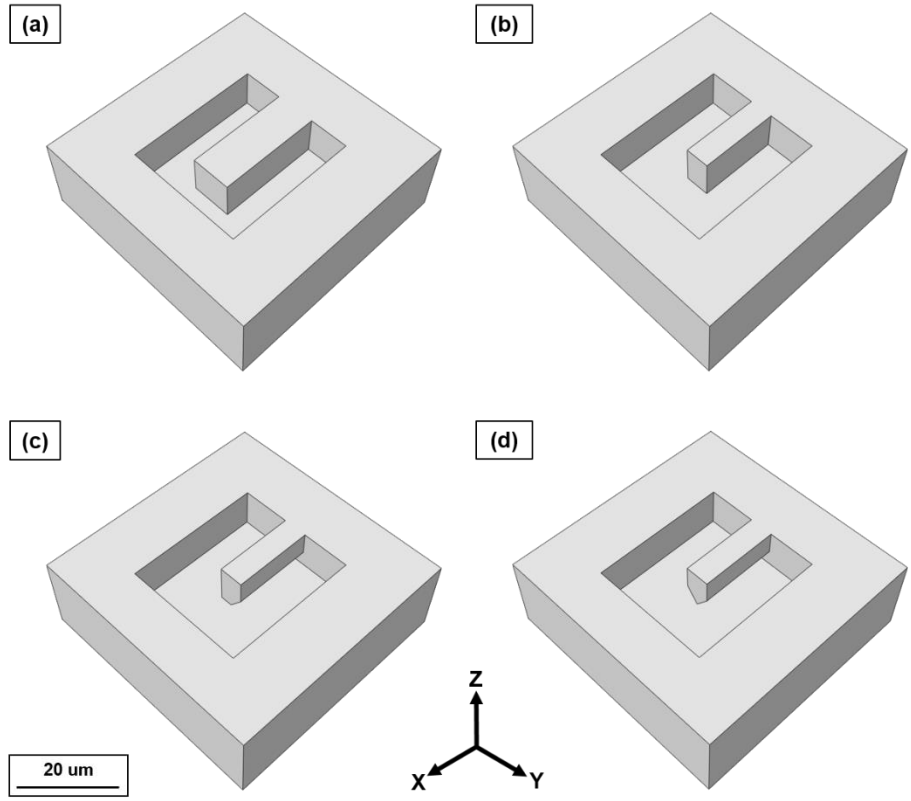


Fig. 3.7 Schematic images showing the various stages during the fabrication of a chevron-notched micro-cantilever

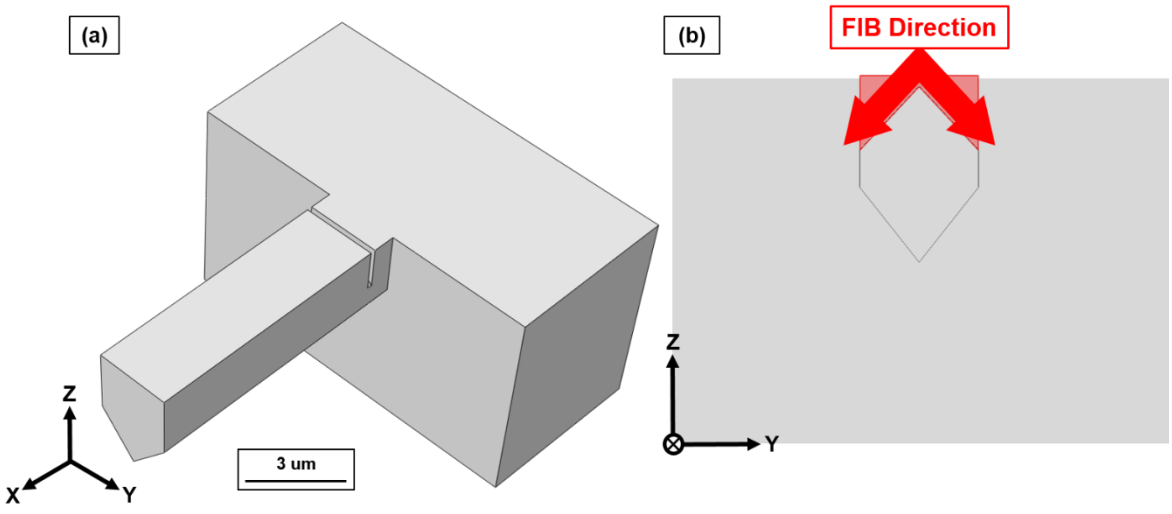


Fig. 3.8 Final geometry of the pentagonal cross-sectioned micro-cantilever and the procedures for introducing the chevron notch

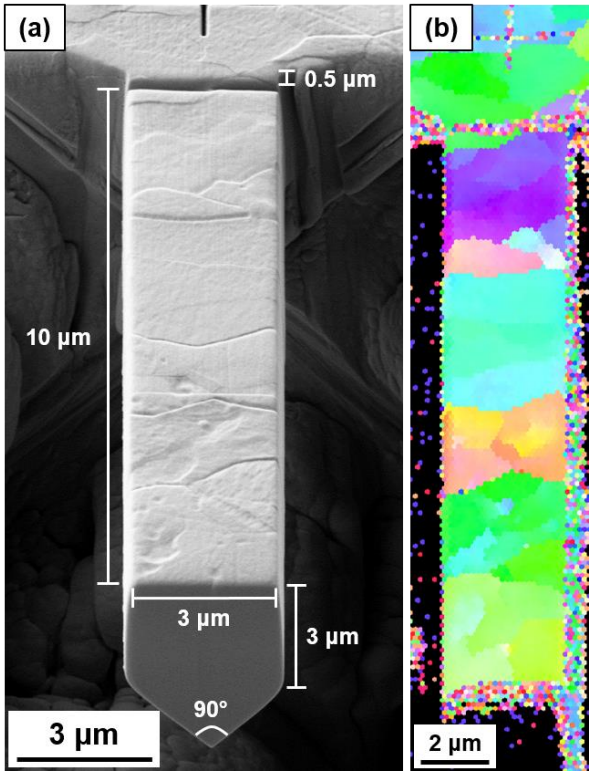


Fig. 3.9 SEM and EBSD images of a typical chevron-notched W-1%Ta micro-cantilever fabricated on the S-T orientation

3.5 Nanoindentation

Since its invention by Pethica, Hutchings, and Oliver in 1983 [77], nanoindentation has become a standard mechanical characterising technique for measuring the mechanical properties of small volume of materials. There are many commercial systems currently available (Keysight®, Micro Materials®, Hysitron®, Nanomechanics Inc., Anton Paar®, Alemnis®) with recent developments that allow nanoindentations to be conducted from cryogenic to high temperatures [78], *in-situ* testing within SEM/TEM [79, 80], and dynamic modules for measuring the thermally-activated volume [81].

This section will first describe basic nanoindentation, then the continuous stiffness measurement (CSM) method, and the NanoVision® scanning stage using a Keysight® G200 Nanoindenter. High temperature nanoindentation were carried out using the Micro Materials® NanoTest Xtreme, which will be discussed separately in section **3.6**.

3.5.1 Basic Operation

The principle goal of nanoindentation is to extract the elastic modulus and hardness from the load and displacement data. This involves a hard tip penetrating into the surface of a material, at a given force and known depth. A schematic representation of the G200 Nanoindenter and a typical load-displacement curve are shown in **Fig. 3.10**. The coil magnet assembly applies a known load to the indenter shaft, and the displacement of the shaft is measured using a capacitance gauge. Nanoindenters are mostly intrinsically load-controlled instruments (Alemnis® nanoindenters are displacement-controlled), however, pseudo displacement-controlled for load-controlled machines are also possible through a PID (proportional-integral-derivative) device. The raw load and displacement data are first processed through the PID controller and new variable are set for actuating the force so that a constant displacement rate can be maintained. However, data processing requires a certain time step, which limits the speed of the feedback loop and therefore pseudo displacement-controlled tests should not to be consider as true displacement-controlled tests. The resolution of the G200 Nanoindenter (XP mode) is 50 nN in force and 0.01 nm in displacement [82]

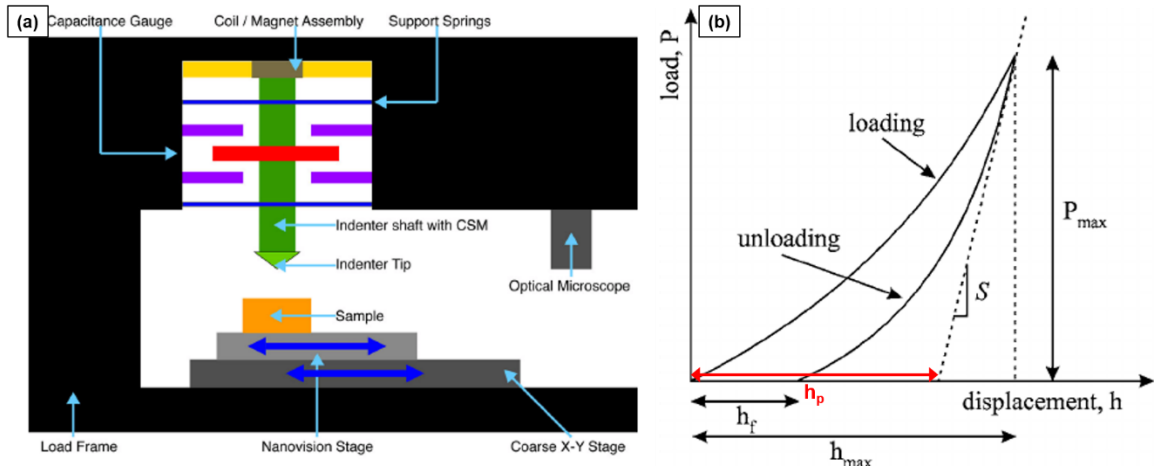


Fig. 3.10 Schematic illustration of a G200 Nanoindenter and a typical load-displacement curve

Indentation hardness can be calculated using the indentation load divided by the projected area of the contact [83]. For a Vickers or Berkovich indenter, the area function can be expressed as a function of the indentation depth using **Eq. 3.1** [84]:

$$A(h) = 24.5{h_p}^2 \ (\boldsymbol{Eq.3.1})$$

where h_p is the indentation depth at maximum load. Measurement of elastic modulus is somewhat more laborious; it requires both the contact stiffness **S** and the elastic contact area **A**. Using the load-displacement curve from **Fig. 3.10(b)**, the contact stiffness at maximum load can be determined by fitting a straight line to the initial portion of the unloading curve, shown in **Eq. 3.2** [85]:

$$S = \frac{dP}{dh} \ (\boldsymbol{Eq.\ 3.2})$$

where P is the indentation load, and h is the indentation depth. For the case of a cylindrical punch, one can rewrite **Eq. 3.2** using the reduced elastic modulus $\mathbf{E_r}$ and the contact area **A**, given in **Eq. 3.3** [85]:

$$\frac{dP}{dh} = 2E_r \frac{\sqrt{A}}{\sqrt{\pi}} \ (\boldsymbol{Eq.3.3})$$

substituting A with **Eq. 3.1,** the contact stiffness can be further simplified to **Eq. 3.4**

$$S = \frac{dP}{dh} = 2h_p E_r \sqrt{\frac{24.5}{\pi}} \ (\boldsymbol{Eq.3.4})$$

consider a non-rigid indenter, elastic modulus of the sample can be calculated using **Eq. 3.5** [85]:

$$\frac{1-\nu^2}{E} = \frac{1}{E_r} - \frac{(1-\nu_i^2)}{E_i} \ (\boldsymbol{Eq.3.5})$$

where **E** and $\boldsymbol{\nu}$ are the elastic modulus and the Poisson's ration of the specimen and $\mathbf{E_i}$ and $\boldsymbol{\nu_i}$ are those of the indenter.

In summary, nanoindentation is a quick and simple way to measure hardness and modulus from a small volume of material. However, this technique relies on empirical assumptions of the contact area (using an area function determined from indenting into a perfectly elastic material, i.e. fused silica) and lacks the ability to measure fracture and plastic properties (yield stress, work hardening coefficient). Additional techniques, such as micro-cantilever bending tests, are therefore required to give a more complete micro-mechanical analysis.

3.5.2 Continuous Stiffness Measurement

The continuous stiffness measurement (CSM) method allows the contact stiffness of the specimen to be measured continuously during the indentation. This is achieved by imposing a small harmonic oscillation on the indenter tip, shown in **Fig. 3.11**. First introduced by Pethica and Oliver [86], and further extended by Oliver and Pharr [85]. It has now become a standard method to measure the modulus and hardness of the material as a function of indentation depth.

The applications of the CSM method on various material systems and its further development can be found in the review paper by Li et. al [87].

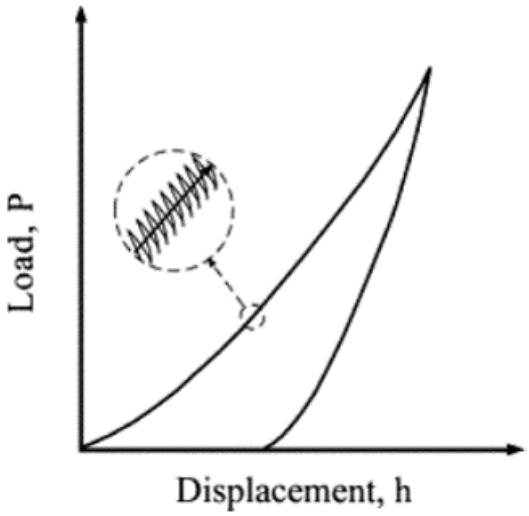


Fig. 3.11 Load displacement curve showing small sinusoidal signal from the CSM method [87]

In addition, the CSM method provides a convenient way to measure the elastic stiffness of the micro-cantilever. This is described and analysed in more detail in Chapter 5.3. However, the CSM method is not available in the Micro Materials® indenter. A newly developed load-partial unload method is utilised to measure the static cantilever stiffness, which will be further discussed in the following section.

3.5.3 NanoVision® Scanning Stage

The NanoVision® Stage can produce a topological image of the sample surface, similar to a contact force AFM. The indenter tip is brought into contact with the sample surface at a constant low load, usually 1~5 μN. The area of interest is then scanned under the indenter tip via the piezoelectric stage. This allows nanometre features to be imaged and accurate load positioning, essential for testing micro-cantilevers. **Fig. 3.12** shows a scanning image of a Si

micro-cantilever, where the larger cross shown in **Fig. 3.12(a)** and **(b)** is firstly scanned to align the cantilever. It is desired to have the cantilever's long axis pointing upwards to avoid the indenter hitting the cantilever edges during the scanning process. The smaller cross shown in **Fig. 3.12(c)** is then used to further align the loading position on the cantilever's long axis, as misalignment can introduce other modes of fracture. This aligning approach is used for all cantilever tests in this thesis. One should also be aware of the resolution of the scan image is not as good as a true AFM due to a much blunter indenter tip. A Berkovich indenter tip has radius of curvature ≈ 40 nm, whereas a typical AFM scanning tip has radius of curvature ≈ 10 nm. However, it still gives better positioning control than the conventional screw thread driven stage and images provided by the optical microscope.

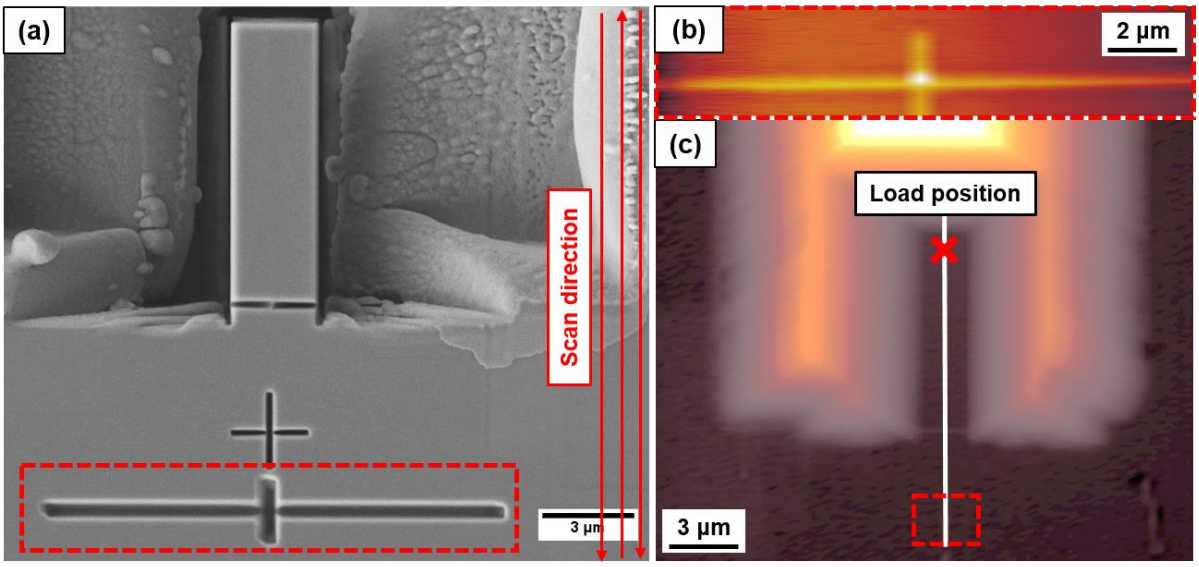


Fig. 3.12 (a) SEM and the surface scan of a silicon micro-cantilever. The scanning direction is indicated in red arrows. The larger cross (red box) shown in **(b)** was firstly scanned first for cantilever alignment, and the smaller cross labelled via red-dotted box shown in **(c)** was then used to align the loading position

3.6 High-Temperature Nanoindentation

The progress made in developing high temperature nanoindentation over the last two decades is summarised in the recent review article by Wheeler et al [78]. **Table 3.1** summarises all the commercial systems currently available, where the heating systems and available operating environments are listed and compared. However, this section will elaborate more on the instrumental setup of the Micro Materials® NanoTest Xtreme, as it is the high temperature nanoindenter used to conduct micro-fracture tests.

Nanoindenter Type	Heating System	Operating Environment
MicroMaterials® NanoTest Xtreme [88]	Independent resistive heaters for tip and sample	Up to ~950 °C in high-vacuum chamber (~10^{-7} mbar)
Hysitron xSol® [89]	Dual heating elements for sample surface and stage	Up to 800 °C in built-in gaseous micro-chamber
Anton Paar® UNHT3 HTV [90]	Three infrared heaters for tip, reference tip, and sample	Up to 800 °C in built-in vacuum chamber
Nanomechanics® InSEM HT [91]	Independent heaters for tip & sample with active cooling system via Peltier elements	Up to 800 °C in SEM
Alemnis® HT Module [92]	Independent temperature control loops for tip & sample	Up to 600 °C in SEM, 200 °C in air
Keysight® G200	Laser-based heaters (SURFACE GmbH) for both sample & tip [93]	Up to 500 °C in air

Table 3.1 Current commercially available high temperature nanoindenter systems

3.6.1 Micro Materials® NanoTest Xtreme

The NanoTest Xtreme was modified from the standard Micro Materials® NanoTest system. Modifications include: **(1)** a built-in high vacuum chamber with roughing and ultra-low vibration turbo-molecular pumps equipped with magnetically-levitated bearings to minimise mechanical vibration, and **(2)** sample stage motor and capacitive displacement sensor compatible with the vacuum environment. Another special feature of the Xtreme system is the horizontal setup - the indenter tip is mounted horizontally on a pendulum assembly, rather than the vertical arrangement of other room temperature systems. This allows heat to be vertically removed via gravity from the sensor region. A heat shield is also added to provide additional shielding from the heat radiation. A schematic drawing of the system is shown in **Fig. 3.13**, and an actual photo of the indenter interior is shown in **Fig. 3.14**.

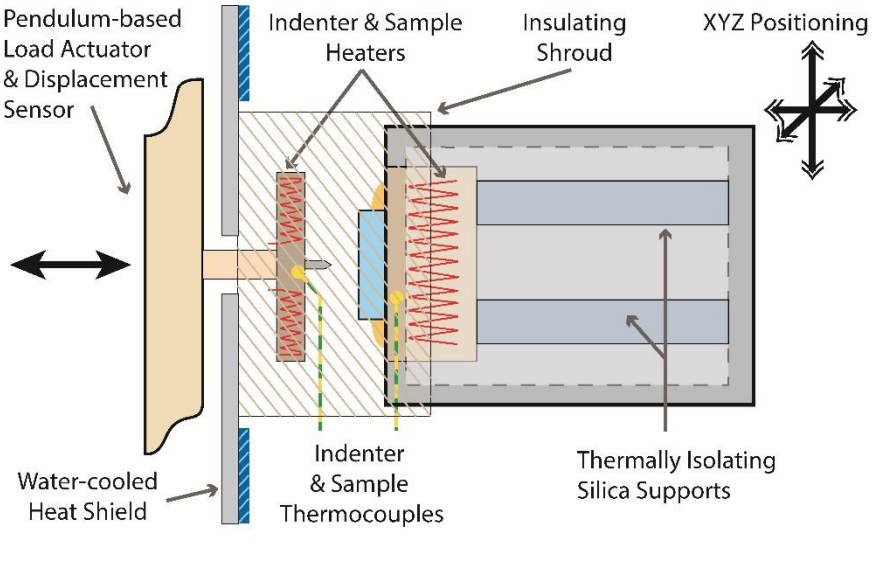


Fig. 3.13 Schematic representation of the Micro Materials® NanoTest Xtreme

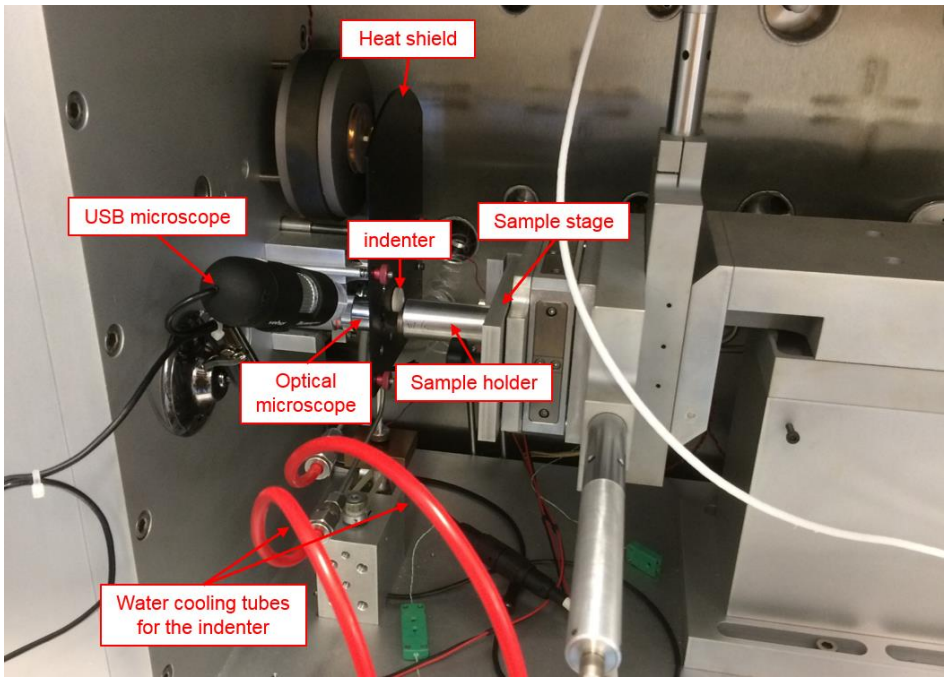
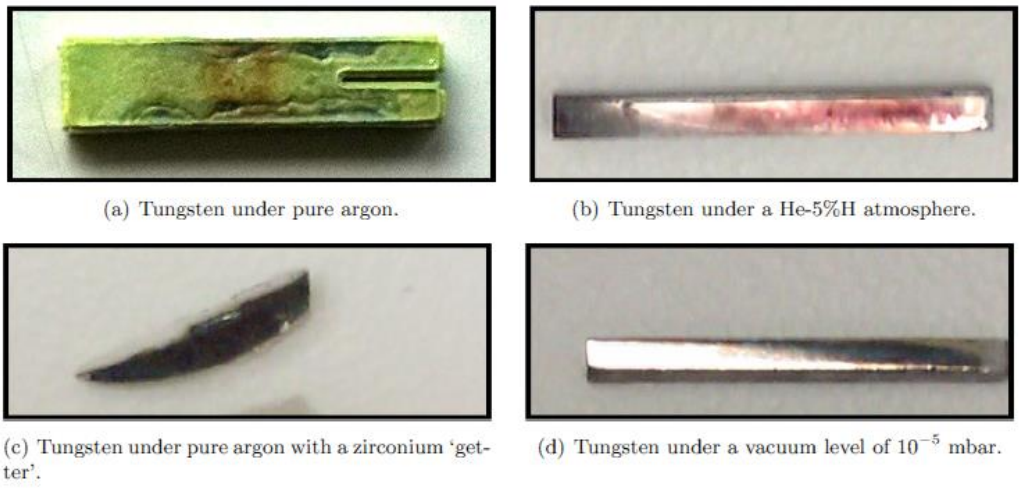


Fig. 3.14 Actual photo of the indenter interior. The sample is mounted on the cylindrical sample holder using high-temperature cement (Forta Fix Autostic FC6)

3.6.2 Testing in Vacuum

For high temperature nanoindentation of tungsten, a vacuum environment is essential due to the following reasons: **(1)** tungsten in a nuclear fusion reactor will operate at high temperature in a vacuum vessel, and **(2)** tungsten is extremely active with oxygen; oxides start to form about 400 °C and sublime completely above 700 °C. Gibson [94] performed high temperature nanoindentation (~700 °C) on pure tungsten under various inert atmospheres: argon, He-5%H atmosphere, and pure argon with zirconium getter. He found all samples exhibited significant oxidation, shown in **Fig. 3.15(a)~(c)**; only sample tested under high vacuum level of ~10^{-5} mbar was able to remain pristine, shown in **Fig. 3.15(d)**.



(a) Tungsten under pure argon.

(b) Tungsten under a He-5%H atmosphere.

(c) Tungsten under pure argon with a zirconium 'getter'.

(d) Tungsten under a vacuum level of 10^{-5} mbar.

Fig. 3.15 (a)~(c) Tungsten sample tested at 700 °C for five hours under various inert atmosphere. **(d)** Tungsten sample tested under high vacuum (~10^{-5} mbar) showed no oxidation

3.6.3 Thermal Drift Control

Thermal drift is a time-dependent error in displacement measurement during nanoindentation. It can originate from: **(1)** the thermal gradient within the system frame, and **(2)** the temperature mismatch between the indenter and sample. The former can be resolved by using a sealed chamber with longer stabilisation period, while the latter is much more troublesome. In vacuum, the atmosphere for heat convection is removed; equilibrating the sample and indenter temperature rely solely on heating both component to identical temperature. The NanoTest Xtreme employs an active dual heating system of indenter and sample through PID temperature control, and a "power-lock" method to overcome this issue. Once the indenter is heated to the target temperature, the output current required to maintain the target temperature is then stopped. This prevents further overheating the indenter and compensates for the heat conduction due to the different thermal masses of the indenter and sample during contact. The thermal drift management procedures used in this thesis were:

(1) Position the sample ~300 μm away from the indenter to prevent thermal expansion of the sample and stage from damaging the indenter

(2) Set the indenter temperature ~15 °C and stage temperature ~20 °C higher than the target temperature. This is because the thermal couple is not directly attached to the indenter tip and the sample surface, but a small distance away, shown in **Fig. 3.16**.

(3) Start heating using the software (stage set to PID control, indenter set to fixed power)

(4) Wait for at least 8 hours for thermal stabilisation (usually leave overnight)

(5) Bring the sample in contact (pendulum depth signal will drop from ~9 to ~3 V upon contact), and retract ~20 μm. Re-calibrate the pendulum depth signal back to ~ 9 V. The indenter temperature will increase due to the radiative heating from the sample. Allow for thermal stabilisation for another 20 minutes.

(6) Set indenter temperature to the current indenter temperature after step 5. This will then adjust the output power (of the indenter heater) to that of the indenter temperature after thermal equilibrium

(7) Perform series of trial indents to determine thermal drift. Pre-indentation thermal drift are used as pre-cursors for determining the temperature mismatch between indenter and sample.

(8) Manually adjust the indenter temperature up or down (using the Eurotherm® controller) based on the slope of the pre-indentation thermal drift. This allows adjusting the power output of the indenter directly. The pre-indentation drift measurements and temperature adjusting are conducted in series of trial and error loops until the drift rate is acceptable. This procedure will be demonstrated on actually tests in **Chapter 6.2**

(9) Once drift rate is acceptable (typically < 0.03 nm/s), allow for thermal stabilisation for another 2 hours. Typical pre-indentation thermal drift measurements for high temperature tests (RT~700 °C) are shown in **Fig. 3.17**

(10) Now the system is ready for test

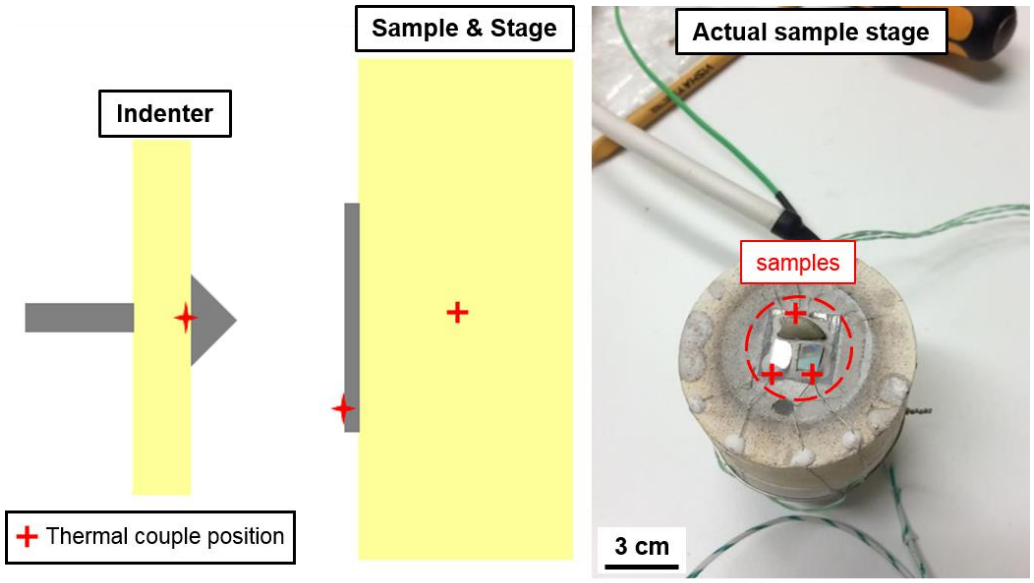


Fig. 3.16 Schematic drawing showing the positions of the thermal couple. Three thermal couples are usually installed to measure the temperature of the indenter, sample surface, and the stage. Right figure shows the actual sample stage with mounted sample and thermal couples

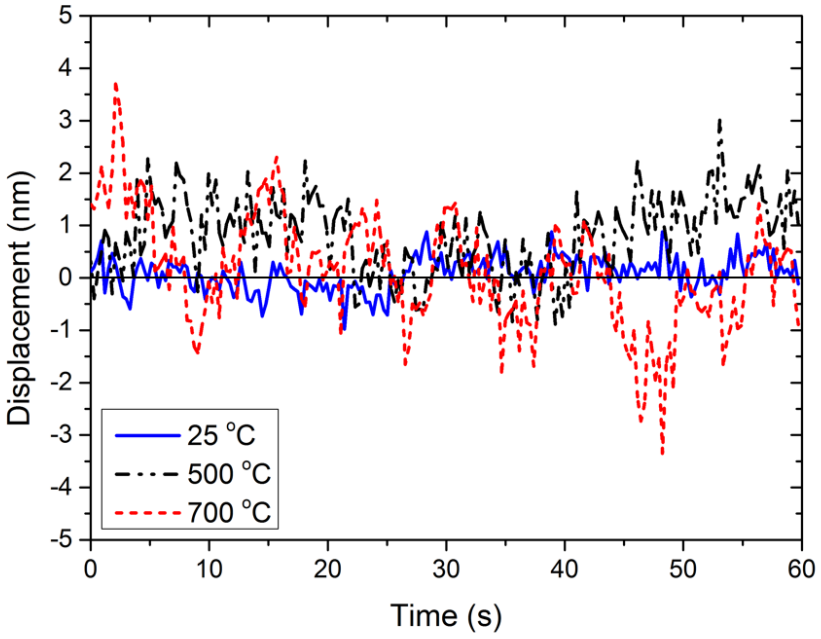


Fig. 3.17 Pre-indentation thermal drift at 25, 500, and 700 °C. Drift values at 700 °C shows larger scatter, but the average drift rate is about 0.03 nm/s

3.6.4 Degradation of Indenter at High Temperature

Degradation (blunting and wearing) of the indenter becomes of an important issue when testing at elevated temperatures. Diamond is the hardest indenter material commercially available (has hardness of approximately 100 GPa). However, it cannot be used to test tungsten due to the formation of tungsten carbide at temperatures above 400 °C [95]. SEM images of a diamond Berkovich tip after indenting tungsten at are shown in **Fig. 3.18**, where formations of tungsten carbide are observed on the tip surface. Therefore, cubic boron nitride (cBN) indenters were chosen, as it is the second hardest indenter material commercially available (~50 GPa) and remains chemically inert with tungsten at elevated temperature.

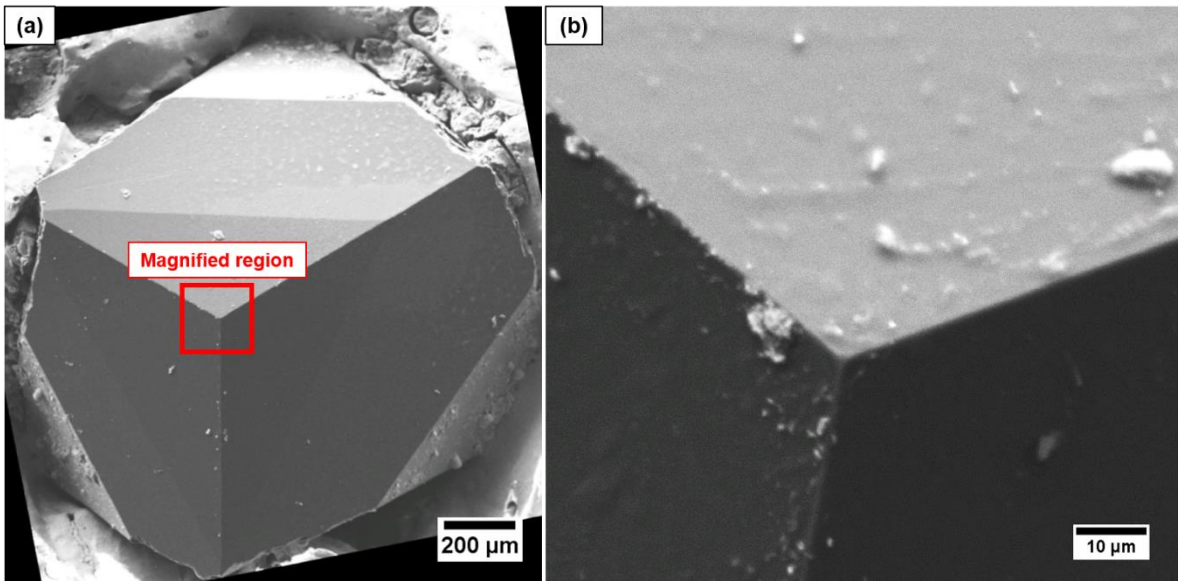


Fig. 3.18 SEM images of a diamond Berkovich tip after indenting tungsten at high temperatures

3.6.5 Load Partial-Unload Method

Mentioned previously, the Micro Materials® NanoTest Xtreme is not equipped with the CSM method. Therefore, the cantilever static stiffness is measured using a newly developed load partial-unload method. In a typical load partial-unload test, the cantilever is first loaded to a maximum load P_{max}, then P_{max} is held for a certain time (5~30 sec), then the cantilever is unloaded partially (usually 50% of the P_{max}) and the hold for 5 sec before the next loading. This cyclic process is repeated several times, with an increasing P_{max} of each cycle (load increment is 50~100 µN per cycle) so that the cantilever will eventually fracture unstably. The elastic cantilever stiffness for crack length estimation can be calculated from the unloading phase in each cycle. A typical load profile (load vs. time) and load-displacement curve for load partial-unload tested cantilever is shown in **Fig. 3.19**. Effects of test parameters (loading/unloading rate, hold time, load increment, and percentage-to-unload) are discussed separately in **Chapter 5**, as the parameters need to be optimised for accurate stiffness measurements.

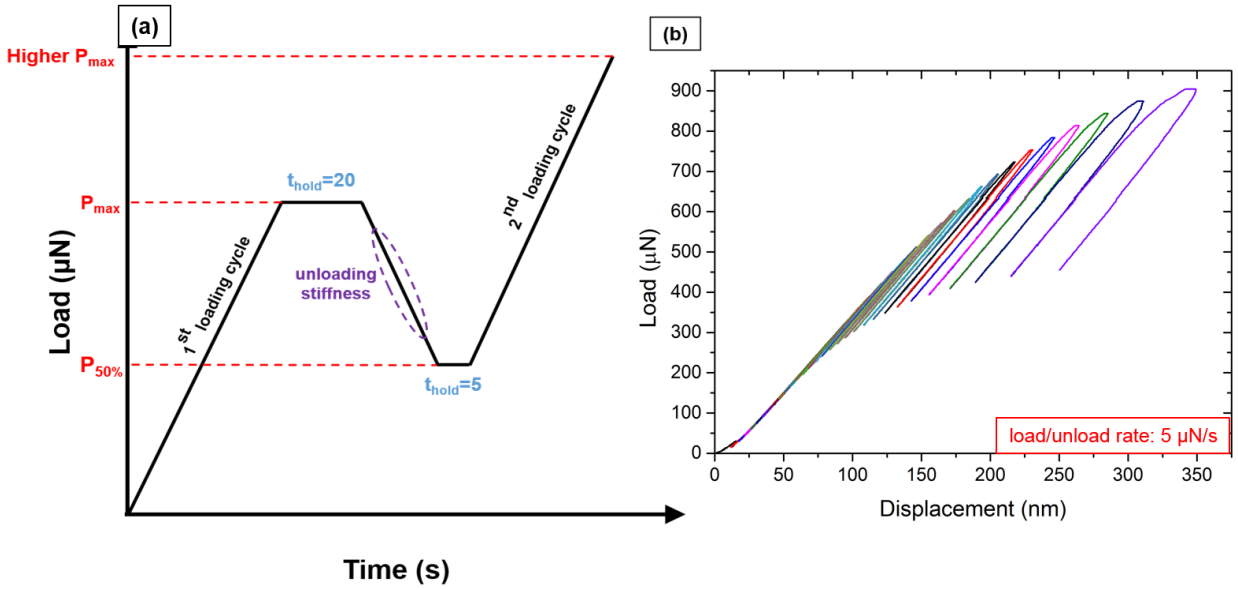


Fig. 3.19 Load profile and load-displacement curve from a load partial-unload tested cantilever

IV FINITE ELEMENT MODELLING AND VALIDATION OF CHEVRON-NOTCHED MICRO-CANTILEVERS

In order to calculate the fracture resistance curves from chevron-notched micro-cantilevers, both geometry-dependent stress intensity factors (SIFs) and cantilever stiffness as a function of the crack length are required. Due to geometry complexity, no analytical solutions for SIFs and stiffness existed. Therefore, SIFs and stiffness were calculated numerically using a commercial finite element (FE) software package ABAQUS^{TM} CAE 6.14 (Dassault Systems, Velizy-Villacoublay, France). This section will first describe the FE methodology for SIF and stiffness calculation, and the chevron notch optimisation. Lastly, micro-fracture tests using single crystal silicon cantilevers were used to validate the chevron notch design.

4.1 Introduction to Finite Element Analysis

In mechanical finite element analysis, the specimen body is divided into a large number of smaller elements. All element equations are then assembled systematically into a global system of equations for the final calculation. FE analysis usually outputs only the displacement, stresses, or strains. Additional information, such as stress intensity factor (SIF) for fracture mechanics analysis, will require additional post-processing steps - a special contour integral method was employed here to calculate the SIFs for chevron-notched micro-cantilevers. Flow chart of the modelling methodologies used is shown in **Fig. 4.1**.

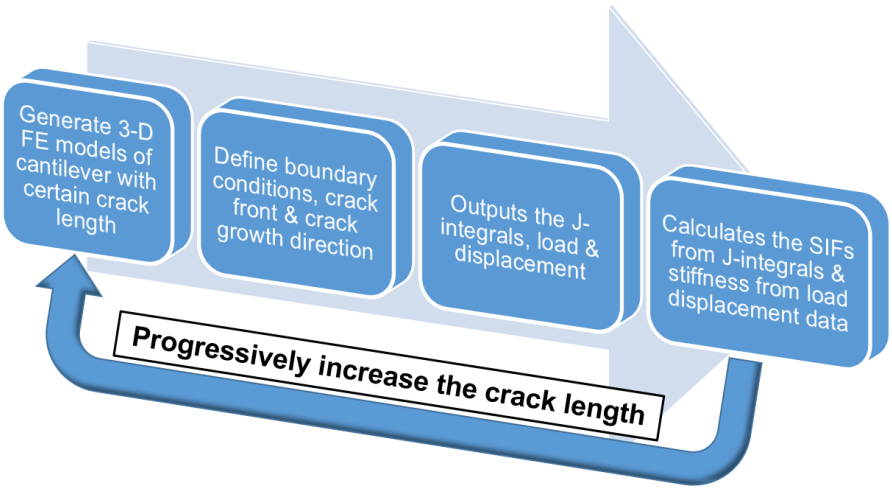


Fig. 4.1 Flow chart of the methodologies used to obtain the SIFs and stiffness via FE modelling

4.2 Modelling Methodologies

4.2.1 3-D Modelling of Chevron-Notched Micro-Cantilever

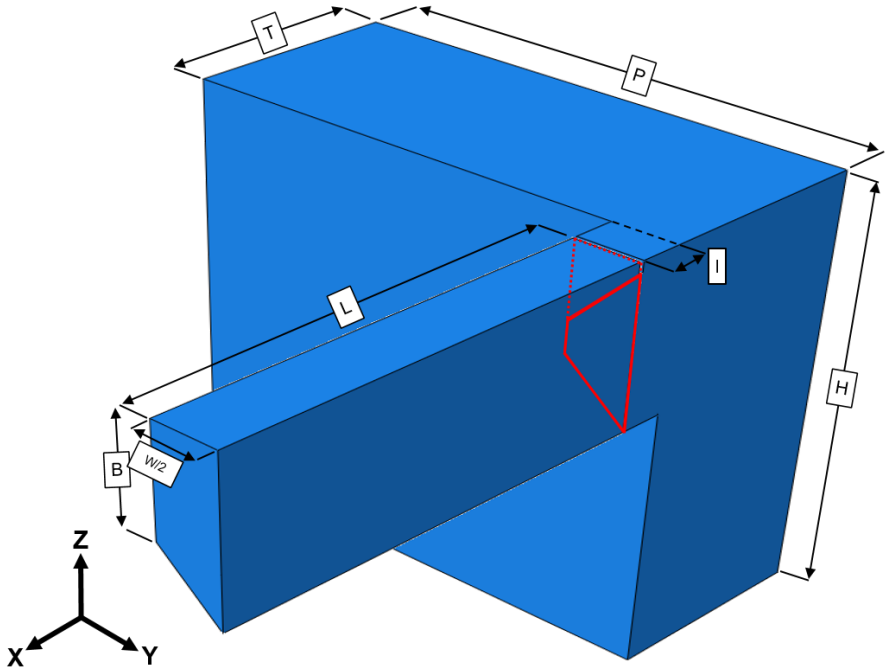
ABAQUS™ CAE 6.14 was used to generate 3-D models of the chevron-notched micro-cantilevers. A typical 3D half-cantilever model and the dimensions are shown in **Fig. 4.2**, and the cross-sectional view of the chevron notch is shown in **Fig. 4.3**. To improve computation efficiency, several approaches were taken to simplify the modelling:

(1) Only half of the cantilever was modelled due to symmetry

(2) A supporting base is included to take into account of the base deformation in real tests

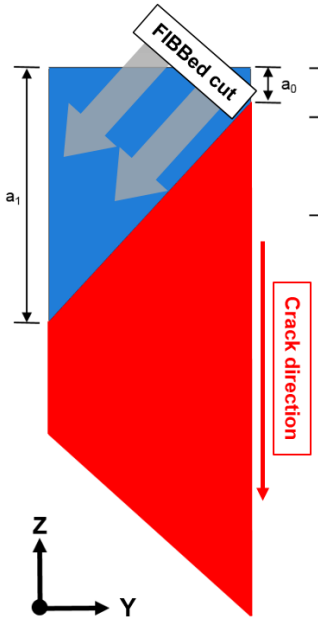
(3) Only the effective cantilever length L is modelled because load is applied at a significant distance away from the notch

(4) The chevron notch thickness is assumed to be zero



Dimension	Length (μm)
L	9
B	3
W/2	1.5
l	1
P	12
H	12
T	5

Fig. 4.2 3-D half cantilever model (with supporting base) and dimensions. The red-sectioned region represents the chevron notch ligament



Dimension	Length (μm)
a_0	0~0.9
a_1	2.1~3

Fig. 4.3 Cross-sectional view of the chevron notch and dimensions. The grey arrows indicate the FIB direction (during chevron notching), and the red arrow indicates the crack direction

Three boundary conditions were applied to the half-cantilever model, shown in **Fig. 4.4**, to simulate the actual test conditions:

(1) ENCASTRE (forbids any displacement and rotation) on the XY, YZ, and XZ planes of the supporting base

(2) SYMMETRY on the YZ plane (the half-cantilever surface)

(3) Fixed displacement of 2 μm in the negative Z direction was applied at the cantilever's free end. This is to ensure the displacement is large enough to introduce enough stress concentration at the notch, but also not too large to create mesh distortion.

In addition, the supporting base and the cantilever were connected using a rigid TIE constraint, which allows two parts to be merged together even though the surface meshes may be dissimilar. Calculations were performed using a solid 3-D 20 node quadratic element (C3D20R).

4.2.2 Mesh Convergence Study

Mesh type used to model the half-cantilever was the solid 3-D 20 nodes quadratic type (C3D20R), as it provided sufficient accuracy in the stress concentrated regions. Mesh convergence studies using various element sizes were performed before applying the contour integral method to calculate the SIFs. This was to ensure a converged stiffness value can be obtained with reasonable computation time. Shown in **Fig. 4.5**, the uniformly yet optimal mesh size was found to be 0.15 μm, where the normalised cantilever stiffness converged to unity (with respect to the modulus-calculated stiffness). A typical half-cantilever model has around ~80000 elements, and the calculation time is around ~15 min. The meshed half-cantilever model with boundary conditions is shown in **Fig. 4.4**.

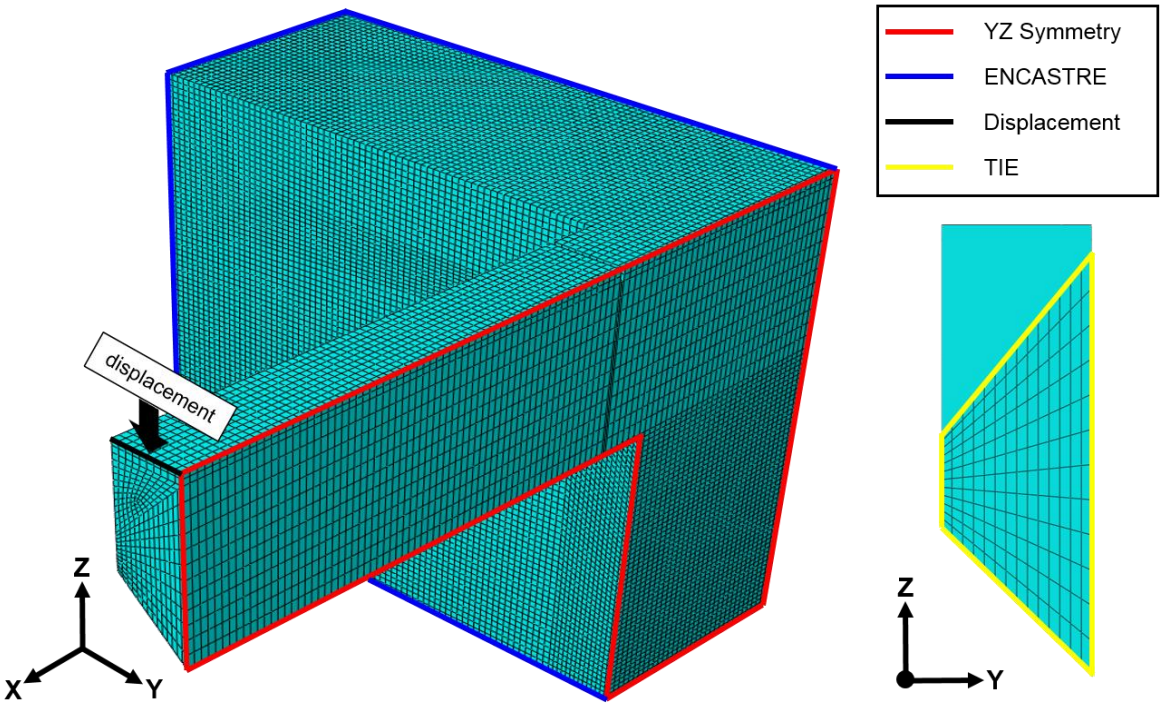


Fig. 4.4 Meshed half chevron-notched cantilever model with boundary conditions labelled (NLGEOM off)

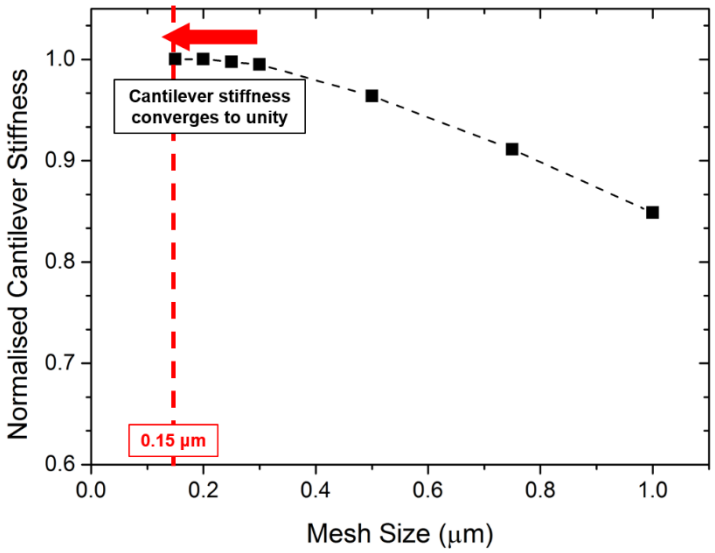


Fig. 4.5 Mesh convergence study of the half cantilever model. Normalised cantilever stiffness converged to unity when mesh size was approximately 0.15 µm

The FE chevron-notched cantilever models were implemented with homogeneous, isotropic, and linear-elastic material properties of silicon and tungsten. Details of the material properties are given in **Table 4.1**.

Materials	Elastic Modulus (GPa)	Poisson's Ratio
Silicon (Si)	169	0.21
Tungsten (W)	410	0.3

Table 4.1 Linear-elastic material properties of silicon and tungsten

4.2.3 Calculation of the J-integral using the Contour Integral Method

ABAQUS calculates the elastic-plastic fracture mechanics parameter, J-integral, via the contour integral method. A more complete description of the J-integral was previously given in **Chapter 2.1.2**. Here the focus is to employ the FE contour integral method to obtain the J-integrals (hence SIFs) from the half-cantilever models.

In the FE model, each contour integral evaluates the virtual motion of a block of material surrounding the crack tip (in 2-D) or the surrounding nodes along the crack front (in 3-D). Each block is defined by contours, and each contour consists of ring of elements that completely surrounded the crack tip, or the nodes along the crack front from one crack face to the opposite crack face. Examples of the contour integral analysis on a 2-D and 3-D crack are illustrated in **Fig. 4.6** and **4.7** [96].

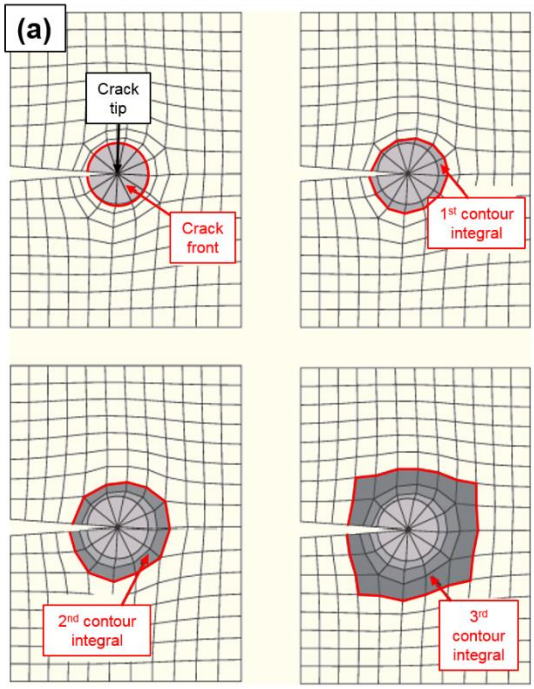


Fig. 4.6 Example of the contour integral analysis of a 2-D crack

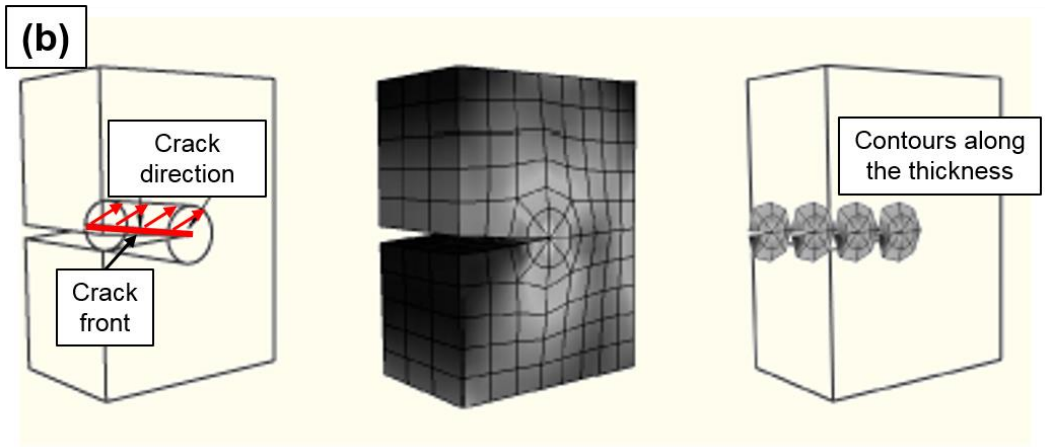


Fig. 4.7 Example of the contour integral analysis of a 3-D crack

In order to perform contour integral analysis on a 3-D crack, the crack front and the crack direction must be defined in the FE model. The stress distribution (von-Mises stress, in MPa) of a half-chevron notch is shown in **Fig. 4.8**. The crack front was defined at an arbitrary crack length a ($a_0 < a < a_1$). The contour integral analysis computed a J-integral at each node along the

crack front, which is indicated in the magnified chevron notch region. In addition to take into account the cantilever geometry and using plane-strain condition [37], the J-integrals were convert into the non-dimensional SIF Y, using **Eq. 4.1** and **4.2**. It can also be seen from **Fig. 4.8** that Y varies slightly from the mid-plane to 80% of the static half crack front ($-0.4 \leq z/2 \leq 0$), and increases rapidly when approaching the cantilever surface. This is a numerical error due to the distortions of the edge elements from the abrupt transition to a free surface. The variance of SIFs along the crack front were also reported by Sarrafi-Nour [97] and Newman [72], in their FE modelling of chevron-notched short rods and bending bars. Therefore, Y were calculated using an average value, from the mid-plane to approximately 80% of the crack front (neglecting the extreme values near free surface).

$$K = \sqrt{\frac{EJ}{1-\nu^2}} \quad (\boldsymbol{Eq.4.1})$$

$$Y = \frac{KB\sqrt{W}}{P} \quad (\boldsymbol{Eq.4.2})$$

where E is the elastic modulus, ν is the Poisson's ratio, P is the load at which the J-integrals were calculated, and B and W are the cantilever thickness and width

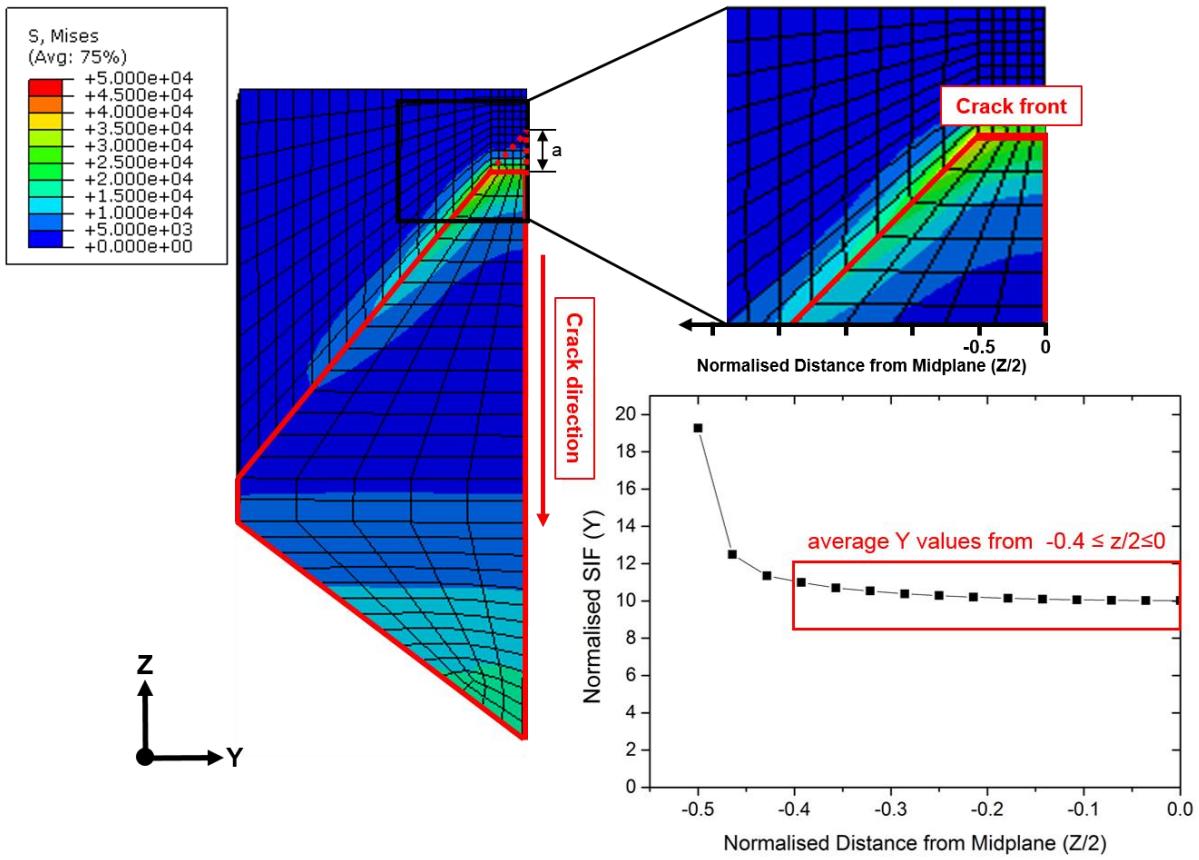


Fig. 4.8 Stress distribution of a half chevron notch of crack length a. The chevron notch ligament and the crack front are highlighted using red lines. Variance of the non-dimensional SIF Y along the crack front (-0.5≤ z/2≤0) is also shown

In order to obtain the full Y and cantilever stiffness vs. crack length relationships for a fixed chevron notch geometry (has same a_0 and a_1), 10 sub-models with progressively increasing crack length were created. Subsequently, Y and cantilever stiffness from each sub-model were plotted against the crack length. Lastly, two third-order polynomial functions were used to fit the Y and stiffness with crack length. An example of the manually/incrementally-grown crack and the Y and stiffness vs. normalised crack length relationships are shown in **Fig. 4.9**. Therefore, the critical crack length α_c and the corresponding Y_{min} (for K_{Ic} calculation) and the stiffness drop (for crack length estimation) were determined for a particular chevron geometry.

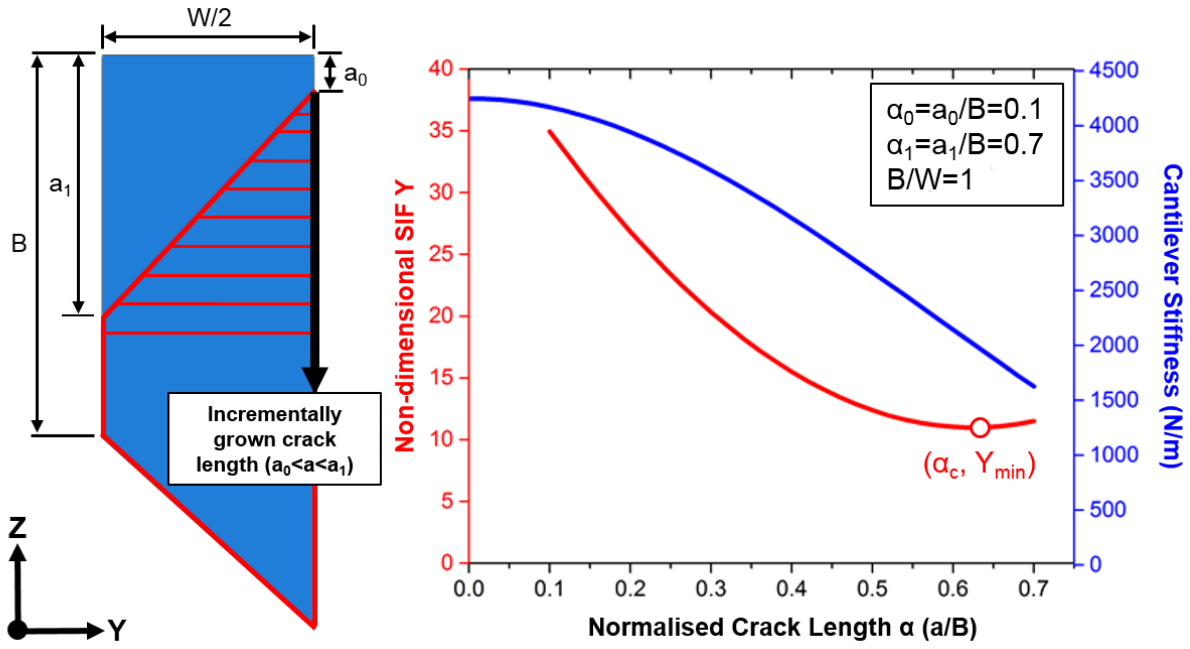


Fig. 4.9 Example of the non-dimensional SIF Y and cantilever stiffness vs. normalised crack length plot for chevron geometry of α_0=0.1 and α_1=0.7.The cantilever geometry used is given in **Fig. 4.2**. The critical crack length α_c for Y_{min} is also labelled, which is the point of crack instability (crack driving force beyond α_c increases with crack length)

4.3 Optimisation of the Chevron Notch Geometry

This section investigates the effects of chevron geometry to the amount of stable crack growth, as it is desirable to have most stable crack growth for elastic-plastic fracture mechanical (EPFM) analysis. He and Evans [98] first conducted systematic 3-D FE modelling on chevron-notched 3PTB and 4PTB specimens. They revealed that the non-dimensional SIFs were strong functions of the chevron tip and base positions (α_0 and α_1), but were only weakly dependent on the cantilever dimensions (L, W and B). Calomino and Ghosn [99] conducted sophisticated studies of chevron-notched four-point bending specimens using the Bluhm slice synthesis model [100]. They revealed that the chevron tip α_0 and base position α_1 had primary effect on the force

required to initiate a sharp crack. A smaller α_0 with larger α_1 maximised the stable crack growth region, however, the tendency for premature failure was also increased due to a narrower initial chevron ligament. For constant α_0 and α_1 values, the stress intensity factors were almost independent of specimen width and thickness. Therefore, systematic FE modelling are required to obtain an optimal chevron notch geometry with the most stable crack growth without the accompanying premature failure.

Dimensions and the implemented material properties of the half-cantilever models are described in **Table 4.2**. The model dimensions were chosen to match closely with the actual FIBed cantilevers. Isotropic, homogeneous, linear-elastic properties of tungsten were implemented. The only variables in the models were the chevron tip (α_0) and base position (α_1). Using the contour integral method and progressive crack length modelling techniques, the non-dimensional SIFs and cantilever stiffness for various chevron geometry were calculated as functions of the normalised crack length (α), which are summarised in **Fig. 4.10** to **4.12**. In addition, the critical crack length α_c, minimum non-dimensional SIF Y_{min}, and the third-order polynomial fit equations for Y and stiffness vs. normalised crack length α were calculated and are summarised in **Table 4.3** (α_c and Y_{min} are labelled in white circles on the third-order polynomial equations).

L (μm)	B (μm)	W (μm)	L (μm)	P (μm)	H (μm)	T (μm)	E (GPa)	ν
9	3	1.5	1	12	12	5	410	0.3

Table 4.2 Dimensions and material properties used in the half-cantilever FE model (see **Fig. 4.2**) for chevron notch optimisation and SIF, stiffness calculation

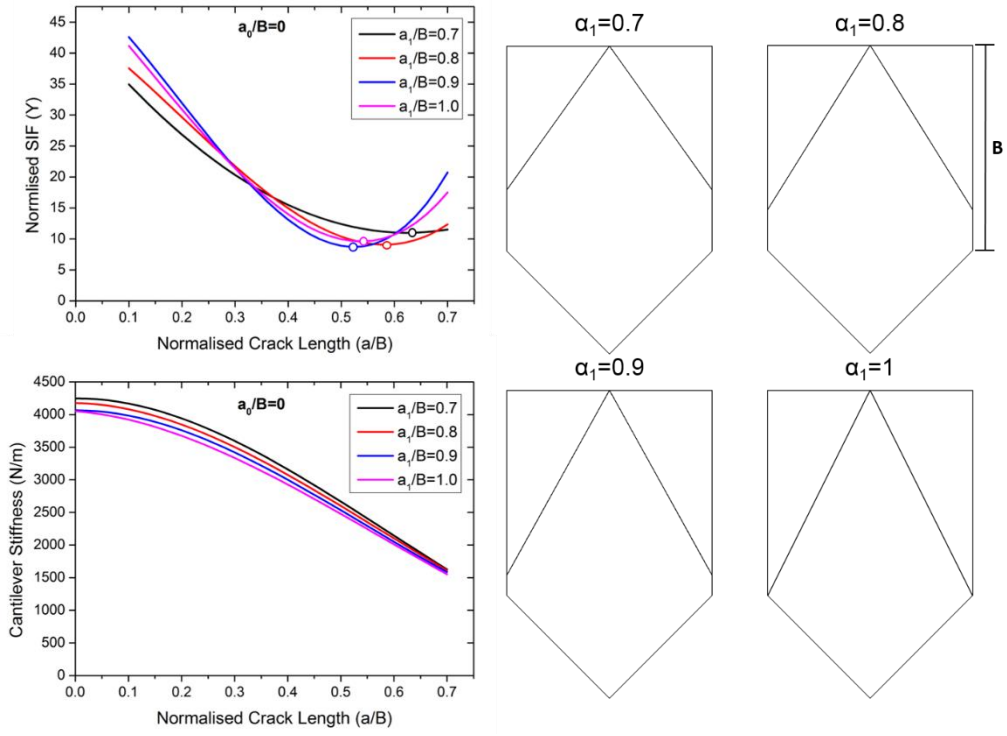


Fig. 4.10 Non-dimensional SIF Y and stiffness for chevron notch geometry of α_0=0, α_1=0.7~1

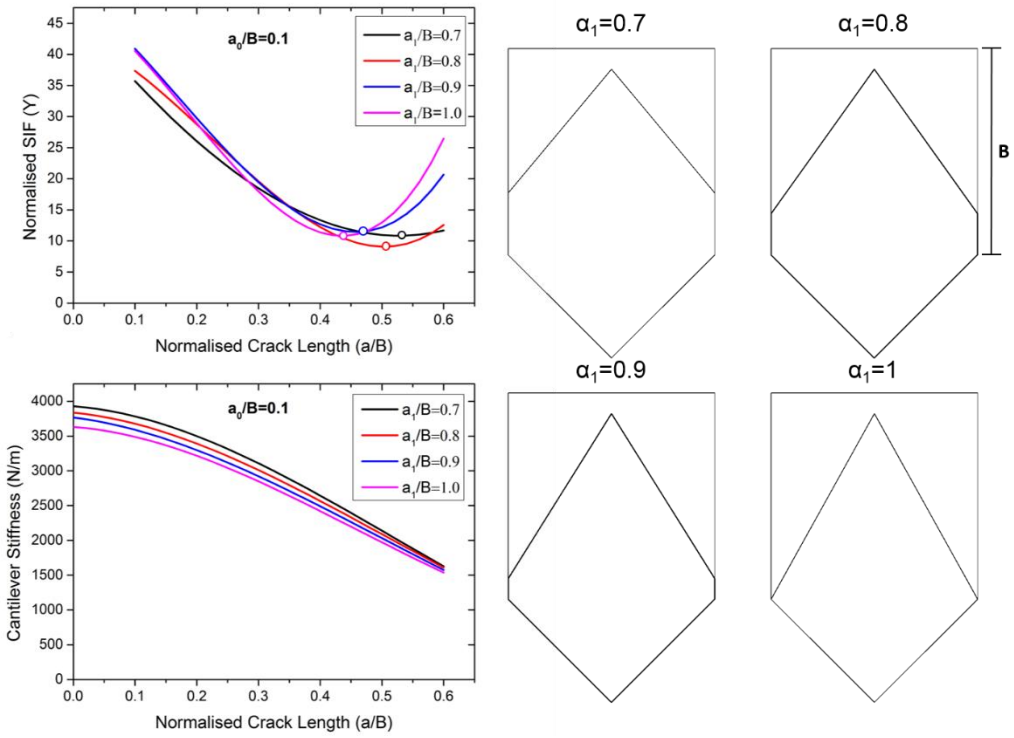


Fig. 4.11 Non-dimensional SIF Y and stiffness for chevron notch geometry of α_0=0.1, α_1=0.7~1

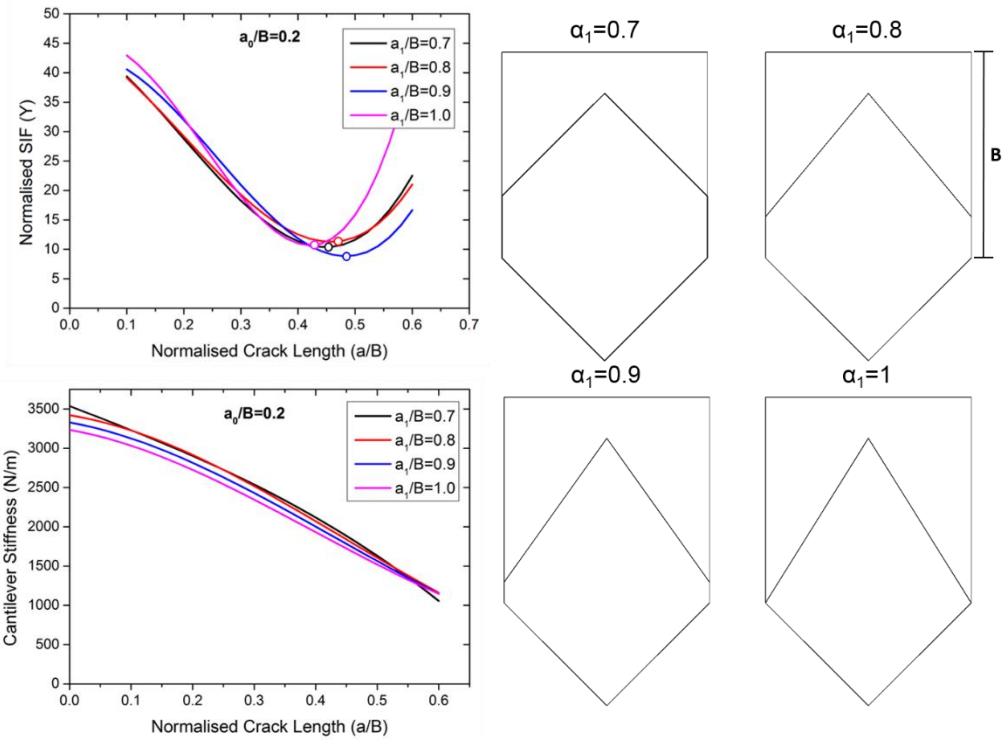


Fig. 4.12 Non-dimensional SIF Y and stiffness for chevron notch geometry of α_0=0.2, α_1=0.7~1

α_0	α_1	α_c	Y_{min}	Y(α)	S(α)
0	**0.7**	**0.62**	**11**	**$Y = 8\alpha^3 + 76\alpha^2 - 105\alpha + 45$**	**$S = 5121\alpha^3 - 9052\alpha^2 + 83\alpha + 4247$**
	0.8	0.58	9.1	$Y = 180\alpha^3 - 111\alpha^2 - 59\alpha + 44$	$S = 4985\alpha^3 - 8519\alpha^2 - 142\alpha + 4177$
	0.9	0.52	8.7	$Y = 330\alpha^3 - 190\alpha^2 - 73\alpha + 51$	$S = 5438\alpha^3 - 8923\alpha^2 + 40\alpha + 4065$
	1.0	0.54	9.6	$Y = 222\alpha^3 - 96\alpha^2 - 89\alpha + 51$	$S = 4162\alpha^3 - 7112\alpha^2 - 634\alpha + 4053$
0.1	0.7	0.53	10.8	$Y = 55\alpha^3 + 72\alpha^2 - 122\alpha + 47$	$S = 5500\alpha^3 - 8623\alpha^2 - 643\alpha + 3929$
	0.8	0.5	9.1	$Y = 400\alpha^3 - 269\alpha^2 - 33\alpha + 43$	$S = 5236\alpha^3 - 7906\alpha^2 - 850\alpha + 3837$
	0.9	0.46	11.5	$Y = 452\alpha^3 - 229\alpha^2 - 75\alpha + 50$	$S = 4799\alpha^3 - 7104\alpha^2 - 1119\alpha + 3768$
	1	0.44	10.8	$Y = 626\alpha^3 - 344\alpha^2 - 57\alpha + 49$	$S = 6089\alpha^3 - 8415\alpha^2 - 632\alpha + 3631$
0.2	0.7	0.45	10.4	$Y = 587\alpha^3 - 348\alpha^2 - 43\alpha + 47$	$S = -2701\alpha^3 - 248\alpha^2 - 3015\alpha + 3537$
	0.8	0.46	11.3	$Y = 521\alpha^3 - 311\alpha^2 - 43\alpha + 46$	$S = 5677\alpha^3 - 7644\alpha^2 - 1226\alpha + 3421$
	0.9	0.48	8.8	$Y = 720\alpha^3 - 552\alpha^2 + 29\alpha + 42$	$S = 5282\alpha^3 - 6897\alpha^2 - 1401\alpha + 3329$
	1	0.42	10.7	$Y = 1282\alpha^3 - 894\alpha^2 + 72\alpha + 43$	$S = 6109\alpha^3 - 7227\alpha^2 - 1341\alpha + 3234$

Table 4.2 Critical crack length α_c, minimum SIF Y_m, and the 3rd order polynomial fit functions for describing the Y & stiffness relationships vs. normalised crack length (α=a/B) for various notch geometry. The optimum chevron notch geometry with the most stable crack growth (α_c=0.62) is highlighted in red (α_0=0, α_1=0.7)

Based on systematic FE modelling of chevron-notched cantilevers, the following conclusions were drawn. The non-dimensional SIF Y are strong functions of the chevron tip and base positions, which is consistent with the conclusions by Calomino et al. [99]. Stiffness drop in the stable crack growth regime is sufficient (~1000 N/m) so it can be reliably measured using nanoindentation methods. An optimum chevron notch geometry (α_0=0, α_1=0.7) with maximum stable crack growth and a sufficient stiffness drop was obtained for a pentagonal cantilever with thickness-to-width ratio of one (B/W=1). Chevron notches with base position lower than 0.7 ($\alpha_1 \leq 0.7$) were not modelled, as re-deposition (FIB artefact near a free surface) introduced curved edges, which reduced the triangular area and increased the chance for pre-mature fracture, shown in **Fig. 4.13**. Hence, chevron notch with $\alpha_1 \leq 0.7$ are avoided in future cantilever design.

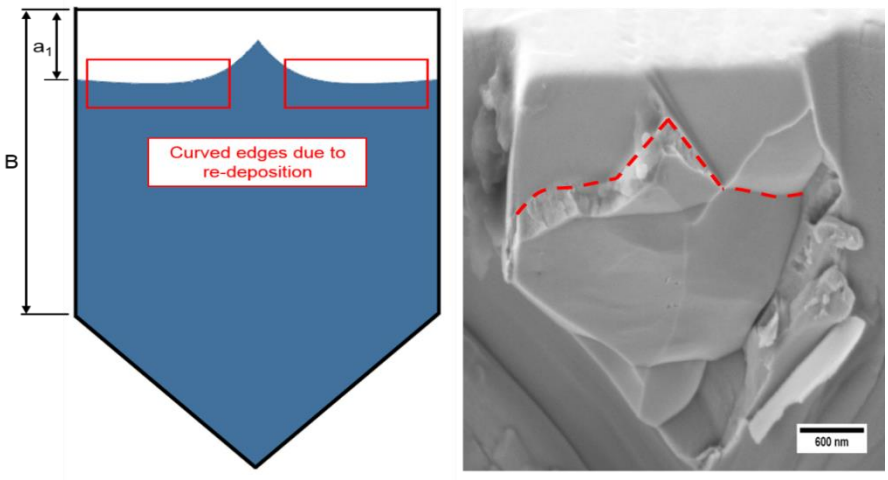


Fig. 4.13 Chevron notch with $\alpha_1 \leq 0.7$. A reduced triangular ligament and curved edges are clearly observed due to the FIB re-deposition

4.4 Validation using Single-Crystal Silicon Micro-Cantilever

Micro-fracture tests using single-crystal silicon were used to validate the FE-calculated SIFs. Pentagonal Si cantilevers with the optimum chevron notch configuration (α_0=0, α_1=0.7) and long axis aligning to the <111> direction (cleavage plane normal), shown in **Fig. 4.14**, were tested at room temperature using a G200 Nanoindenter. The load-displacement curves and the unstable fracture load P_c for two successfully tested cantilevers (A2, B2), are shown in **Fig. 4.15**.

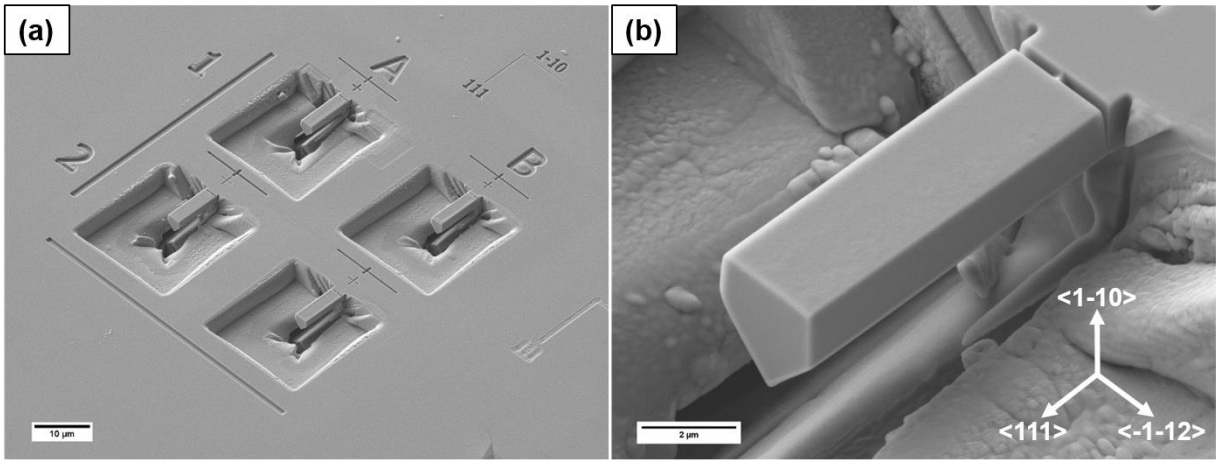


Fig. 4.14 Chevron-notched Si micro-cantilevers with long axis aligning to the <111> direction

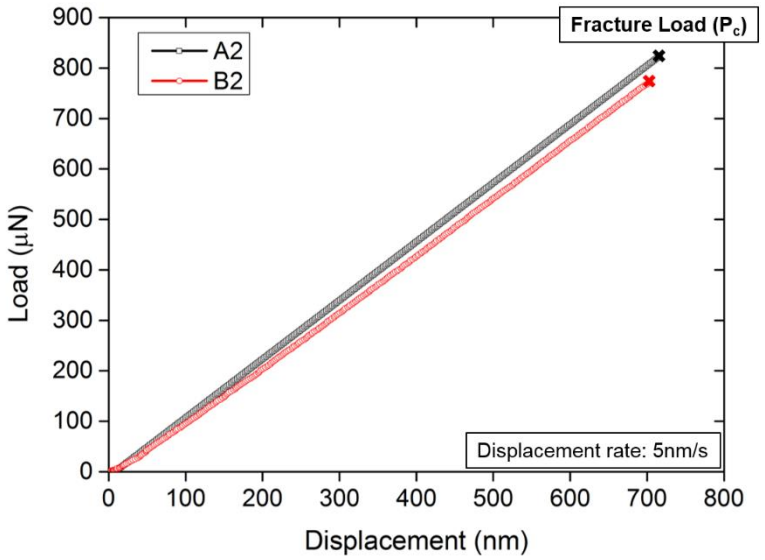


Fig. 4.15 Load-displacement curves for Si cantilevers of A2 and B2

Chevron notch geometries were measured via post-test SEM, shown in **Fig 4.16** and **4.17**. For a chevron-notched, purely brittle material, unstable fracture occurs when the non-dimensional SIF Y is at its minimum, hence the fracture toughness (K_{Ic}) can be calculated using the unstable fracture load P_c and the FE-calculated Y_{min} (Si: E=169 GPa, ν=0.21) through **Eq. 4.3**. The transition between stable/unstable fracture is distinguished on the fracture surface using a curved red-dotted line. As the SIFs near the free surface were the highest, it was highly likely for the crack to initiate first at the cantilever edges, then propagated to the mid-plane, resulting in the curved crack front. The displacement rate, fracture load, cantilever/chevron geometries, Y_{min}, stable crack length, and K_{Ic} are summarised in **Table 4.3**.

$$K_{Ic} = P_c \frac{Y_{min}}{B\sqrt{W}} \quad (\boldsymbol{Eq.4.3})$$

where B and W are the cantilever thickness & width, P_c is the unstable fracture load, and Y_{min} is the minimum non-dimensional SIF

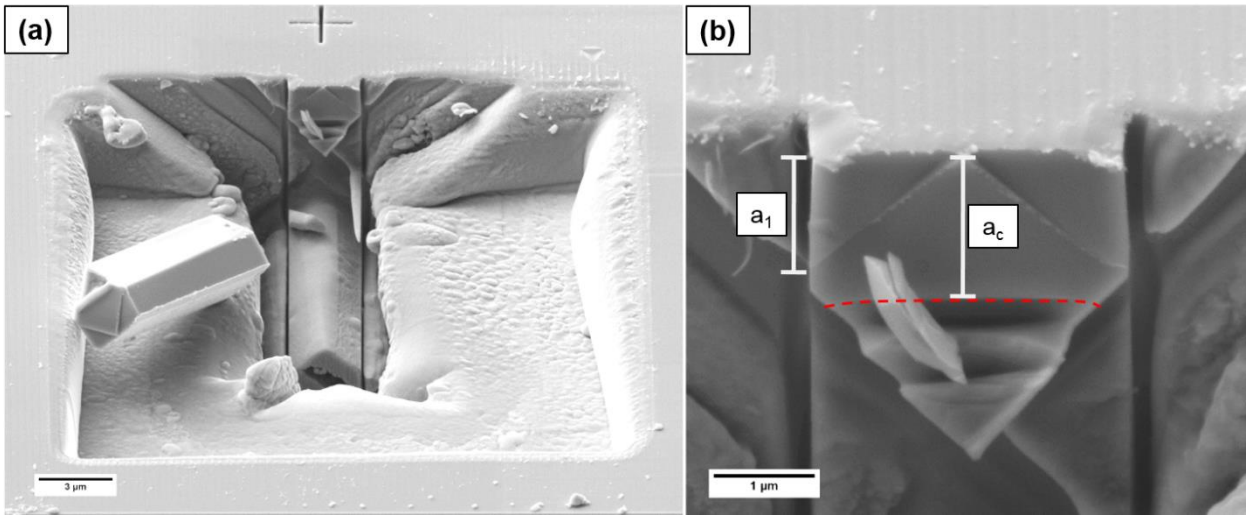


Fig. 4.16 Post-test SEM fractography of cantilever A2, and a higher-magnification image of the chevron fracture surface

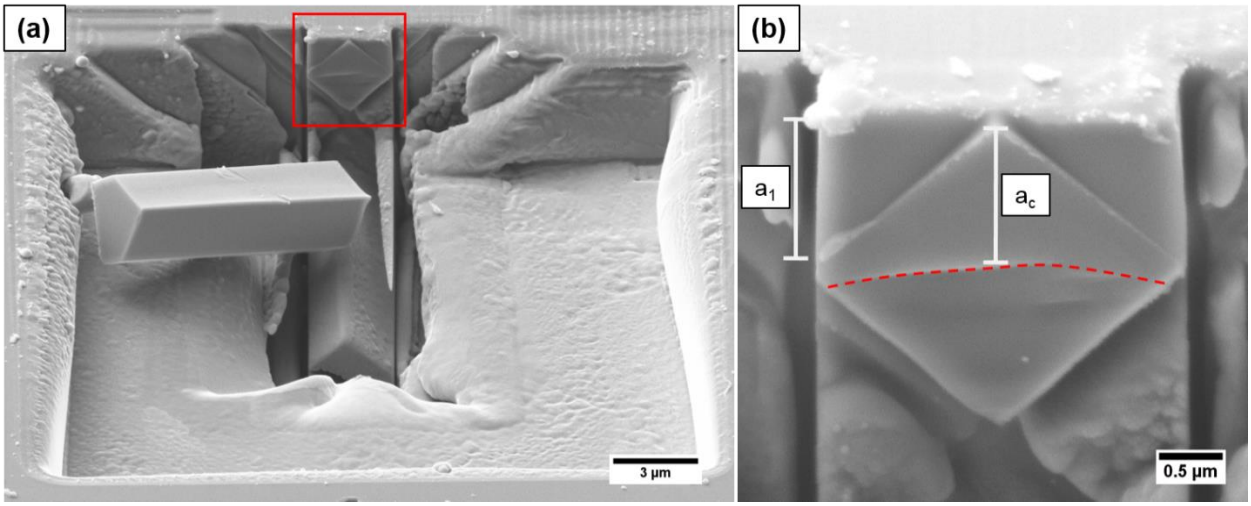


Fig. 4.17 Post-test SEM fractography of cantilever B2, and a higher-magnification image of the chevron fracture surface

#	D ($\frac{nm}{s}$)	W (µm)	B (µm)	L (µm)	a_1 (µm)	a_c (µm)	Y_{min}	P_c (µN)	K_{Ic} (MPa·$m^{0.5}$)
A2	5	2.9	2.8	9.1	2.3	2.6	3.1	825.5	0.82
B2	5	3.1	2.9	8.5	2.3	2.4	3.2	772.7	0.87

Table 4.3 Test summary of two chevron-notched Si micro-cantilevers

Plane-strain fracture toughness (K_{Ic}) values for two Si cantilevers with cleavage plane of (111) was 0.85 ± 0.03 MPa·$m^{0.5}$. The stable crack length a_c, however, was noticeably deeper than the chevron base position a_1. This is possibly due to the compressive stresses beneath the neutral axis of the cantilever. The compressive stress generated during cantilever bending could effectively promotes stable crack growth. This was also reported recently by Mueller et al. [101], where the intentionally introduced compressive stress at the crack tip was used to promote stable crack growth (for pre-cracking) of chevron-notched Si micro-cantilevers.

Overall, fracture toughness measured from chevron-notched micro-cantilevers are in good agreement with macroscopic value of ~0.9 MPa·$m^{0.5}$ using four-point bending matchsticks

[60], and with microscopic value of ~1.1 $MPam^{0.5}$ using straight-notched micro-cantilevers [41]. Note that the slightly higher value from straight-notched micro-cantilevers was due to the FIBed straight notch with a blunter notch root radius of ~30 nm, which required additional load to initiate a real crack. Whereas the chevron-notched cantilevers were able to create a sharp crack upon initial loading, hence effectively avoiding the notch root radius effect.

4.5 Summary

Finite element modelling, demonstrated in this chapter, was used as a simulation tool to calculate the non-dimensional SIFs from chevron-notched cantilevers. It effectively reduced the needs for expensive and cumbersome FIB experiments to optimise the chevron notch geometry. Microscopic fracture toughness measured from chevron-notched single crystal silicon cantilevers showed good agreement with macroscopic values, hence validating the FE-calculated SIFs. Chevron-notched cantilevers are proven to be an effective specimen geometry for future micro-fracture tests, and the optimised notch geometry obtained from FE modelling will serve as a guideline for later tungsten cantilever fabrication.

V ROOM TEMPERATURE MICRO-FRACTURE TESTS OF W-1%TA MICRO-CANTILEVERS

5.1 Introduction

This chapter discusses the micro-fracture tests performed on W-1%Ta chevron-notched micro-cantilevers. Triangular un-notched micro-cantilevers were used to measure the size-dependent yield stresses (σ_{ys}), which were then used to provide an experimental estimation of the crack tip plastic zone. Pentagonal chevron-notched micro-cantilevers were used to measure the fracture resistance curves (J-R curves), using the elastic-plastic fracture parameter of the J-integral. Two test methods: **(1)** dynamic continuous stiffness measurement (CSM) method, and **(2)** quasi-static load partial-unload method for crack length measurement are also discussed. Lastly, fracture toughness values from both linear-elastic fracture mechanical (LEFM) and elastic-plastic fracture mechanical (EPFM) analysis will be compared with macroscopic values.

Micro-cantilevers were fabricated via FIB on the L-S orientation from a W-1%Ta matchstick, shown in **Fig. 5.1**. The detailed procedures for fabricating and testing the cantilevers were described in Chapter 3. Due to the elongated grains resulted from the forging process, each cantilever contained approximately 10~15 grains. Cantilevers with dimensions of 10 μm x 3 μm x 3 μm, (length x thickness x width, L x B x W) and the corresponding EBSD map are shown in **Fig. 5.2** and **5.3**. The cantilever dimensions were chosen to match with the specimen design guideline provided in Chapter 4.

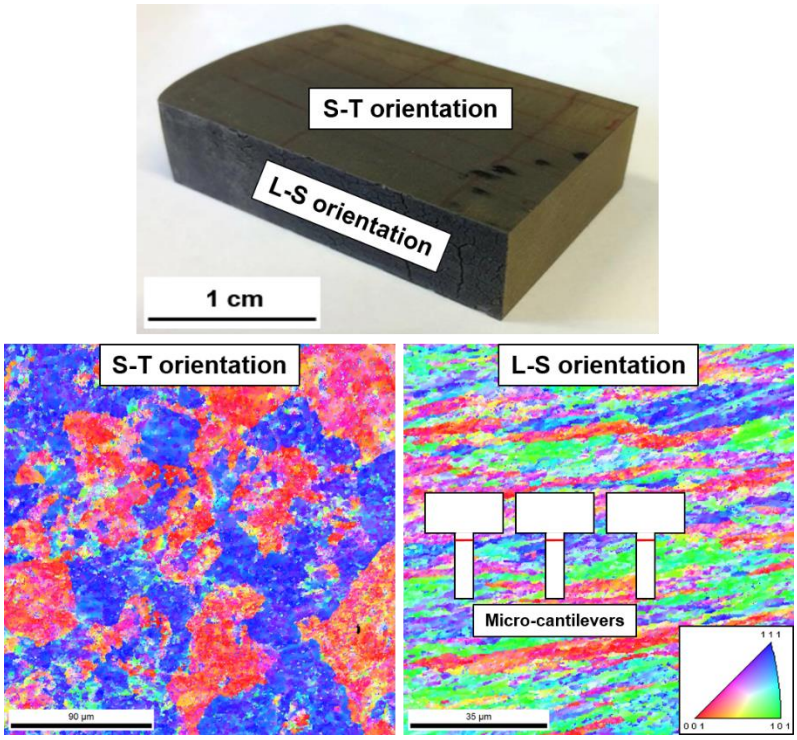


Fig. 5.1 Ingot of the sintered & forged W-1%Ta and EBSD scans of the two orientations

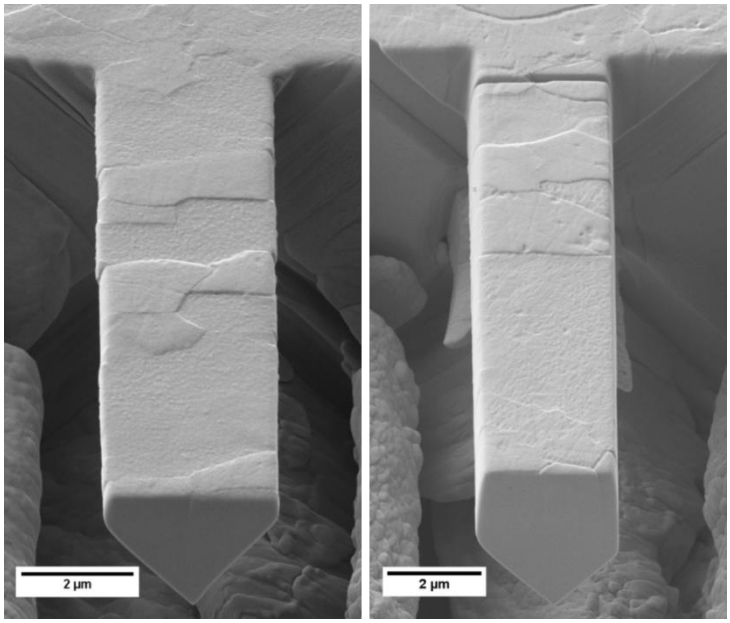


Fig. 5.2 Typical dimensions of triangular (un-notched, for elastic-plastic test) and pentagonal (chevron-notched, for fracture test) micro-cantilevers

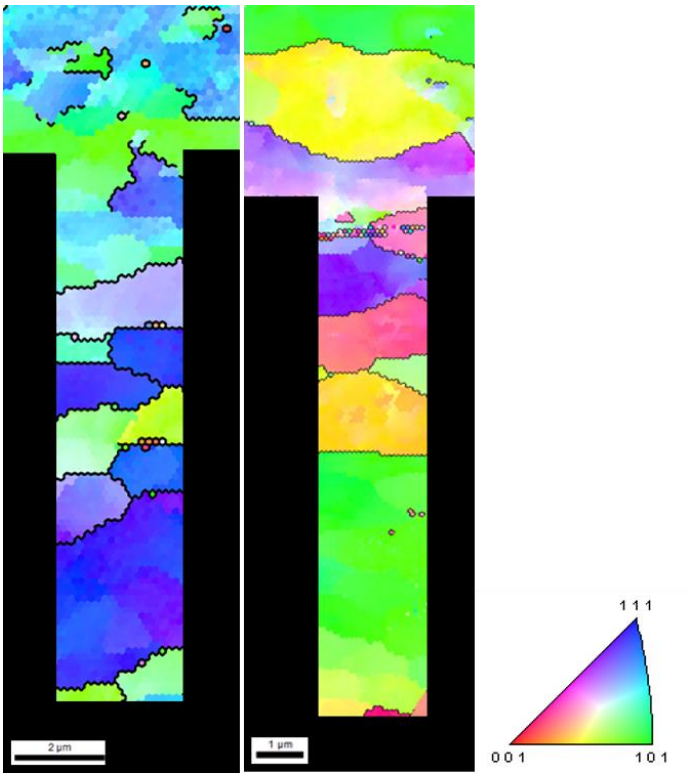


Fig. 5.3 EBSD scan of the cantilevers in **Fig. 5.2**. Grain boundaries with mis-orientations larger than 15° were labelled using black borderlines

5.2 Elastic-Plastic Triangular Cantilevers

Triangular cantilevers are tested using the quasi-static load partial-unload method, with constant loading/unloading rate of 5 μN/s. Details of the load partial-unload method will be described in later section **5.4**. The load-displacement curve is converted into maximum stress-strain curve using simple beam theory equations **Eq. 5.1** and **5.2** [102]. The elastic modulus, yield stress, and flow stress were extracted from the stress-strain curve, and labelled in **Fig. 5.4**.

$$\sigma_{max} = \frac{24PL}{WB^2} \ (\mathbf{Eq.\ 5.1})$$

$$\varepsilon_{max} = \frac{2B\delta}{L^2} \ (\mathbf{Eq.\ 5.2})$$

where P is the applied load, L is the effective length, B is the cantilever thickness, W is the cantilever width, and δ is the bending displacement measured from the nanoindenter

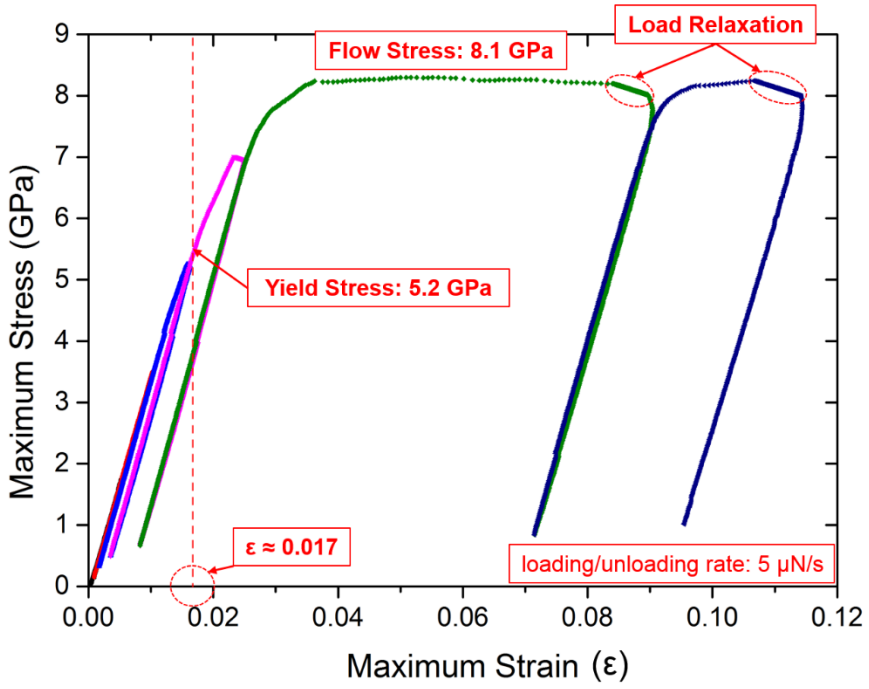


Fig. 5.4 Stress-strain curve of the elastic-plastic triangular cantilever. The yield stress, flow stress, and load relaxation (in the last two cycles) are labelled

Fig. 5.4 is the cyclic stress-strain curve of an elastic-plastic tested cantilever. Most cycles exhibited an initial linear-elastic region, followed by yielding, constant flow stress, and some load relaxation (final two cycles). The yield point is defined at which the initial slope of the stress-strain curve dropped to 90% of the initial value. Details of the method is shown in **Fig. 5.5**, where the yield point was defined at approximately 0.017 of the maximum strain. The modulus (367 GPa) was calculated using a flowing average over 3 points, which was approximately 90% of its literature value (410 GPa) [103]. The reason for the smaller modulus value was because simple beam theory assumed a "fixed" cantilever base, whereas in real tests

there were always small deflections in the base. Neglecting this base deflection resulted a higher strain (a more compliant cantilever), hence obtaining a lower modulus value.

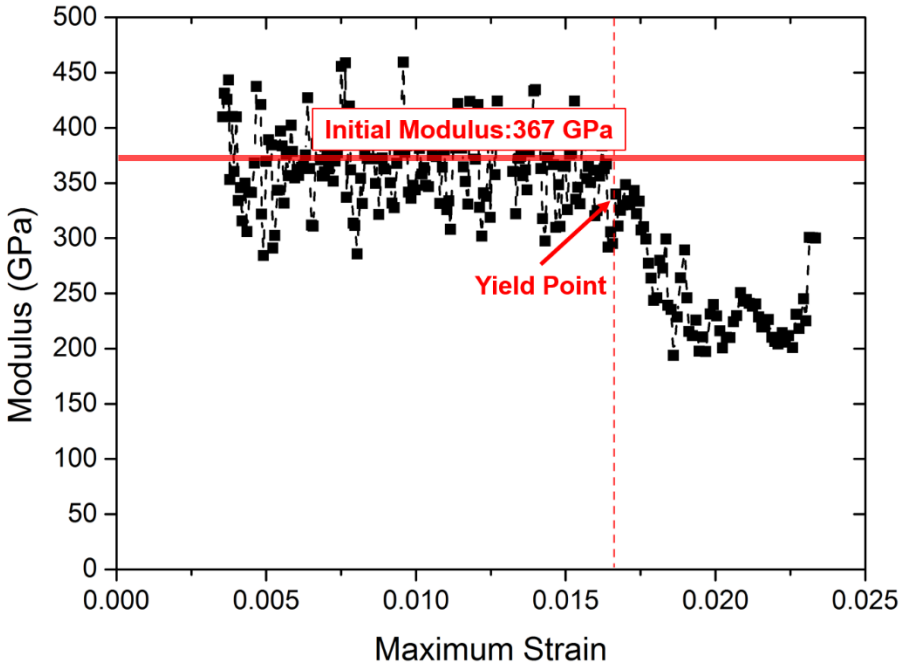


Fig. 5.5 Modulus vs. maximum cantilever strain. The yield point is defined at 0.017 of the maximum strain, and an average modulus of 367 GPa was calculated

Fig. 5.6 and **5.7** are post-test SEM images of the elastic-plastic cantilever. Cross slip traces of mobile screw dislocations were clearly observed at both top surface and bottom apex, which is commonly seen in BCC metals as the slip planes are less well defined. The localised plastic deformation at both sites generated dislocation pile-up, and the mobile dislocations were pushed towards the surface by their mutual elastic interactions, and if they got close enough to the surface, will be pulled out of the surface by image force. Similar observations were reported in the work by Gong et al. [104], where pure titanium micro-cantilevers were deflected similarly to extract the size-dependent critical resolved shear stress (CRSS).

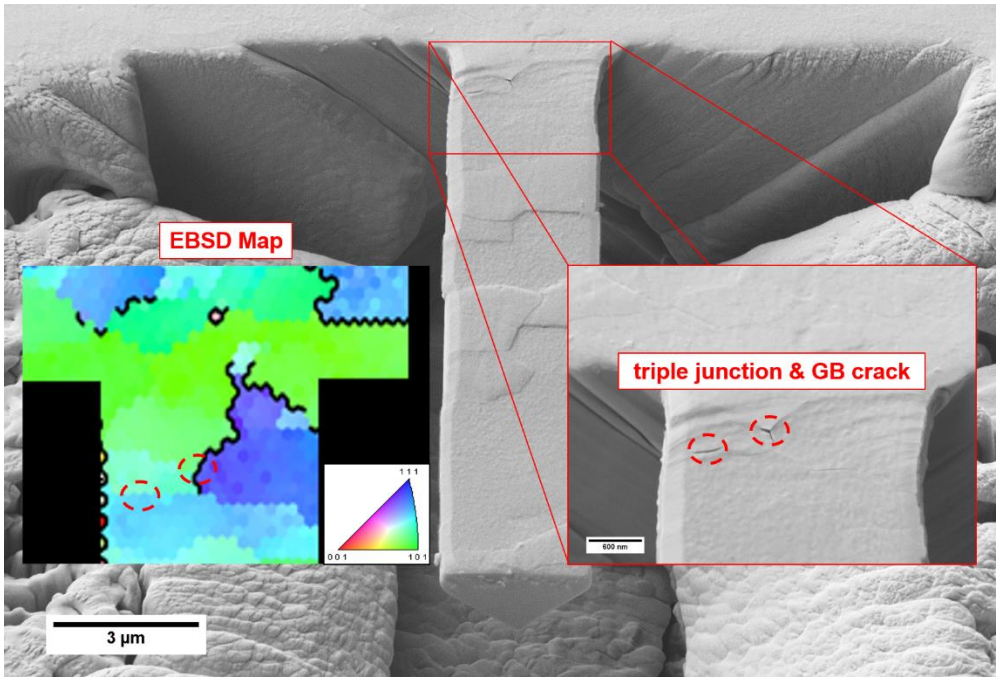


Fig. 5.6 Post-test SEM image of the cantilever. The cross slip lines, grain boundary and triple junction cracks (shown in the EBSD scan) at the top fixed end are observed

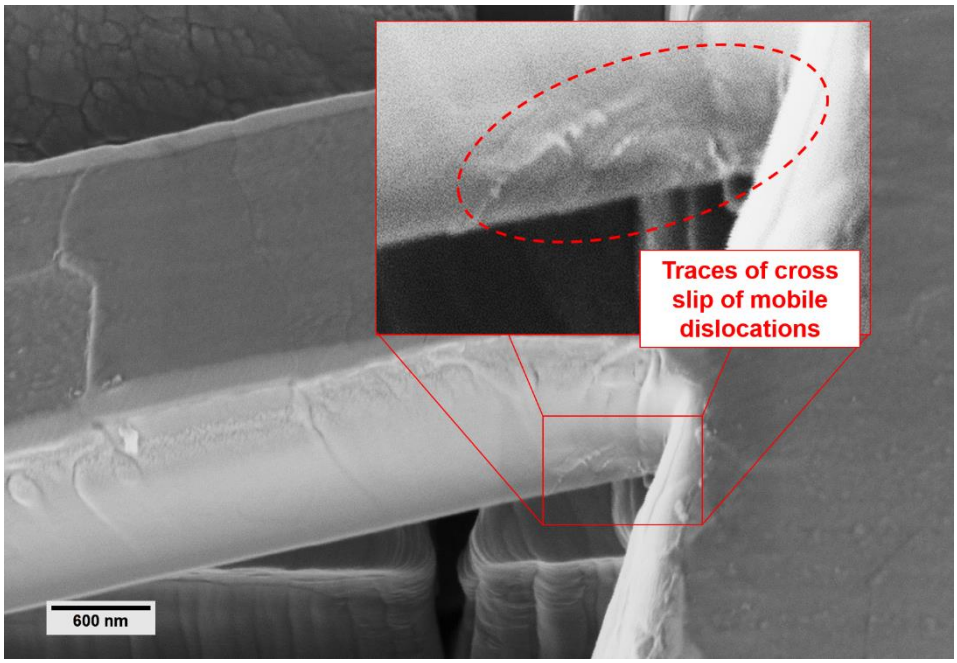


Fig. 5.7 Cross slips traces of mobile screw dislocations were observed at the bottom apex, which were pulled out by the image forces (when close enough to the free surface)

Small cracks were also observed at triple junctions (intersection of three grain boundaries) and low-angle grain boundaries (misorientation<15°). This was confirmed by the EBSD prior to testing, shown in **Fig. 5.6**. Triple junctions and grain boundaries are obstacles for dislocations generated during plastic deformation, hence forming hot spots (stress concentration sites) which are favourable for crack nucleation [105]. Therefore, grain boundaries are carefully avoided when introducing the chevron notches to cantilevers used in micro-fracture tests.

Elastic moduli and yield stresses measured from two triangular cantilevers were compared with Gibson's results for pure tungsten cantilevers [106], summarised in **Table 5.1**. Due to the simple beam assumption, smaller modulus were measured compared to Gibson's work. However, the higher yield stresses (~33%) were possibly due to the strengthening effect from the tantalum addition [107]. Gibson's result also showed a strong dependence yield stress on cantilever thickness. However, the focus of this thesis is not to investigate the size-dependent yield stress; having values from micro-cantilevers of similar thickness (compared to the chevron-notched micro-cantilevers) are sufficient for the crack tip plastic zone estimation.

Cantilever No.	Thickness (μm)	Elastic Modulus (GPa)	Yield Stress (GPa)
A2 (W-1%Ta)	2.8	367±35	5.2±0.2
D2 (W-1%Ta)	2.6	370±28	5.1±0.3
Gibson (W)	2	418±86	2.7±0.4

Table 5.1 Moduli and yield stresses obtained from W-1%Ta and W (Gibson) cantilevers

Estimation of the crack tip plastic zone size expected in the fracture toughness testing of the chevron cantilevers was based on Irwin's approach given in **Eq. 5.3**, where elastic stress analysis was applied to estimate the elastic-plastic boundary [34]. To apply LEFM, the condition of small scale yielding must apply, i.e. the crack tip plastic zone should be confined in the

vicinity of the crack tip, which allowed LEFM analysis to be used to calculate a valid fracture toughness value (K_{Ic}). A linear-elastic FE half model, shown in **Fig. 5.8**, was used to illustrate the confined crack tip plastic zone. However, in the semi-brittle tungsten, the estimated plastic zone radius calculated using **Eq. 5.3** was approximately 160 nm (using 5 GPa for yield stress and a lower bound value of 5 MPa·m$^{0.5}$ for fracture toughness [108]).

The estimated plastic zone radius is well within the confine of the micro-cantilever, hence LEFM is likely to be valid. However, this rough estimation was calculated using tungsten's cleavage fracture toughness. In fact, polycrystalline tungsten possesses a fracture resistance behaviour at room temperature, which can reach 15 MPa·m$^{0.5}$ before unstable fracture [109]. Using this higher bound value, the estimated plastic zone radius was approximately 1.5 μm, approximately half of the cantilever thickness. Therefore, EPFM analysis is still required to give a more precised description of the semi-brittle fracture process.

$$r_y = \frac{1}{2\pi}\left[\frac{K}{\sigma_{ys}}\right]^2 \quad (\boldsymbol{Eq.\,5.3})$$

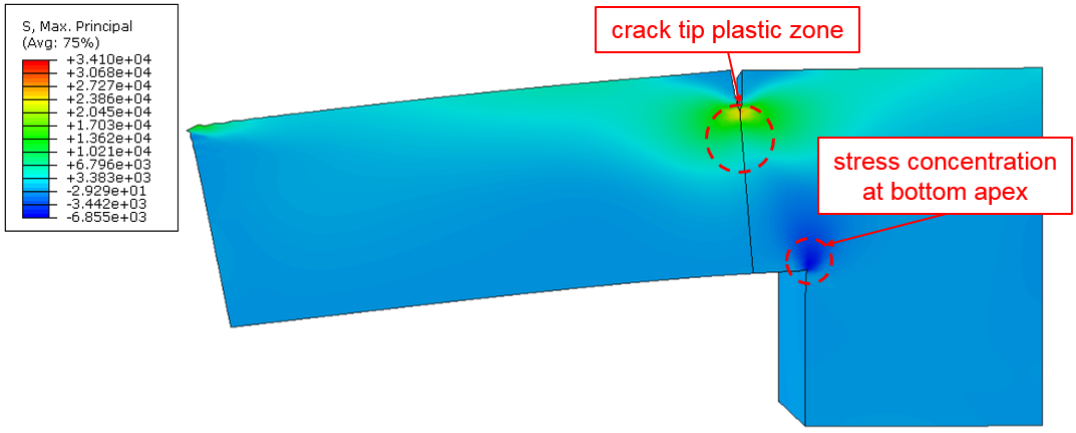
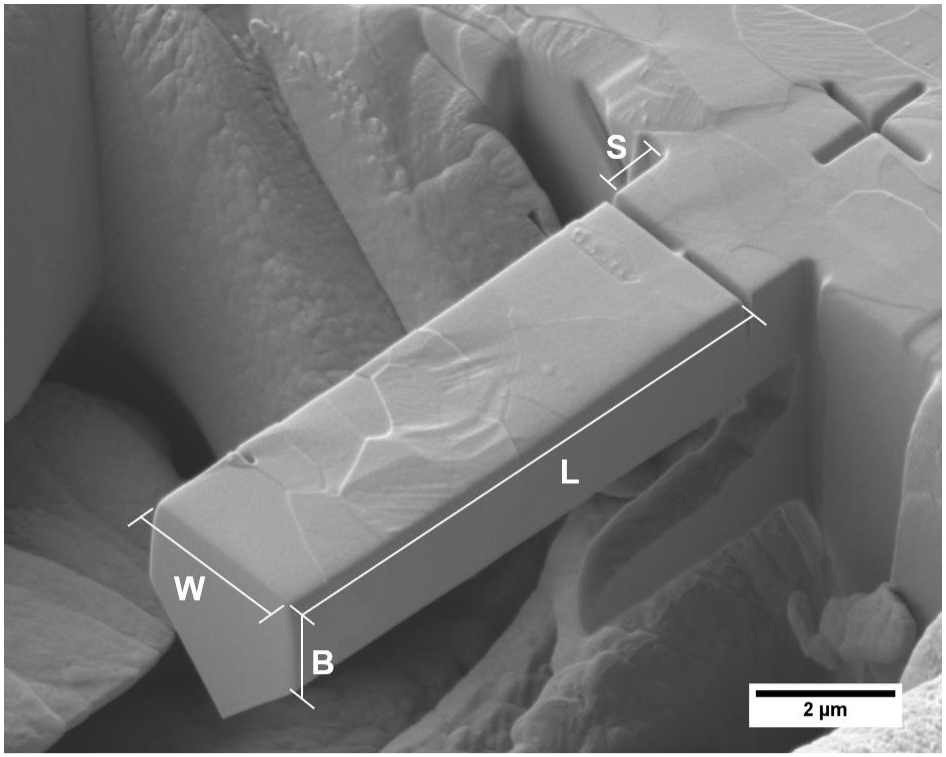


Fig. 5.8 Linear-elastic FE half model of a chevron-notched cantilever. The confined crack tip plastic zone and stress concentration at the bottom apex are labelled

5.3 Continuous Stiffness Measurement Tested Cantilever

Chevron-notched pentagonal micro-cantilever was tested on a G200 Nanoindenter (Keysight® Technologies, USA) using the dynamic continuous stiffness measurement (CSM) method. The cantilever and its dimensions are given in **Fig. 5.9**. The test method was programmed using a load-controlled proportional–integral–derivative (PID) closed loop to maintain a constant displacement rate of 5 nm/s. The CSM function was embedded into the method so that the cantilever stiffness could be monitored during loading. Harmonic frequency of 39 Hz with a displacement amplitude of 2 nm was imposed to the indenter to ensure the oscillation response remained purely elastic, during both elastic and plastic deformations.



L (µm)	B (µm)	W (µm)	S (µm)
9.1	3	3	0.6

Fig. 5.9 SEM image and dimensions of the CSM-tested chevron-notched cantilever

5.3.1 Effect of the Indenter Spring Stiffness

The load-displacement curve of a CSM-tested chevron-notched cantilever is presented in **Fig. 5.10**. It should be specified that the load plotted here is the "load on sample", which was calculated using the nanoindentation data processing software NanoSuite®. When the point of surface contact was defined, the raw load and displacement at contact and the indenter spring stiffness were used to calculate the load on sample according to **Eq. 5.4**.

$$L_{sample} = L_{raw} - L_{surf} - \left(D_{surf} \times S_{spring}\right) \ (\boldsymbol{Eq.5.4})$$

where L_{sample} is the load on sample, L_{raw} is the raw load, L_{surf} is the raw load at contact, D_{surf} is the raw displacement at contact, S_{spring} is the indenter spring stiffness

At lower loads, the indenter penetrated into the cantilever rather than deflecting it, resulting a lower slope, shown in **Fig. 5.10(b)**. At larger load, the load-displacement curve was dominated by the elastic response of the cantilever. During stable crack growth, small displacement steps were visible on the load-displacement curve, indicating that the crack growth was probably by small and discrete jumps, which are highlighted in the red-dotted circles in **Fig. 5.10(c)**. A gentle load relaxation was also observed prior to unstable fracture, shown in section d in **Fig. 5.10** and **Fig. 5.11**. The indenter system was programmed to keep a constant load on the indenter, but the deformations at this stage were rapid (continuous plastic flow and crack growth), hence the ramp rate programmed in would not call for a large changes of indenter load or displacement. As the displacement increased, the load on the specimen itself dropped because the indenter spring support was increasingly taking its share of the load, which resulted the observed load relaxation. The slope in **Fig. 5.11** has a negative slope of 72 N/m, which is in good agreement with the indenter spring stiffness of 70 N/m, extracted from the NanoSuite® software.

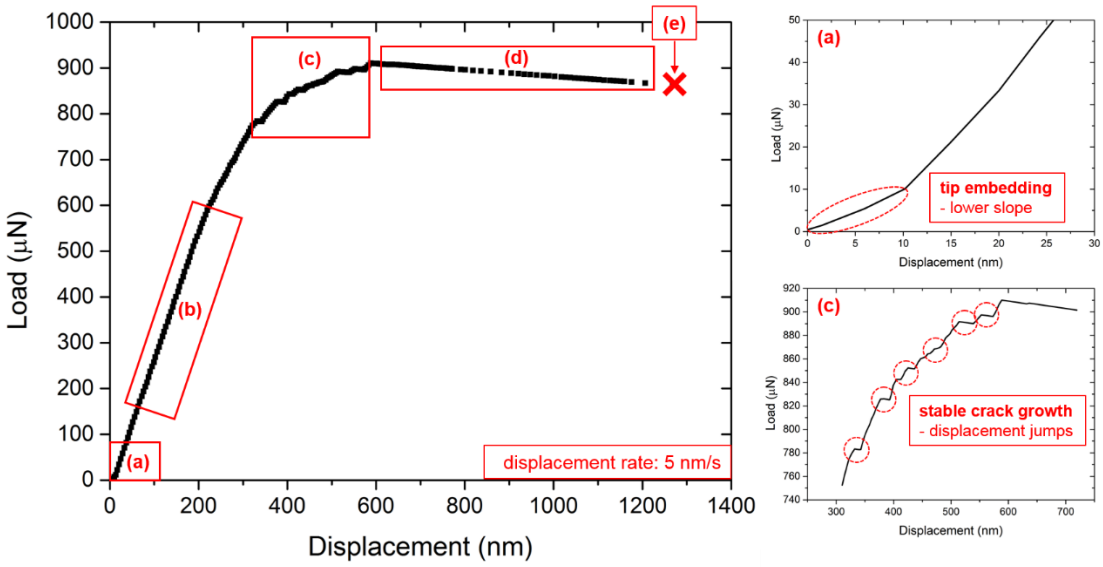


Fig. 5.10 Load-displacement curve of a CSM-tested chevron-notched cantilever (indenter stiffness corrected). The different deformation stages are labelled: **(a)** tip embedding, **(b)** elastic deformation, **(c)** stable crack growth, **(d)** load relaxation, and **(e)** final unstable fracture

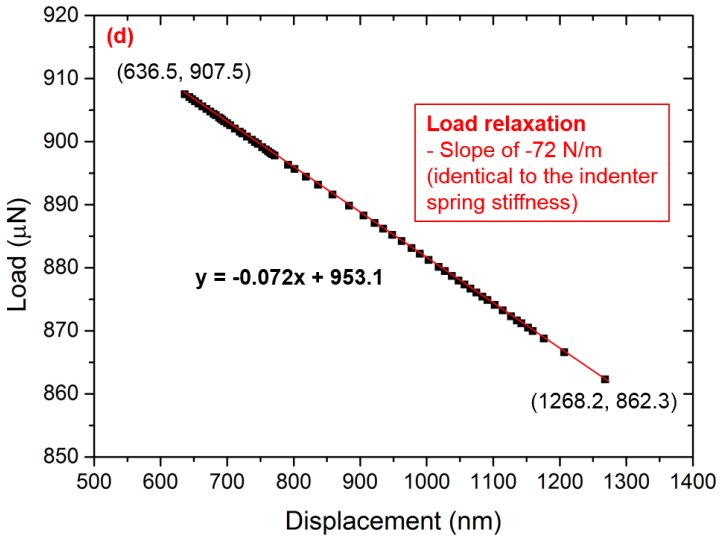


Fig. 5.11 Load relaxation segment from **Fig. 5.10(d**), where the slope is -72 N/m

For consistency, all load-displacement curves shown in this thesis are plotted using the "load on sample" values, i.e. load values shown are after the correction for the effect of spring stiffness, using **Eq. 5.4**.

5.3.2 Scattering of the CSM-Measured Stiffness

A total stiffness drop of approximately ~300 N/m were measured before the cantilever fractured unstably. This is shown in **Fig. 5.12**, where the initial stiffness value (3700 N/m) was calculated from a linear-elastic FE cantilever model of similar dimension (α_0=0.1, α_1=0.9). Initial stiffness were significantly lower due the tip embedding at shallow depth, which will be discussed in more details in the next section. The periodic wave-shaped scattering is probably an artefact due to the superimposed sinusoidal load signals from the CSM method. Crack opened up during loading, resulting the stiffness drop. Crack closed partially during unloading, resulting the stiffness rise, from the contact between two rough crack surfaces. A schematic drawing of this CSM-induced crack opening/closure interaction is shown in **Fig. 5.13**. It is also worth mentioning that the CSM-measured cantilever stiffness were probably unaffected by any consideration of the indenter spring stiffness, because the CSM displacement were very small (2 nm), therefore any effects from the indenter spring stiffness should be insignificant.

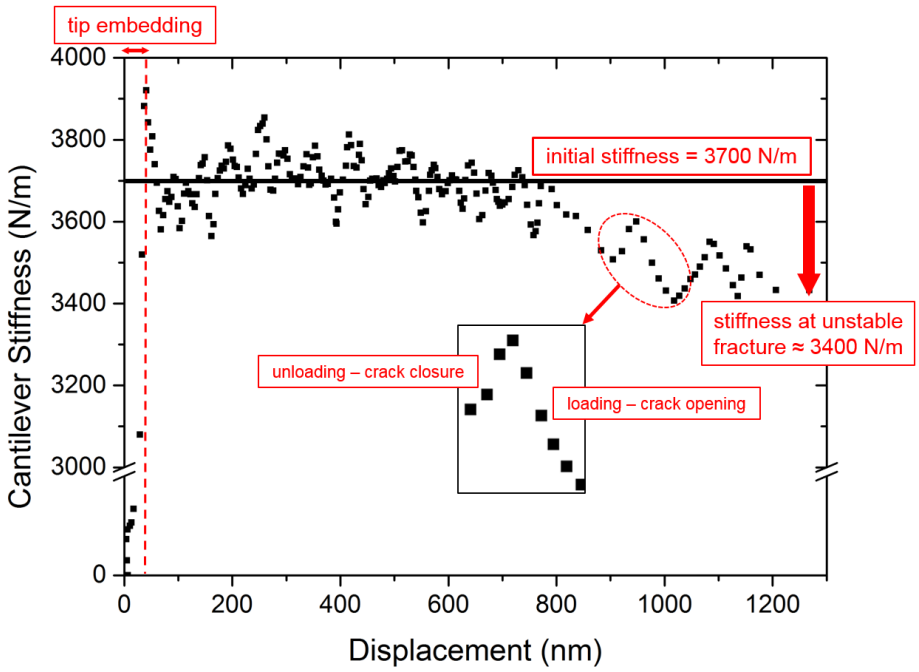


Fig. 5.12 CSM-measured stiffness vs. displacement. Lower cantilever stiffness were observed for displacement < 50 nm due to tip embedding. The wave-shaped scattering occurred periodically. A total stiffness drop of approximately 300 N/m was measured at end of test.

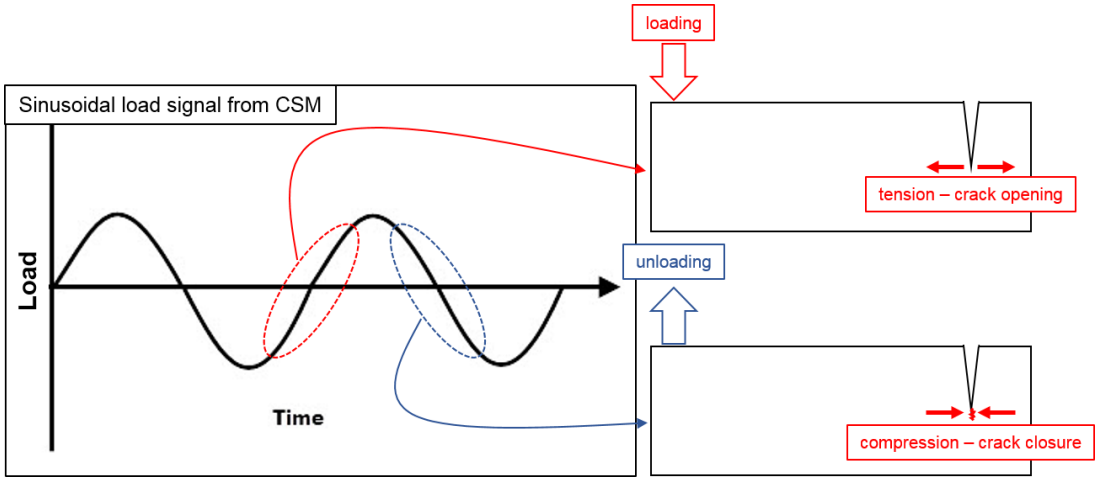


Fig. 5.13 Schematic drawing of the sinusoidal load (displacement) signal and the crack opening/partially-closure during the loading/unloading phases

5.3.3 Post-Test Fractography and Crack Length Measurements

Post-test SEM fractography was used to examine the tested cantilever and fracture surface in greater details. The embedding mark on the cantilever was from the initial tip penetration, which can be conveniently used to determine the effective length L. Scratches on the cantilever surface were damage from the AFM-like scanning. To avoid undesirable surface damage, the scanning load was decreased from 3 to 1 μN in later tests. The remaining cantilever was removed using a Kleindiek® micromanipulator so that the features on the fracture surface can be examined.

Ductile tearing ligaments at the top chevron apex were evidence for the significant plasticity observed from the load-displacement curve. Cleavage-like fracture surface underneath the tearing ligaments were good evidence for the consequential unstable fracture. The stable crack length estimated from the stiffness drop is approximately 500 nm, which was calculated using the stiffness vs. crack length relationship given in **Fig. 5.15**. Unfortunately, the chevron fracture surface was covered by the ligaments, hence stable crack length cannot be measured experimentally via fractography. Nevertheless, post-examination of the fracture surface is extremely important as it provides qualitative and sometime quantitative information on the fracture behaviour.

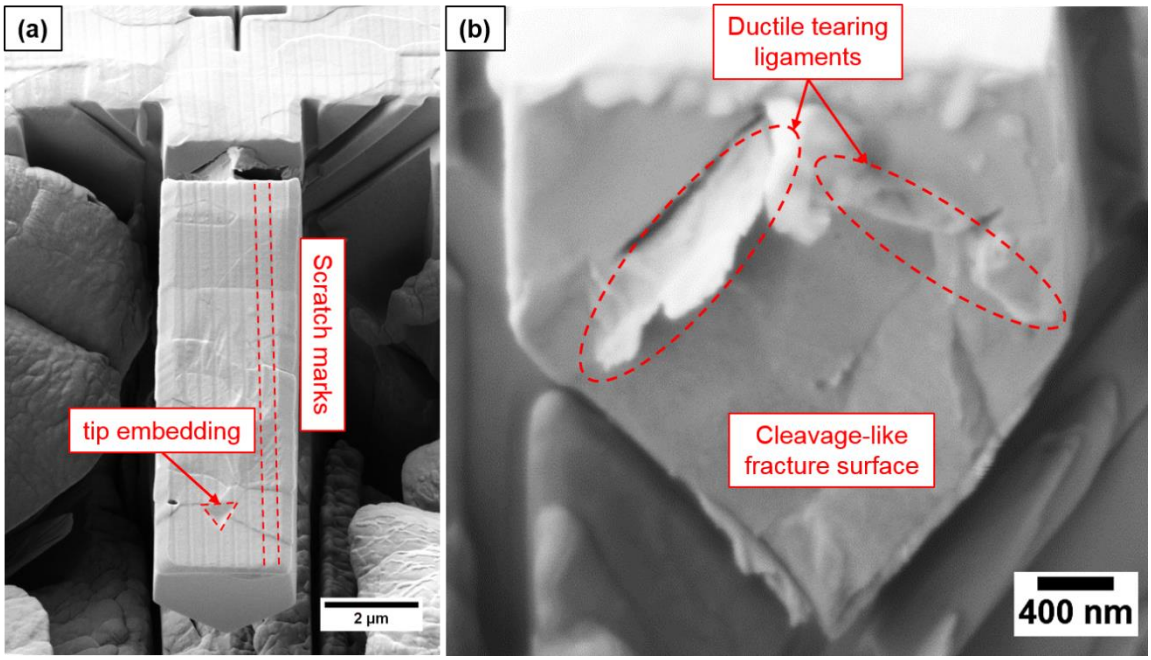


Fig. 5.14 (a) Post-test SEM image of the CSM-tested cantilever, where the fracture surface and features **(b)** are revealed after the micromanipulator removal

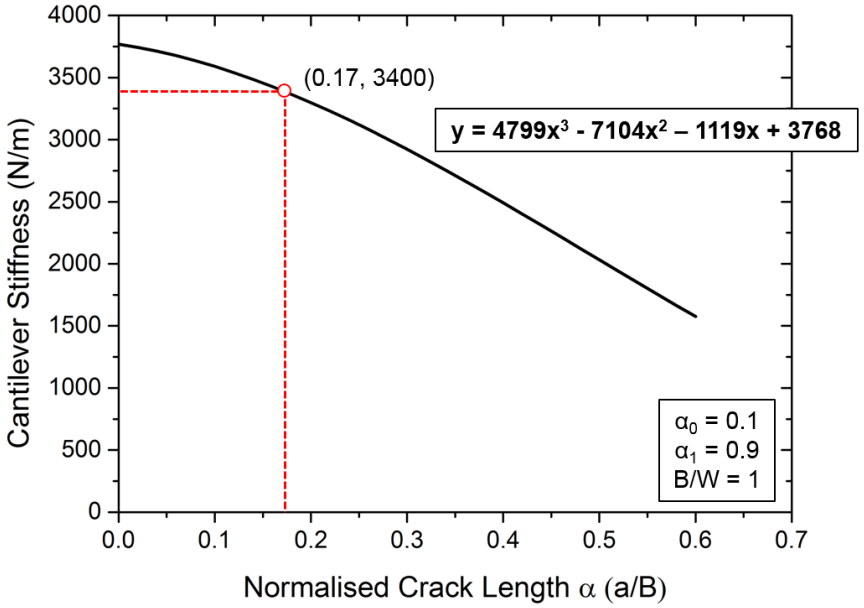


Fig. 5.15 Cantilever stiffness vs. normalised crack length (α) relationship from the FE chevron-notched micro-cantilever model (α_0=0.1, α_1=0.9) described in Chapter 4

The CSM method was capable of measuring dynamic cantilever stiffness without additional load/unload cycles. However, the main drawbacks were the highly-scattered stiffness values from the sinusoidal force/displacement signals and the closed feedback control loop which was incapable of capturing the dynamic responses of the cantilever post-yielding. Most importantly, the CSM method is not available in the Micro Material® NanoTest Xtreme, therefore a quasi-static stiffness measurement method which is compatible with the high-temperature nanoindenter will be developed.

5.4 The Load Partial-Unload Stiffness Measurement Method

As high temperature micro-fracture experiments are extremely difficult due to the complicated test setup and limited instrument time, it is therefore important to have an optimised method for accurately measuring the cantilever stiffness. One major contribution of this thesis is to develop a quasi-static load partial-unload method to accurately measure the cantilever stiffness during stable crack growth. All load partial-unload tests were performed using a G200 Nanoindenter (Keysight® Technologies, USA) under closed-loop, load-controlled mode. A typical load profile (load vs. time) is shown in **Fig. 5.16**. Experimental artefacts such as the indenter tip embedding and thermal drift, as well as the test parameters (loading/unloading rate, load increment, hold time, unloading percentage) will all be discussed. Unless otherwise noted, tests were conducted on a chevron-notched W-1%Ta cantilever (H1), at room temperature. The SEM/EBSD images and the cantilever dimensions are given in **Fig. 5.17** and **Table 5.2**.

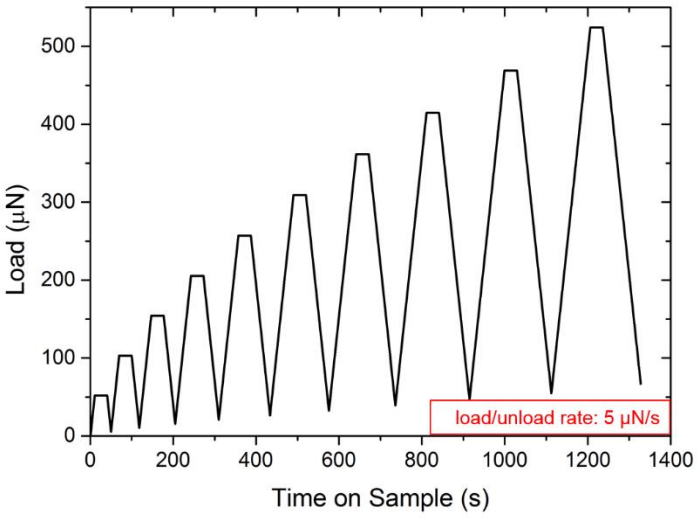


Fig. 5.16 Load profile of a typical load partial-unload test

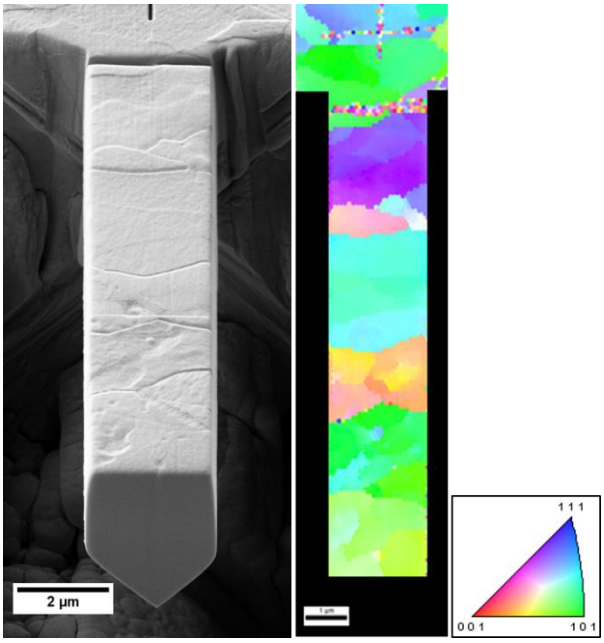


Fig. 5.17 SEM and EBSD images of cantilever H1

Cantilever	L (μm)	B (μm)	W (μm)	S (μm)	α_0 (μm)	α_1 (μm)
H1	11.3	3	2.9	0.6	0.1	0.8

Table 5.2 Dimensions of cantilever H1

5.4.1 Effects of Tip Embedding to Loading/Unloading Stiffness

To investigate the effect of tip embedding to cantilever stiffness measurements, cantilever H1 was loaded to 300 μN, held for 5 sec, and unloaded back to 150 μN, all using the same loading/unloading rate of 5 μN/s. The maximum load was set considerably lower than the yield load of cantilevers of such size (typically around 700 μN), so the deflection remained fully in the elastic regime, and the stiffness calculated from the loading/unloading phases should not be affected by plasticity. The load-displacement curve is shown in **Fig. 5.18**, where a discrepancy between the loading/unloading due to tip embedding was observed.

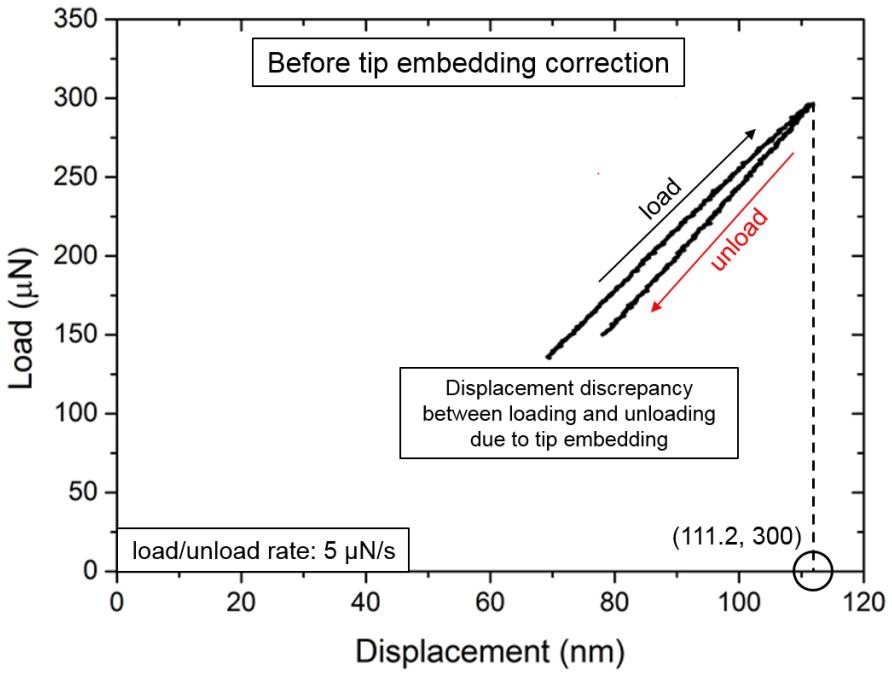


Fig. 5.18 Load-displacement curve of cantilever H1 before the tip embedding correction. No significant yielding and a displacement dicrepancy (~10 nm) between the loading/unloading phases are observed

To further investigate the amount of tip embedding into the cantilever, bulk indentation was conducted on the same materials (W-1%Ta) using the same load (300 μN), shown in **Fig. 5.19**. A second-order polynomial function (red curve) was fitted to the load-displacement curve, so that the tip embedding displacement at corresponding load could deduced and subtracted from the raw displacement in cantilever tests. Therefore, the deflection of the cantilever alone were calculated using **Eq. 5.5**. The tip embedding corrected load-displacement curve for cantilever H1 is given in **Fig. 5.20**, where the displacement discrepancy is significantly reduced.

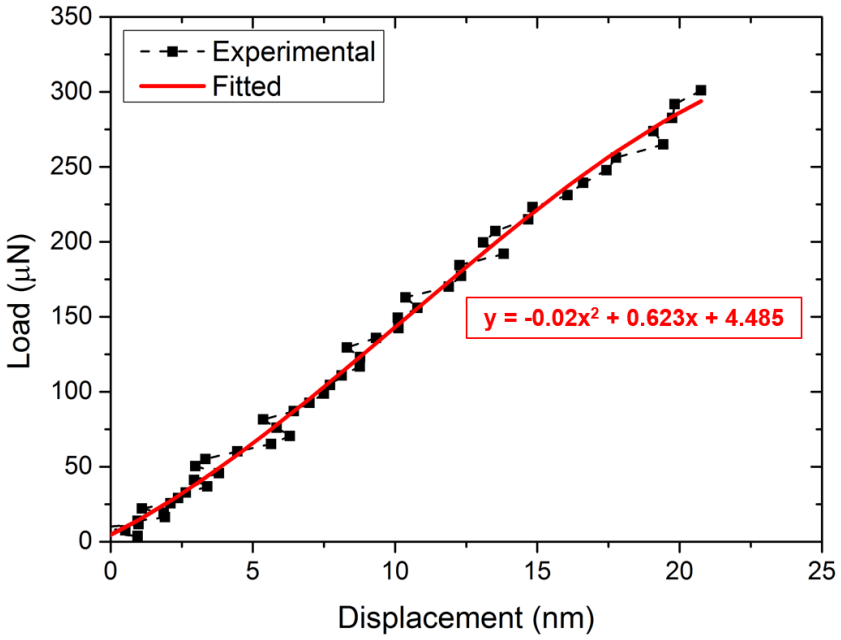


Fig. 5.19 Bulk indentation load-displacement curve of W-1%Ta to 300 μN and the 2nd order polynomial fit (red curve)

$$h_{cantilever} = h_{raw} - h_{embedding} \ (\boldsymbol{Eq.\ 5.5})$$

where $h_{cantilever}$ is the cantilever deflection, h_{raw} is the measured displacement, and $h_{embedding}$ is the tip embedding depth

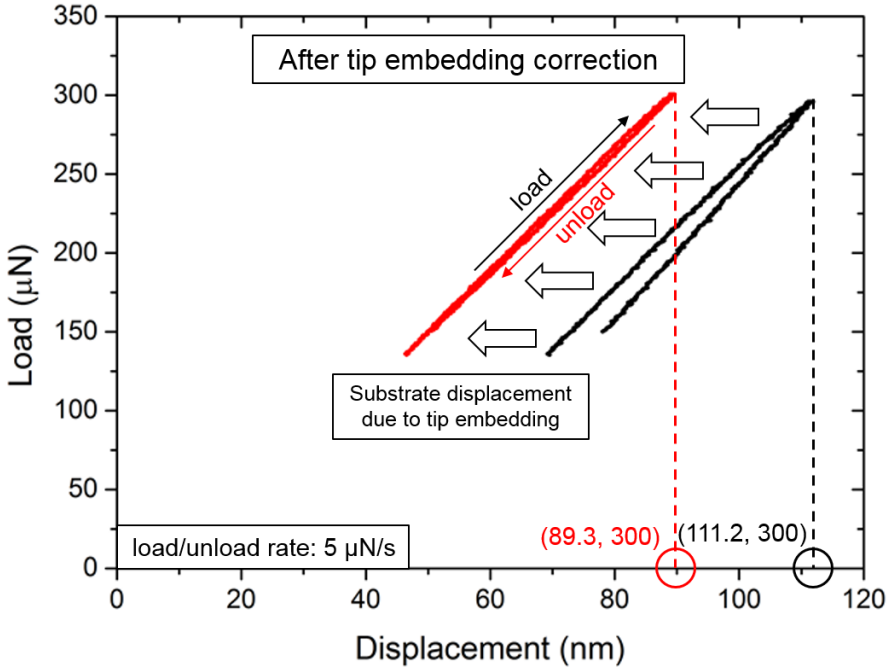


Fig. 5.20 Load-displacement curve of cantilever H1 after the tip embedding correction

Before the tip embedding correction, the cantilever stiffness was lower on loading compared to on unloading. This is due to the more compliant elasto-plastic tip embedding during initial contact. After correction, the cantilever stiffness on loading and unloading were more consistent, and also closer to the FE-calculated stiffness (3768 N/m). Exact cantilever stiffness measured from loading/unloading phases, both before/after the tip embedding correction are summarised in **Table 5.3**. Gong et al. [110] also observed a discrepancy between the loading and unloading stiffness measured from single crystal Ti micro-cantilevers. By doing a second test on the same position (tip embedding was already developed), the stiffness discrepancy was significantly reduced. Post-test SEM micrograph of cantilever H1 is shown in **Fig. 5.21**, which can confirm the tip embedding. This tip embedding correction approach will be used to correct

for all the load-displacement curves in later cantilever tests, especially during the initial cycles where tip embedding is more significant.

Test	Loading Stiffness (N/m)	Unloading Stiffness (N/m)	Change in Loading/Unloading Stiffness (%)
Before correction	3621±4	3989±5	9.2
After correction	3893±5	3816±3	2

Table 5.3 Summary of cantilever H1's stiffness measured from loading and unloading phases, before and after the tip embedding correction

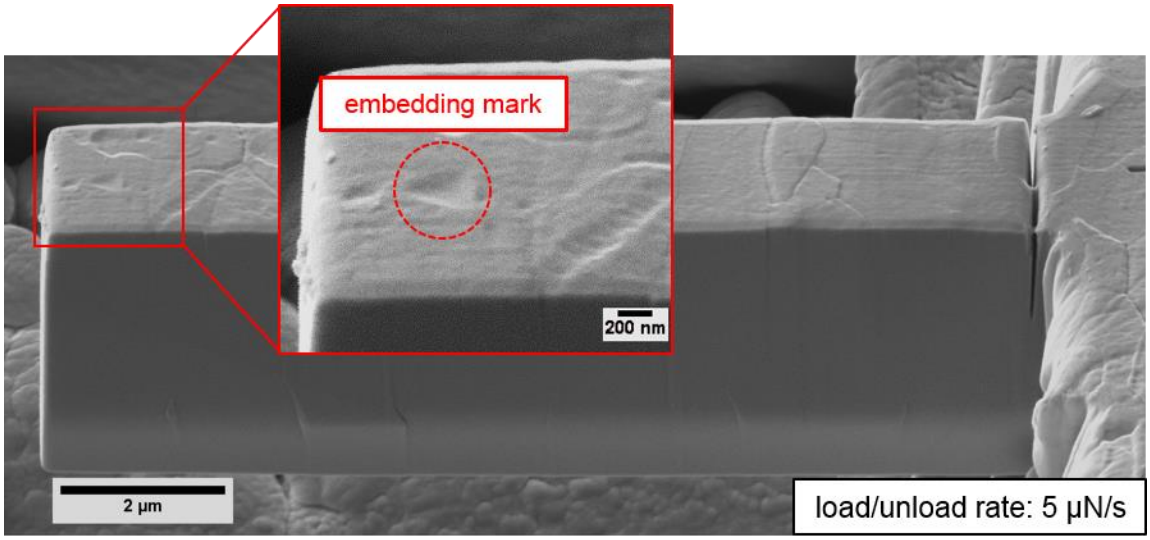


Fig. 5.21 Post-test SEM micrograph of cantilever H1. A faint embedding mark is observed

5.4.2 Effects of Loading/Unloading Rate and Thermal Drift to Displacement

The loading/unloading rate has to be sufficiently low to avoid any over-loading effect which may introduces premature failure [50]. It also has to be sufficiently high to maintain a reasonable test duration, and so the contribution of thermal drift to displacement can be effectively minimised. Two sets of load partial-unload tests, using different loading/unloading

rate (2 and 5 μN/s) were conducted sequentially on cantilever H1. Shown in **Fig. 5.24**, the tests were conducted intentionally on the developed embedding marks, it was assumed no embedding was further developed. The load-displacement curves for both tests are shown in **Fig. 5.22**. The maximum load was set to 600 μN (still within the elastic regime), so the maximum displacement could be extrapolated from previous 300 μN test. The estimated maximum displacement (~178 nm) was in good agreement with the maximum displacement of the 5 μN/s test (~175 nm). However, the maximum displacement of the 2 uN/s test is 233.6 nm. Since tip embedding was excluded, the remaining factor for the displacement discrepancy was the thermal drift, which contributed to a significant amount of "false" displacement over a long test duration.

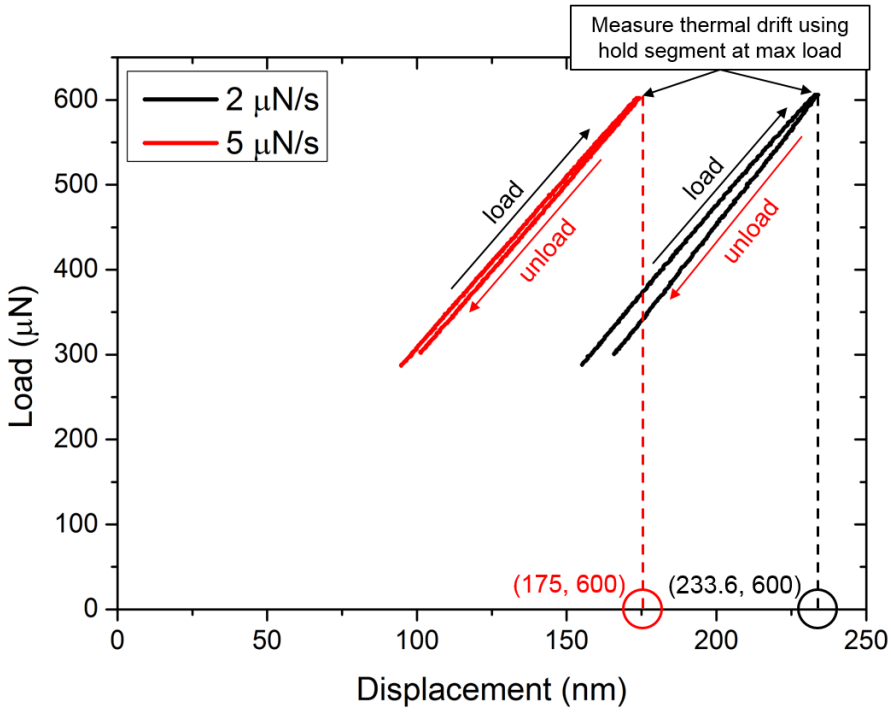


Fig. 5.22 Load-displacement curves for tests using two different loading/unloading rate

The average thermal drift rates for two tests (nm/s) were calculated by fitting a straight line over the 5 sec hold segment at maximum load, and the slope of the line represents the

average thermal drift rate. The hold segment, and the drift rate for two tests are shown in **Fig. 5.23**. If drift rate was constant throughout the test, it could accumulated into approximately 55 nm of false displacement in the 2 μN/s test, which was consistent with the displacement discrepancy found in **Fig. 5.22**. Therefore, thermal drift can contribute significantly to displacement and should be corrected for. The load-displacement curves were corrected using **Eq. 5.6**, and the average drift rate was calculated using the hold segment at each cycle. For typical cantilevers used in this thesis, a loading/unloading rate of 5 μN/s is recommended.

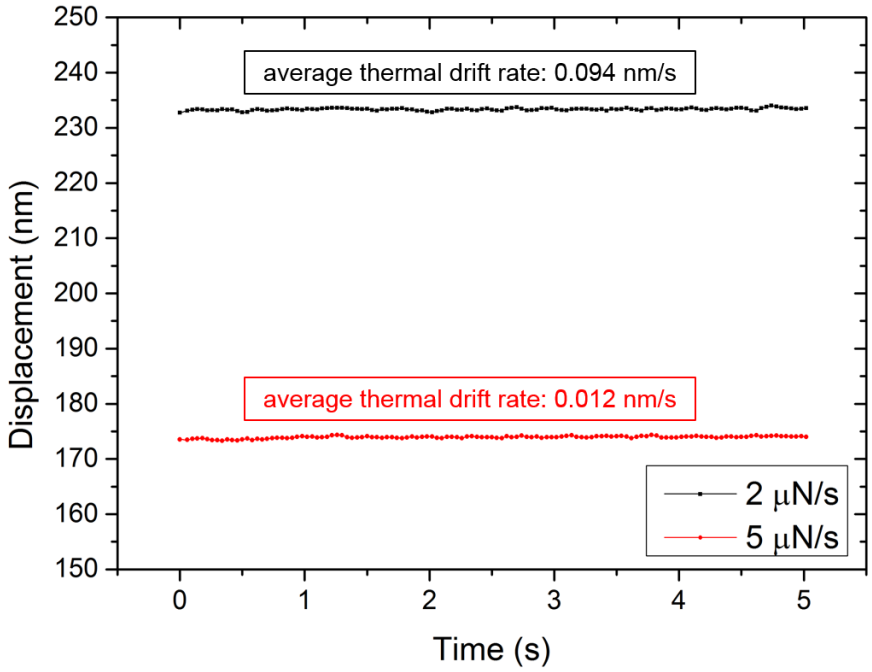


Fig. 5.23 Displacement vs. time during the hold segment at maximum load for both tests

$$D_{bend} = D_{raw} - \left(Drift_{avg} \times T\right) \ (\boldsymbol{Eq.\ 5.6})$$

where D_{bend} is the cantilever bending deflection, D_{raw} is the displacement measured via the nanoindenter, $Drift_{avg}$ is the average drift rate, and T is the time on sample

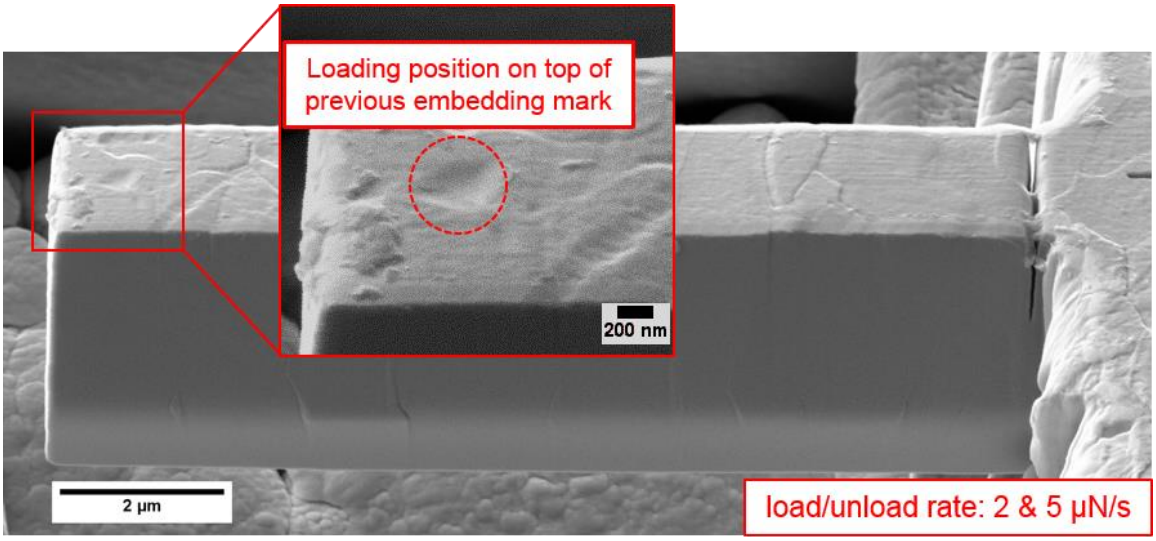


Fig. 5.24 Post-test SEM micrograph of cantilever H1, after 2 & 5 μN/s tests. The loading position was intentionally positioned on top of previous indent to prevent further embedding

5.4.3 Effects of Tip Embedding to Stiffness Values at Initial Cycles

The effect of tip embedding to stiffness values at initial cycles is also investigated. Another set of load partial-unload test using loading/unloading rate of 5 μN/s was performed on cantilever H1. The cantilever is loaded to 900 μN, using load increment of 30 μN. The loading position, however, was different than the previously developed embedding mark, so the effects of embedding could investigated. The load-displacement curve and cantilever stiffness vs. maximum load (tip embedding uncorrected) are given in **Fig. 5.25** and **Fig. 5.26**.

In the low load regime (< 300 μN), cantilever stiffness were significantly smaller. This was due to the compliant elasto-plastic tip embedding which took place during the loading phase, and therefore decrease the stiffness which were calculated from the unloading phases. In an actual test, the indenter is not perfectly fixed with the cantilever, so the unloading displacement can be separated into three terms: (1) thermal drift, (2) elastic deflection of the cantilever, and the (3) elasto-plastic extraction from tip embedding. Contribution from thermal drift was negligible,

due to the extremely low thermal drift rate (<0.01 nm/s), and the faster rate used. Elastic displacement of the cantilever is linear with load, so stiffness calculated from this term should be constant (before any fracture occurred). Shown schematically in **Fig. 5.27**, the tip extraction depth h_p depends on the amount of embedding generated during loading. Similar to section **5.4.1**, the tip embedding were calculated using the 2nd order polynomial fit given in **Fig. 5.19,** and subtracted from the measured displacement. The cantilever stiffness were then re-calculated using the corrected load-displacement curve, shown in **Fig. 5.28**. Stiffness values during initial cycles after correction were significantly higher, and closer to the ideal cantilever stiffness, This is because most tip embedding occurred at lower loads, and were subtracted from as-received displacement measurements.

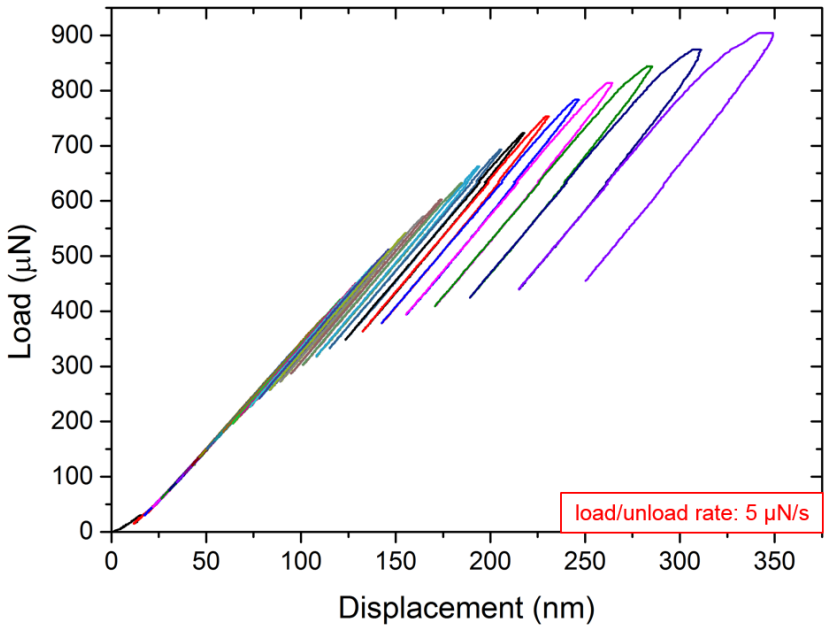


Fig. 5.25 Load-displacement curve of the load partial-unload tested cantilever H1

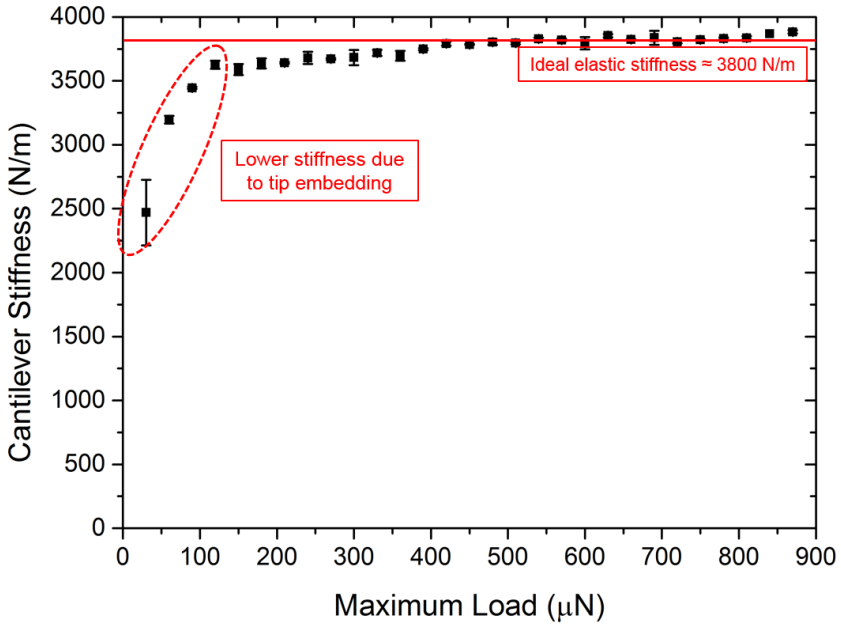


Fig. 5.26 Cantilever stiffness vs. maximum load (tip embedding uncorrected)

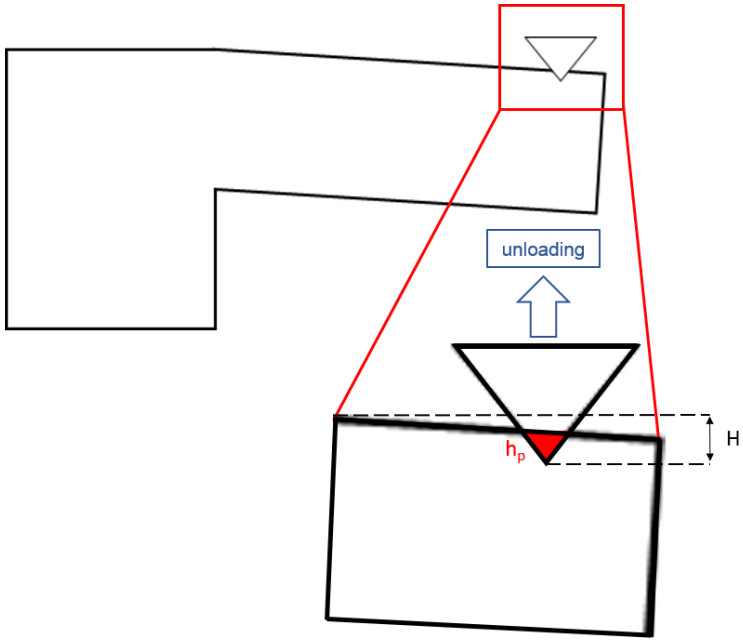


Fig. 5.27 Schematic illustration of the cantilever during unloading. The total unloading displacement is the sum of the tip extraction and cantilever's elastic deflection

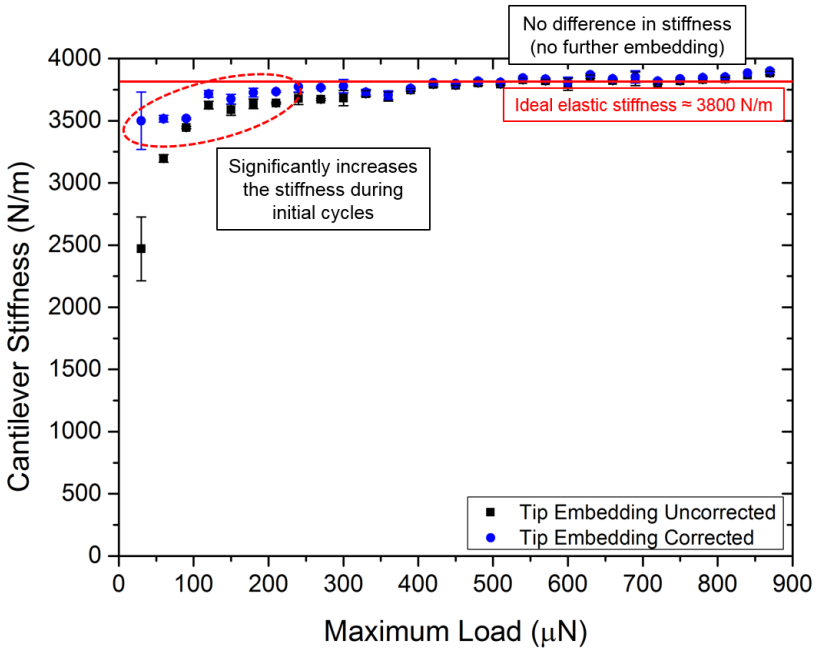


Fig. 5.28 Cantilever stiffness vs. maximum load (both tip embedding corrected/uncorrected)

5.4.4 Effects of Hold Time to Unloading Stiffness

Hold segments were implemented at the maximum load of each cycle. This allowed the plasticity deformations introduced during the loading phase to relax, until the load became stable at a constant displacement prior unloading. This "load relaxation" phenomenon were also observed in previous elastic-plastic cantilever tests (see section 5.2). By using sufficient hold time, the amount of non-linearity deformation in the unloading phase were effectively reduced, hence improving the stiffness measurements. Two sets of load partial-unload tests were conducted on cantilevers G1. Cantilever was loaded to approximately 900 μN to introduce similar amount of plastic deformation. However, hold time at maximum load were set differently to 5 and 20 sec, so its effect to the unloading curves could be investigated. SEM and EBSD images of cantilever G1 are shown in **Fig. 5.29**, dimensions are given in **Table 5.4**, and the load-displacement curves for two tests with different hold time are shown in Fig. **5.30**.

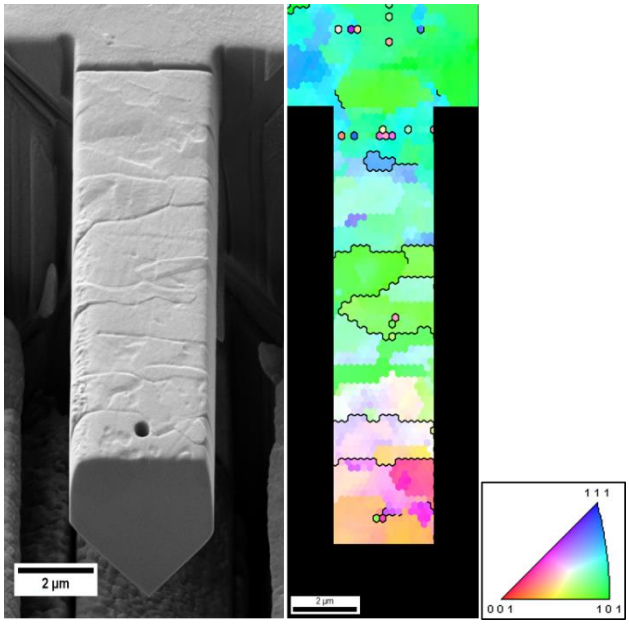


Fig. 5.29 SEM and EBSD images of cantilever G1

Cantilever	L (µm)	B (µm)	W (µm)	S (µm)	α_0 (µm)	α_1 (µm)
H1	12.3	3	2.9	0.6	0.1	0.8

Table 5.4 Dimensions of cantilever G1

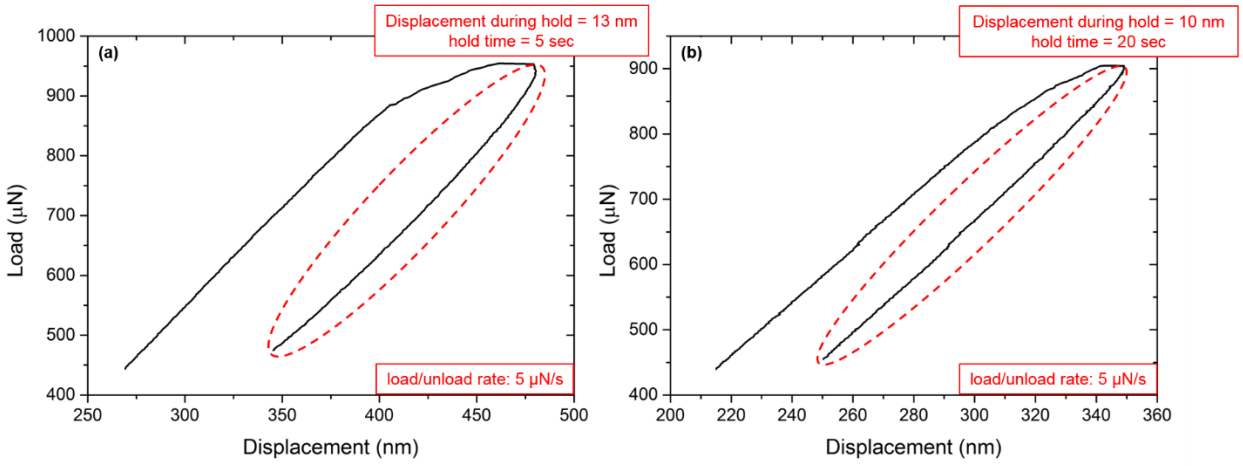


Fig. 5.30 Load-displacement curves of cantilever G1 with different hold time (5 vs 20 sec). The unloading phase for the 5 sec test is slightly more elbowed

Stiffness for both tests calculated from the unloading phase, using a flowing average over 3 points, then plotted against load, are shown in **Fig. 5.31**. In the higher load regime, stiffness for both tests were significantly higher. One should also note that the displacement during the hold segment for the 5 sec test was slightly larger, possibly due to the higher load (~950 μN) and hence the larger creep deformation. Therefore, the stiffening effect for the 5 sec test during the high load regime was also more obvious. It is probable that the stiffening effect was the result of dislocation pile up at the cantilever's neutral axis plastic and creep deformations. Dislocation pile up generates significant back stresses, which stiffens the cantilever significantly during the initial stage of the unloading phase. This was also experimentally proven in the work by Kirchlechner et al. [111] and Demir et al. [112]. They used μLaue diffraction and EBSD techniques to investigate the accumulation and dissolution of dislocation pile up at the neutral axis of the cantilever, during both loading and unloading. It was possible that the longer hold time in the 20 sec test provided sufficient time for pile up dislocations to dissolute, hence resulting the less stiffening. In the lower load regime (<600 μN), stiffness for both tests were found to be significantly lower. This softening behaviour was probably from the more compliant elasto-plastic tip extraction at lower loads, as deformation in this stage is largely influenced by the tip extraction (similar to the tip embedding effect discussed in section 5.4.3). Stiffness at the mid-load regime, however, were rather flat. The influences of dislocation pile up and tip extraction were less, suggesting cantilever stiffness should be calculated from this regime. A straight line using the LINEST function was fitted to the mid-50% load regime. The unloading phase of the 20 sec test with the linearly-fitted function is shown in **Fig. 5.32**, and the slope of the linear function represents the elastic cantilever stiffness.

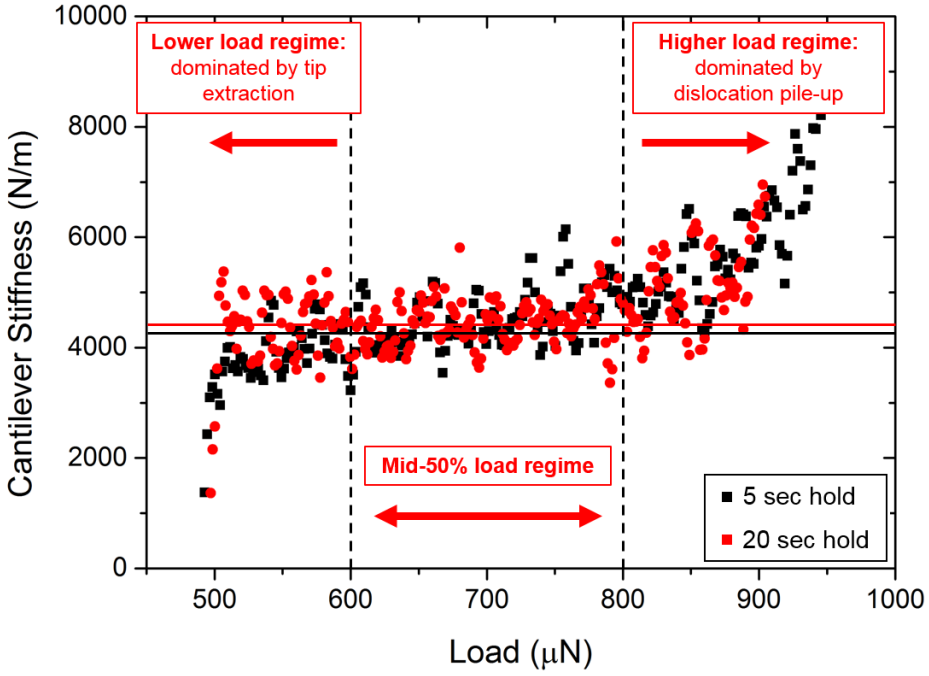


Fig. 5.31 Stiffness vs. load (during unloading phase) for both tests

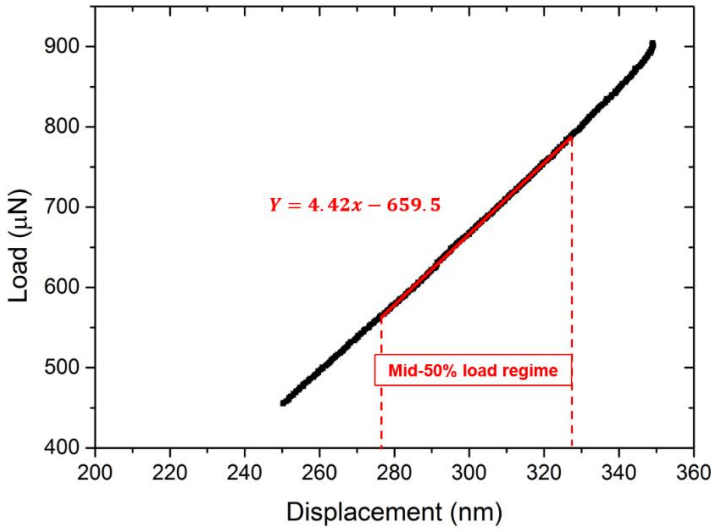


Fig. 5.32 Unloading phase of the 20 sec test. Cantilever stiffness was calculated using the slope of the linearly fitted function (red curve) in the mid-50% unload regime

5.4.5 Summary of Load Partial-Unload Method Optimisation

The effects of tip embedding, thermal drift, loading/unloading rate, hold time, and the percentage-to-unload were all discussed. Without appropriate experimental considerations, significant errors can be introduced to the load and displacement measurements, hence affecting the fracture toughness calculations. The suggested test parameters are listed in **Table 5.5,** which will serve as a guideline for later room and high temperature micro-fracture tests. Only when spring stiffness, thermal drift, and tip embedding are all taken into account, the load-displacement curves generated from the optimised load partial-unload method will be capable of measuring reliable cantilever stiffness for crack length estimation. Therefore, all load-displacement curves shown in the next section are corrected from spring stiffness, thermal drift and tip embedding.

Thermal Drift	Loading/Unloading Rate	Load Increment	Hold Time	% to Unload
<0.01 nm/s	5 μN/s	30~50 μN	20 sec	50%

Table 5.5 Recommended test parameters for optimal load partial-unload test

5.5 Room Temperature Load Partial-Unload Tested Cantilevers

Three chevron-notched W-1%Ta cantilevers (B1, B2, and B3) were tested successfully using the load partial-unload method. The SEM/EBSD images, dimensions, and test parameters are given in **Fig. 5.33**, **Table 5.6** and **5.7**. Load-displacement curves (spring stiffness, thermal drift and tip embedding corrected), stiffness vs. maximum load, and post-test SEM fractography are then discussed individually, depending on the fracture behaviour.

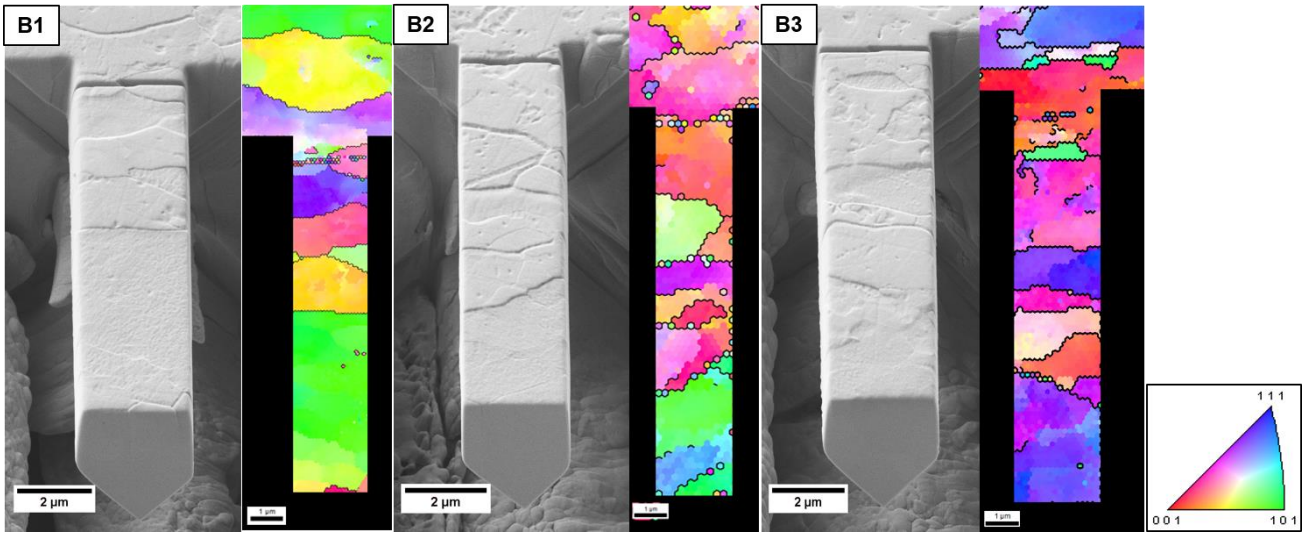


Fig. 5.33 SEM/EBSD images of cantilever B1, B2, and B3

Cantilever	L (µm)	B (µm)	W (µm)	S (µm)	α_0 (a_0/B)	α_1 (a_1/B)
B1	11.4	3.2	3	0.6	0.1	0.9
B2	11.2	3	3	0.5	0.1	0.9
B3	11.2	3	3	0.5	0.1	0.9

Table 5.6 Dimensions of cantilever B1, B2, and B3

Cantilever	Loading/Unloading Rate	Load Increment	Hold Time	% to Unload
B3	5 μN/s	30 μN	20 sec	50%
B2	5 μN/s	50 μN	30 sec	50%
B1	5 μN/s	100 μN	30 sec	90%

Table 5.7 Test parameters for cantilever B3, B2, and B1

5.5.1 Cantilever B3 (stable crack growth with clear distinction between stable/unstable crack growth regime)

Load-displacement curve of cantilever B3 is shown in **Fig. 5.34**. The cantilever was loaded incrementally to unstable fracture at 643 μN. Significant amount of non-linearity deformations were observed in the later cycles, which were associated with stable crack growth and plasticity. Cantilever stiffness were calculated using the tip embedding corrected load-displacement curves, which is shown in **Fig. 5.35**. One should also note that, after the tip embedding correction, initial stiffness remained slightly lower. This is because the 2nd order polynomial fit from the bulk indent (shown in **Fig. 5.19**) which was used to estimate the embedding depth doesn't necessarily represents the exact load-displacement response of the cantilever grain (where the tip embedded into); it also depend on the exact hardness of that specific grain. Therefore, the total embedding depth may not be fully taken into account due to some hardness anisotropy, resulting the slightly lower stiffness values during initial cycles. Stiffness drop of approximately 360 N/m was measured before unstable failure, and was converted to crack length using the stiffness vs. crack length relationship from previous FE-modelled cantilever (α_0=0.1, α_1=0.9), shown in **Eq. 5.7**. The estimated stable crack length for cantilever B3 was approximately 510 nm.

$$S = 4799\alpha^3 - 7104\alpha^2 - 1119\alpha + 3768 \ (\mathbf{Eq.\ 5.7})$$

where S is the cantilever stiffness (N/m), α is the normalised crack length (a/B)

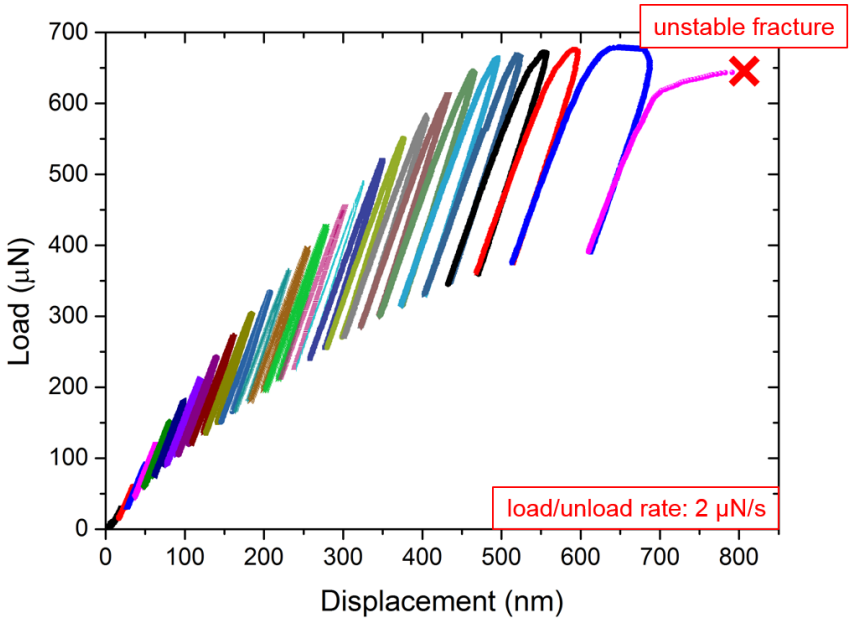


Fig. 5.34 Load-displacement curve of cantilever B3. A smaller load increment (30 μN) was used

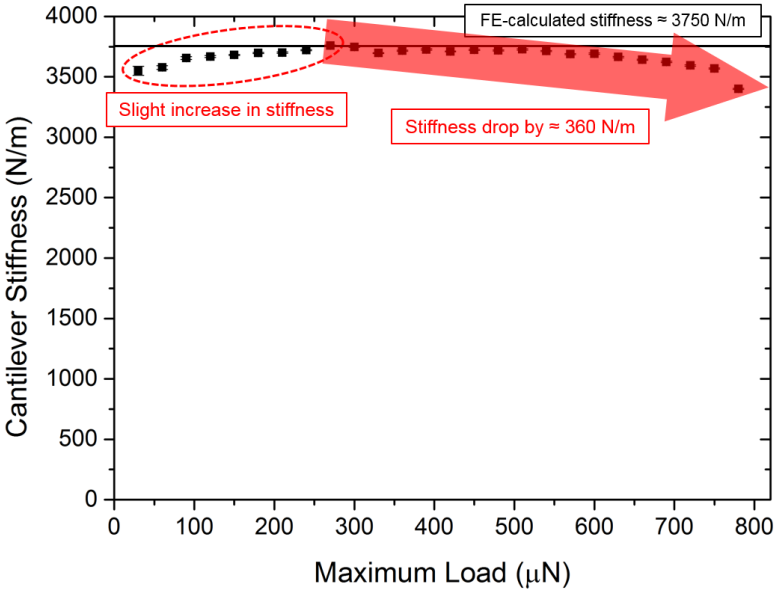


Fig. 5.35 Stiffness of cantilever B3 calculated from the tip embedding corrected load-displacement curve. About 360 N/m of stiffness drop was measured before unstable failure

SEM fractography for cantilever B3 is shown in **Fig. 5.36**, where a clear distinction between the stable and unstable crack growth regime is observed. The stable crack growth regime is dominated by ductile dimple-like fracture features, where the unstable regime is dominated by brittle cleavage-like fracture features. The stable crack length measured from the fracture surface is approximately 520 nm, which is in good agreement with the crack length estimated from stiffness drop.

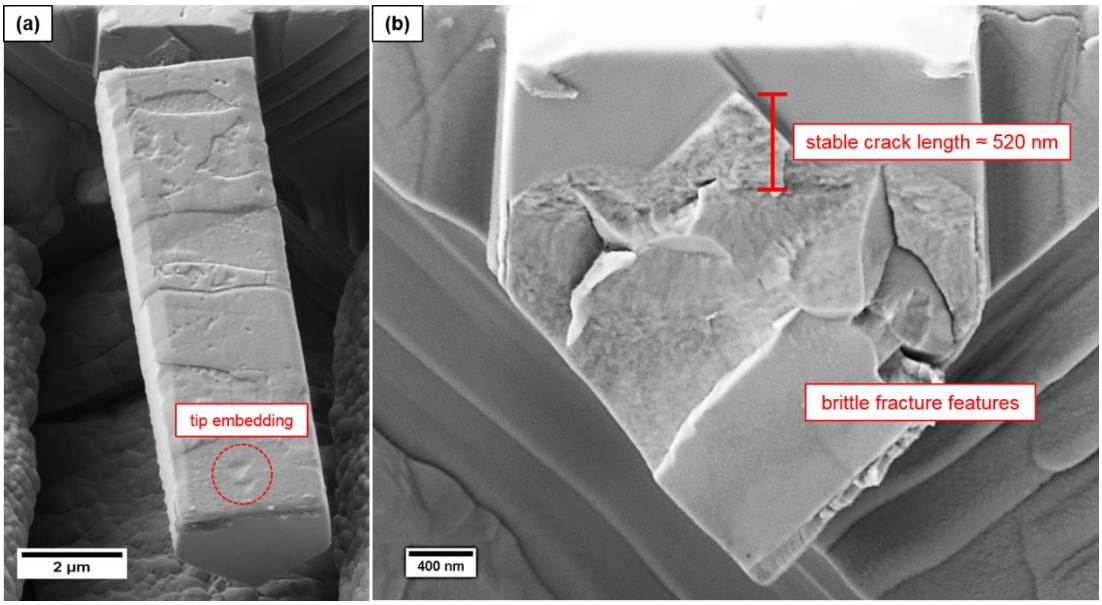


Fig. 5.36 Post-test fractography of cantilever B3, where a distinct borderline between stable and unstable fracture is clearly observed

5.5.2 Cantilever B2 (stable crack growth with ductile fracture surface)

Load-displacement curve of cantilever B2 is shown in **Fig. 5.37**. The cantilever was loaded incrementally to unstable fracture at 536 µN. Similar to cantilever B3, most plasticity and crack growth were again observed before final failure. Cantilever stiffness were calculated using the tip embedding corrected load-displacement curve, which is shown in **Fig. 5.38**. Approximately 370 N/m of stiffness drop was measured before unstable failure. The stiffness

drop were converted to crack length using **Eq. 5.7**. The estimated stable crack length for cantilever B2 is approximately 530 nm.

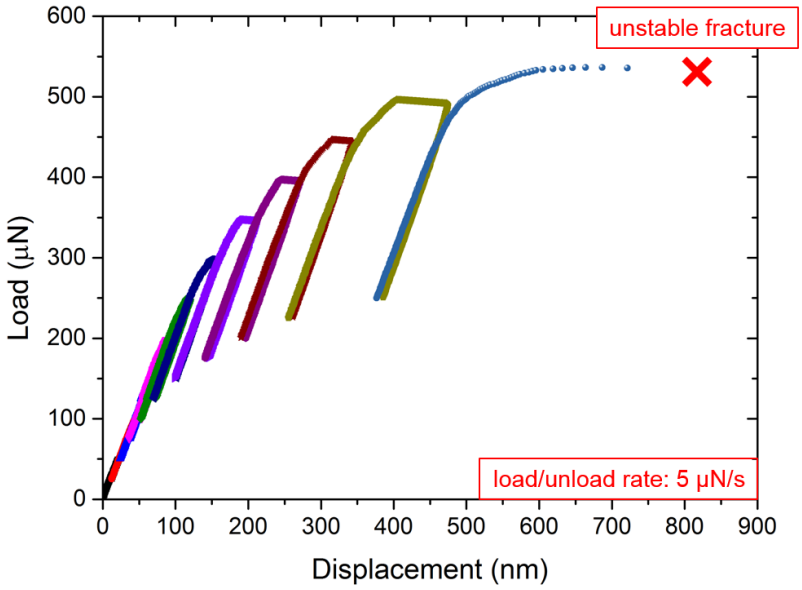


Fig. 5.37 Load-displacement curve of cantilever B2, using load increment of 50 μN

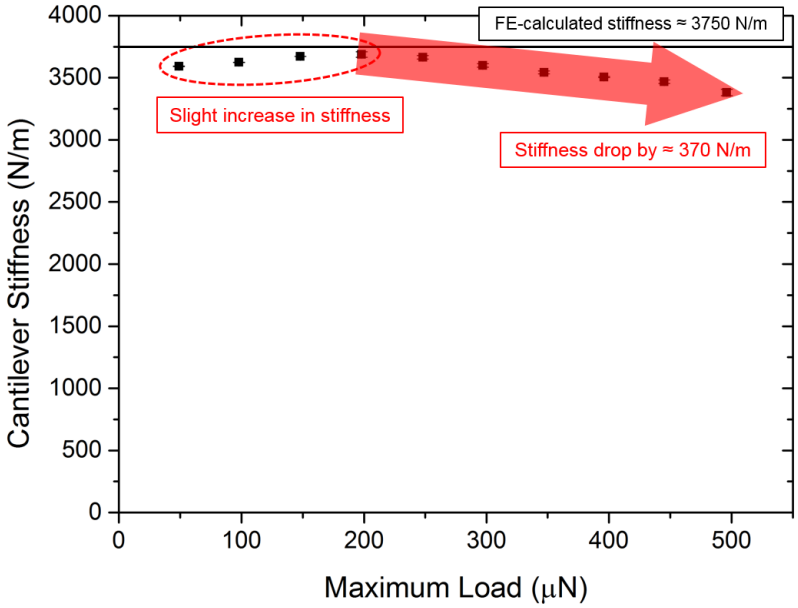


Fig. 5.38 Stiffness of cantilever B2 calculated from the tip embedding corrected load-displacement curve. About 370 N/m of stiffness drop was measured before unstable failure

SEM fractography for cantilever B2 is shown in **Fig. 5.39**, where the fracture surface is mainly dominated by ductile dimple-like fracture features. The small bridging ligament at the chevron apex is evidence for the possible overloading, due to the additional load that was required to tear the ductile ligament. This is a possible explanation of the early termination of the stable crack growth and leads to the consequential crack instability, even when the dominating fracture mechanism is ductile (from fracture surface). The stable crack length measured from the fracture surface was also in good agreement with the values estimated from the stiffness drop.

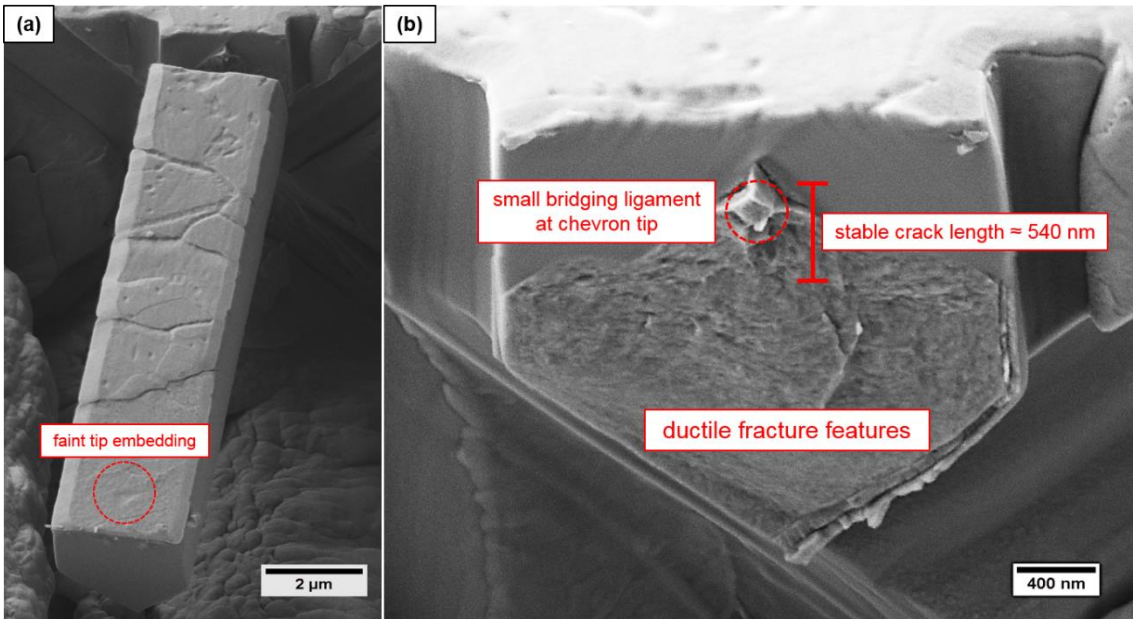


Fig. 5.39 Post-test fractography of cantilever B2. Fracture surface is mainly dominated by ductile dimple-like fracture features with no distinct borderline between stable and unstable fracture. The ductile bridging ligament is observed at the chevron top apex

5.5.3 Cantilever B1 (no stable crack growth, fracture along grain boundary)

Load-displacement curve of cantilever B1 is shown in **Fig. 5.40**. It was loaded incrementally to unstable fracture at 997 μN. Due to the slightly larger cantilever width (3.1 μm), the stiffness measured are higher (~3900 N/m) compared to the stiffness measured from cantilever B2 and B3 (3750 N/m). In contrary to previous cantilevers, only very little plastic deformation and crack growth were observed before unstable fracture. Hence, stiffness drop was not detectable before unstable fracture, shown in **Fig. 5.41**.

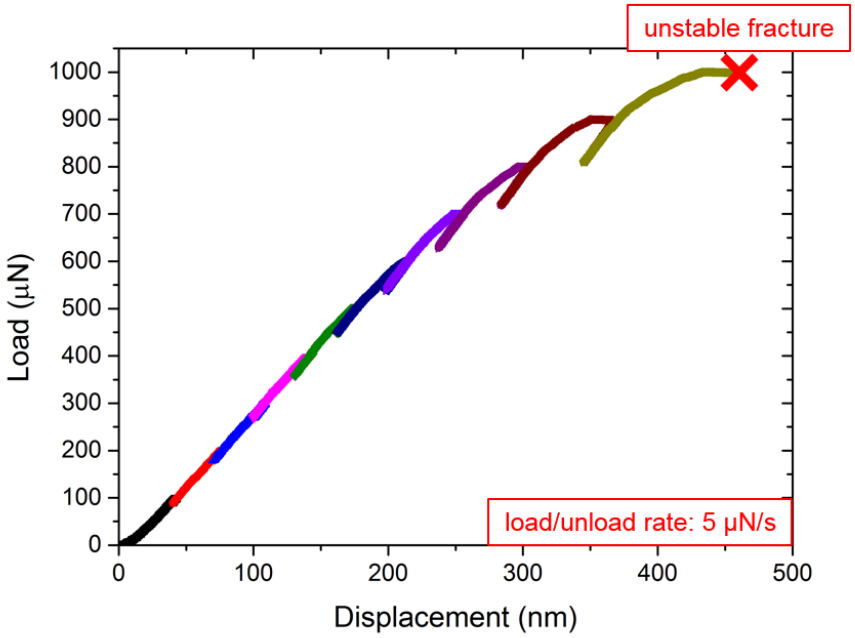


Fig. 5.40 Load-displacement curve of cantilever B1, using a larger load increment (100 μN)

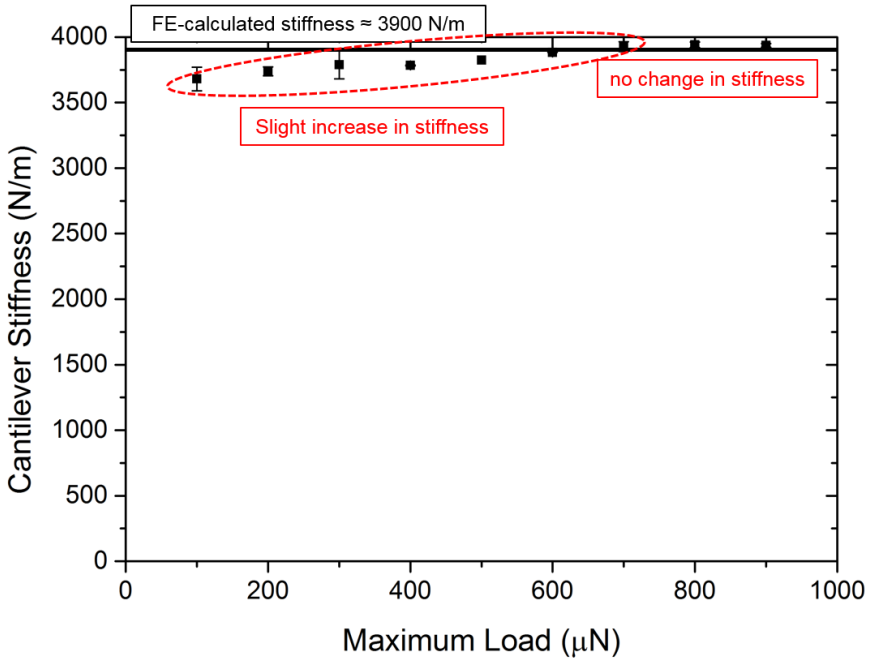


Fig. 5.41 Stiffness of cantilever B1 calculated from the tip embedding corrected load-displacement curve. The higher stiffness (3900 N/m) was due to the larger cantilever width

Post-test SEM fractography of cantilever B1 are shown in **Fig. 5.42**. The fracture surface is mainly dominated by the facet-like intergranular features, with some bridging ligaments near the top chevron apex, shown in **Fig. 5.42(c)**. Once the crack initiated at the top apex, it immediately ran into a weak grain boundary and caused the unstable fracture, shown in **Fig. 5.42(b)**. The small amount of non-linearity observed in the load-displacement curve was probably associated with the tearing of the ductile ligaments, resulting the overloading and consequential unstable fracture.

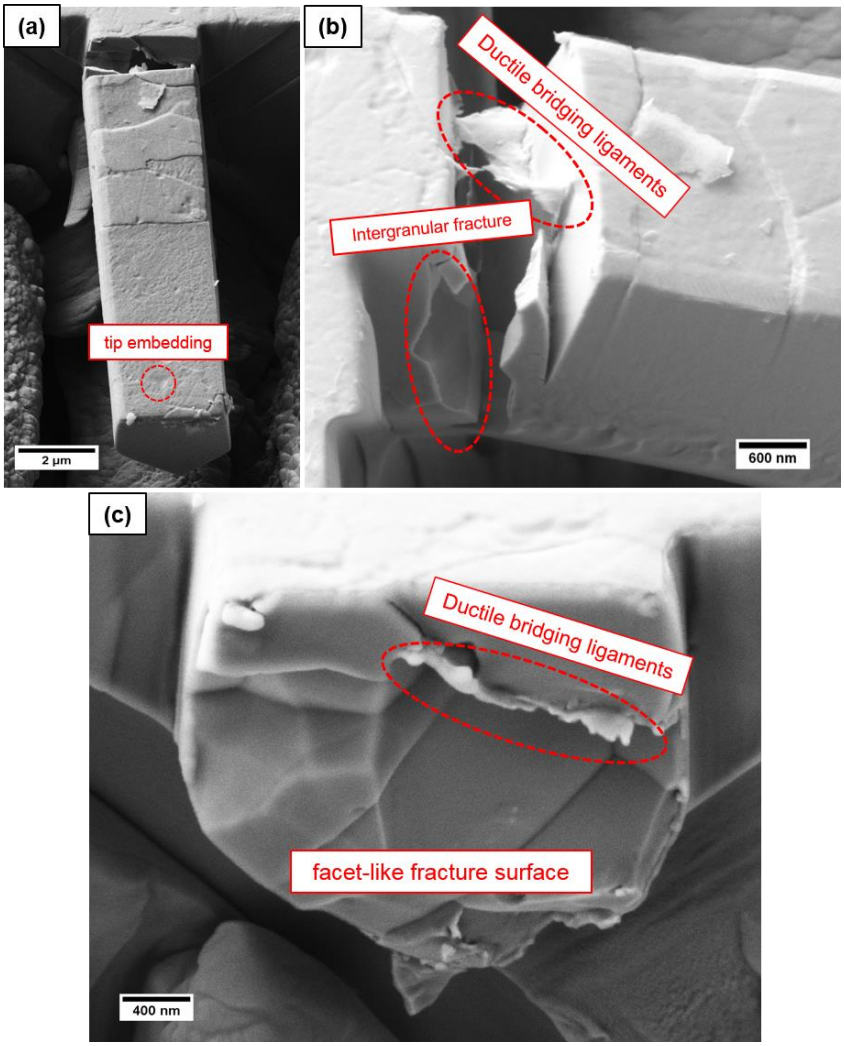


Fig. 5.42 Post-test fractography of cantilever B1. The crack ran into a weak grain boundary after initiation, causing the consequential unstable fracture

5.5.4 Tests Summary

Results of three chevron-notched W-1%Ta cantilevers are summarised in **Table 5.7**. Chevron notched cantilever provided sensible amount of stable crack growth before unstable fracture (cantilever B2 & B3), and eliminated the need for pre-cracking (real crack was used for fracture mechanical analysis). It also provided the opportunity for detailed EPFM analysis, because the stable crack length were measured quantitatively via the optimised load partial-

unload method. In order to compare microscopic fracture toughness results with macroscopic results, both LEFM and EPFM analysis will be used to calculate the linear-elastic fracture toughness K and the elastic-plastic fracture parameter, the J-integral.

Cantilever	Unstable Fracture Load (μN)	Stiffness Drop (N/m)	Stable Crack Length (nm)
B1	997	X	X
B2	536	370±4	525±10
B3	643	360±5	507±12

Table 5.7 Test summary of cantilever B1, B2, and B3, where the stable crack length is calculated from the stiffness drop

5.6 Fracture Mechanical Analysis

5.6.1 Linear-Elastic Fracture Mechanics – Methodology & Analysis

Linear-elastic fracture mechanical (LEFM) analysis was first used to calculate the critical plane-strain fracture toughness K_{Ic} ($MPa \cdot m^{0.5}$) for three cantilevers. The non-dimensional stress intensity factors (Y) were obtained from a FE-modelled cantilever with similar notch geometry (α_0=0.1, α_1=0.9). The relationship between Y and the normalised crack length α are shown in **Fig. 5.43** and **Eq. 5.8**. The chevron notch allowed the crack to initiate at a very small load and grow stably until the critical crack length α_c is reached, where the Y is also at its minimum $Y_{min.}$ Both α_c and Y_{min} were known *a priori* from the FE model, and the only experimental parameter required to calculate the LEFM K_{Ic} using **Eq. 5.9** is the unstable fracture load P_c. However, LEFM analysis is only applicable when the material exhibits a flat R-curve behaviour, which is not the case for the semi-brittle tungsten and will be demonstrated later via the EPFM analysis. Therefore, the LEFM K_{Ic} were only suitable as the lower bound fracture toughness value for tungsten micro-cantilevers.

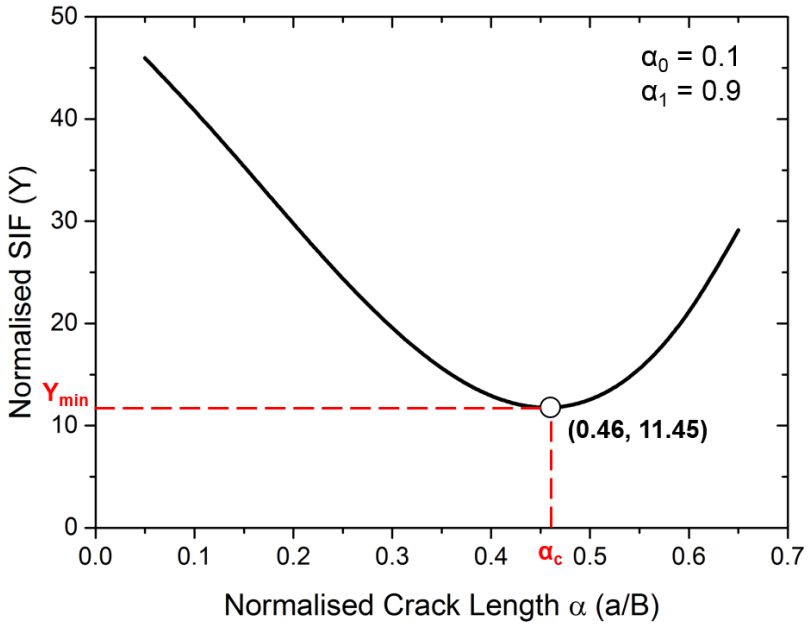


Fig. 5.43 Non-dimensional SIF (Y) vs. normalised crack length (α), showing the geometry-dependent α_c and Y_{min} for a specific chevron notch geometry

$$Y = 425.1\alpha^3 - 229\alpha^2 - 74.5\alpha + 50.2 \ (\boldsymbol{Eq.5.8})$$

$$K_{Ic} = \frac{P_c}{B\sqrt{W}} Y_{min} \ (\boldsymbol{Eq.5.9})$$

where α is the normalised crack length, B and W are the cantilever thickness and width, P_c is the unstable fracture load, Y_{min} the minimum non-dimensional SIF

K_{Ic} calculated using **Eq. 5.9** are plotted in **Fig. 5.44**. The results were relative close to the macroscopic value of 5 MPa·m$^{0.5}$ [108] (calculated from EDM-notched, four-point bending W-1%Ta matchsticks), but were slightly higher than Gibson's microscopic value of ~2 MPa·m$^{0.5}$ (calculated from straight-notched W micro-cantilevers). The overloading effect due to the bridging ligaments in cantilever B1 was captured, showing slightly higher K_{Ic} of 8.6 MPa·m$^{0.5}$

(fracture load was considerably higher than cantilever B2, B3). However, LEFM neglects any plastic work that contributes to the crack extension. Whereas in cantilever B2 and B3, stable crack growth were always accompanied by considerable amount of plasticity, therefore K_{Ic} for B2 and B3 should only serve as the lower bound fracture toughness. Stable crack length measured from three cantilevers were also much shorter than the FE-estimated stable crack length of 1380 nm (α_c=0.46), possibly due to: **(1)** overloading due to the bridging ligaments which led to early termination of the stable crack growth regime, and **(2)** rounded chevron edges due to FIB re-deposition (shown in **Fig 4.12**) which reduced the stable crack growth regime.

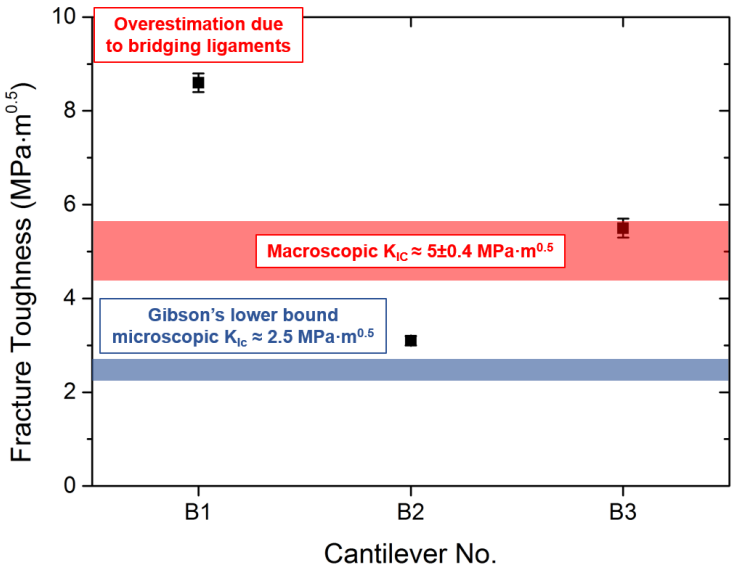


Fig. 5.44 LEFM K_{Ic} calculated from three chevron-notched cantilevers

5.6.2 Elastic-Plastic Fracture Mechanics - Methodology

Mentioned previously, stable crack growth in cantilever B2 and B3 were accompanied with considerable amount of plastic deformation, so LEFM analysis should only serve as the lower bound fracture toughness values for the semi-brittle tungsten. EPFM analysis, on the other

hand, takes into account of both elastic and plastic work that contributed to the crack extension, using the fracture parameter J-integral [37]. Details of the current standard for measuring the J-integral from ductile metallic materials are described in ASTM E 1820 [35], where the J-integrals are calculated as a function of the crack length to construct a fracture resistance curve (J-R curve). This method requires detailed information of the crack length during stable crack growth. Here, this can be captured naturally via the stable chevron notch geometry and the load partial-unload method. Consequently, the J-R curve and critical J value for describing crack instability are obtained.

The J-integral at each crack length $J_{(i)}$ is divided into the elastic and plastic components, shown in **Eq. 5.10**. The elastic component $J_{el(i)}$ was calculated using the LEFM equation given in **Eq. 5.11**. This is similar to the previous section, where the SIF $Y_{(i)}$ and fracture load $P_{(i)}$ at each crack length were used to calculate the linear-elastic $K_{(i)}$. With the assumption that the crack front is straight, and crack surfaces are fully open and continuous (i.e. no bridging ligaments). The plastic component $J_{pl(i)}$ can be calculated in term of fracture energy, using the work-of-fracture (WOF), which is the area under the load-displacement curve $A_{pl(i)}$, and the crack surfaces created during each cycle. Due to the well-defined chevron notch geometry, the crack surfaces were calculated conveniently using the estimated crack length $a_{(i)}$ and the crack front $B_{(i)}$, both obtained from the stiffness drop. The constant η was to take into account the two crack surfaces created [35]. To compare with the macroscopic K, the J-integrals at crack instability were converted to the conditional fracture toughness K_{Qc} (assumed plane-strain condition), using **Eq. 5.12**. Schematic load-displacement curve and the corresponding crack surfaces opened are shown in **Fig. 5.45** to illustrate the EPFM analysis.

$$J_{(i)} = J_{i,elastic} + J_{i,plastic} = \frac{K_{(i)}^2(1-\nu^2)}{E} + \frac{2\eta A_{pl(i)}}{\left[B_{(i)}a_{(i)} - B_{(i-1)}a_{(i-1)}\right]} \quad (\boldsymbol{Eq.5.10})$$

$$K_{(i)} = \frac{P_{(i)}}{B\sqrt{W}} Y_{(i)} \quad (\boldsymbol{Eq.5.11})$$

$$K_{Q(i)} = \sqrt{\frac{J_{(i)}E}{(1-\nu^2)}} \quad (\boldsymbol{Eq.5.12})$$

where E is the elastic modulus 410 GPa, , ν is the Poisson's ratio 0.3, η is the constant 2

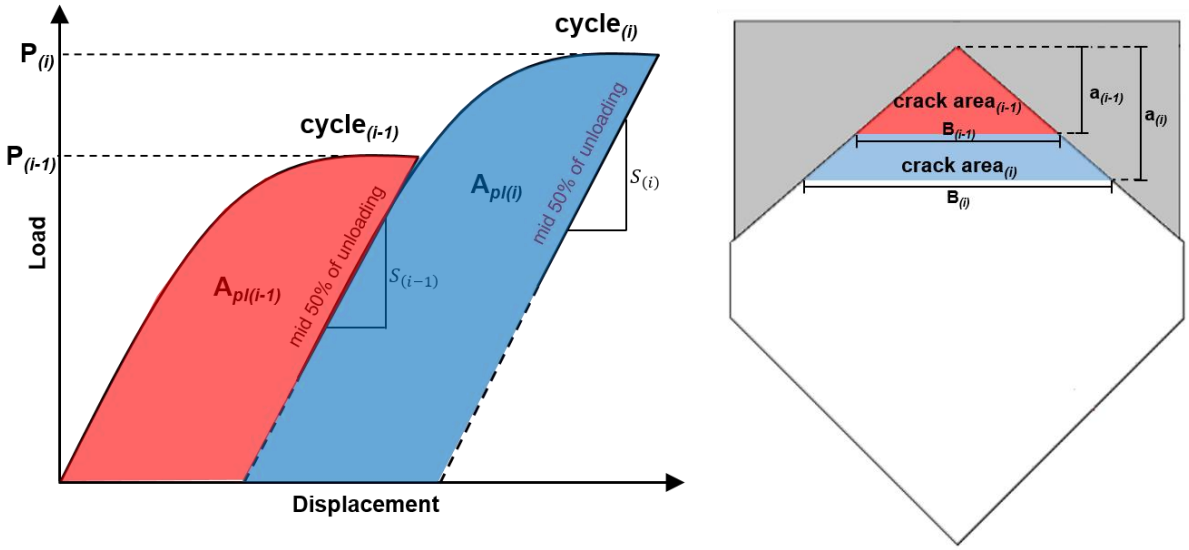


Fig. 5.45 Schematic load-displacement curves and chevron geometry used in the EPFM analysis. Cantilever stiffness $S_{(i)}$, fracture load $P_{(i)}$, WOF $A_{pl(i)}$ (shaded area under the LD curve), crack length $a_{(i)}$, and crack front $B_{(i)}$ are labelled

5.6.3 Elastic-Plastic Fracture Mechanics - Analysis

Detailed EPFM analysis procedures are listed below. Elastic-plastic fracture parameters for cantilever B2 and B3 are given in **Table 5.8** and **5.9**, and the fracture resistance curves (J-R curves) are shown in **Fig. 5.47**

(1) Cantilever stiffness at each cycle was measured using the load partial-unload method

(2) Crack length was calculated using the stiffness vs. crack length relationship from **Eq. 5.7**

(3) SIFs at each crack length were calculated using the SIF vs. normalised crack length relationship from **Eq. 5.8**

(4) Fracture load at each crack length were assumed to be the maximum load of each cycle

(5) The linear-elastic term K at each crack length were calculated using **Eq. 5.11**, and were converted to $J_{elastic}$ using the first half of **Eq. 5.10**

(6) WOF of each cycle were calculated by integrating the area under the load-displacement curve (excluding the elastic contribution, which is the triangular area)

(7) Crack surface area was calculated using the crack length and crack front from each cycle

(8) $J_{plastic}$ at each crack length were calculated using the second half of **Eq. 5.10**

(8) J_{total} at each crack length were calculated by combining $J_{elastic}$ and $J_{plastic}$

(9) J_{total} at each crack length were converted to the conditional fracture toughness K_Q using **Eq. 5.12**

Cycle	Fracture Load (μN)	Crack Length (nm)	SIF	WOF (μN·nm)	Crack Area (nm^2)	K ($MPa \cdot m^{0.5}$)	J_{el} (J/m^2)	J_{pl} (J/m^2)	J_{total} (J/m^2)	K_Q ($MPa \cdot m^{0.5}$)
4	198	165±16	45.5	0	6850	1.7±0.4	6.7	0	6.7±0.4	1.7±0.4
5	248	198±12	44.4	2388	8700	2.1±0.3	10	274	284±11	11.3±1.6
6	297	291±15	41.2	8614	9450	2.4±0.1	12.3	912	924±38	20.4±2.7
7	347	357±14	38.9	12551	10752	2.6±0.2	14.9	1234	1249±45	23.7±3.1
8	396	399±13	37.3	18400	13400	2.8±0.2	17.9	1373	1391±37	25±2.7
9	445	438±10	35.8	28067	19200	3.1±0.2	20.9	1462	1483±33	25.8±2.6
10	496	525±10	32.6	58200	38725	3.1±0.1	21.5	1502	1524±26	26.2±2.3

Table 5.8 EPFM-calculated fracture parameters for cantilever B2

Cycle	Fracture Load (μN)	Crack Length (nm)	SIF	WOF (μN·nm)	Crack Area (nm^2)	K ($MPa \cdot m^{0.5}$)	J_{el} (J/m^2)	J_{pl} (J/m^2)	J_{total} (J/m^2)	K_Q ($MPa \cdot m^{0.5}$)
18	540	105±11	47.3	0	5900	4.7±0.4	48.7	0	48.7±0.7	4.7±0.4
19	570	150±12	46	3360	7815	4.8±0.3	51.1	430	481±19	14.7±1.7
20	600	174±15	45.2	5327	8314	5±0.3	54.8	641	695.5±34	17.7±2.2
21	630	201±13	44.3	8850	9978	5.1±0.3	58.1	887	945.1±29	20.6±2
22	660	231±17	43.3	11750	10500	5.2±0.2	60.9	1119	1180±31	23.1±2.7
23	690	258±12	42.4	13530	11000	5.4±0.3	63.7	1230	1294±36	24.1±2.3
24	720	297±11	41	17210	13280	5.4±0.1	65	1296	1361±32	24.7±2.2
25	750	327±13	39.9	19000	14250	5.5±0.2	66.9	1333	1400±50	25.1±2.8
26	780	507±12	33.3	41400	29950	5.5±0.2	67	1382	1449±31	25.4±2.3

Table 5.9 EPFM-calculated fracture parameters for cantilever B3

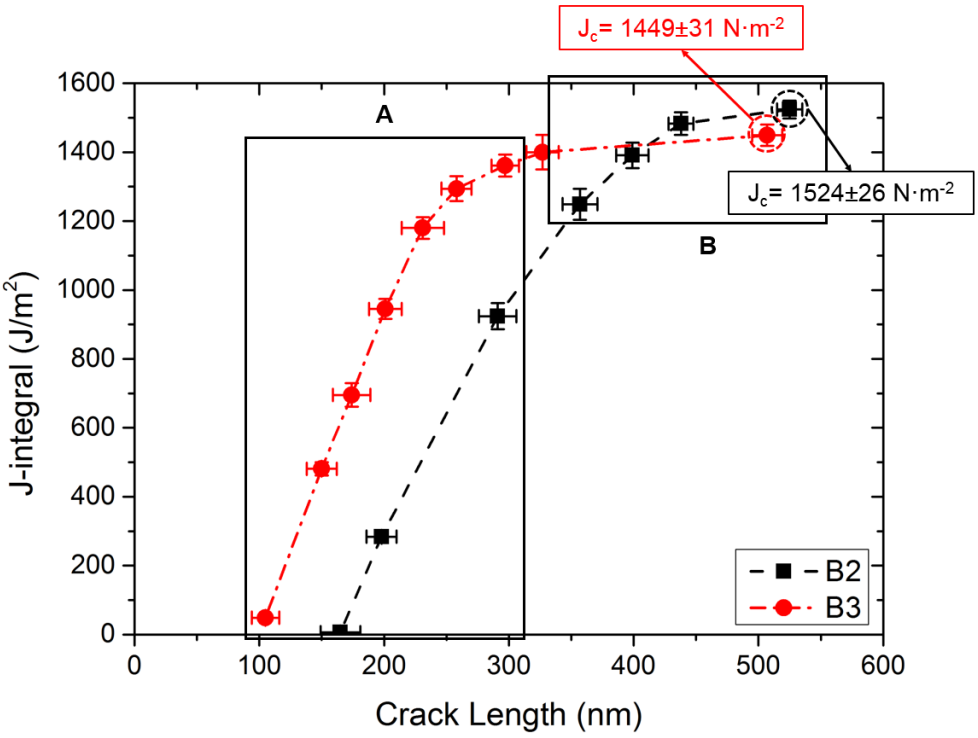


Fig. 5.46 J-integrals vs. crack length plot (J-R curve) for cantilever B2 and B3. Different crack growth stages (A and B) and the critical J at crack instability are labelled

Fracture resistance curves (J-R curves) for two cantilevers are shown in **Fig. 5.46**, exhibiting the typical trend which was consistent with macroscopic J-R curve. The initial slope (stage A) was very steep, as only little crack growth was measured during this region and possibly crack blunting was the dominating mechanism responsible for the sharp increase. J then increased gradually with the stable crack growth until a steady state is reached (stage B), where J almost converged to a constant value. All cantilevers fractured unstably at end of test, therefore, the critical J, J_c, were used to describe the fracture energy for crack instability. The LEFM K_{Ic}, EPFM J_c, the conditional K_{Qc} (converting J_c to K_{Qc} using **Eq. 5.12**), and the ratio between K_{Ic} and K_{Qc} are all summarised in **Table 5.10**.

Cantilever	K_{Ic} (MPa·m$^{0.5}$)	J_c (J/m^2)	K_{Qc} (MPa·m$^{0.5}$)	K_{Ic}/K_{Qc} (%)
B2	5.5±0.2	1524±26	26.2±2.3	21±9.4
B3	3.1±0.1	1447±31	25.4±2.3	12.2±9.6

Table 5.10 EPFM results for cantilever B2 and B3

5.6.4 Fracture Mechanical Analysis Summary

LEFM and EPFM analysis were used to calculate both linear-elastic and elastic-plastic fracture toughness (K_{Ic} & K_{Qc}) from chevron-notched W micro-cantilevers. The results are summarised and compared with macroscopic K_{Ic} in **Fig. 5.47**. LEFM K_{Ic} values are in good agreement with macroscopic values, with the exception for cantilever B1 (overloading due to ductile ligaments). However, due to the larger crack tip plastic zone to specimen size ratio, K_{Qc} are approximately five times higher than macroscopic K_{Ic}. EPFM analysis assumes all plastic work contributes to the stable crack growth, which may not always be the case (i.e. ductile bridging ligaments or creep deformation). From the ductile dimple-like fracture surface of cantilever B2 (and the upper region of cantilever B3), it is reasonable to think that stable crack growth is not fully provided by the stable chevron notch geometry, but also associated with the crack tip plastic zone. This implies that the room temperature microscopic fracture resistance behaviour of W-%Ta is mostly contributed by the specimen size effect. However, in the work by Gludovatz et al. [102], macroscopic fracture tests of polycrystalline pure tungsten also exhibited a fracture resistance behaviour (from fracture initiation value of 6 MPa·m$^{0.5}$ to instability value of 16 MPa·m$^{0.5}$). Therefore, it is reasonable to suggest that our microscopic K_{Qc} are suitable as the higher bound fracture toughness for the semi-brittle W-1%Ta. In addition, the ASTM standard defines several specimen size criterions for valid EPFM values, which should also be

considered. The next section will discuss on the validity of the EPFM K_{Qc}, using the specimen size criterions provided by the ASTM standard.

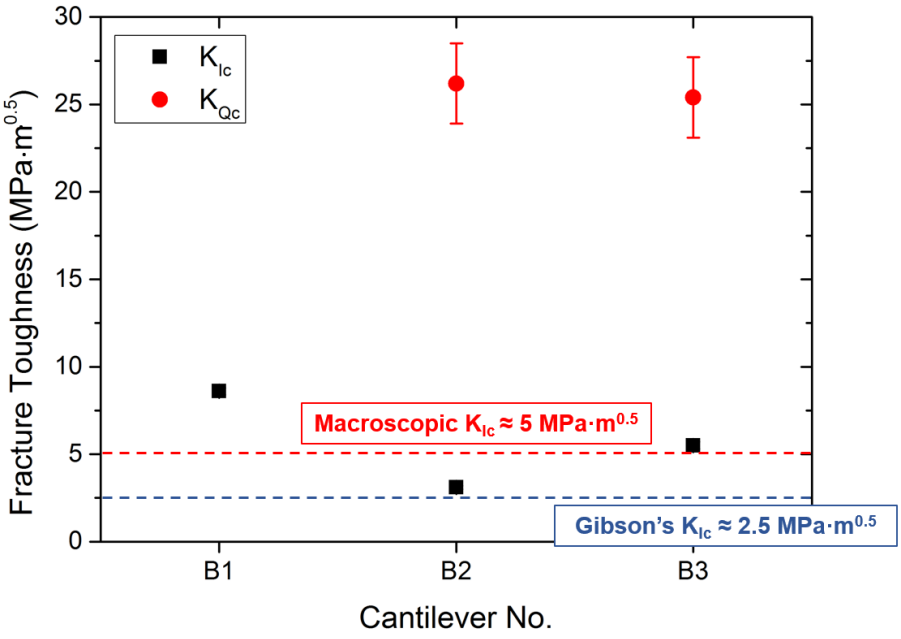


Fig. 5.47 Summaries of K_{Ic} (both micro/macroscopic) and K_{Qc} values for three cantilevers

5.6.5 Specimen Size for Elastic-Plastic Fracture Mechanical Analysis

The size requirement for K_{Qc} provided in ASTM standard is to ensure that the specimen has sufficient crack tip stress triaxiality [35], and decreasing the specimen size to the micrometre regime will not significant affect the triaxiality state. For valid K_{Qc} value, ASTM E 1820 defines a minimum specimen size requirement using **Eq. 5.13** [113], where B is the specimen thickness, b_o is the initial ligament size, $\boldsymbol{\lambda}$ is a dimensionless constant of 100, and σ_{ys} is the yield stress.

$$B, b_0 \geq \frac{\lambda J_Q}{\sigma_{ys}} \quad (\boldsymbol{Eq.\,5.13})$$

Take cantilever B2 as an example, using σ_{ys} of 5.2 GPa (obtained from previous elasto-plastic cantilever) and J_{Qc} of 1524 N/m, the minimum value for cantilever thickness is about 32 μm. Similarly, the minimum thickness for B3 is about 28 μm. The actual cantilever thickness is only 3 μm, which is significantly smaller than the given size criterion, hence making the EPFM K_{Qc} values invalid. Converting the LEFM K_{Ic} of cantilever B1 to J_{Qc} (160 N/m) using **Eq. 5.12**, the lower limit for cantilever thickness is about 3 μm. This is close to the actual cantilever thickness (2.8 μm) and hence validates the K_{Ic} calculated from cantilever B1. The second validity criterion for K_{Qc} is the maximum allowable stable crack growth prior to stable fracture, defined using **Eq. 5.12**. However, this criterion is not applicable to micro-fracture experiments, as the crack length measured here is in the nanometre regime; Δa will always be smaller than the given criterion.

$$\Delta a < 0.2mm + \frac{J_{Qc}}{M\sigma_y} \quad (\boldsymbol{Eq.\,5.12})$$

where M is another dimensionless constant of 2

5.7 Summary of the Room Temperature Cantilevers

Crack stability of chevron-notched W-1%Ta micro-cantilevers and crack length measurements were successfully demonstrated in this chapter. Both LEFM and EPFM analysis were used to calculate for K_{Ic} and K_{Qc}, and the values were discussed using post-test fracture surface analysis and the ASTM 1820 standard specimen size criterion. It is still impossible for cantilevers B2 and B3 to obey the EPFM specimen size criterions, hence making the K_{Qc} values not directly comparable with macroscopic K_{Ic} values (5~16 MPa·$m^{0.5}$). This suggests that the true fracture toughness for the semi-brittle W-1%Ta micro-cantilever is probably between the LEFM K_{Ic} (4.3±0.2 MPa·$m^{0.5}$) and the EPFM K_{Qc} (25.8±2.2 MPa·$m^{0.5}$).

VI HIGH TEMPERATURE MICRO-FRACTURE TESTS OF W-1%TA MICRO-CANTILEVERS

This chapter will first present the improved temperature matching procedures for high-temperature nanoindentation. Temperature mismatch between the indenter and sample is of most concern for stable high-temperature tests, and the consequential thermal drift can significantly affects the displacement measurements and surface scans. Results from chevron-notched W-1%Ta micro-cantilevers up to 700 °C are presented, and EPFM analysis were used to calculate the fracture resistance curves and conditional fracture toughness values for crack instability. Effects of temperature to fracture behaviour and the brittle-to-ductile transition are also discussed via dislocation activity and fracture surface analysis.

6.1 Thermal Drift Effects in High-Temperature Micro-Fracture Tests

Degradation of indenter materials during high-temperature nanoindentation was already discussed in **Chapter 3**. Moreover, because the indenter only acted as a loading apparatus in cantilever tests, therefore maintaining a well-defined indenter shape was not strictly required for displacement measurements, assuming the indenter was not blunted significantly (compared to the cantilever displacement). Thermal drift, on the other hand, has a decisive effect on both displacement measurements and surface scanning quality. Examples were used to demonstrate the deleterious effects and a suggested maximum drift rate is defined as criterion for excellent thermal stability.

6.1.1 Thermal Drift Effects to Displacement Measurements

Two cases were used to demonstrate the thermal drift effect to displacement measurements. In one extreme case, the indenter was initially hotter than the sample by 50 °C. During loading, the hot indenter heated the cold sample up and introduced localised thermal expansion, which caused the indenter to retract from the sample surface, even when the indenter load was continually being ramped up. Load-displacement curve from this intentionally-mismatched test is shown in **Fig. 6.1**, where the indenter retraction is observed after 60 nm of penetration. Both pre- and post-indentation (still in contact with sample) thermal drift data are also given in **Fig. 6.2**. As heat flow were transferred continuously from the indenter to the sample during loading, resulting significantly larger post-indentation drift rate. The negative pre-indentation drift rate of -0.16 nm/s indicated the indenter drifting away from the sample, which further increases to -5.8 nm/s during post-indentation due to the larger thermal expansion of the sample (hotter sample).

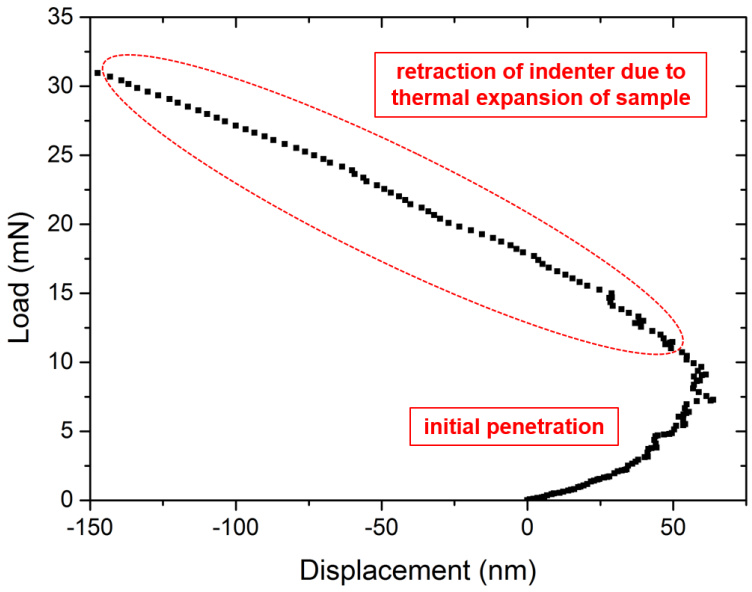


Fig. 6.1 Load-displacement curve of an intentionally temperature mismatched indentation test. The indenter temperature is set higher than the sample by 50 °C

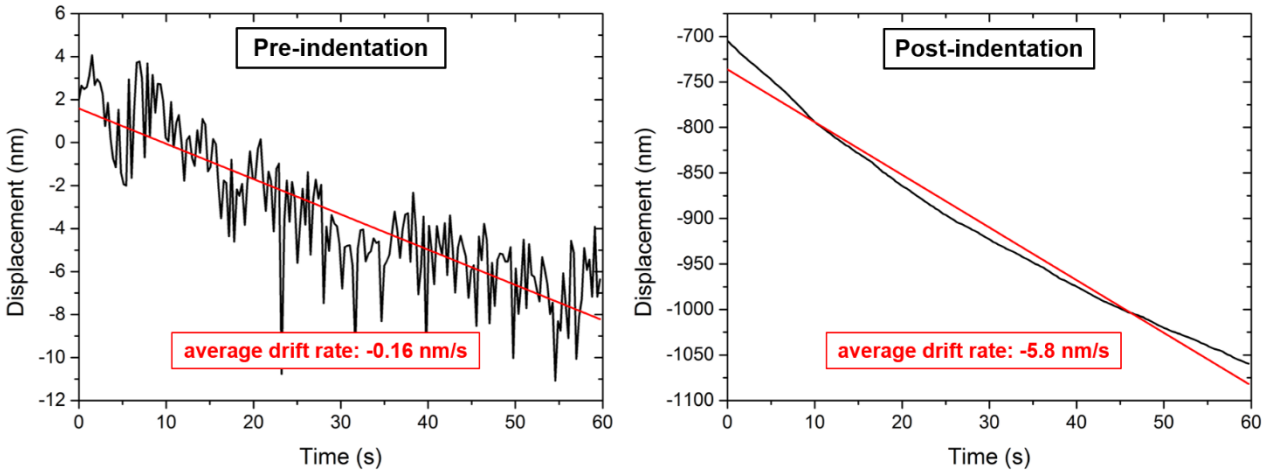


Fig. 6.2 Pre- and post-indentation thermal drift. The average drift rate was calculated as the slope of the fitted linear function (shown in red)

The effect of thermal drift to displacement measurements is also cumulative, especially when test time is long. This accumulative effect was demonstrated previously in section 5.4.2, but is now emphasised again due to the possible larger drift rate at elevated temperatures. In a low-cycle fatigue test, a tungsten cantilever was loaded to 2000 μN (mostly within the elastic regime) and unloaded back to 1000 μN repetitively for 40 times. The loading/unloading rate was set at 10 μN/s. Due to the large number of cycles performed and the relatively low loading rate, it was possible for the thermal drift to accumulate into considerable amount of "false" displacement. Shown in **Fig. 6.3**, a constant displacement difference (~4 nm) is observed between cycles from the as-received load-displacement curve, which was suspected to be an effect arising from the thermal drift. Post-test SEM and AFM scan were performed to measure

the permanent deformation of the cantilever, so that the contribution of thermal drift to displacement measurement could be distinguished.

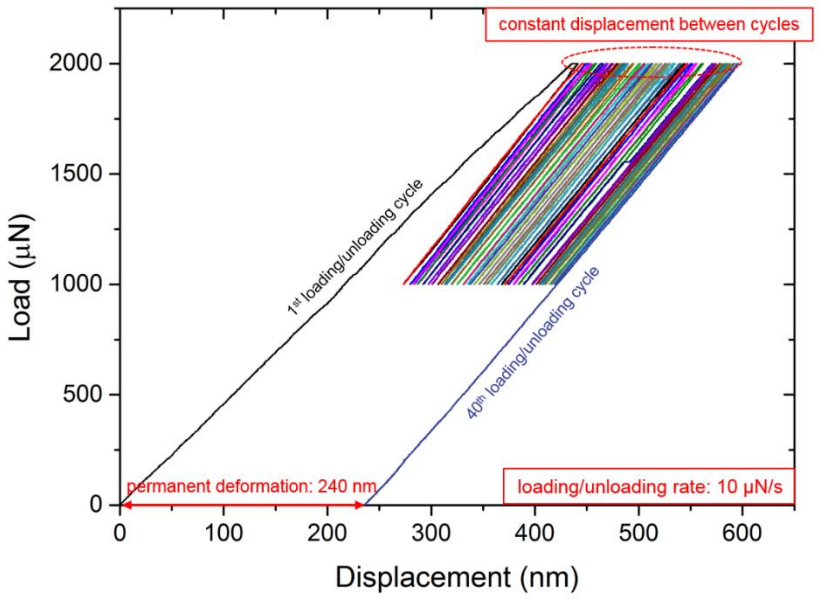


Fig. 6.3 As-received load-displacement curve from the low-cycle fatigued cantilever. Permanent deformation of 240 nm was measured at end of test

Permanent deformation of 240 nm was measured from the as-received load-displacement curve shown in **Fig. 6.3**. However, it is not consistent with the deformation measured from post-test SEM (**Fig. 6.4**) and AFM surface scan (**Fig. 6.5**). The SEM image in **Fig. 6.4** provides no quantitative measurements, whereas 90 nm of bending displacement was measured from the AFM line scan along the cantilever's long axis. Pre-indentation thermal drift, shown in **Fig. 6.6**, has an average drift rate of 0.03 nm/s. The positive drift rate suggests the indenter was slightly colder than the sample. Assuming the drift rate was constant throughout the test, it could contribute approximately 160 nm of false displacement, which was in good agreement with the

displacement discrepancy found between the as-received load-displacement curve and the post-test AFM scan.

It is therefore demonstrated that thermal drift contribution to displacement can be significant and should be taken into account, especially when the test time is long during cyclic loading and fatigue tests, or at elevated temperatures when the drift rate is unavoidably higher. The load-displacement curve from the low-cycle fatigued cantilever was therefore re-calculated using **Eq. 6.1** and replotted in **Fig. 6.7**. In the drift-corrected load-displacement curve, the permanent deformation is mostly found in the first cycle, whereas the latter cycles overlap with each other. The final deformation at the end of test was approximately 80 nm, which is far more consistent with the actual deformation measured via AFM.

$$D_{bend} = D_{ind} - \left(Drift_{pre} \times T\right) \ (\boldsymbol{Eq.6.1})$$

where D_{bend} is cantilever bending displacement, D_{ind} is the displacement measured from the nanoindenter, $Drift_{pre}$ is the pre-indentation thermal drift rate, and T is the time on sample

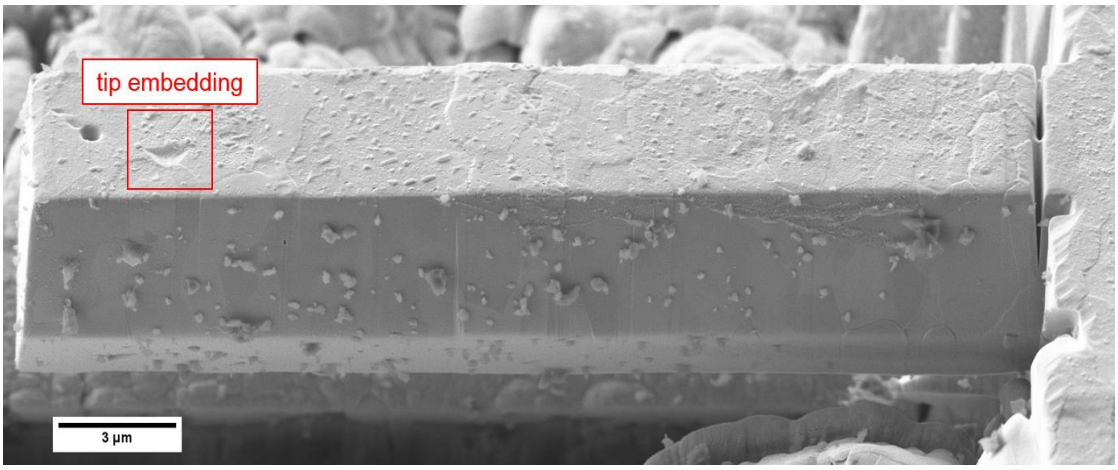


Fig. 6.4 Post-test SEM image of the low-cycle fatigued cantilever. No significant plastic deformation and cracks were observed

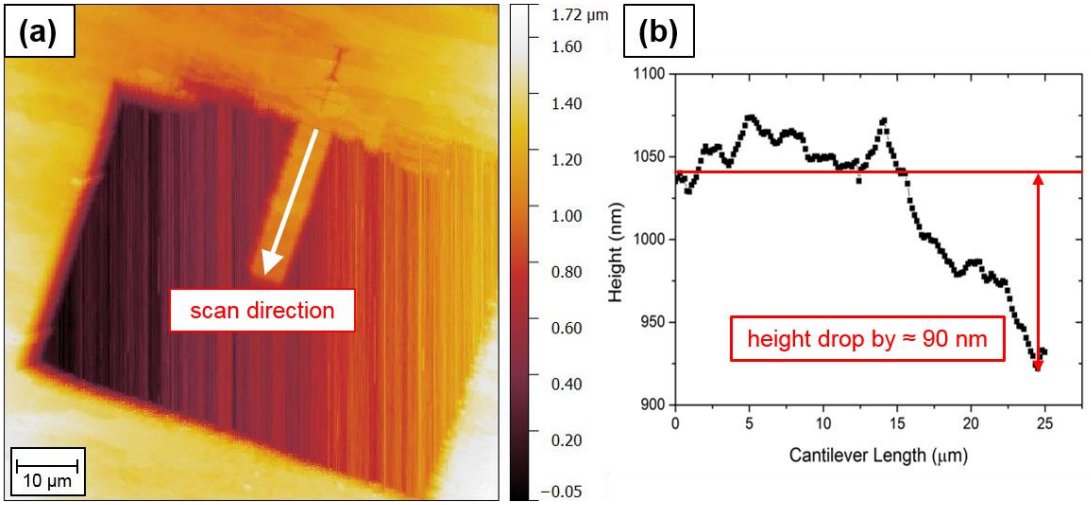


Fig. 6.5 Post-test AFM scan of the cantilever. A line scan (white arrow) was performed along the cantilever's long axis to measure its permanent bending deformation

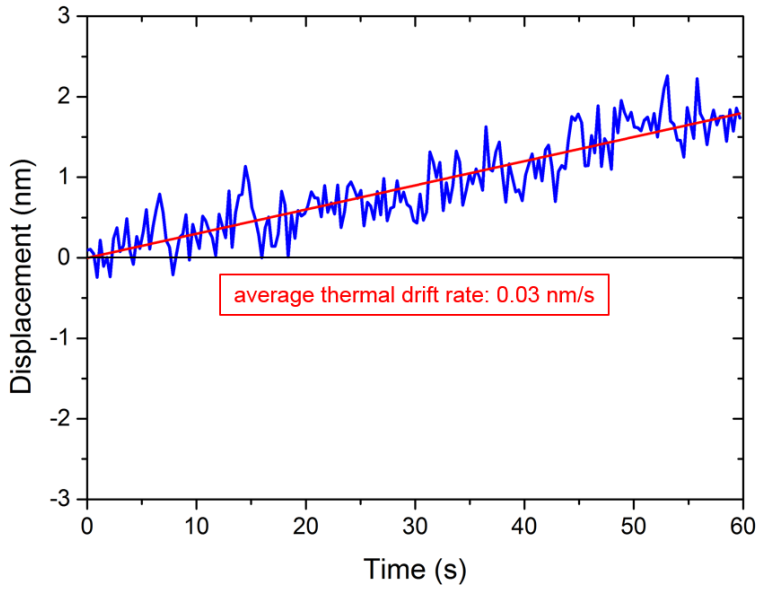


Fig. 6.6 Pre-indentation thermal drift of the low-cycle fatigue test. The positive drift rate (0.03 nm/s) suggests the indenter is slightly colder than the sample

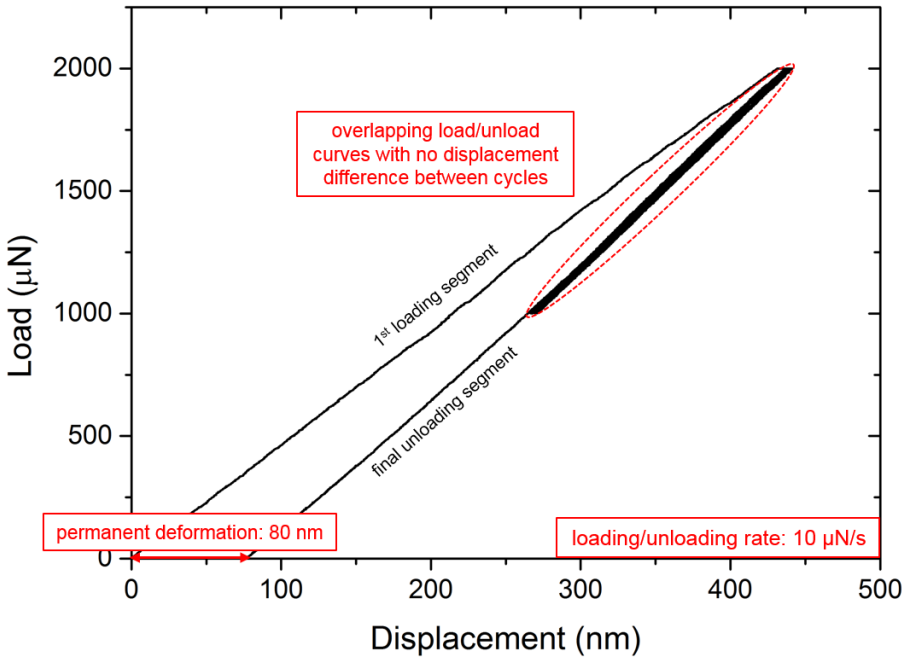


Fig. 6.7 Load-displacement curve of the low-cycle fatigued cantilever, after thermal drift correction. The permanent plastic deformation measured at end of test was about 80 nm, which is consistent with the value measured from the AFM scan

6.1.2 Thermal Drift Effects to Surface Scanning

Thermal drift may also affects the surface scanning quality. Two scans were performed on the same cantilever at 700 °C, one with the intentionally introduced temperature mismatch (left) and one without (right), all shown in **Fig. 6.8**. All experimental parameters, shown in **Table 6.1**, were kept the same except for the indenter temperature to introduce a temperature mismatch of 5 °C. A drift rate of approximately 0.1 nm/s was observed in the 5 °C mismatch scan, where the surface scanning quality was significantly worse, preventing accurate positioning of the loading point. Scan image with better temperature control (right image) was considerably sharper and the corresponding drift rate was 0.03 nm/s. The pre-indentation thermal drift data are given

in **Fig. 6.14**, where a positive slope is observed for the scan with the indenter colder than the sample by 5 °C.

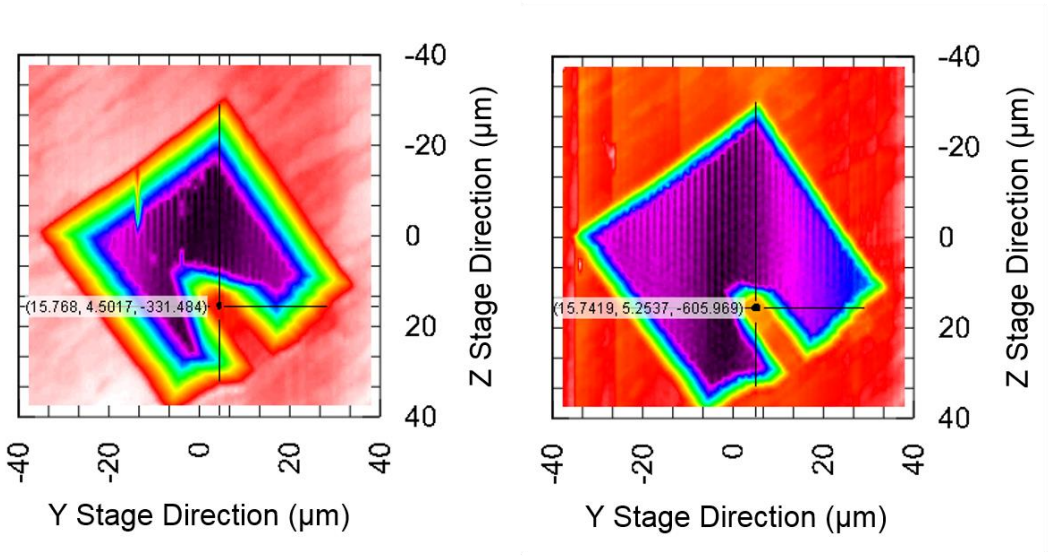


Fig. 6.8 Scans of cantilever M4 at approximately 700 °C

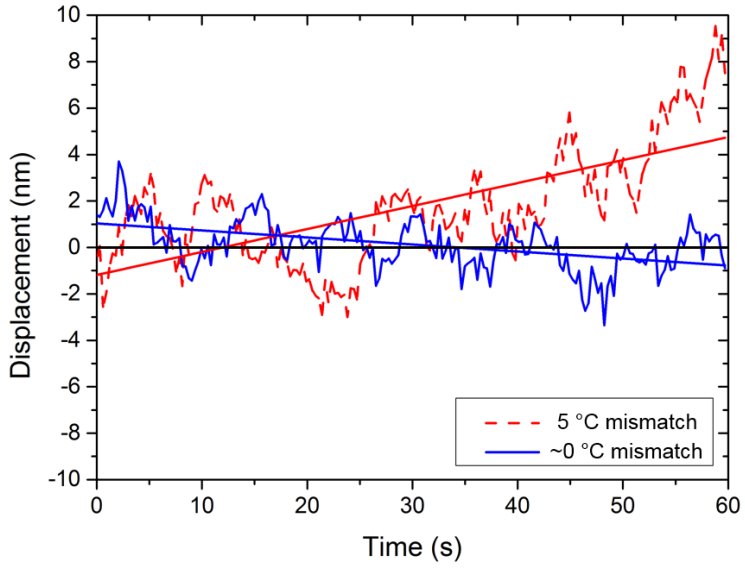


Fig. 6.9 Pre-indentation thermal drift for the two scans. The positive drift (0.1 nm/s) is introduced by the 5 °C mismatch (indenter colder than sample)

Indenter Temp (°C)	Sample Temp (°C)	Scanning Area (μm^2)	Scanning Load (μN)	Step Size (μm)	Thermal Drift (nm/s)
695	700	75 x 75	1	0.75	0.1
700	700	75 x 75	1	0.75	0.03

Table 6.1 Experimental parameters and pre-indentation thermal drift rate for the two scans

6.1.3 Thermal Drift Effects Summary

The examples in this section demonstrated that the indenter and sample temperature have to be nearly perfectly matched in order to minimise the **t**hermal drift effects. Before each test, a protocol was established in which a series of single indents were performed to check the thermal stability from pre-indentation thermal drift data. Pre-indentation thermal drift were measured when the indenter was in contact with the sample, using an initial load of approximately ~0.02 mN (not too large to deform the micro-cantilever, but large enough to maintain contact). Pre-indentation drift can be a good representative measure of the thermal stability, and is not convoluted with thermal creep. Therefore, the slopes of the pre-indentation drift data from indents can be used as a criterions for increasing/decreasing the indenter temperature.

If the slope is negative, the indenter is too hot (thermal expansion of the sample pushes the indenter away); and if the slope is positive, the indenter is too cold (thermal contraction of the sample pulls the indenter towards sample). This is demonstrated in **Fig. 6.10**, where an initial temperature mismatch of 10 °C was intentionally introduced. Indenter temperature is continuously adjusted until the slope flattens out (scattering only due to thermal fluctuation). As demonstrated previously, the surface scan was able to remain sharp when the drift rate is around 0.03 nm/s. This drift rate is defined as a thermal stability criterion. Pre-indentation thermal drift at three temperature regimes (25 °C, 500 °C, 700 °C) are given in **Fig. 6.11**. Although scattering

due to thermal fluctuation increased slightly with temperature, however, all drift rates still fall within 0.03 nm/s. This drift rate criterion is followed by all high-temperature tests performed in this thesis, and as-received load-displacement curves are thermal drift corrected using **Eq. 6.1**.

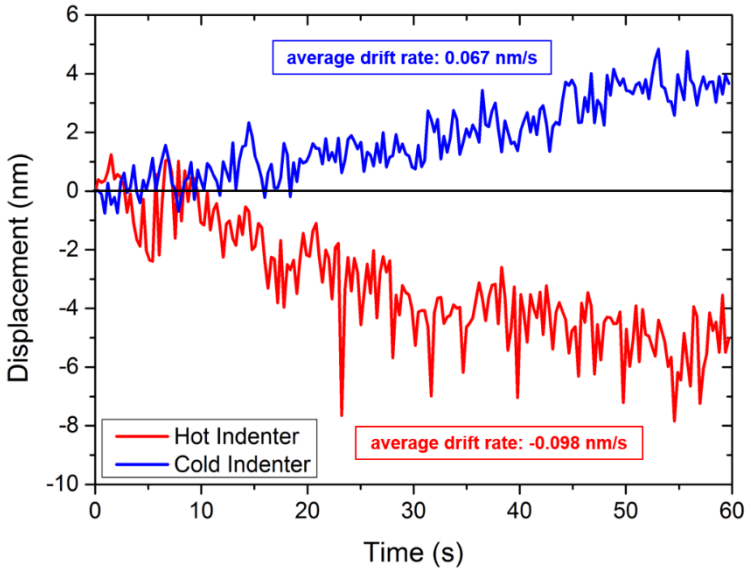


Fig. 6.10 Pre-indentation thermal drift from a temperature mismatch of 10 °C

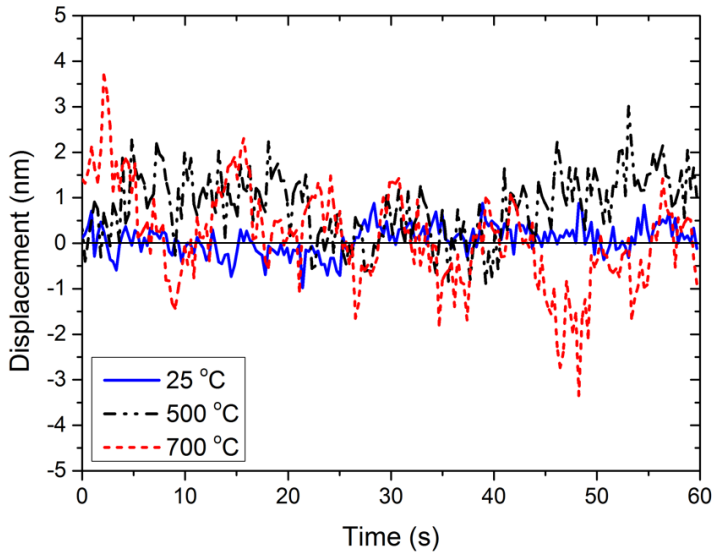


Fig. 6.11 Pre-indentation thermal drift for tests performed at 25 °C, 500 °C, and 700 °C

6.2 High-Temperature Micro-Fracture Tests

High-temperature micro-fracture tests of chevron-notched W-1%Ta micro-cantilevers were performed using the Micro Materials NanoTest Xtreme®. Load-displacement curve, stiffness (calculated using the mid-50% of the unloading curve), and fractography of each cantilever are presented and discussed. Although twelve cantilevers were tested, only four were successful; six fractured during the scanning stage, two fractured at the fixed end rather than at the chevron notch. Therefore, one should be aware of that the success rate for high-temperature micro-fracture tests is low (~30%), even when the thermal drift is minimised.

SEM and EBSD images of the cantilevers, dimensions, and test parameters are given in **Fig. 6.12**, **Table. 6.2** and **Table 6.3**. Slight variation of the cantilever dimensions were due to the unstable FIB source, therefore it was also not possible to follow the optimum chevron notch geometry (α_0=0, α_1=0.7), which was obtained previously in **Chapter IV**. Therefore, the slight dimensional variation, together with tungsten's temperature-dependent modulus, should all be taken into account in the FE-calculated SIFs and beam stiffness.

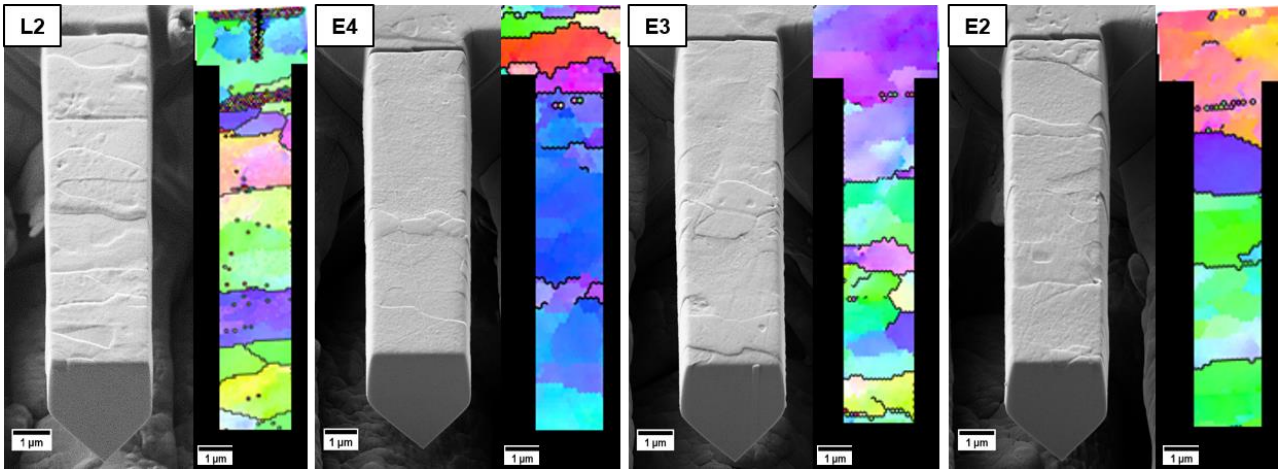


Fig.6.12 SEM/EBSD images of the cantilevers before test (L2, E4, E3, E2)

Cantilever	L (μm)	B (μm)	W (μm)	α_0 (a_0/B)	α_1 (a_1/B)
L2	10.7	2.9	3	0.1	0.9
E4	10.3	2.8	3	0.1	0.7
E3	10.8	2.8	2.9	0	0.7
E2	10.5	2.9	3	0.1	0.7

Table 6.2 Dimensions of the high-temperature tested cantilevers (L x B x W). Note the slight variation in cantilever and chevron notch geometry

Cantilever	Temperature	Loading/Unloading Rate	Load Increment	Hold Time	% to Unload
L2	400 °C	10 μN/s	50 μN	20 sec	50%
E4	500 °C	10 μN/s	50 μN	20 sec	50%
E3	600 °C	10 μN/s	50 μN	20 sec	50%
E2	700 °C	10 μN/s	50 μN	20 sec	50%

Table 6.3 Test parameters for the high-temperature tested cantilevers. The loading/unloading rate was set higher to 10 μN/s to reduce test time, so the contribution of thermal drift was less

6.2.1 Temperature Effects to Modulus, Yield Stress, and Hardness of Tungsten

Elastic moduli were used in FE models as material parameters for calculating the cantilever stiffness for crack length estimation. Nanoindentation hardness (GPa) was used first to provide rough estimation of the yield stress, using Tabor's relationship in **Eq. 6.2** [83]. Yield stress was then be used to estimate the crack tip plastic zone for EPFM analysis validation. Therefore, it is important to know the temperature dependence of both properties. Values from past literatures [114, 115] were used to establish the temperature dependence for both properties. Although literature values were obtained from polycrystalline tungsten, however, one should not

expect much difference in the elastic moduli. Hardness values (hence yield stresses) were only used to provide a rough estimation of the crack tip plastic zone, therefore it was not necessarily to use exact value. The elastic modulus, indentation hardness, and estimated yield stress of tungsten as a function of temperature are summarised in **Fig. 6.18.**

$$H_v = 3\sigma_y \ (\boldsymbol{Eq.6.2})$$

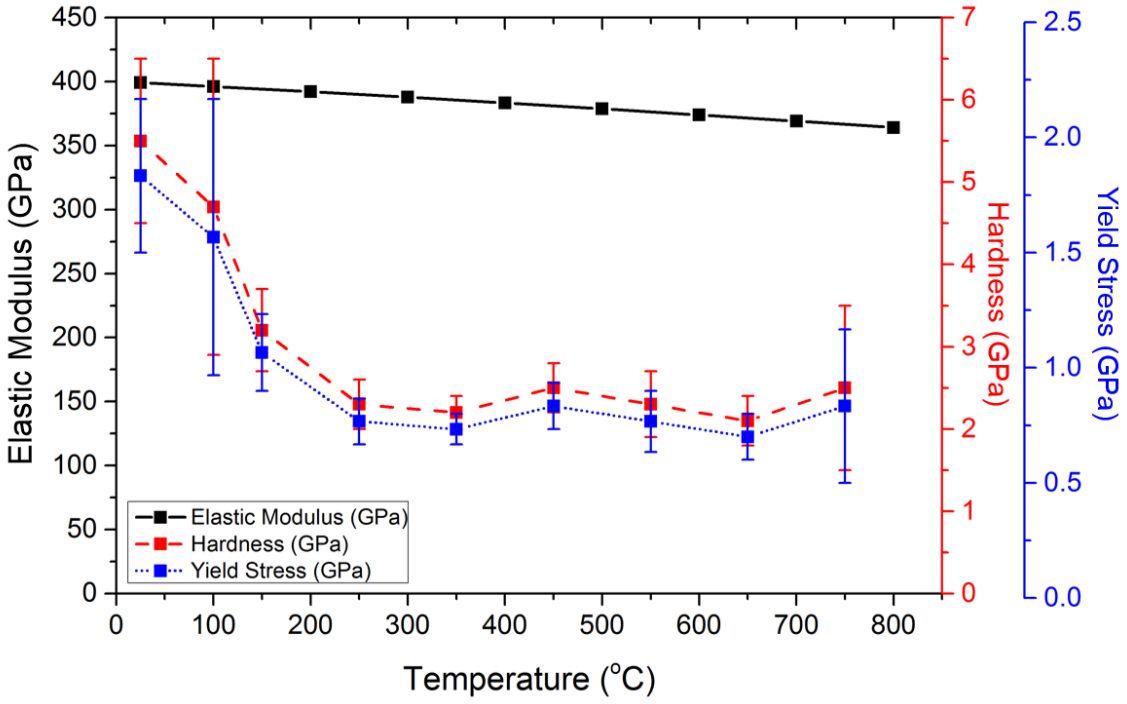


Fig. 6.13 Modulus, hardness, and estimated yield stress of tungsten vs. temperatures

Cantilever stiffness (for crack length estimation), and the non-dimensional SIFs (for LEFM K calculation) were re-calculated to take into account of both: (1) slight variance in cantilever and chevron notch geometry, and (2) drop of modulus. The updated stiffness and SIF vs. crack length plots for each cantilever are given in **Fig. 6.14** and **6.15**, and the critical crack length (α_c) at minimum SIF (Y_{min}) are also listed in **Table 6.4**.

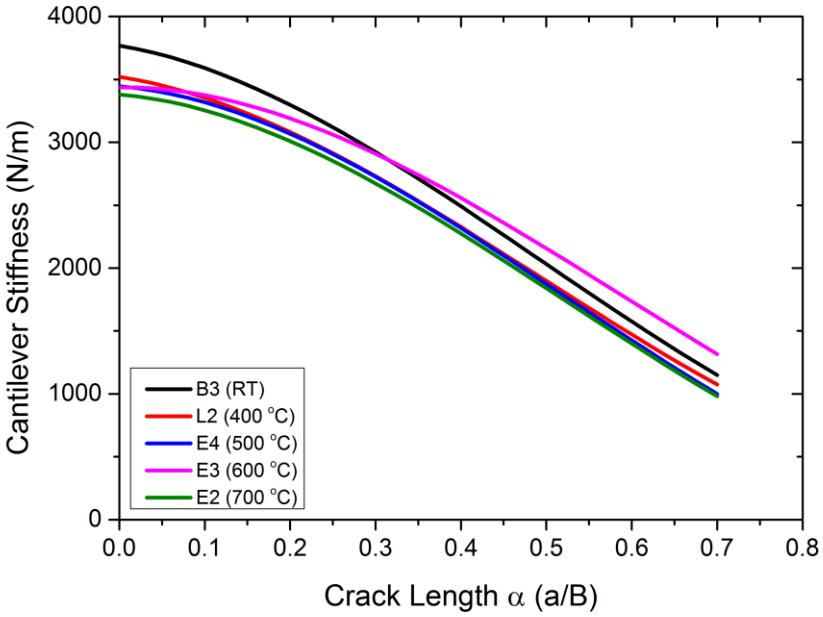


Fig. 6.14 Stiffness vs. normalised crack length for each cantilever

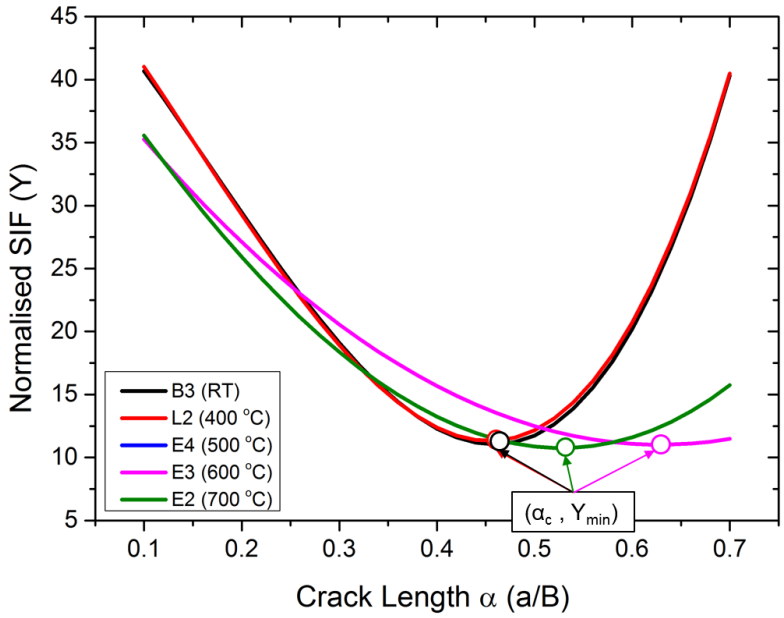


Fig. 6.15 Non-dimensional SIF vs. normalised crack length for each cantilever. The SIF curves for cantilever E4, E2 and B3, L2 overlapped each other due to same chevron notch geometry

Cantilever	Temperature (°C)	Modulus (GPa)	α_c	Y_{min}	Y(α)	S(α) (N/m)
B3	25	400	0.46	11.5	$Y = 452\alpha^3 - 229\alpha^2 - 75\alpha + 50$	$S = 4799\alpha^3 - 7104\alpha^2 - 1119\alpha + 3768$
L2	400	383	0.45	11.5	$Y = 410\alpha^3 – 176\alpha^2 - 93\alpha + 52$	$S = 4483\alpha^3 - 6637\alpha^2 - 1045\alpha + 3520$
E4	500	379	0.53	10.8	$Y = 448\alpha^3 – 224\alpha^2 – 76\alpha + 50$	$S = 5493\alpha^3 - 7880\alpha^2 – 565\alpha + 3445$
E3	600	374	0.62	11	$Y = 452\alpha^3 – 229\alpha^2 – 75\alpha + 50.2$	$S = 4377\alpha^3 - 6480\alpha^2 - 1021\alpha + 3437$
E2	700	369	0.53	10.8	$Y = 452\alpha^3 – 229\alpha^2 – 75\alpha + 50.2$	$S = 4320\alpha^3 - 6395\alpha^2 - 1007\alpha + 3391$

Table 6.4 Numerical values of the critical crack length α_c, minimum SIF Y_{min}, and the SIF and stiffness vs. normalised crack length relationships for each cantilever

Because SIFs were strong functions of the chevron geometry, change in modulus had almost no effect on both α_c and Y_{min}. However, modulus did have an effect on the cantilever stiffness, therefore the newly calculated stiffness vs. crack length relationships are used to estimate the stable crack length for each successfully tested cantilevers.

6.2.2 Micro-Cantilever Tested at 400 °C (L2)

Load-displacement curve of cantilever L2 (400 °C) is shown in **Fig. 6.16**. It was loaded incrementally to ultimate failure at 600 μN. Good thermal stability was demonstrated by the overlapping loading/unloading curves in the elastic regime. Cantilever stiffness were first tip embedding corrected (details see section **5.4.1**), then measured from the mid-50% of each unloading phase (details see section **5.4.4**). Stiffness plotted against the maximum load of each cycle, is shown in **Fig. 6.17**. Stiffness drop, and the estimated stable crack length (using the stiffness vs. crack length relationship provided in **Table 6.4**) are given in **Table 6.5**; a final stable crack length of approximately 657 nm was measured before unstable fracture.

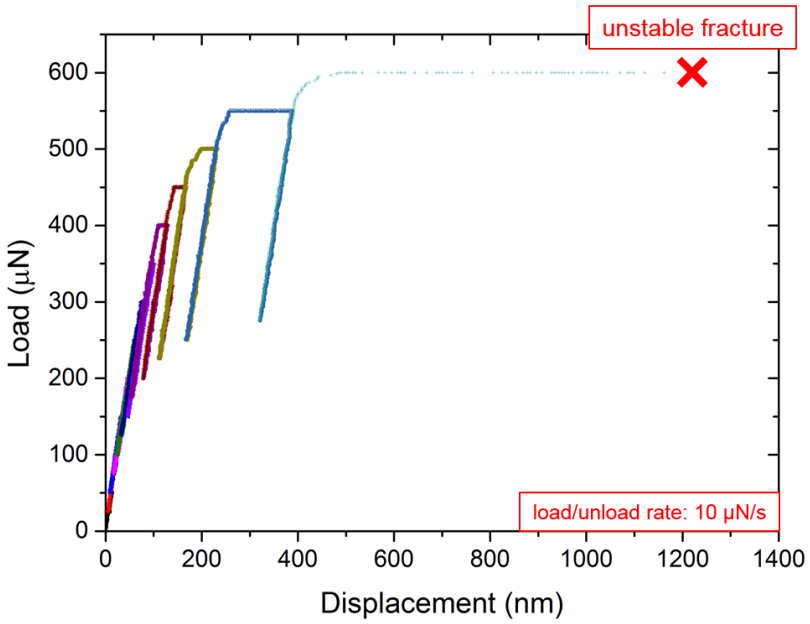


Fig. 6.16 Load-displacement curve of cantilever L2. The cantilever fractured unstably at 600 µN

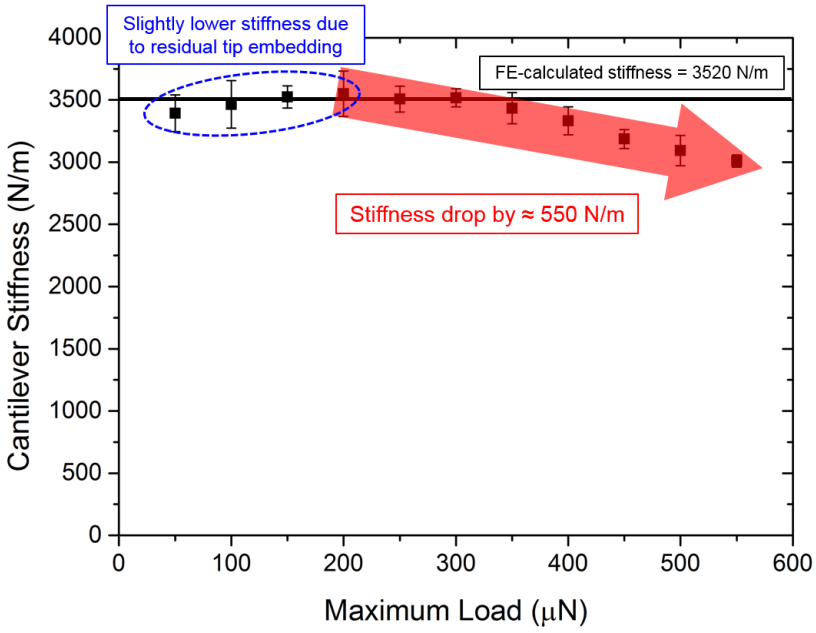


Fig. 6.17 Stiffness of cantilever L2 after the tip embedding correction. About 550 N/m of stiffness drop was measured before unstable failure

Max Load (μN)	Initial FE Stiffness (N/m)	Measured Stiffness (N/m)	Normalised crack Length α (a/B)	Estimated Crack Length (nm)
50		3394±147	0	0
100		3464±190	0	0
150		3489±90	0	0
*200		3550±184	0	0
250		3507±104	0.028	81±12
300	**3520±121**	3518±73	0.035	102±8
350		3434±124	0.08	231±14
400		3333±113	0.126	366±13
450		3187±76	0.182	528±8
500		3093±121	0.213	618±10
550		3008±49	0.228	660±4

Table 6.5 Stiffness drop and the estimated stable crack length of each cycle for cantilever L2

A crack length of approximately 1200 nm was measured from the post-test fractography, shown in **Fig. 6.18**. This SEM-measured crack length (~1200 nm) was considerable longer than the stiffness-estimated crack length, possibly due to the crack growth at the final loading cycle (up to 600 μN). The cantilever eventually failed unstably during the final hold segment, therefore the unloading stiffness from the final cycle wasn't measured. In addition, the intergranular crack shown in **Fig. 6.18(b)** might correspond to the final fast fracture observed in the load-displacement curve. The transition from stable to unstable crack growth could also be affected by material-related factors (intergranular crack due to a weak grain boundary in this case), which caused the discrepancy of stable crack length measurements.

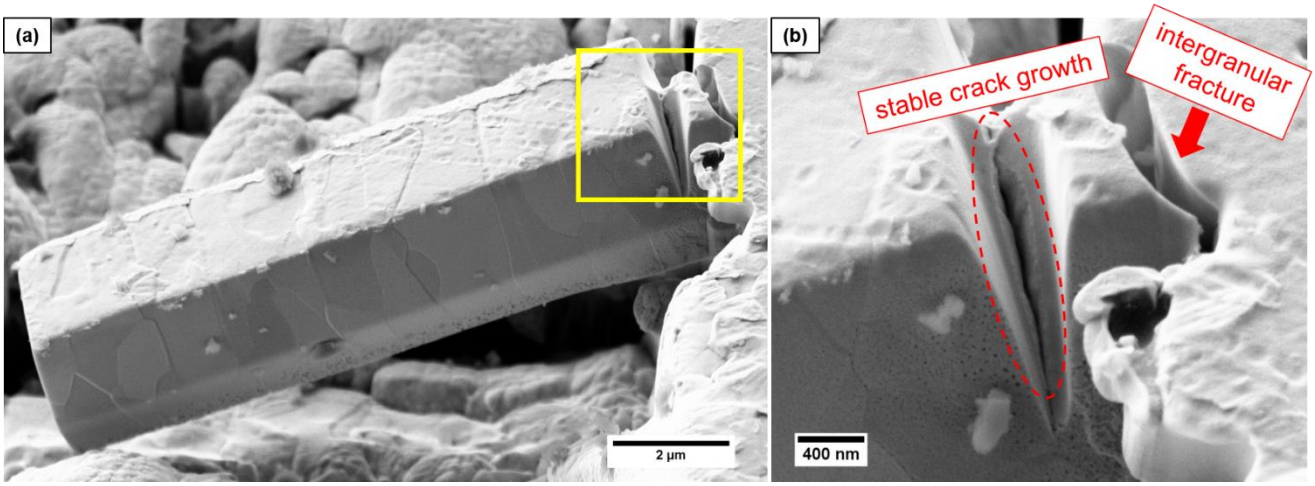


Fig. 6.18 Fractography of cantilever L2. Stable crack growth of approximately 1200 nm was measured. An intergranular crack near the fixed end was also observed

6.2.3 Micro-Cantilever Tested at 500 °C (E4)

Load-displacement curve of cantilever E4 (500 °C) is shown in **Fig. 6.19**. It was loaded incrementally to unstable fracture at 540 µN. Because the cantilever didn't failed catastrophically (from post-test fractography, shown in **Fig. 6.21**), this load should be better termed as the onset of unstable fracture. Stiffness plotted against the maximum load of each cycle, is shown in **Fig. 6.20**. Stiffness drop, and the estimated stable crack length (using the stiffness vs. crack length relationship provided in **Table 6.4**) are given in **Table 6.6**; a final stable crack length of approximately 573 nm was measured before unstable fracture.

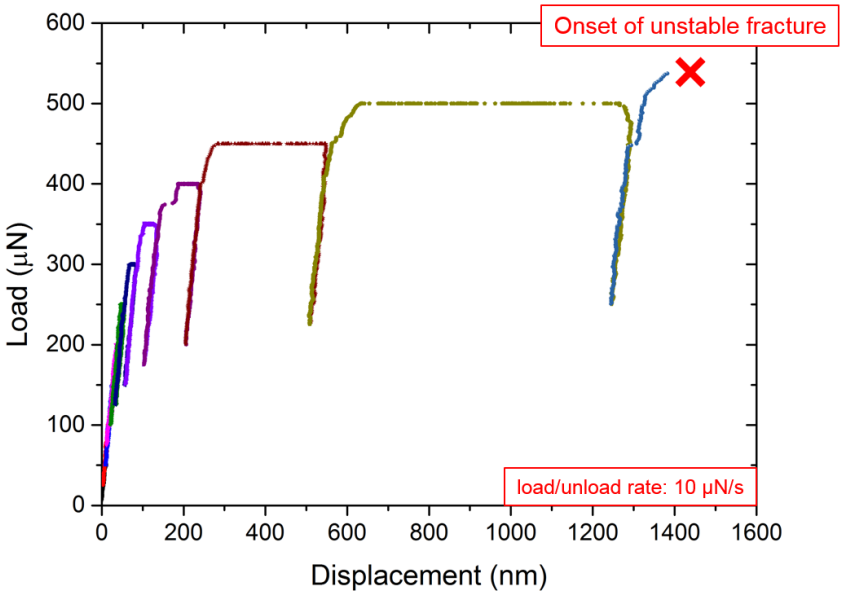


Fig. 6.19 Load-displacement curve of cantilever E4. The cantilever fractured unstably at 540 μN

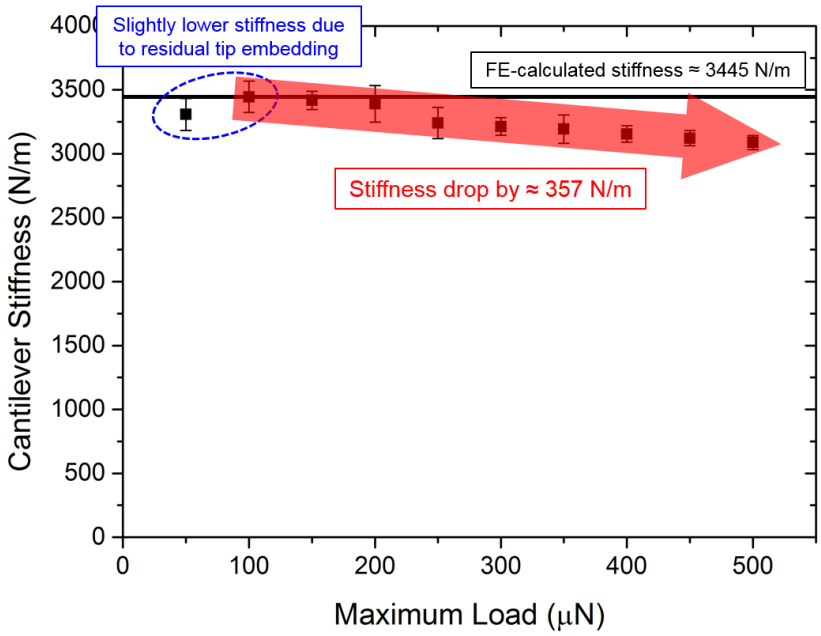


Fig. 6.20 Stiffness of cantilever E4 after the tip embedding correction. About 360 N/m of stiffness drop was measured before the onset of unstable failure

Max Load (μN)	Initial FE Stiffness (N/m)	Measured Stiffness (N/m)	Normalised crack Length α (a/B)	Estimated Crack Length (nm)
50		3308±126	0	0
*100		3440±123	0	0
150		3418±72	0.039	102±8
200		3391±142	0.06	168±14
250		3241±123	0.144	402±12
300	3445±15	3214±69	0.155	435±7
350		3193±112	0.164	459±11
400		3155±64	0.18	504±7
450		3122±60	0.192	537±7
500		3088±55	0.205	573±6

Table 6.6 Stiffness drop and the estimated stable crack length of each cycle for cantilever E4

Fig. 6.21 shows the post-test fractography of cantilever E4 after the test. To reveal the fracture surface, a micro-manipulator (Kleindiek Nanotechnik GmbH, Germany) equipped within the SEM was used to remove the remaining cantilever. It was operated carefully to prevent additional damage to the fracture surface. Stable crack length of approximately 590 nm was measured from the apex to the curved crack front, which is in good agreement with the estimated value (~570 nm). Two possible reasons were discussed for the formation of faint river-like patterns found beneath the crack front. The first reason is due to that the average fracture plane in the particular grain, imposed initially by the orientation of the notch relative to the grain crystallography, did not correspond exactly to a cleavage plane; so steps might arise on the fracture surface because of this mismatch. The second reason is due to the forest of thermally-activated screw dislocations that pierced through the cleavage plane, hence creating multiple

microscopic steps on the fracture surface. It is more likely the occurrence of the river-like pattern is a combination of both reasons.

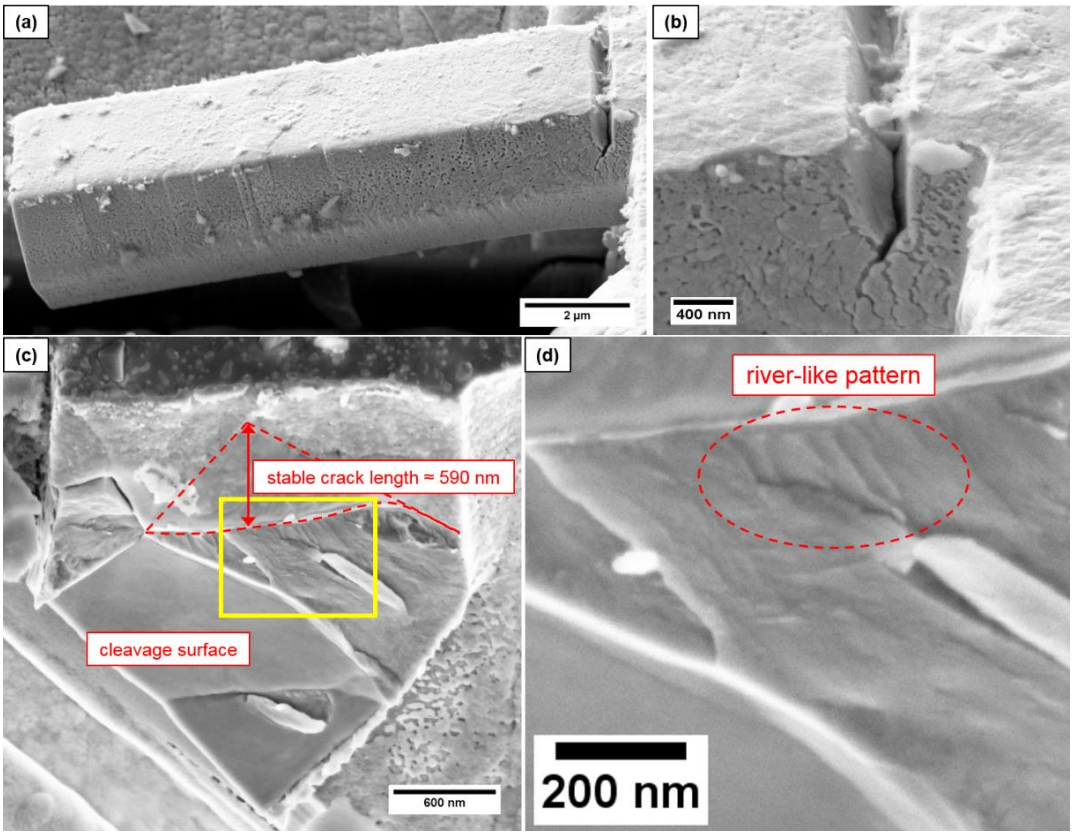


Fig. 6.21 Fractography of cantilever E4. Faint river-like patterns were observed beneath the crack front, and stable crack length of ≈ 590 nm was measured

6.2.4 Micro-Cantilever Tested at 600 °C (E3)

Load-displacement curve of cantilever E3 (600 °C) is shown in **Fig. 6.22**. It was loaded incrementally to unstable fracture at 450 µN. Stiffness plotted against the maximum load of each cycle, is shown in **Fig. 6.23**. Stiffness drop, and the estimated stable crack length (using the stiffness vs. crack length relationship provided in **Table 6.4**) are given in **Table 6.7**; a final stable crack length of approximately 750 nm was measured before unstable fracture.

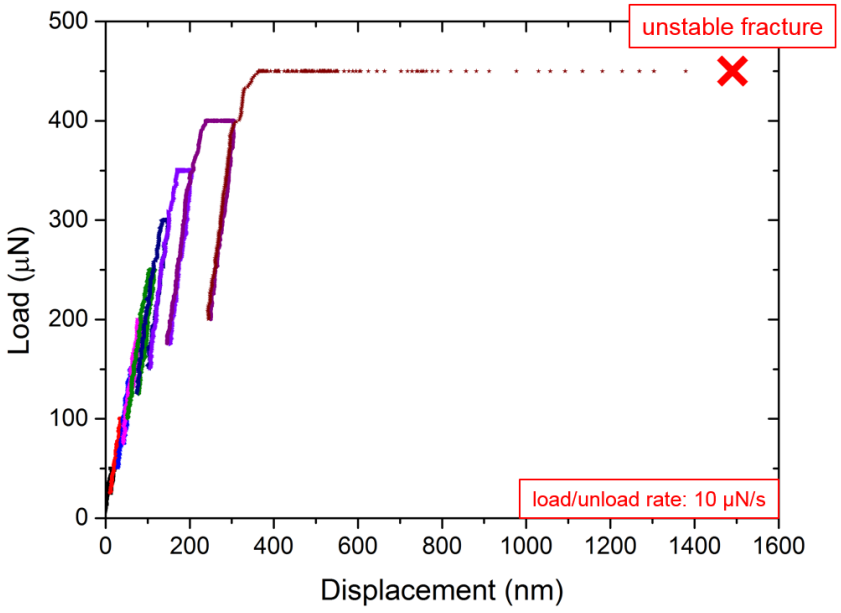


Fig. 6.22 Load-displacement curve of cantilever E3. The cantilever fractured unstably at 450 μN

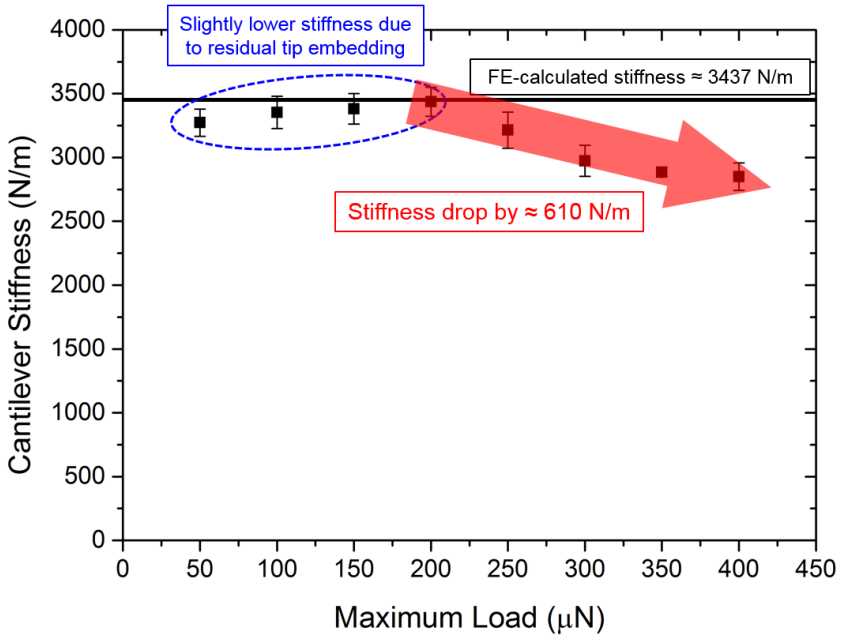


Fig. 6.23 Stiffness of cantilever E3 after the tip embedding correction. About 610 N/m of stiffness drop was measured before unstable fracture

Max Load (μN)	Initial FE Stiffness (N/m)	Measured Stiffness (N/m)	Normalised crack Length α (a/B)	Estimated Crack Length (nm)
50		3273±106	0	0
100		3353±127	0	0
150		3381±119	0	0
*200	3437±98	3437±114	0	0
250		3214±142	0.136	378±15
300		2973±122	0.226	633±12
350		2884±38	0.255	714±5
400		2850±107	0.27	756±11

Table 6.7 Stiffness drop and the estimated stable crack length of each cycle for cantilever E3

Post-test fractography of cantilever E3 is shown in **Fig. 6.24**. The measured stable crack length was approximately 720 nm, which is slightly lower than the estimated value (~756 nm). Extensive river-like patterns are observed on the fracture surface, possibly due to the higher dislocation activity at this temperature regime. In addition, as the initial crack encountered a grain boundary, the nearest cleavage plane in the adjoining grain was oriented at a twist angle from the current crack plane. The crack then accommodated the twist mismatch by forming several parallel planes, resulting the river-like patterns. Illustrated schematically in **Fig. 6.25**, the patterns usually have a curvilinear shape, and run roughly parallel to each other and normal to the propagating crack front. This pattern configuration is expected because the surface tension of the step is fairly isotropic, hence reducing the step energy required to extend the crack to a minimum.

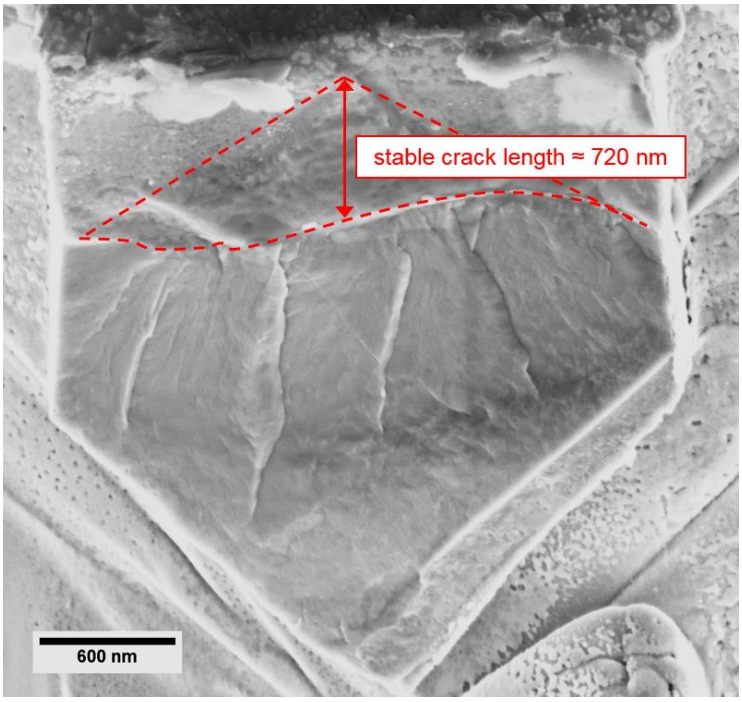


Fig. 6.24 Fractography of cantilever E3. Stable crack length of ≈ 720 nm was measured

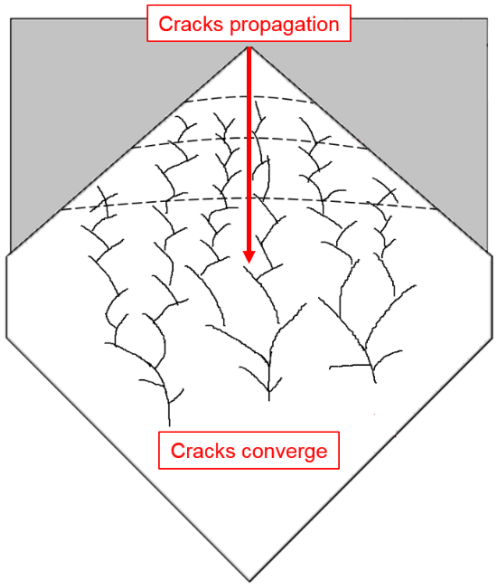


Fig. 6.25 River-like crack patterns on a fracture surface. The dotted black lines indicates successive positions of the crack front. A tendency for the multiple cracks to converge into a single crack was observed, due to the less energy consumption

6.2.5 Micro-Cantilever Tested at 700 °C (E2)

Load-displacement curve of cantilever E2 (700 °C) is shown in **Fig. 6.26**. It was loaded incrementally to unstable fracture at 420 μN, then the cantilever eventually hit the bottom trench due to the large displacement (~2000 nm). Creep relaxation was observed during the initial unloading phase of cycle 8. Stiffness plotted against the maximum load of each cycle, is shown in **Fig. 6.27**. Stiffness drop, and the estimated stable crack length (using the stiffness vs. crack length relationship provided in **Table 6.4**) are given in **Table 6.8**; a final stable crack length of approximately 790 nm was measured before unstable fracture.

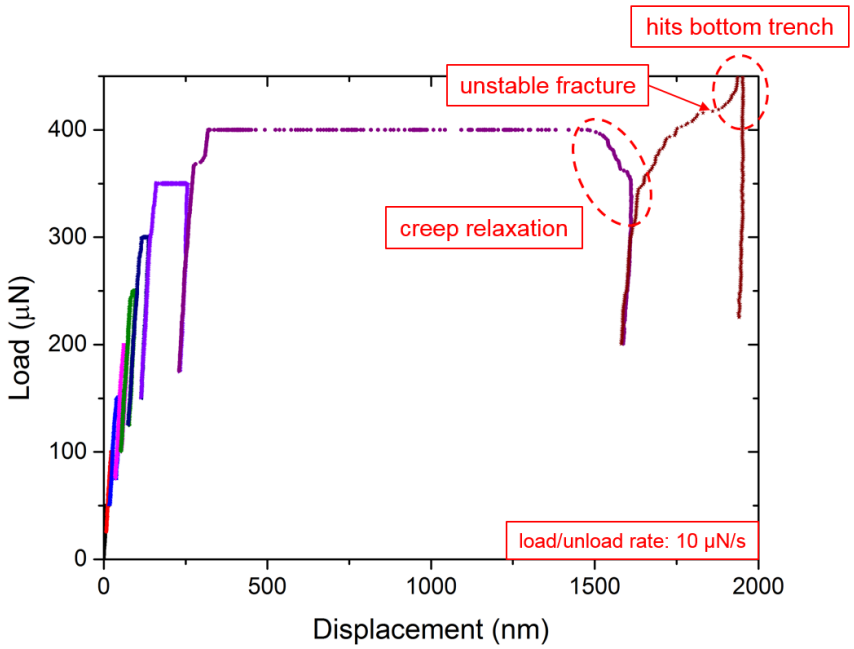


Fig. 6.26 Load-displacement curve of cantilever E2. Creep relaxation at the unloading phase of cycle 8, the unstable fracture load of 420 μN, and contact with the bottom trench are all labelled

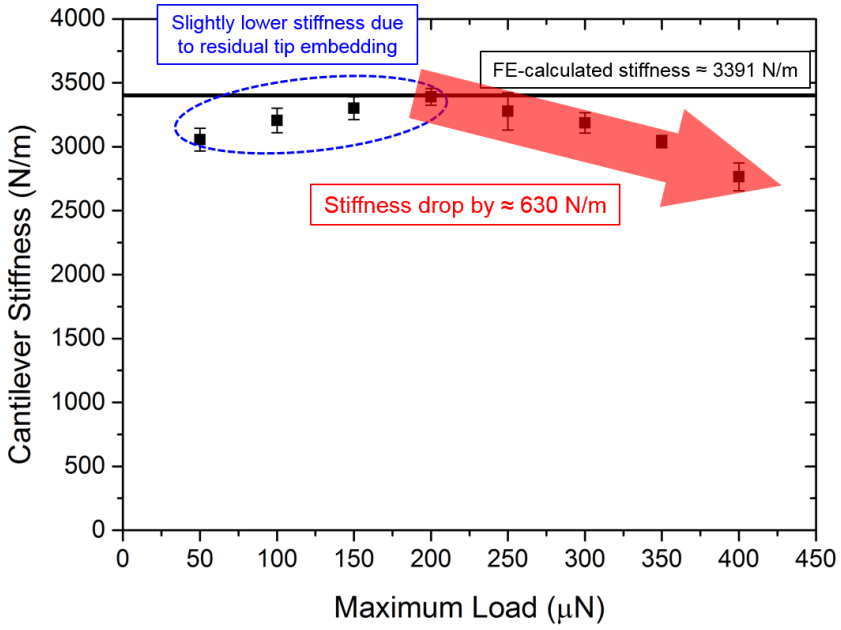


Fig. 6.27 Stiffness of cantilever E2 after the tip embedding correction. About 613 N/m of stiffness drop was measured before the onset of unstable fracture

Max Load (μN)	Initial FE Stiffness (N/m)	Measured Stiffness (N/m)	Normalised crack Length α (a/B)	Estimated Crack Length (nm)
50		3056±89	0	0
100		3206±96	0	0
150		3302±88	0	0
*200	3391±129	3391±66	0	0
250		3277±147	0.088	246±15
300		3187±79	0.133	372±7
350		3040±48	0.192	537±5
400		2764±108	0.282	790±10

Table 6.8 Stiffness drop and the estimated stable crack length of each cycle for cantilever E2

Post-test fractography of cantilever E2 is shown in **Fig. 6.28**. The cantilever remained attached to the fixed end at end of test, therefore the micro-manipulator was used again to reveal the chevron fracture surface. Stable crack length of approximately 800 nm was measured from the fracture surface, with extensive river-like patterns. Increased formation of river-like patterns suggested that 700 °C was possibly higher the brittle-to-ductile transition temperature (BDTT). This possible transition temperature will be discussed more quantitatively using EPFM analysis in the next section.

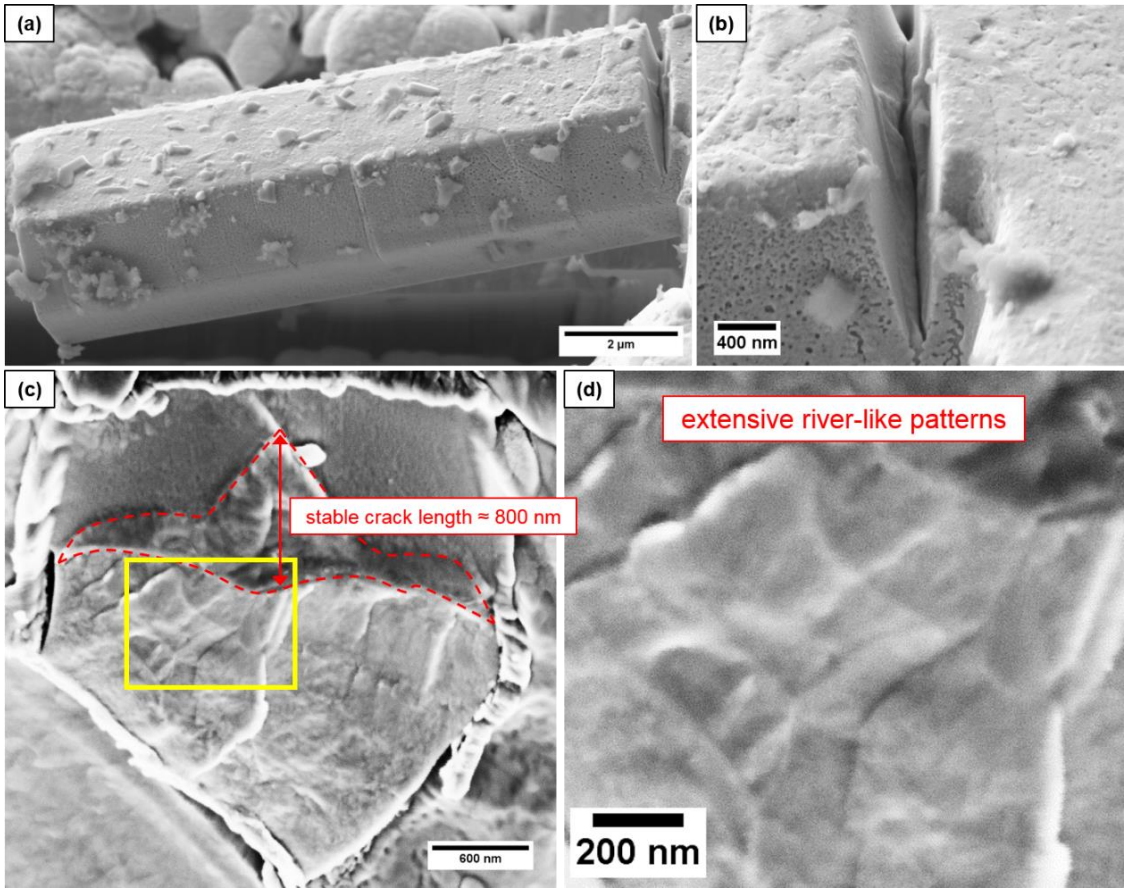


Fig. 6.28 Fractography of cantilever E2. Extensive river-like patterns are clearly observed at the chevron fracture surface. Stable crack length is approximately 800 nm

6.2.6 Tests Summary

Four chevron-notched cantilevers were tested successfully from 400 to 700 °C. Stable crack growth were observed in all cantilevers, and were measured quantitatively using the load partial-unload method. Crack length estimated via the stiffness drop were mostly in good agreement with direct SEM measurements from the fracture surface, except for cantilever L2 where crack stability was influenced by the weaker grain boundary located close to the chevron notch. Summary of crack length measurements at elevated temperatures are summarised in **Fig. 6.29**, where the amount of stable crack growth increases with temperature. Load-displacement curves of cantilevers tested from RT to 700 °C are plotted in **Fig. 6.30**. A brittle-to-ductile transition (BDT) behaviour is observed: elongation to failure increases, but yield/fracture load decreases, all with increasing temperature. Tests results are summarised in **Table. 6.9**.

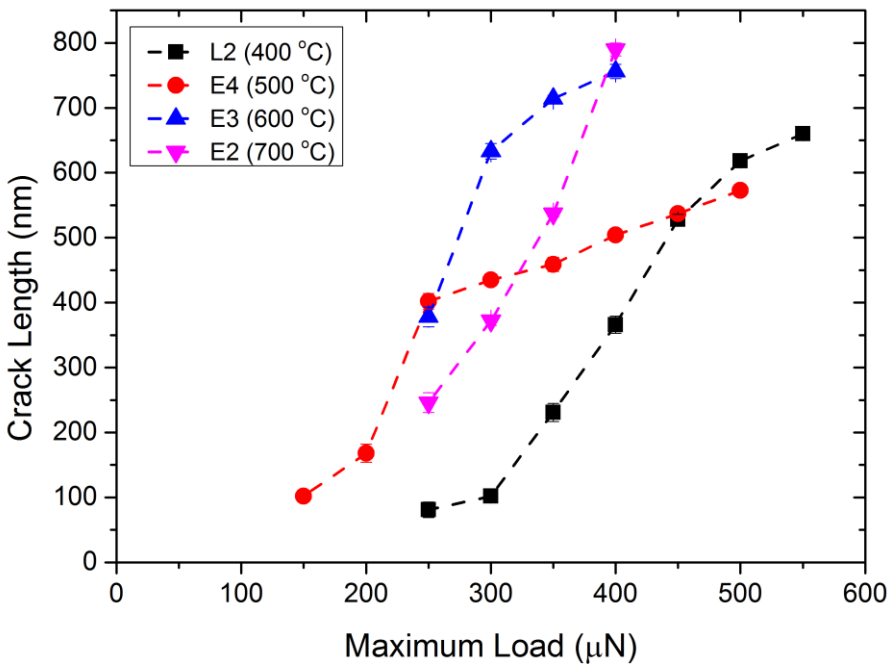


Fig. 6.29 Stable crack length at each load increment for four high-temperature cantilevers

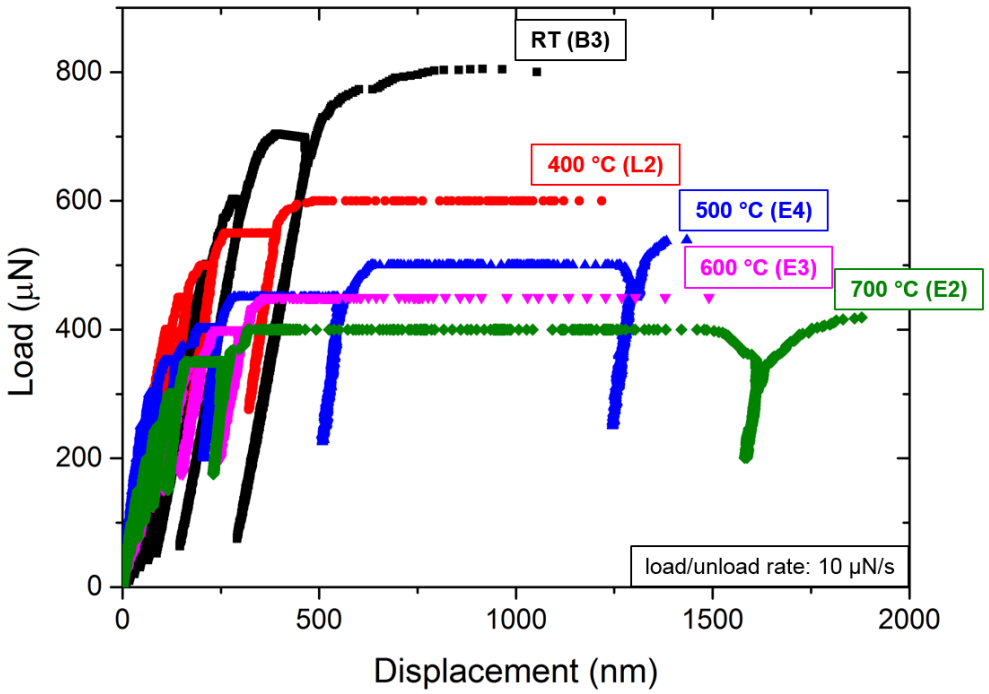


Fig. 6.30 Load-displacement curves of cantilevers tested from RT to 700 °C. Elongation to failure increases with temperature, but fracture load (yield load) decreases with temperature

Cantilever	Temperature (°C)	Avg Thermal Drift (nm/s)	Fracture Load (μN)	Total Displacement (nm)	Stiffness Drop (N/m)	Stable Crack Length (nm)
L2	400	0.02	600	1250	500	660±4
E4	500	0.01	539	1417	357	573±6
E3	600	0.03	450	1525	600	756±11
E2	700	0.03	419	1933	630	790±10

Table 6.9 Test results summary of the high-temperature tested cantilevers. Average thermal drift rate was kept below 0.03 nm/s for good thermal stability of both surface scan and test

6.3 Elastic Plastic Fracture Mechanical Analysis

Stable crack growth of tungsten cantilevers at elevated temperatures were accompanied by considerable amount of plastic deformation, as observed from the load-displacement curves. The thermally-activated plasticity further extended the crack tip plastic zone, making it comparable to the thickness of the cantilever beam (2~3 μm) and hence invalidated any LEFM-calculated K_{Ic}. EPFM analysis was used to include the plastic work that contributed to stable crack growth, and provided a more valid J value (or K value). Due to the chevron notch geometry and load partial-unload method, both stress intensity factors (SIFs) and work-of-fracture (WOF) were calculated at each crack increment, allowing fracture resistance curves (J-R curves) to be calculated. Fracture resistance curve provided a more detailed description of the fracture process when significant plasticity were associated.

Detailed methodologies for EPFM analysis were already described in **Chapter 5.6**. The required parameters for the EPFM analysis (crack length, SIFs, WOF, crack area, J, and the conditional fracture toughness K_Q) for four cantilevers are given in **Table 6.10~6.13**, and the J-R curves and EPFM analysis summary for four micro-cantilevers are shown in **Fig. 6.31** and **Table 6.14**.

Cycle	Fracture Load (μN)	Crack Length (nm)	SIF	WOF (μN·nm)	Crack Area (nm^2)	K ($MPa \cdot m^{0.5}$)	J_{el} (J/m^2)	J_{pl} (J/m^2)	J_{total} (J/m^2)	K_Q ($MPa \cdot m^{0.5}$)
4	200	0	51.7	0	0	2±0.4	8.8	0	8.8±0.4	1.9±0.4
5	250	81±12	49.1	900	2800	2.4±0.2	12.4	321	333.4±9	12.3±2
6	300	102±8	48.3	1550	3700	2.8±0.3	17.3	419	436.3±21	14±3.1
7	350	231±14	43.7	6000	6300	2.9±0.4	19.2	952	971.2±14	20.9±2.5
8	400	366±13	38.4	12000	8500	3±0.25	20	1412	1432±11	25.4±2.2
9	450	528±8	32	22000	13280	3±0.2	20	1657	1677±16	27.5±2.7
10	500	618±10	28.6	40500	23000	3±0.2	20	1761	1781±21	28.3±3.1
11	550	660±4	27	60050	33600	3.1±0.2	21.3	1790	1811.3±20	28.6±3

Table 6.10 EPFM parameters of cantilever L2. J_{el} and J_{pl} are the elastic and plastic contribution of the fracture energy, respectively. K_Q is the conditional fracture toughness calculated from J_{total}, assuming plane-strain condition

Cycle	Fracture Load (μN)	Crack Length (nm)	SIF	WOF (μN·nm)	Crack Area (nm^2)	K ($MPa \cdot m^{0.5}$)	J_{el} (J/m^2)	J_{pl} (J/m^2)	J_{total} (J/m^2)	K_Q ($MPa \cdot m^{0.5}$)
3	150	102±8	47.5	0	6500	1.9±	7.4	0	7.4±0.1	1.8±0.2
4	200	168±14	45.4	2225	8140	2.2±0.3	10.6	273.4	284±2	11.3±0.9
5	250	402±12	37.1	12600	8200	2.3±0.4	10.2	1536.6	1546.8±15	26.4±2.6
6	300	435±7	35.9	19200	11260	2.4±0.4	13	1704.7	1717.7±8	27.8±1.9
7	350	459±11	35	28900	16000	2.7±0.35	16.1	1806.3	1822.4±9	28.7±2
8	400	504±7	33.3	40500	21080	2.9±0.2	18.5	1920.9	1939.4±10	29.6±2.1
9	450	537±7	32.1	58500	29870	3.1±0.2	21.1	1958.2	1979.3±10	29.9±2.1
10	500	573±6	30.7	89750	45200	3.2±0.3	23.4	1985.6	2009±17	30.1±2.8

Table 6.11 EPFM parameters for cantilever E4

Cycle	Fracture Load (μN)	Crack Length (nm)	SIF	WOF (μN·nm)	Crack Area (nm^2)	K ($MPa \cdot m^{0.5}$)	J_{el} (J/m^2)	J_{pl} (J/m^2)	J_{total} (J/m^2)	K_Q ($MPa \cdot m^{0.5}$)
4	200	0	51.7	0	0	2±0.3	8.9	0	9±0.2	2±0.3
5	250	378±15	38	8350	8210	2.3±0.25	11.7	1017.2	1029±5	21.5±1.5
6	300	633±12	28	26800	14050	2.4±0.4	12.8	1907.2	1920±6	29.4±1.7
7	350	714±5	25	54800	26700	2.7±0.35	16.2	2052.4	2069±20	30.5±3
8	400	756±11	22.7	95000	45000	2.9±0.3	18.7	2111.1	2130±17	31±2.8

Table 6.12 EPFM parameters for cantilever E3

Cycle	Fracture Load (μN)	Crack Length (nm)	SIF	WOF (μN·nm)	Crack Area (nm^2)	K ($MPa \cdot m^{0.5}$)	J_{el} (J/m^2)	J_{pl} (J/m^2)	J_{total} (J/m^2)	K_Q ($MPa \cdot m^{0.5}$)
4	200	0	51.7	0	0	2.4±0.3	12.8	0	13±0.2	2.4±0.3
5	250	246±15	43.1	10250	7322	2.5±0.5	13.9	1400	1414±12	25.2±2.3
6	300	372±14	38.2	37800	18320	2.6±0.4	15	2063.3	2078±6	30.6±1.7
7	350	537±13	31.7	96000	32494	2.8±0.35	17.4	2954.4	2972±7	36.6±1.8
8	400	790±10	22.2	320000	88000	3.1±0.2	21.3	3636.3	3658±23	40.6±3.2

Table 6.13 EPFM parameters for cantilever E2

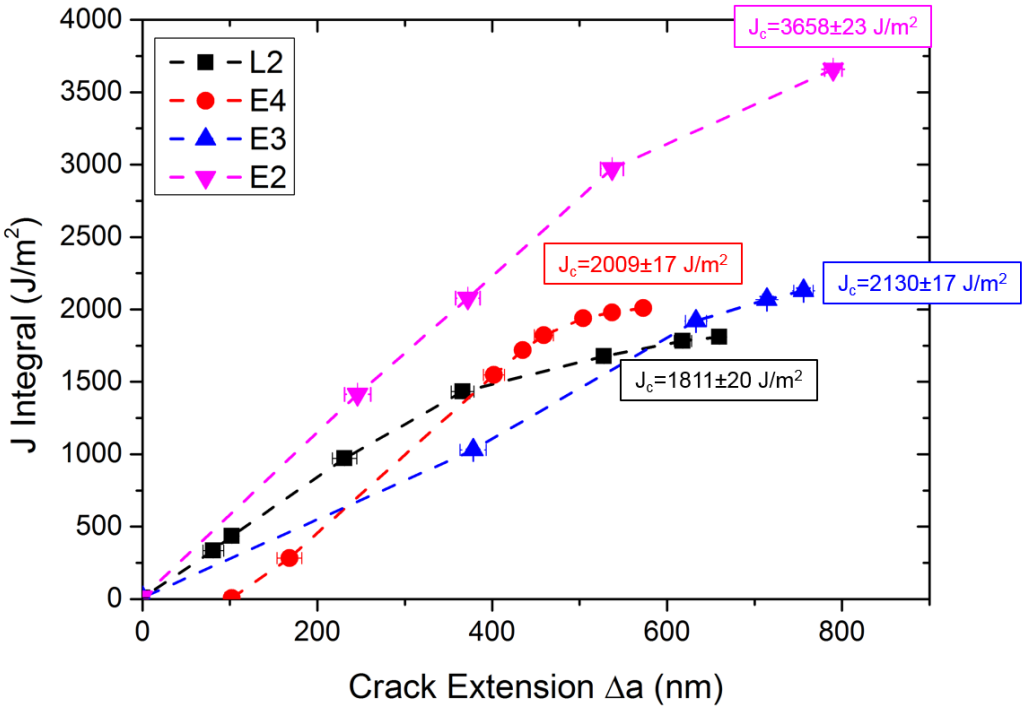


Figure 6.31 Fracture resistance curves (J-R curves) of W-1%Ta micro-cantilevers tested from 400~700 °C. The J values just before crack instability, J_c, are labelled

Cantilever	Temperature (°C)	J_c (J/m^2)	K_{Qc} (MPa·m$^{0.5}$)
L2	400	1811±20	28.5±3
E4	500	2009±17	30.1±2.8
E3	600	2130±17	30.9±2.8
E2	700	3658±23	40.5±3.2

Table 6.14 Summary of the EPFM analysis. J_c is the maximum J value before crack instability and K_{Qc} is the equivalent fracture toughness value, calculated using **Eq. 6.3** (assuming plane-strain condition). Both K and J increase steadily with temperature

For ease of comparison with macroscopic K, the maximum J values before crack instability, J_c, were converted to K_{Qc} (denotation Q stands for conditional, due to the non-standard specimen size), using **Eq. 6.3** (assuming plane-strain condition). The microscopic crack instability toughness K_{Qc}, and the crack initiation toughness K_{Qi} (K value at where crack initiates), were compared with macroscopic K_{Ic} from the same W-1%Ta alloy (only initiation value) [108], and plotted in **Fig. 6.32**. The microscopic K_{Qc} at each temperature regime were significant larger than the macroscopic K_{Ic} by approximately 20 MPa·$m^{0.5}$. On the contrary, the microscopic initial toughness K_{Qi} are slightly lower, and remain constant at around 2 MPa·$m^{0.5}$ throughout the entire temperature range. It should also be noted that the macroscopic K_{Ic} were calculated using the first load drop, and in most cases, further increases in load were observed after the first load drop. This suggests a fracture resistance behaviour for W-1%Ta is possible, even at macroscale tests. Therefore, the macroscopic K_{Ic} were probably more suitable as the lower bound fracture toughness value and the difference between the micro/macroscale toughness may not necessarily represent a true specimen size effect.

At temperature below 600 °C, K_{Qc} only increased slightly from 28.5 to 30.9 MPa·$m^{0.5}$. A drastic increase was observed at 700 °C, suggesting this might be the brittle-to-ductile transition temperature (BDTT) for the tungsten micro-cantilevers. Macroscopic K_{Ic} increases gradually with temperature, with no abrupt transition between brittle and ductile failure. The macroscopic BDTT labelled on **Fig. 6.32** is approximately 600 °C, which is in good agreement with microscopic BDTT. However, macroscale experiments by Giannattasio et al. [116] on sintered polycrystalline pure tungsten reported lower BDTT values ranging from 200 to 350 °C, depending on the strain rate used. This temperature range is about 300 °C lower than the BDTT measured from micro-cantilever tests. However, as BDTT is a function of the strain rate and also

extremely sensitive to the impurity content, it is possible that the 1%Ta addition and higher strain rate used in the micro-cantilever tests attributed to the higher BDTT. These will be discussed in more details in the following section.

$$K_{Qc} = \sqrt{\frac{J_c E}{(1-\nu^2)}} \quad (\boldsymbol{Eq.6.3})$$

where E is the elastic modulus at corresponding temperature, and ν is the Poisson's ratio

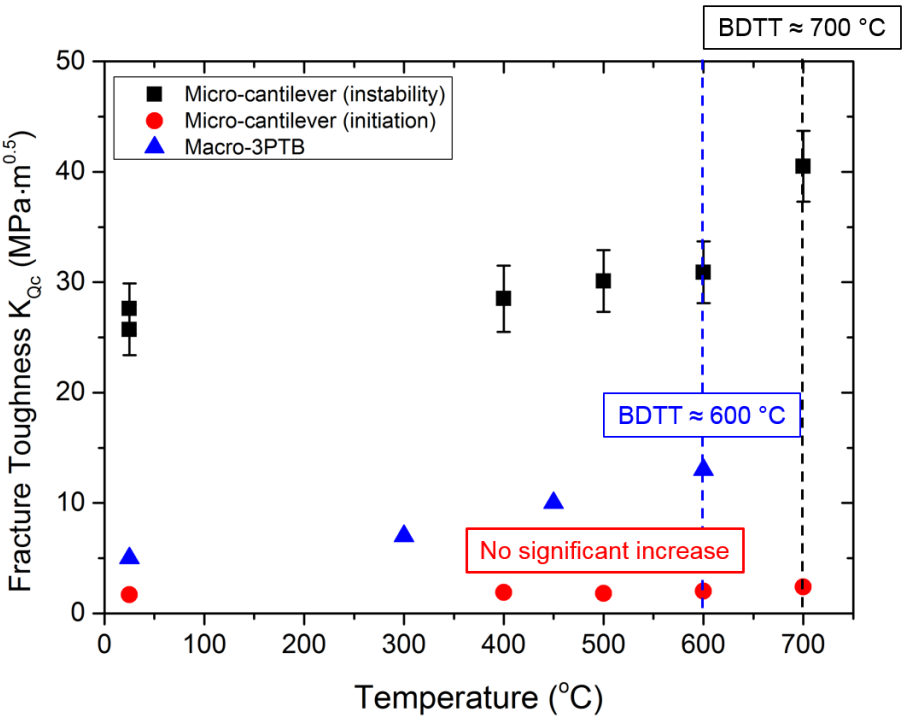


Figure 6.32 Microscopic K_{Qc}, K_{Qi}, and the macroscopic K_{Ic}, all from W-1%Ta. The vertical dotted lines are the BDTT from both micro-cantilever and macro-3PTB tests

6.4 Discussions

At elevated temperature, the interactions between the crack tip and the plastic zone is even more complicated. Using the EPFM fracture resistance curve approach, it is possible to discuss the initial crack blunting behaviour quantitatively. In addition, the creep relaxation in the 700 °C test will also be discussed. Lastly, the brittle-to-ductile transition and the temperature effect to the stable crack growth (SCG) will be discussed in term of dislocation activation energy.

6.4.1 Temperature Effects to Crack Blunting

The ASTM standard for fracture resistance curve analysis is described in E 1820 [117]. A schematic J-R curve is shown in **Fig. 6.33**, where two exclusion lines at crack length of 0.15 and 1.5 mm are drawn. These lines have a slope of $M\sigma_y$, where σ_y is the yield stress, and M is a non-dimensional constant, having a default value of 2. The slope of the exclusion lines is then used to represent the component of crack extension that is due to crack blunting.

However, the crack length defined in the ASTM standard was designed for fracture specimen of millimetre size, it no longer applies when specimen is down-scaled to the micrometre regime. Instead, the initial linear region of the J-R curves were used to measure the effective crack blunting slope from micro-cantilever tests. Use cantilever B3 as an example, the J-R curve is shown in **Fig. 6.34**, where a linear function was fitted to the initial part. The slope of this linear function, $M\sigma_y$, was then used to describe the crack blunting behaviour. **Table 6.15** summarises the blunting slopes and the experimentally-obtained M values for cantilevers tested from RT to 700 °C.

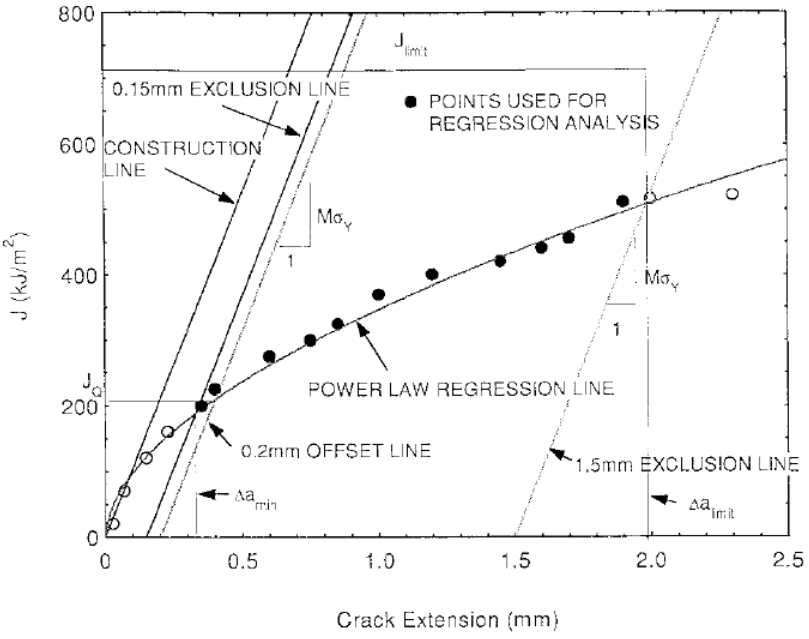


Fig. 6.33 ASTM E 1820 determination of the crack blunting slope using two exclusion lines (a=0.15, 1.5 mm) from a schematic macroscopic J-R curve

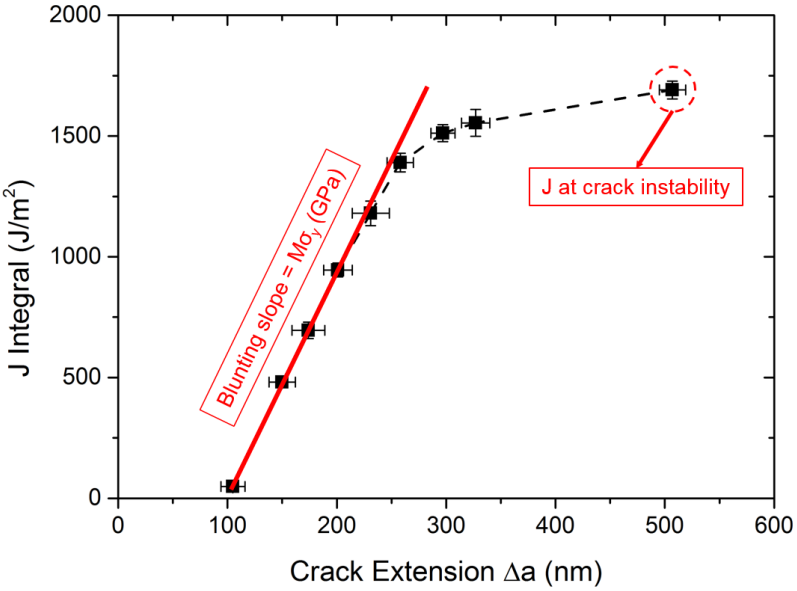


Fig. 6.34 Determination of the crack blunting slope using a microscopic J-R curve (B3). The blunting slope was defined as the initial linear fit, and the final J value indicated crack instability

Cantilever No.	Temperature (°C)	Blunting Slope (GPa)	Yield Stress (GPa)	M
B2	25	6.4	5.2*	1.23
B3	25	9.3	5.2*	1.8
L2	400	4.2	0.77	5.48
E4	500	5.1	0.8	6.38
E3	600	3	0.73	4.11
E2	700	5.6	0.77	7.27

Table 6.15 Summary of the blunting slopes from microscopic J-R curves. The yield stresses were estimated values from nanoindentation hardness (only the RT yield stress, marked with an asterisk *, was obtained from micro-cantilever tests)

The experimentally-determined blunting constant M are listed in **Table 6.15**. M at elevated temperatures were considerably higher than RT values, suggesting an enhanced crack blunting behaviour due to the thermally-activated dislocations. However, yield stresses used here were estimated values from nanoindentation hardness, which neglected the size-dependent plasticity. Accurate yield stresses obtained from micro-cantilevers were probably larger than the nanoindentation hardness estimations, hence the M values should be smaller for high-temperature tests. For future tests that aim to determining accurate crack blunting slopes, elastic-plastic tests using un-notched cantilevers should be performed in parallel with micro-fracture tests at each temperature regime.

6.4.2 Temperature Effects to Creep Relaxation

Considerable amount of creep relaxation was observed for cantilevers tested at 700 °C, shown in **Fig. 6.35**. Upon unloading, the cantilever continued to deform (downwards, same as the loading direction) for approximately 350 nm, resulting an additional area under the load-displacement curve. Due to the crack stability provided from chevron notch configuration (SIF decreases as crack extends), crack can only propagate when load is increased. Therefore, the area under the load-displacement curve was solely contributed by creep deformation, and should not be included in the work-of-fracture (WOF) used in the EPFM analysis.

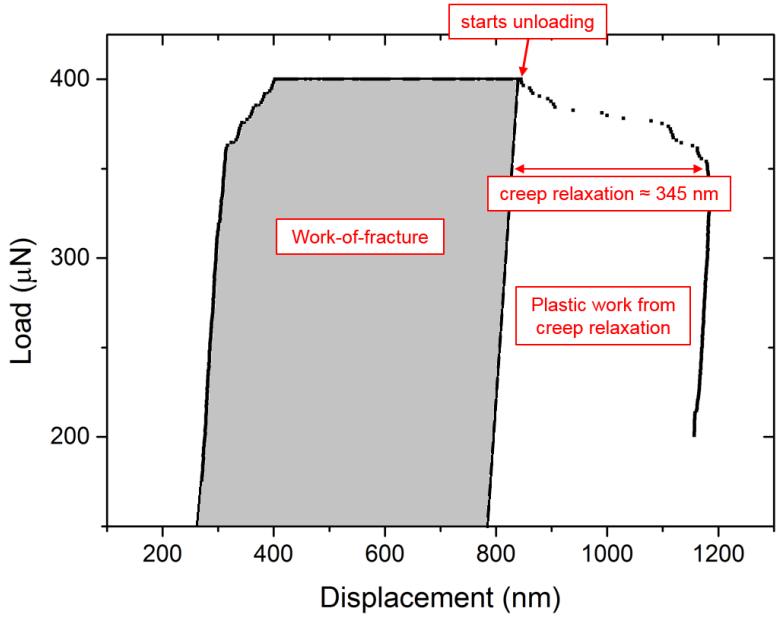


Fig. 6.35 Creep relaxation of cantilever E2 (tested at 700 °C) during the initial unloading phase of the final cycle. Approximately 350 nm of relaxation was observed before the actual unloading of the cantilever (cantilever crept downwards)

6.4.3 Brittle-to-Ductile Transition Temperature

The fracture behaviour of tungsten cantilevers can change drastically over a small temperature range. At lower temperature, tungsten was semi-brittle, and failed mainly by cleavage. At higher temperature, it was more ductile, and failed mainly by ductile tearing. In the transition region, both micro-mechanisms of fracture could occur in the same specimen, resulting the mixed cleavage and ductile features found in the fracture surfaces. This fracture transition behaviour is illustrated schematically in **Fig. 6.36**. From previous EPFM analysis and post-test fractography, both fracture toughness (see **Fig. 6.32**) and the amount of ductile tearing (stable crack growth) increased gradually with temperature. The cantilever fracture surfaces from RT to 700 °C are shown in **Fig. 6.37**, where the stable crack growth (SCG) increased with temperature.

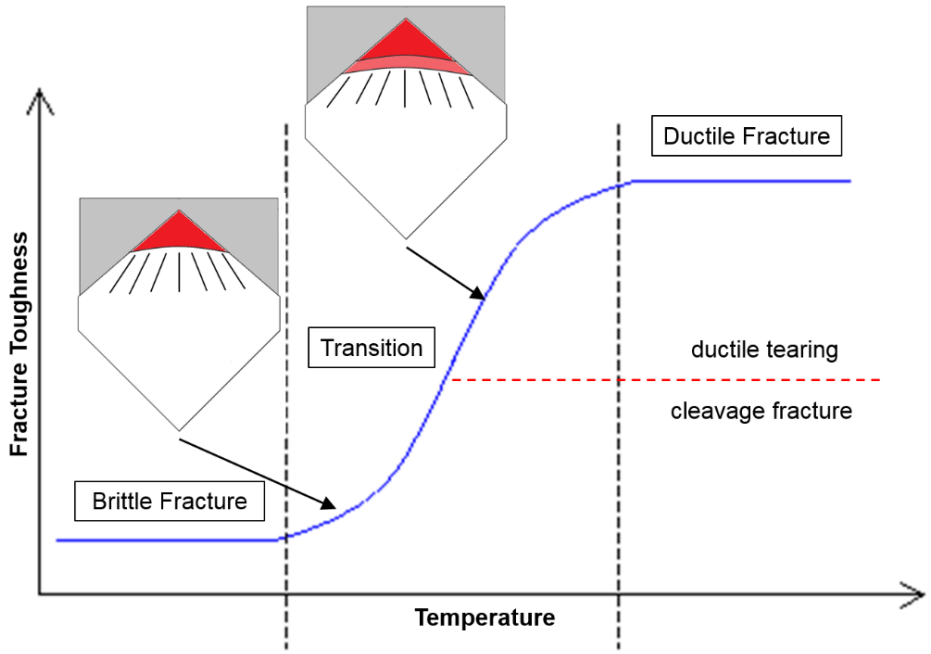


Fig. 6.36 Schematic drawing illustrating the BDT in tungsten cantilevers. The fracture mechanism transits from mainly cleavage to more ductile tearing as the temperature increases

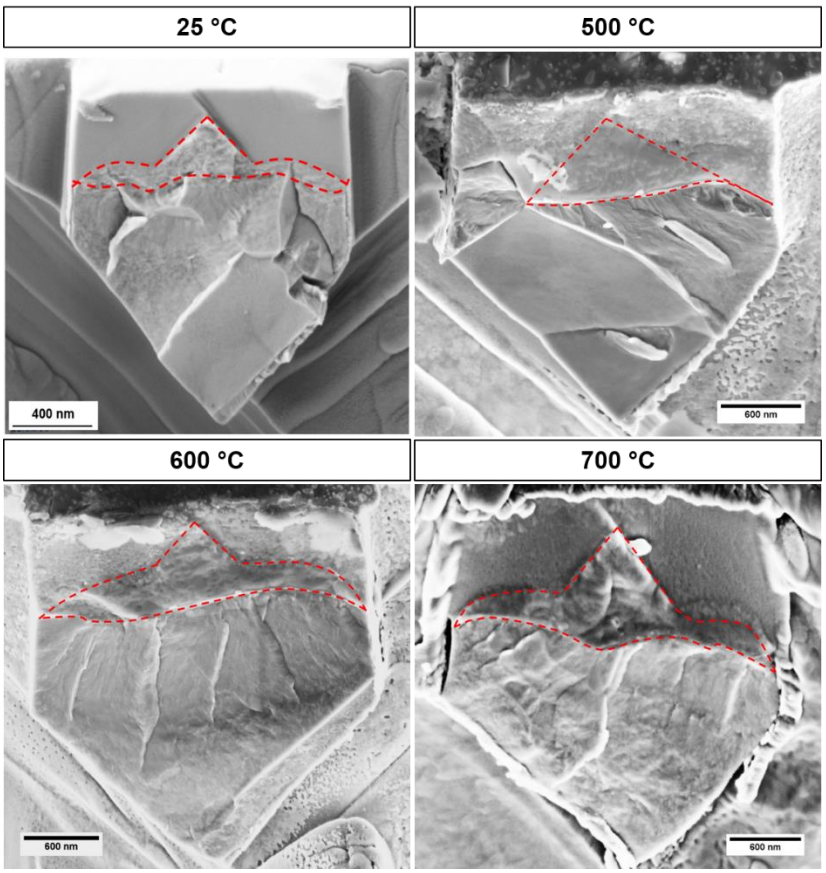


Fig. 6.37 Fracture surfaces of the tungsten cantilevers tested from RT to 700 °C. The ductile tearing fracture surface (stable crack growth region) increased with temperature

Crack extension in the upper transition region often displayed isolated islands of ductile ligaments; unbroken ligaments are often found behind the arrested crack tip. This implied a propagating cleavage crack encountered barriers, leaving isolated unbroken ligaments in its wake. Therefore, the energy required to break the ductile ligaments might provide additional fracture resistance behaviour. **Fig. 6.38** shows the post-test SEM image of a cantilever tested at 700 °C. Multiple ductile ligaments were found behind the arrested crack tip. Stable crack growth vs. temperature is plotted in **Fig. 6.39**, where the amount of stable crack growth increased steadily with temperature.

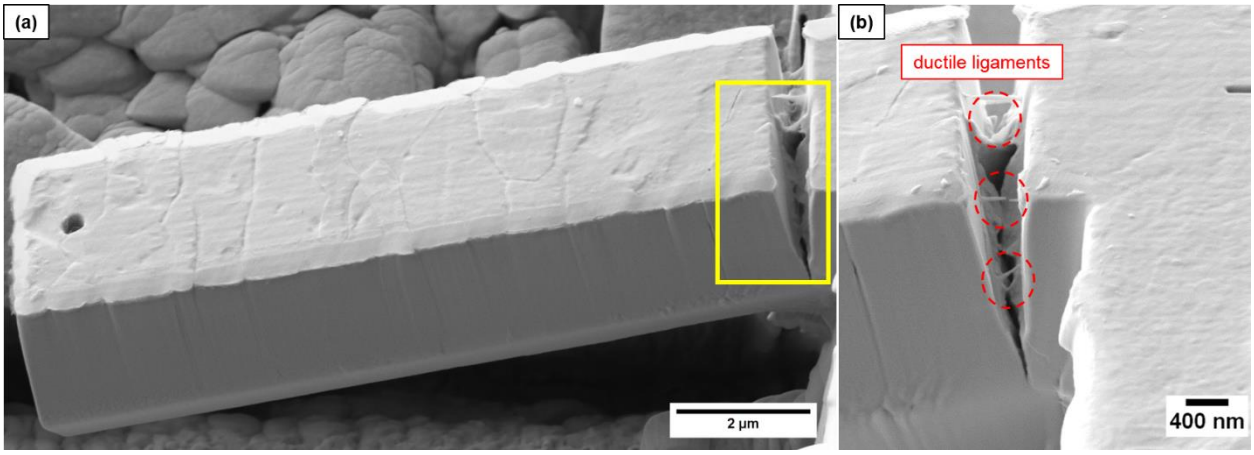


Fig. 6.38 Post-test SEM image of cantilever tested at 700 °C (before the micro-manipulator removal). Multiple ductile ligaments were found ahead of the crack tip, resulting in the increased fracture resistance behaviour

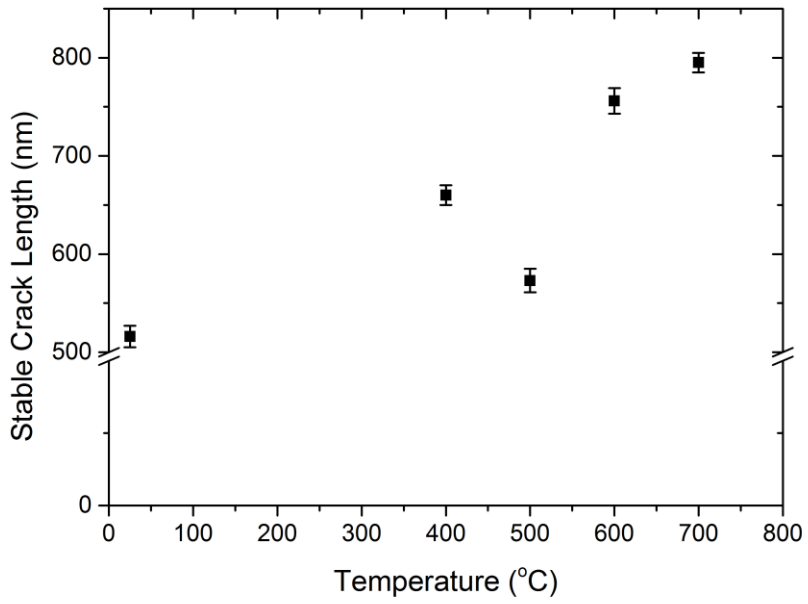


Fig. 6.39 Stable crack growth (SCG) vs. temperature from tungsten micro-cantilevers. The amount of stable crack growth increased with temperature (except for the 500 °C test)

6.4.4 Strain Rate and Impurity Effects to the BDTT

BDTT measured from W-1%Ta micro-cantilevers was about 700 °C, which was approximately 500 °C higher than the macroscopic BDTT (150~250 °C) reported by Gianattasio et al. [13]. The effect of impurities was discussed by Murphy et al. [118]. The CVD-grown tungsten was brittle throughout the entire test range (RT~967 °C), due to the segregation of fluorine impurities to the grain boundaries. Therefore, no distinguishable BDTT was observed. It is possible for the tantalum addition to introduce a similar effect. As reported by Wurster et al. [108], macroscopic 3PTB (three-point bending) tests W-1%Ta matchsticks remained brittle up to 600 °C (5~8 MPa·$m^{0.5}$), and grain boundaries were often found as preferable sites for crack nucleation (see section 5.2).

The effects of strain rate to the BDTT of tungsten was discussed in great details by Gianattasio and Roberts [14]. They found that the strain rate/BDTT follows an Arrhenius relationship with an activation energy equal to that for dislocation glide [119], shown in **Eq. 6.4**. The strain rate used in their macro-fracture tests were in the range of 4 x 10^{-5}~5 x 10^{-2} s^{-1}, corresponding to BDTT ranging from 150~250 °C [120]. The Arrhenius plot for strain rate and BDTT from macroscopic fracture tests of pure tungsten (single and polycrystalline) is shown in **Fig. 6.40**.

$$\dot{\varepsilon} = Aexp\left(-\frac{U}{kT_{BDT}}\right) \quad (\boldsymbol{Eq.\,6.4})$$

where $\dot{\varepsilon}$ is the strain rate, U is the activation energy for dislocation glide (1.05±0.05 eV for pure tungsten), k is the Boltzmann constant, T_{BDT} is the brittle-to-ductile transition temperature

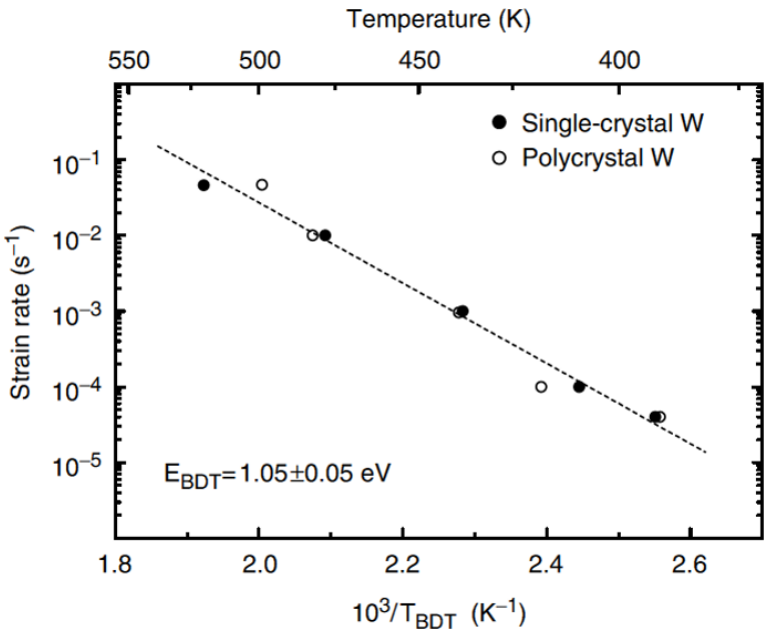


Fig. 6.40 Arrhenius plot of the strain rate vs. $1/T_{BDT}$ for single-crystal (solid symbols) and polycrystalline (open symbols) tungsten [120]

For micro-cantilever tests, the effective strain rate was approximately 10^{-3}~5×10^{-2} s^{-1}, which is about 1~2 order of magnitude higher than macro-fracture tests. The strain rate used for cantilever E2 (700 °C) is plotted in **Fig. 6.41**, along with the stress-strain data. One should also be aware that the Micro Materials® NanoTest Xtreme is intrinsically load-controlled instrument, therefore, the strain rate is only constant in the elastic regime; any non-linear events, i.e. plasticity and fracture, will force the indenter to move abruptly, raising the strain rate significantly higher. Because the activation energy for dislocation glide is constant regarding the specimen size, using the highest strain rate from cantilever tests (~5×10^{-2} s^{-1}) will estimate a BDTT of approximately 300 °C, which is still considerable lower than the microscopic value. Therefore, it is more likely the tantalum addition contributed to the higher BDTT. **Table 6.16** summarises the strain rate and BDTT of both micro- and macro-fracture tests for polycrystalline tungsten.

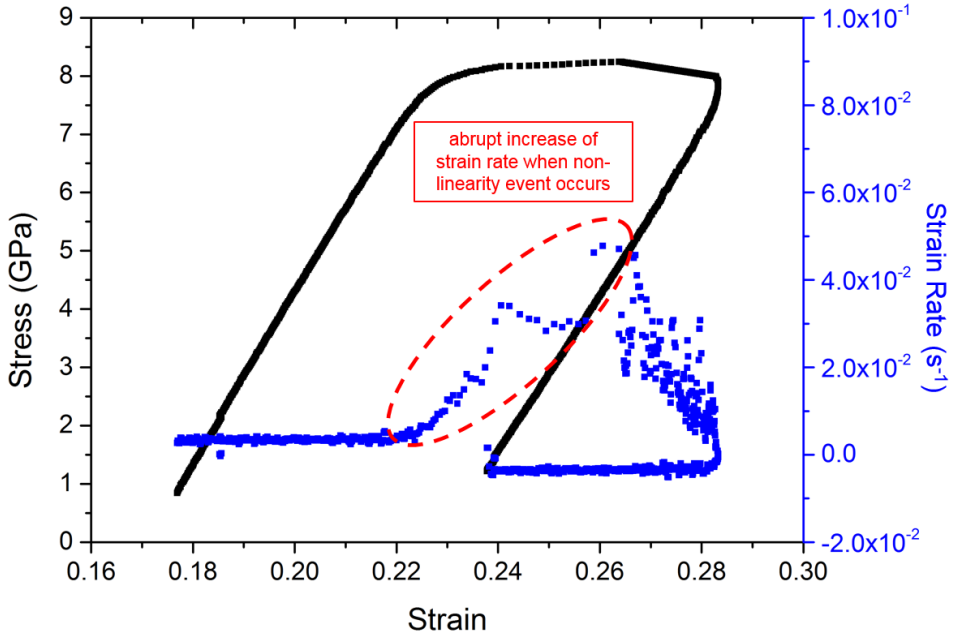


Fig. 6.41 Strain rate plotted along the stress-strain curve of cycle 7 of cantilever E2 (700 °C). The abrupt increase strain rate was observed when plasticity (or fracture) occurred

	Strain Rate (s^{-1})	**BDTT (°C)**
Micro-fracture Tests	10^{-3}~$5x10^{-2}$	~700
Macro-fracture Tests	$4x10^{-5}$~10^{-2}	150~250

Table 6.16 Summary of the strain rate and BDTT of both micro- and macro-fracture tests from polycrystalline tungsten (W-1%Ta for micro, pure W for macro)

6.5 Summary

Quantitative high-temperature micro-fracture tests and EPFM analysis were performed on chevron-notched W-1%Ta cantilevers. Fracture resistance behaviour were clearly observed for all cantilevers, possibly due to the thermally-activated dislocation activities and the further extension of the crack tip plastic zone. The conditional fracture toughness at crack instability, K_{Qc}, increased steadily with temperature. In addition, crack blunting was analysed using the initial part of the fracture resistance curves, via the blunting slope approach. The blunting coefficient, M, also increased with temperature, suggesting the thermally-activated dislocations contributed to crack blunting through dislocation shielding. The BDTT measured from W-1%Ta micro-cantilevers was approximately 700 °C, which is considerably higher than macroscopic BDTT of ~200 °C. The higher microscopic BDTT was probably due to the higher strain rate used (~10^{-2} s^{-1}), and the tantalum addition. All cantilevers failed ultimately by unstable cleavage fracture, but the amount of stable crack growth (SCG) increased steadily with temperature, suggesting the thermally-activated dislocations also promoted stable crack growth via dislocation shielding [121].

VII CONCLUSIONS AND FUTURE WORK

7.1 Summary of Results

The aim of this thesis is to improve current room temperature micro-fracture tests so that it can be applied to semi-brittle tungsten at high temperatures. This was achieved by introducing a chevron notch for pre-cracking automatically and providing crack stability. In addition, a nanoindentation-based load partial-unload method was developed for accurate crack length measurements. Combination of these two implements allowed the elastic-plastic fracture mechanical (EPFM) analysis to be applied on the microscale W-1%Ta sample, which provided a better description of the fracture process in the presence of plasticity. The EPFM parameter, J-integral, were measured at each crack increment, allowing the fracture resistance curve (J-R curve) to be calculated. Conditional fracture toughness value at crack initiation (K_{Qi}) and instability (K_{Qc}) were deduced from the J-R curves. An improved indenter/sample temperature matching methodology was also developed on the high-temperature nanoindenter (Micro Materials® NanoTest Xtreme) to effectively minimise the thermal drift during high-temperature tests. Fracture toughness and stable crack growth all increased with temperature, and a brittle-to-ductile transition temperature was captured at approximately 700 °C. This improved high-temperature micro-fracture testing technique can now be readily applied to both ion- and neutron-irradiated tungsten.

Chapter IV used finite element modelling (FEM) to optimise the chevron notch design. An optimum chevron notch geometry (a_0=0, a_1=0.7) was designed for maximum stable crack growth with sensible stiffness drop in a pentagonal cross-sectioned cantilever with constant thickness and width (B/W=1). The FE models also provided the unique relationships between

cantilever stiffness and crack length, which were used to estimate the stable crack length. Due to intrinsic brittleness, single crystal silicon was chosen to validate the chevron notch design. Fracture toughness measured from two chevron-notched Si micro-cantilevers were 0.85±0.04 $MPa \cdot m^{0.5}$. This value was in good agreement with macroscopic literature values (0.7~1 $MPa \cdot m^{0.5}$), and significantly reduce the amount of overestimation from straight-notched micro-cantilevers (due to additional load to generate a sharp pre-crack).

Chapter V successfully demonstrated the usage of chevron-notched micro-cantilevers for measuring the RT fracture resistance behaviour of W-1%Ta. Test parameters of the load partial-unload method were also discussed, so that accurate elastic cantilever stiffness could be measured and used for crack length estimation. LEFM fracture toughness (K_{Ic}) and EPFM fracture toughness (condition value calculated from J-R curves at crack instability, K_{Qc}) from two W-1%Ta micro-cantilevers were 4.3±0.2 and 26.7±2.3 $MPa \cdot m^{0.5}$. The EPFM-calculated value was significantly higher than macroscopic values (6~16 $MPa \cdot m^{0.5}$). Possible reason for this is the larger crack tip plastic zone (r_y=200~1500 nm) in comparison with the microscale cantilever, which may supress the crack propagation. Stable crack growth along with significant plasticity were observed in most cantilevers, suggesting crack stability was provided by the stable chevron geometry and also crack tip plasticity.

Chapter VI first demonstrated the importance of thermal stability to surface scanning quality and displacement measurements. Temperature mismatch between the indenter and the sample could be diagnosed via the slope of the pre-indentation thermal drift. A criterion for good thermal stability was defined (pre-indentation drift rate < 0.03 nm/s). Results from high-temperature micro-fracture tests of W-1%Ta cantilevers exhibited a gradual brittle-to-ductile transition behaviour. The EPFM-calculated fracture instability toughness K_{Qc} were found to

increase steadily with temperature, ranging from 28.5±3 MPa·$m^{0.5}$ at 400 °C to 40.5±3.2 MPa·$m^{0.5}$ at 700 °C, whereas the fracture initiation toughness K_{Qi} maintained constant (~2 MPa·$m^{0.5}$) throughout the entire temperature range. Microscopic K_{Qc} were again significantly higher than the macroscopic values, possibly due to the thermally-activated dislocation activities and the extended crack tip plastic zone (~ 5 μm at 700 °C). Stable crack growth were also found to increase stably with temperature (from 500 nm at RT to 800 nm at 700 °C). Post-test SEM fracture surface examinations showed extensive river-like patterns, providing strong evidence for the thermally-activated dislocation activities, which contributed to the larger fracture toughness and stable crack growth through enhanced dislocation shielding.

This thesis demonstrated that the fracture resistance behaviour of W-1%Ta can be measured using chevron-notched micro-cantilevers. The technique is also compatible with high-temperature nanoindentation. This chevron-notched micro-fracture testing technique has advantages over conventional macro-fracture tests in both ion- and neutron-irradiated sample. It allows fracture properties to be measured from micrometre thick ion-irradiated layer, and significantly reduce the amount of radioactive material as working with neutron-irradiated sample. However, field measurements of the crack tip plastic zone will be essential for understanding the size-dependent crack tip plasticity effect to the fracture behaviour, by using a combination of *in-situ* techniques (EBSD, TEM, μ-Laue) and dislocation-based crack tip modelling.

7.2 Future Works

7.2.1 Micro-Fracture Tests on Ion-Irradiated Tungsten

High-temperature micro-fracture tests using chevron-notched cantilevers can be performed on ion-irradiated tungsten. If the ion-irradiated layer overlaps with the stable crack growth regime, the EPFM fracture resistance curve approach can provide quantitative analysis on the crack path in the presence of irradiation-induced defects. This can be conducted in parallel with microstructural characterisation via cross-sectional TEM and SRIM (Stopping Range of Ions in Matter) estimation of the irradiated layer, shown in **Fig. 7.1**. Shift of BDTT due to irradiation-induced defects can also be obtained experimentally. As nanoscale defect clusters may act as barriers for the dislocation glide, it will be possible to measure the change in activation energy and provide experimental validation for using ion-irradiation as surrogates to neutron-irradiation.

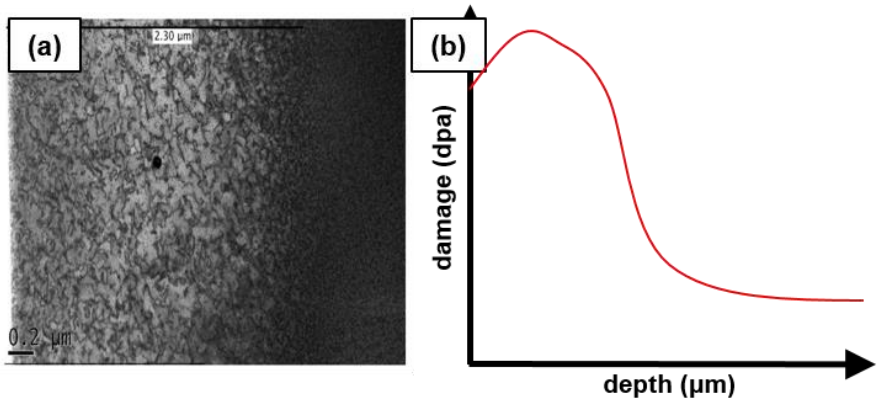


Fig. 7.1 (a) Cross-sectional TEM analysis, and the **(b)** SRIM calculation of the ion-irradiated damaged zone

7.2.2 Measuring the Macroscopic Fracture Resistance Behaviour of Tungsten

Macroscopic fracture tests using chevron-notched four-point bending matchsticks (11 x 1 x 1 mm) can be conducted on the same tungsten alloy (W-1%Ta). The macroscopic fracture specimens tested by Wurster et al. [108] used razor-blade cut notches, shown in **Fig. 7.2**. They did not perform stable crack growth experiments and EPFM analysis due to the blunter notch. Chevron-notched fracture specimens, as demonstrated previously, provide an attractive notching strategy for performing stable crack growth tests. Therefore, macroscopic fracture toughness values considering plasticity can be calculated via EPFM analysis. This will provide a more precise comparison with microscopic fracture toughness values. Currently, a house-made chevron notching apparatus is available for introducing chevron notches to four-point bending matchsticks. The apparatus, specimen, and test setup are shown in **Fig. 7.3** and **7.4**.

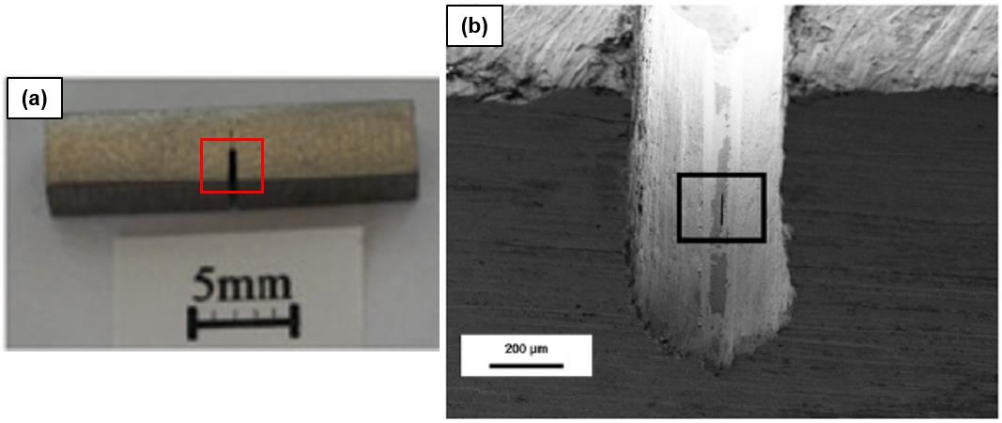


Fig. 7.2 (a) Macroscopic three-point bending fracture specimen used by Wurster et al. [108], and the **(b)** razor blade cut notch

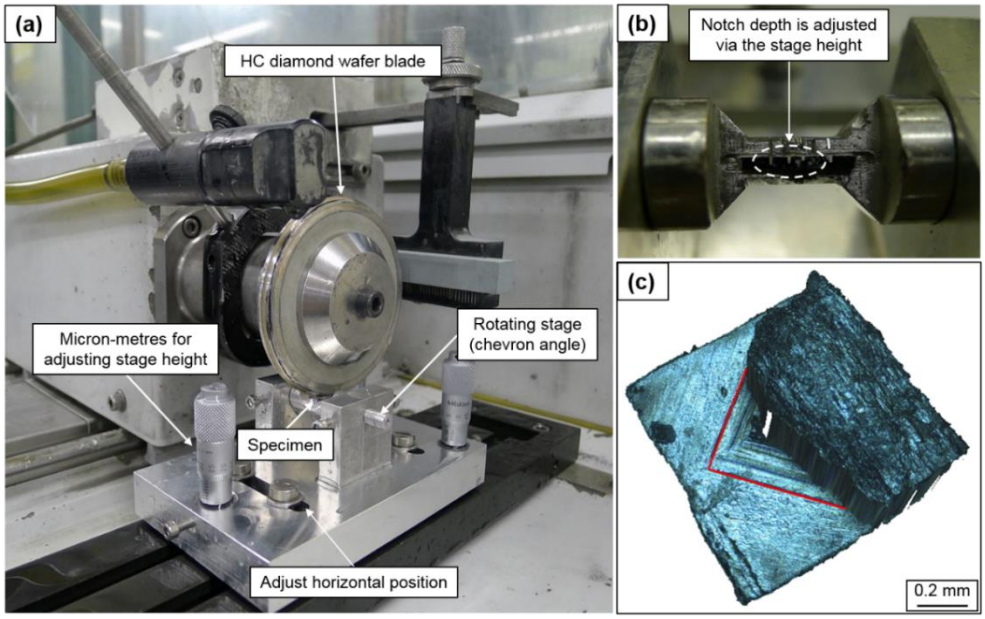


Fig. 7.3 Chevron notching apparatus. The chevron angle and notch depth can be adjusted via the rotation and height of the stage. **Figure 7.1(c)** is a surface profilometry of a chevron-notched fractured surface

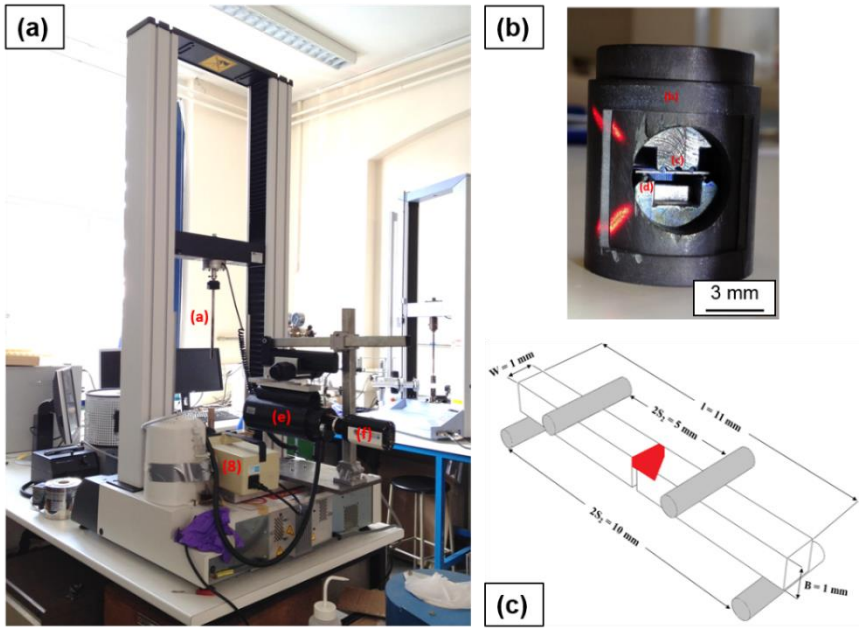


Fig. 7.4 (a) Oxford four-point bending setup (with camera for digital image correlation), the **(b)** high-temperature rig, and the **(c)** chevron notched matchsticks design

7.2.3 Modelling of Dislocation-Crack Tip Interaction

Micro-cantilever fracture tests can provide valuable information for dislocation dynamic modellers. As individual microstructural features (i.e. slip planes, crystal orientations, grain boundaries, and precipitates) can be isolated on a single specimen, it is therefore possible to model the effects of real microstructural features to the micro-deformation behaviour, using dislocation-based models. Previous work by Roberts et al. [116, 120, 122-128] has successfully estimated the BDT of single crystal BCC metals using 2D dislocation dynamic models. While an Arrhenius-type strain-rate/activation energy relationship can be explicitly deduced from their model, in term of realistic microstructure and boundary conditions, it was rather simplified. Modellers can now benefit from micro-fracture tests using cantilevers with well-defined crystal orientation and cleavage plane, shown in **Fig. 7.5**. This will allow crack tip plasticity with real microstructures and boundary conditions, to be modelled using 3D discrete dislocation dynamic (3D-DDD).

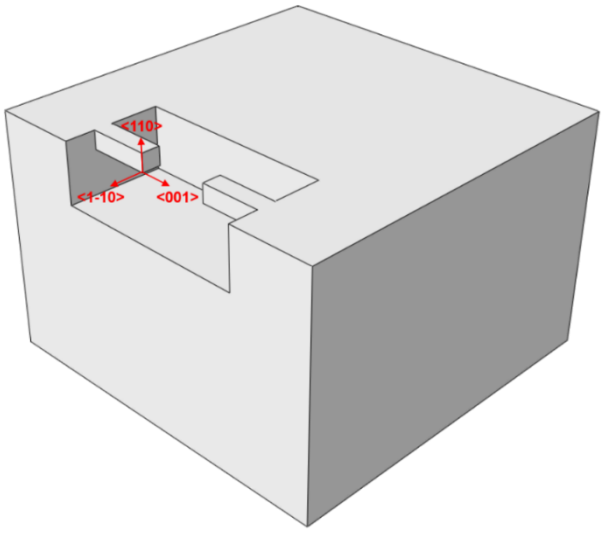


Fig. 7.5 Micro-cantilevers with rectangular cross section and well-defined crystal orientations

VIII REFERENCES

1. Marquis, E.A., Hyde, J.M., Saxey, D.W., Lozano-Perez, S., de Castro, V., Hudson, D., Williams, C.A., Humphry-Baker, S., Smith, G.D.W., *Nuclear reactor materials at the atomic scale.* Materials Today, 2009. **12**(11): p. 30-37.
2. Zinkle, S.J. and G.S. Was, *Materials challenges in nuclear energy.* Acta Materialia, 2013. **61**(3): p. 735-758.
3. Zinkle, S.J. and J.T. Busby, *Structural materials for fission & fusion energy.* Materials Today, 2009. **12**(11): p. 12-19.
4. Miyazawa, J., *Fusion Triple Product and the Density Limit of High-Density Internal Diffusion Barrier Plasma in LHD,* in *35th EPS Conference on Plasma Physics*2008. p. 4-7.
5. Culham Centre for Fusion Energy, *ITER: a brief introduction*. Available from: http://www.ccfe.ac.uk/ITER.aspx
6. EUROfusion, *Comparison of JET and ITER*. 2014; Available from: https://www.euro-fusion.org/2014/01/comparison-of-jet-and-iter/.
7. Bolt, H., Barabash, V., Krauss, W., Linke, J., Neu, R., Suzuki, S., Yoshida, N., Asdex Upgrade Team, *Materials for the plasma-facing components of fusion reactors.* Journal of Nuclear Materials, 2004. **329-333**(Part A): p. 66-73.
8. Bloom, E.E., *The challenge of developing structural materials for fusion power systems.* Journal of Nuclear Materials, 1998. **258-263**(Part 1): p. 7-17.
9. Baluc, N., Schaublin, S., Spatig, P., Victoria, M., *On the potentiality of using ferritic/martensitic steels as structural materials for fusion reactors.* Nuclear Fusion, 2004. **44**(1): p. 56.
10. Kim, Y.M., Hong, M.H., Lee, S.H., Kim, E.P., Lee, S., Noh, J.W., *The Effect of Yttrium Oxide on the Sintering Behaviour and Hardness of Tungsten.* Metals and Materials International, 2006. **12**(3): p. 245-248.
11. Rieth, M., et al., *Recent progress in research on tungsten materials for nuclear fusion applications in Europe.* Journal of Nuclear Materials, 2013. **432**(1-3): p. 482-500.
12. Riedle, J., P. Gumbsch, and H.F. Fischmeister, *Cleavage Anisotropy in Tungsten Single Crystals.* Physical Review Letters, 1996. **76**(19): p. 3594-3597.
13. Giannattasio, A., Tarleton, E., Yao, Z., Roberts, S.G., *Brittle-ductile transitions in polycrystalline tungsten.* Philosophical Magazine, 2010. **90**(30): p. 3947-3959.
14. Giannattasio, A. and S.G. Roberts, *Strain-rate dependence of the brittle-to-ductile transition temperature in tungsten.* Philosophical Magazine, 2007. **87**(16-17): p. 2589-2598.
15. Gumbsch, P., Riedle, J., Hartmaier, A., Fischmeister, H.F., *Controlling Factors for the Brittle-to-Ductile Transition in Tungsten Single Crystals.* Science, 1998. **282**(5392): p. 1293.
16. Romaner, L., C. Ambrosch-Draxl, and R. Pippan, *Effect of Rhenium on the Dislocation Core Structure in Tungsten.* Physical Review Letters, 2010. **104**(19): p. 195503.
17. Medvedeva, N.I., Y.N. Gornostyrev, and A.J. Freeman, *Electronic Origin of Solid Solution Softening in bcc Molybdenum Alloys.* Physical Review Letters, 2005. **94**(13): p. 136402.

18. Garfinkle, M., *Room-temperature tensile behaviour of <100> oriented tungsten single crystals with rhenium in dilute solid solution.* NASA-TN-D-3190, 1966.
19. Fukuda, M., Yabuuchi, K., Nogami, S., Hasegawa, A., Tanaka, T., *Microstructural development of tungsten and tungsten–rhenium alloys due to neutron irradiation in HFIR.* Journal of Nuclear Materials, 2014. **455**(1): p. 460-463.
20. Rieth, M. and A. Hoffmann, *Influence of microstructure and notch fabrication on impact bending properties of tungsten materials.* International Journal of Refractory Metals and Hard Materials, 2010. **28**(6): p. 679-686.
21. Németh, A.A.N., Reiser, J., Armstrong, D.E.J., Rieth, M., *The nature of the brittle-to-ductile transition of ultra fine grained tungsten (W) foil.* International Journal of Refractory Metals and Hard Materials, 2015. **50**(Supplement C): p. 9-15.
22. Faleschini, M., Kreuzer, H., Kiener, D., Pippan, R., *Fracture toughness investigations of tungsten alloys and SPD tungsten alloys.* Journal of Nuclear Materials, 2007. **367-370**(Part A): p. 800-805.
23. Kurishita, H., Matsuo, S., Arakawa, H., Kobayashi, S., Nakai, K., Takida, T., Takebe, K., Kawai, M., *Superplastic deformation in W–0.5wt.% TiC with approximately 0.1μm grain size.* Materials Science and Engineering: A, 2008. **477**(1): p. 162-167.
24. He, G., Xu, K., Guo, S., Qian, X., Yang, Z., Liu, G., Li, J., *Preparation of tungsten fiber reinforced-tungsten/copper composite for plasma facing component.* Journal of Nuclear Materials, 2014. **455**(1): p. 225-228.
25. Du, J., Hoschen, T., Rasinski, M., You, J.H., *Shear debonding behavior of a carbon-coated interface in a tungsten fiber-reinforced tungsten matrix composite.* Journal of Nuclear Materials, 2011. **417**(1): p. 472-476.
26. Was, G.S., *Fundamentals of Radiation Materials Science - Metals and Alloys*. 2nd ed. 2017: Springer.
27. Odette, G.R. and Lucas, G.E., *Recent progress in understanding reactor pressure vessel steel embrittlement.* Radiation Effects and Defects in Solids, 1998. **144**(1-4): p. 189-231.
28. Odette, G.R. and Lucas, G.E., *Embrittlement of nuclear reactor pressure vessels.* JOM, 2001. **53**(7): p. 18-22.
29. Hosemann, P., Shin, C., and Kiener, D., *Small scale mechanical testing of irradiated materials.* Journal of Materials Research, 2015. **30**(9): p. 1231-1245.
30. Hosemann, P., Kiener, D., Wang, Y., Maloy, S.A., *Issues to consider using nano indentation on shallow ion beam irradiated materials.* Journal of Nuclear Materials, 2012. **425**(1): p. 136-139.
31. Griffith, A.A., *The phenomena of rupture and flow in solids.* Philosophical Transactions of the Royal Society of London. Series A, 1921. **221**(582-593): p. 163.
32. Westergaard, H.M., *Bearing Pressures and Cracks.* Journal of Applied Mechanics, 1939. **6**: p. 49-53.
33. Irwin, G.R., *Analysis of Stresses and Strains Near the End of a Crack Traversing a Plate.* J. Appl. Mech., 1957.
34. Irwin, G.R. *Plastic zone near a crack and fracture toughness*. in *Proceeding Seventh Sagamore Conference*. 1961.
35. Anderson, T.L., *Fracture Mechanics: Fundamentals and Applications*. Third Edition ed. 2005.
36. ASTM International, *ASTM E399-12e3 Standard Test Method for Linear-Elastic Plane-Strain Fracture Toughness K_{Ic} of Metallic Materials*, 2012.

37. Rice, J.R., *A Path Independent Integral and the Approximate Analysis of Strain Concentration by Notches and Cracks.* Journal of Applied Mechanics, 1968. **35**(2): p. 379-386.
38. Rice, J.R., *Mathematical Analysis in the Mechanics of Fracture: An Advanced Treatise.* Academic Press New York 1968. **2**: p. 191-311.
39. Hertzberg, R.W., *Deformation and Fracture Mechanicas of Engineering Materials*. 3 ed. 1989: John Wiley & Sons.
40. Lawn, B.R., Evans, A.G., Marshall, D.B., *Elastic/Plastic Indentation Damage in Ceramics: The Median/Radial Crack System.* Journal of the American Ceramic Society, 1980. **63**(9-10): p. 574-581.
41. Di Maio, D. and Roberts, S.G., *Measuring fracture toughness of coatings using focused-ion-beam-machined microbeams.* Journal of Materials Research, 2005. **20**(2): p. 299-302.
42. Armstrong, D.E.J., Wilkinson, A.J., and Roberts, S.G., *Micro-mechanical measurements of fracture toughness of bismuth embrittled copper grain boundaries.* Philosophical Magazine Letters, 2011. **91**(6): p. 394-400.
43. Armstrong, D.E.J., Wilkinson, A.J., and Roberts, S.G., *Nanoindentation and micro-mechanical fracture toughness of electrodeposited nanocrystalline Ni-W alloy films.* Thin Solid Films, 2012. **520**(13): p. 4369-4372.
44. Norton, A.D., Falco, S., Young, N., Severs, J., Todd, R.I., *Microcantilever investigation of fracture toughness and subcritical crack growth on the scale of the microstructure in Al2O3.* Journal of the European Ceramic Society, 2015. **35**(16): p. 4521-4533.
45. Chan, H., Roberts, S.G., and Gong, J., *Micro-scale fracture experiments on zirconium hydrides and phase boundaries.* Journal of Nuclear Materials, 2016. **475**(Supplement C): p. 105-112.
46. Wurster, S., Motz, C., and Pippan, P., *Characterization of the fracture toughness of micro-sized tungsten single crystal notched specimens.* Philosophical Magazine, 2012. **92**(14): p. 1803-1825.
47. Eisenhut, L., Schaefer, F., Gruenewald, P., Weiter, L., Marx, M., Motz, C., *Effect of a dislocation pile-up at the neutral axis on trans-crystalline crack growth for micro-bending fatigue.* International Journal of Fatigue, 2017. **94**(Part 1): p. 131-139.
48. Kiener, D., Motz, C., Rester, M., Jenko, M., Dehm, G., *FIB damage of Cu and possible consequences for miniaturized mechanical tests.* Materials Science and Engineering: A, 2007. **459**(1): p. 262-272.
49. Hofmann, F.T., Tarleton, E., Harder, R.J., Philips, N.W., Clark, J.N., Robinson, I.K., Abbey, B., Liu, W., Beck, C., *Coherent X-ray measurements of ion-implantation-induced lattice strains in nano-crystals.* ARXIV: Condensed Matter - Materials Science, 2016.
50. Mueller, M.G., Pejchal, V., Zagar, G., Singh, A., Cantoni, M., Mortensen, A., *Fracture toughness testing of nanocrystalline alumina and fused quartz using chevron-notched microbeams.* Acta Materialia, 2015. **86**: p. 385-395.
51. Sebastiani, M., Johanns, K.E., Herbert, E.G., Carassiti, F., Pharr, G.M., *A novel pillar indentation splitting test for measuring fracture toughness of thin ceramic coatings.* Philosophical Magazine, 2015. **95**(16-18): p. 1928-1944.
52. Sebastiani, M., Bemporad, E., Carassiti, F., Schwarzer, N., *Residual stress measurement at the micrometer scale: focused ion beam (FIB) milling and nanoindentation testing.* Philosophical Magazine, 2011. **91**(7-9): p. 1121-1136.

53. Liu, S., Wheeler, J.M., Howie, P.R., Zeng, X.T., Michler, J., Clegg, W.J., *Measuring the fracture resistance of hard coatings.* Applied Physics Letters, 2013. **102**(17): p. 171907.
54. Jaya B, N., Jayaram, V., and Biswas, S.K., *A new method for fracture toughness determination of graded (Pt,Ni)Al bond coats by microbeam bend tests.* Philosophical Magazine, 2012. **92**(25-27): p. 3326-3345.
55. Jaya, B.N., Bhowmick, S., Asif, S.A.S., Warren, O.L., Jayaram, V., *Optimization of clamped beam geometry for fracture toughness testing of micron-scale samples.* Philosophical Magazine, 2015. **95**(16-18): p. 1945-1966.
56. Jaya, B.N. and Jayaram, V., *Crack stability in edge-notched clamped beam specimens: modeling and experiments.* International Journal of Fracture, 2014. **188**(2): p. 213-228.
57. McLean, M.J., Wade, C.A., Watanabe, M., Vinci, R.P., *Microscale Fracture Toughness of Bismuth Doped Copper Bicrystals Using Double Edge Notched Microtensile Tests.* Experimental Mechanics, 2014. **54**(4): p. 685-688.
58. Jaya, B.N., Kirchlechner, C., and Dehm, G., *Can microscale fracture tests provide reliable fracture toughness values? A case study in silicon.* Journal of Materials Research, 2015. **30**(5): p. 686-698.
59. Hintsala, E.D., Bhowmick, S., Yueyue, X., Ballarini, R., Asif, S.A.S., Gerberich. W.W., *Temperature dependent fracture initiation in microscale silicon.* Scripta Materialia, 2017. **130**: p. 78-82.
60. Samuels, J. and Roberts, S.G., *The Brittle Ductile Transition in Silicon .1. Experiments.* Proceedings of the Royal Society of London Series a-Mathematical Physical and Engineering Sciences, 1989. **421**(1860): p. 1-&.
61. Armstrong, D.E.J. and Tarleton, E., *Bend Testing of Silicon Microcantilevers from 21°C to 770°C.* JOM, 2015. **67**(12): p. 2914-2920.
62. Best, J.P., Zechner, J., Wheeler, J.M., Schoeppner, R., Morstein, M., Michler, J., *Small-scale fracture toughness of ceramic thin films: the effects of specimen geometry, ion beam notching and high temperature on chromium nitride toughness evaluation.* Philosophical Magazine, 2016. **96**(32-34): p. 3552-3569.
63. Jaya, B.N., Wheeler, J.M., Wehrs, J., Best, J.P., Soler, R., Michler, J., Kirchlechner, C., *Microscale Fracture Behavior of Single Crystal Silicon Beams at Elevated Temperatures.* Nano Letters, 2016. **16**(12): p. 7597-7603.
64. Castaing, J., Veyssiere, P., Kubin, L.P., Rabier, J., *The plastic deformation of silicon between 300°C and 600°C.* Philosophical Magazine A, 1981. **44**(6): p. 1407-1413.
65. Wheeler, J.M. and Michler, J., *Elevated temperature, nano-mechanical testing in situ in the scanning electron microscope.* Review of Scientific Instruments, 2013. **84**(4): p. 045103.
66. Liu, S., Wheeler, J.M., Michler, J., Zeng, X.T., Clegg, W.J., *Plastic flow at the theoretical yield stress in ceramic films.* Scripta Materialia, 2016. **117**(Supplement C): p. 24-27.
67. Junn, N., *A Bending Method for Direct Measurement of Fracture Energy of Brittle Material.* Japanese Journal of Applied Physics, 1964. **3**(7): p. 422.
68. Tattersall, H.G. and Tappin, G., *The work of fracture and its measurement in metals, ceramics and other materials.* Journal of Materials Science, 1966. **1**(3): p. 296-301.
69. Pook, L.P., *An approach to a quality control KIc testpiece.* International Journal of Fracture Mechanics, 1972. **8**(1): p. 103-104.

70. Barker, L.M., *A simplified method for measuring plane strain fracture toughness.* Engineering Fracture Mechanics, 1977. **9**(2): p. 361-369.
71. Munz, D., Bubsey, R.T., and Srawley, J.E., *Compliance and stress intensity coefficients for short bar specimens with chevron notches.* International Journal of Fracture, 1980. 16(4): p. 359-374.
72. Raju, I.S., Newman, J.C., *Three-dimensional finite-element analysis of chevron-notched fracture specimens.* Chevron-Notched Specimens: Testing and Stress Analysis, 1984. ASTM STP 855: p. 33-48.
73. Ingraffea, A.R. *Three-Dimensional Finite and Boundary Element Calibration of the Short-Rod Specimen*. Symposium on Chevron-Notched Specimens: Testing and Stress Analysis 1983.
74. Mendelson, A., Ghosen, L.J., *Three-Dimensional Analysis of Short Bar Chevonr-Notched Specimens by Boundary Integral Method.* Symposium on Chevron-Notched Specimens: Testing and Stress Analysis, 1983
75. Bubsey, R.T., Orange, T.W., Pierce, W.S., Shannon Jr., J.L., *Closed-Form Expressions for Crack-Mouth Displacements and Stress Intensity Factors for Chevron-Notched Short Bar and Short Rod Specimens Based on Experimental Compliance Measurements.* NASA Techanical Memorandum, 1992. **83796**.
76. Volkert, C.A. and Minor, A.M., *Focused Ion BeamMicroscopy and Micromachining.* MRS Bulletin, 2007. **32**.
77. Pethicai, J.B., Hutchings, R., and Oliver, W.C., *Hardness measurement at penetration depths as small as 20 nm.* Philosophical Magazine A, 2006. **48**(4): p. 593-606.
78. Wheeler, J.M., Armstrong, J.M., Heinz, W., Schwaiger, R., *High temperature nanoindentation: The state of the art and future challenges.* Current Opinion in Solid State and Materials Science, 2015. **19**(6): p. 354-366.
79. Nowak, J.D., Rzepiejewska-Malyska, K.A., Major, R.C., Warren, O.L., Michler, J., *In-situ nanoindentation in the SEM.* Materials Today, 2009. **12**(Electron Microscopy Special Issue): p. 44-45.
80. Warren, O.L., Shan, Z.W., Asif, S.A.S, Stach, E.A., Morris, J.W., Minor, A.M., *In situ nanoindentation in the TEM.* Materials Today, 2007. **10**(4): p. 59-60.
81. Durst, K. and Maier, V., *Dynamic nanoindentation testing for studying thermally activated processes from single to nanocrystalline metals.* Current Opinion in Solid State and Materials Science, 2015. **19**(6): p. 340-353.
82. Agilent Technologies, *G200 Nanoindenter Application Note.*
83. Tabor, D., *The Hardness of Metals*. 1951: Oxford University Press.
84. Fischer-Cripps, A.C., *Nanoindentation*. 2005: Springer.
85. Oliver, W.C. and Pharr, G.M., *An improved technique for determining hardness and elastic modulus using load and displacement sensing indentation experiments.* Journal of Materials Research, 1992. **7**(6): p. 1564-1583.
86. Pethica, J.B. and Oliver, W.C., *Tip Surface Interactions in STM and AFM.* Physica Scripta, 1987. **1987**(T19A): p. 61.
87. Li, X. and Bhushan, B., *A review of nanoindentation continuous stiffness measurement technique and its applications.* Materials Characterization, 2002. **48**(1): p. 11-36.
88. Micro Materials. *The NanoTest Xtreme*. Available from: http://www.micromaterials.co.uk/products/nanotest-xtreme/.

89. Hysitron, *xSol High Temperature Stage*. Available from: https://www.hysitron.com/products-services/options-upgrades/xsol-high-temperature-stage.
90. Anton Paar, *High Temperature Ultra Nanoindenter (UNHT^3 HTV)*. Available from: http://www.anton-paar.com/uk-en/products/details/high-temperature-nanoindentation-unht3-htv/.
91. Nanomechanics Inc., *InSEM HT Microprobe*. Available from: http://nanomechanicsinc.com/insem-systems-page/.
92. Alemnis, *High Temperature Module*. Available from: http://alemnis.com/products/high-temperature-module/.
93. Surface Tec GmbH, *Laser Heater for Nanoindentation.*
94. Gibson, J.S.K.-L., *Mechanical Behaviour of Irradiated Tungsten for Fusion Power*, DPhil Thesis, Department of Materials, University of Oxford, 2015.
95. Wheeler, J.M. and Michler, J., *Invited Article: Indenter materials for high temperature nanoindentation.* Review of Scientific Instruments, 2013. **84**(10): p. 101301.
96. *ABAQUSCAE User's Manual 6.14.* Dassault Systèmes Simulia Corp 2009.
97. Sarrafi-Nour, G.R., Coyle, T.W., and Fett, T., *A weight function for the crack surface tractions in chevron-notched specimens.* Engineering Fracture Mechanics, 1998. **59**(4): p. 439-445.
98. He, M.Y., Evans, A.G. *Three dimensional finite element analysis of chevron-notched, three-point and four-point bend specimens*. in *Fracture Mechanics: Twenty-Second Symposium*. 1990. Atlanta, Georgia, USA.
99. Calomino, A.M. and Ghosn, L.J., *Optimum notch configurations for the chevron-notched four-point bend specimens.* International Journal of Fracture, 1995. **72**(4): p. 311-326.
100. Bluhm, J.I., *Slice synthesis of a three dimensional "work of fracture" specimen.* Engineering Fracture Mechanics, 1975. **7**(3): p. 593-604.
101. Mueller, M.G., Žagar, G., and Mortensen, A., *Stable room-temperature micron-scale crack growth in single-crystalline silicon.* Journal of Materials Research, 2017. **32**(19): p. 3617-3626.
102. Armstrong, D.E.J., Wilkinson, A.J., and Roberts, S.G., *Measuring anisotropy in Young's modulus of copper using microcantilever testing.* Journal of Materials Research, 2009. **24**(11): p. 3268-3276.
103. Plansee SE, *Tungsten Product Sheet*. Available from: https://www.plansee.com/en/materials/tungsten.html#c902.
104. Gong, J. and Wilkinson, A.J., *Anisotropy in the plastic flow properties of single-crystal α titanium determined from micro-cantilever beams.* Acta Materialia, 2009. **57**(19): p. 5693-5705.
105. Hirth, J.P., *The influence of grain boundaries on mechanical properties.* Metallurgical Transactions, 1972. **3**(12): p. 3047-3067.
106. Gibson, J.S.K-L, Armstrong, D.E.J., Roberts, S.G., *The micro-mechanical properties of ion irradiated tungsten.* Physica Scripta, 2014. **2014**(T159): p. 014056.
107. Wang, Z., uan, Y., Arshad, K., Wang, J., Zhou, Z., Tang, J., Lu, G.H., *Effects of tantalum concentration on the microstructures and mechanical properties of tungsten-tantalum alloys.* Fusion Engineering and Design.

108. Wurster, S., Gludovatz, B., Hoffmann, A., Pippan, R. *Fracture behaviour of tungsten–vanadium and tungsten–tantalum alloys and composites.* Journal of Nuclear Materials, 2011. **413**(3): p. 166-176.
109. Gludovatz, B., Wurster, S., Hoffmann, A., Pippan, R., *A study into the crack propagation resistance of pure tungsten.* Engineering Fracture Mechanics, 2013. **100**(Supplement C): p. 76-85.
110. Gong, J. and Wilkinson, A.J., *Investigation of elastic properties of single-crystal α-Ti using microcantilever beams.* Philosophical Magazine Letters, 2010. **90**(7): p. 503-512.
111. Kirchlechner, C., Grosinger, W., Kapp, M.W., Imrich, P.J., Micha, J.S., Ulrich, O., Keckes, J., Dehm, G., Motz, C., *Investigation of reversible plasticity in a micron-sized, single crystalline copper bending beam by X-ray μLaue diffraction.* Philosophical Magazine, 2012. **92**(25-27): p. 3231-3242.
112. Demir, E. and Raabe, D., *Mechanical and microstructural single-crystal Bauschinger effects: Observation of reversible plasticity in copper during bending.* Acta Materialia, 2010. **58**(18): p. 6055-6063.
113. ASTM International, *E 1820 Standard Test Method for Measurement of Fracture Toughness of Metallic Materials.* 2003.
114. Lowrie, R. and Gonas, A.M., *Single-Crystal Elastic Properties of Tungsten from 24° to 1800°C.* Journal of Applied Physics, 1967. **38**(11): p. 4505-4509.
115. Gibson, J.S.K.L., Roberts, S.G., and Armstrong, D.E.J., *High temperature indentation of helium-implanted tungsten.* Materials Science and Engineering: A, 2015. **625**(Supplement C): p. 380-384.
116. Giannattasio, A., Yao, Z., Tarleton, E., Roberts, S.G., *Brittle–ductile transitions in polycrystalline tungsten.* Philosophical Magazine, 2010. **90**(30): p. 3947-3959.
117. ASTM International, *ASTM E1820-16 Standard Test Method for Measurement of Fracture Toughness*, 2016.
118. Murphy, J.D., Giannattasio, A., Yao, Z., Hetherington, C.J.D., Nellist, P.D., Roberts, S.G., *The mechanical properties of tungsten grown by chemical vapour deposition.* Journal of Nuclear Materials, 2009. **386-88**: p. 583-586.
119. Brede, M. and Haasen, P., *The brittle-to-ductile transition in doped silicon as a model substance.* Acta Metallurgica, 1988. **36**(8): p. 2003-2018.
120. Giannattasio, A. and Roberts, S.G., *Strain-rate dependence of the brittle-to-ductile transition temperature in tungsten.* Philosophical Magazine, 2007. **87**(17): p. 2589-2598.
121. Booth, A.S., Ellis, M., Roberts, S.G., Hirsch, P.B., *Dislocation-Controlled Stable Crack-Growth in Mo and Mgo.* Materials Science and Engineering a-Structural Materials Properties Microstructure and Processing, 1993. **164**(1-2): p. 270-274.
122. Hirsch, P.B. and Roberts, S.G., *Modeling the Brittle Ductile Transition.* Materials Modelling : From Theory to Technology, 1992: p. 181-186.
123. Hirsch, P.B. and Roberts, S.G., *Modelling plastic zones and the brittle-ductile transition.* Philosophical Transactions of the Royal Society a-Mathematical Physical and Engineering Sciences, 1997. **355**(1731): p. 1991-2001.
124. Hirsch, P.B., Roberts, S.G., and Samuels, J., *The Brittle Ductile Transition in Silicon .2. Interpretation.* Proceedings of the Royal Society of London Series a-Mathematical Physical and Engineering Sciences, 1989. **421**(1860): p. 25-53.
125. Joseph, T.D., Tanaka, M., Wilkinson, A.J., *Brittle-ductile transitions in vanadium and iron-chromium.* Journal of Nuclear Materials, 2007. **367**: p. 637-643.

126. Roberts, S.G., *Modelling brittle-ductile transitions.* Multiscale Phenomena in Plasticity: From Experiments to Phenomenology, Modelling and Materials, 2000. **367**: p. 349-364.
127. Serbena, F.C. and Roberts, S.G., *The Brittle-to-Ductile Transition in Germanium.* Acta Metallurgica Et Materialia, 1994. **42**(7): p. 2505-2510.
128. Tanaka, M., Tarleton, E., and Roberts, S.G., *The brittle–ductile transition in single-crystal iron.* Acta Materialia, 2008. **56**(18): p. 5123-5129.